

UNIVERSITY OF PRETORIA – DEPARTMENT OF MECHANICAL AND AERONAUTICAL  
ENGINEERING



UNIVERSITEIT VAN PRETORIA  
UNIVERSITY OF PRETORIA  
YUNIBESITHI YA PRETORIA

Denkleiers • Leading Minds • Dikgopolo tša Dihlalefi

# Numerical performance analysis of novel solar tower receiver

---

By

**Marcel Slotweg**

Submitted in partial fulfilment of the requirements for the degree of

**Master of Engineering**

Department of Mechanical and Aeronautical Engineering  
Faculty of Engineering, Built Environment and Information Technology

University of Pretoria

February 2019

Supervisor: Prof KJ Craig  
Co-supervisor: Prof JP Meyer

## Summary

---

### **Numerical performance analysis of novel solar tower receiver**

by

**Marcel Slootweg**

Supervisor: Prof KJ Craig  
Co-supervisor: Prof JP Meyer  
Department: Mechanical and Aeronautical Engineering  
University: University of Pretoria  
Degree: Master of Engineering (Mechanical Engineering)  
Keywords: Concentrating solar power (CSP), central receiver, optical, thermal, computational fluid dynamics (CFD), ray tracing, ANSYS Fluent, SolTrace

Concern over the altering climate due to the release of anthropogenic greenhouse gases has caused a major shift in the developments of ways to minimise human impact on the climate. Solar energy is seen as one of the most promising sources to transform the energy market for low-carbon energy generation. Currently, solar power is generated via photovoltaic (PV) and concentrating solar power (CSP) technologies. The advantage of CSPs to scale up renewable energy to utility level, as well as to store thermal energy for electrical power generation when the sun is not available (after sunset or during cloudy periods) makes this technology an attractive option for sustainable clean energy. CSP development, however, is still in its infancy, and for it to be a competitive form of energy-generation technology, techno-economic developments in this field need to improve the efficiency and decrease the costs of this technology. A policy report by the European Academies' Science Advisory Council (EASAC) (2011) indicated that central receiver (solar tower) CSP systems show the greatest margin for technological improvements (40% to 65% is estimated), and that an improvement in receiver technology could make the greatest contribution to increase efficiency.

This study therefore focused on analysing the optical and thermal performance of a new proposed solar cavity molten salt receiver design for a central receiver CSP system using a numerical approach. In this study, the receiver's performance was analysed by first selecting an existing heliostat field, Planta Solar 10 (PS-10). For the numerical analysis to reflect conditions that are as realistic as possible, numerical models for different aspects were selected and validated. For modelling the sun, the solar tracking numerical model proposed by Iqbal (1983) was selected and implemented after literature and comparison showed adequate results. The direct normal irradiation (DNI) was modelled by applying a clear sky model, with the parameterisation model C proposed by Iqbal (1983) as the chosen model. The variables in this model that were subject to temperature, and humidity values were more accurately presented by adding numerical approximations of the region's actual weather data. The DNI model reflected realistic fluctuations. For the thermal modelling, a validation study was conducted on impingement flow heat transfer to select an appropriate Reynolds-averaged Navier-Stokes (RANS) model that would provide accurate results when conducting the thermal performance test on the

receiver. The study concluded that the transitional Shear Stress Transport (SST) turbulence model performed the best.

A new method was also developed and validated that allows one to not only simulate complex geometries within the Monte Carlo ray tracing environment SolTrace, but also to apply the results obtained by simulating this model as a heat source within the computational fluid dynamics (CFD) environment ANSYS Fluent. This allows SolTrace modelling to be more accurate, since models do not need to be approximated to simple geometries. It also provides an alternative for solar modelling in ANSYS Fluent.

The optical analysis was conducted by first performing an analysis on the receiver aperture and studying its sensitivity on the captured flux. This was followed by analysing the optics of the proposed receiver, the flux distributions on a simplified absorber surface area, and how these distributions are altered by changing some parameters. An in-depth analysis was finally done on the absorber area by applying the aforementioned model to simulate complex geometries within SolTrace, with the results illustrating the difference of the detailed geometry on optical modelling. An alternative receiver design with improved optical features was proposed, with an initial study providing promising results. The thermal analysis was done within the CFD environment, with only a section of the absorber surface area considered, and by applying the solar flux simulated during the optical analysis as heat source within the geometry model. This allowed the model to simulate the effects of re-radiation at the surface of the absorber while simulating the heat transfer at the fluid molten salt side simultaneously. The results showed that, for the current design and requirements, the absorber surface temperature reaches impractical temperatures. Altering the design or being more lenient on the requirements has, however, shown dramatic improvements in terms of thermal performance. Sensitivity studies for both the optical and thermal analyses have shown that changes in design can dramatically improve the performance of the design, making it a possible feasible receiver design for central receiver systems.

## Acknowledgements

I would hereby like to acknowledge the following people:

- My sincere gratitude and appreciation to my supervisor, Prof Ken J Craig, for his technical guidance, in-depth feedback, general good supervisor-student relationship and the opportunities given during this study.
- My deepest thanks to my co-supervisor, Prof Josua P Meyer, for his financial and technical support in the attainment of this degree.
- My sincere appreciation for the support of my family and friends, with a special thanks to my parents, Willem and Ada Slootweg, for their endless support on so many levels.
- My thanks to all the other colleagues, academic as well as non-academic staff members of the Clean Energy Research Group in the Department of Mechanical and Aeronautical Engineering, University of Pretoria, for the pleasant and friendly working environment.

*This work is based on research supported by the National Research Foundation (NRF) and the University of Pretoria. The financial assistance of the NRF is hereby acknowledged. Opinions expressed and conclusions arrived at are those of the author and are not necessarily to be attributed to the NRF.*

## Publications

### Manuscripts under review in international journals

1. Slootweg, M., Craig, K.J., Meyer, J.P., “A computational approach to simulate the optical and thermal performances of a novel complex-geometry solar tower molten salt cavity receiver”, Solar Energy, Submitted (**IF=4.374**)

### Conference papers

1. **Slootweg, M.**, Craig, K.J., Meyer, J.P., “Investigation into central receiver design for optimal optical and thermal performance”, South African Solar Energy Conference (SASEC 2018), 25–27 June 2018, Durban, South Africa.
2. Craig, K.J., **Slootweg, M.**, Meyer, J.P., “Heat transfer enhancement in molten salt central receiver using jet impingement”, South African Solar Energy Conference (SASEC 2018), 25–27 June 2018, Durban, South Africa.
3. Craig, K.J., **Slootweg, M.**, Meyer, J.P., Robbin, S.R., Kotzé, J.C., Honiball, R., Grobler, N.J.M., Oosthuizen, E., Winterbach, T.J., Moll, W., “CFD simulation of solar receiver jet impingement heat transfer: RANS vs LES”, Proceedings of the 16th International Heat Transfer Conference (IHTC-16), 10–15 August 2018, Beijing, China.



## Contents

Summary .....	i
Acknowledgements .....	iii
Publications .....	iv
Manuscripts under review in international journals .....	iv
Conference papers .....	iv
List of figures .....	viii
List of tables .....	xiv
Nomenclature .....	xv
Symbols .....	xv
Greek symbols .....	xvi
Subscripts .....	xvii
List of abbreviations .....	xviii
Chapter 1 Introduction .....	1
1.1 Background .....	1
1.2 Motivation .....	4
1.3 Problem statement .....	6
1.4 Objective .....	6
1.5 Methodology .....	6
1.6 Layout of the thesis .....	7
Chapter 2 Literature study .....	8
2.1 Introduction .....	8
2.2 Concentrating solar power .....	8
2.2.1 Parabolic trough collector .....	9
2.2.2 Linear Fresnel collector .....	10
2.2.3 Parabolic dish .....	11
2.2.4 Central receiver .....	12
2.3 Central receiver systems .....	13
2.3.1 History and development .....	13
2.3.2 Heliostat field design .....	21
2.3.3 Receiver design .....	26
2.3.4 Secondary concentrator .....	44
2.4 Monte Carlo ray tracing .....	45
2.5 Computational fluid dynamics thermal analysis .....	46
2.5.1 Jet impingement .....	47



2.5.2	Numerical investigations.....	49
2.6	Proposed new central receiver concept.....	50
2.7	Summary and conclusion.....	51
Chapter 3	Solar tracking, DNI and heliostat field numerical modelling.....	53
3.1	Introduction.....	53
3.2	Solar tracking numerical model.....	53
3.3	Direct normal irradiance model.....	54
3.3.1	Temperature and relative humidity modelling.....	55
3.3.2	DNI model results.....	59
3.4	Heliostat field test case layout.....	60
3.5	Summary and conclusion.....	63
Chapter 4	Solar receiver setup and numerical modelling.....	64
4.1	Introduction.....	64
4.2	Receiver optical setup.....	64
4.2.1	New approach to model complex geometries in SolTrace.....	64
4.2.2	Validation of the new approach.....	67
4.3	Computational fluid dynamics thermal model.....	73
4.3.1	Vertical round jet impingement on a horizontal flat surface.....	74
4.3.2	Vertical round jet impingement on a concave surface.....	78
4.4	Conclusion.....	82
Chapter 5	Optical analysis, preliminary scoping and optimisation.....	84
5.1	Introduction.....	84
5.2	Aperture analysis and optimisation.....	84
5.2.1	Aperture angle optimisation.....	85
5.2.2	Field-to-aperture analysis.....	90
5.2.3	Aperture analysis.....	91
5.3	Receiver optical analysis.....	93
5.4	Detailed absorber flux distribution.....	99
5.4.1	Single absorber element flux analysis.....	100
5.4.2	Full absorber flux analysis.....	101
5.4.3	Flux region for heat source.....	102
5.5	New proposed design for future work.....	103
5.6	Conclusion.....	105
Chapter 6	Thermal analysis and optimisation.....	107
6.1	Introduction.....	107
6.2	Absorber design.....	107



6.3	Absorber thermal analysis.....	109
6.3.1	Geometry and computational model setup.....	109
6.3.2	Results.....	114
6.3.3	Sensitivity study.....	116
6.4	Summary and Conclusion.....	120
Chapter 7	Technical evaluation, conclusion and recommendations.....	122
7.1	Technical evaluation.....	122
7.2	Summary and conclusion.....	123
7.3	Recommendations and future work.....	125
References.....		126
Appendix A	Solar Tracking and DNI Iqbal model.....	143
A.1	Solar tracking numerical model.....	143
A.2	Direct normal irradiance model.....	147
Appendix B	Transformation from mesh element to SolTrace primitive geometry.....	151
Appendix C	Model integration.....	154
Appendix D	Polynomial response surface analysis for aperture optimisation.....	157
Appendix E	Sensitivity studies on the impingement models.....	158
E.1	Outlet boundary.....	158
E.2	Fully developed inlet profiles.....	158
E.3	Inlet turbulence kinetic energy.....	160
E.4	Constant vs piecewise linear fluid properties.....	163
Appendix F	Original receiver design.....	164
Appendix G	Volumetric heat source implementation in ANSYS Fluent.....	166
G.1	UDF script.....	166
Appendix H	Script for SolTrace simulation.....	168
H.1	SolTrace script.....	168

## List of figures

Figure 1.1: The total anthropogenic greenhouse gas emissions by economic sector (Merz, 2015). A graphic representation of the anthropogenic greenhouse gas emissions divided into its separate sector. The inner circle depicts the greenhouse gas emission shares that are emitted directly (as a percentage of the total greenhouse gas emissions) of the five sectors (results from 2010). The indirect CO <sub>2</sub> emission shares are shown on the right. “Other energy” refers to all greenhouse gas emission sources in the energy sector that exclude heat and electricity production. The data obtained from the agriculture, forestry and other land use (AFOLU) sector includes CO <sub>2</sub> emissions from decay and fires. The emissions are converted into CO <sub>2</sub> -equivalents based on the IPCC Second Assessment Report’s GWP1006 (Alley et al., 2004). .....	2
Figure 1.2: An example of the development of the world energy supply, from the current situation to the global renewable energy scenario predicted for 2050 (IRENA, 2018). .....	3
Figure 1.3: World map of the long-term average of solar DNI (Solargis, 2016). .....	3
Figure 1.4: An example of the layout of a simplified central receiver CSP plant (SQM, 2018). .....	5
Figure 2.1: A schematic illustration of PTC (International Energy Agency (IEA), 2010). .....	10
Figure 2.2: A schematic illustration of an LFC (International Energy Agency (IEA), 2010). .....	11
Figure 2.3: A schematic illustration of a parabolic dish (International Energy Agency (IEA), 2010). .....	12
Figure 2.4: A schematic illustration of a central receiver system (International Energy Agency (IEA), 2010). .....	13
Figure 2.5: The SHS concept developed by VA Baum et al. (Baum, Aparasi, & Garf, 1956). .....	14
Figure 2.6: A schematic design of the 1 000 kW Montlouis solar furnace constructed in 1957 (Trombe, 1957). .....	15
Figure 2.7: St Ilario-Nervi, Genoa: (a): Solar plant No. 1; (b): solar plant No. 2; and (c): solar plant No. 3 under construction (Francia, 1968). .....	16
Figure 2.8: (a): A comparison is made between the heliostat design and field of the PS-10 power plant in Seville, Spain, developed by Abengoa Solar (Eco-friendly-world, 2018); and (b): the Sierra SunTower power plant in Lancaster, USA, developed by eSolar (Infaimon, 2016). .....	21
Figure 2.9: The different types of heliostats (starting from the top left): (a): a serial type heliostat shown from the back used in the PS-10 heliostat field in Seville, Spain (Solúcar, 2006); (b): a universal solar tracker shown at different angles (Orshan, 2010); (c): an octahedral hexapod concept (Wikipedia, 2018); (d): a Google wire heliostat designed by Google Corporation (Google.org, 2011); and (e): a wire heliostat developed by Solaflect Energy (Solaflect Energy, 2018). .....	23
Figure 2.10: (a): The PS-20 north-facing heliostat polar field in Seville, Spain, is on the left (Wordpress.com, 2013); and (b): the Crescent Dunes surround field constructed near Tonopah, USA, on the right (Proud Green Building, 2017). .....	24
Figure 2.11: Heliostat field layouts developed with different approaches: (a): dense radially staggered method; (b): Campo code; (c): graphical method; (d) DELSOL method; and (e): biomimetic pattern. ....	25
Figure 2.12: (a): Multiple aperture field studies conducted by Schmitz et al. (2006) with multiple (six in this case) aperture design (MAD) compared to single aperture design (SAD) and surround field; and (b): Three polar fields spaced at 120° (Ramos & Ramos, 2012). .....	26
Figure 2.13: Single heliostat spot size aperture flux distribution of the PS-10 heliostat field using SolTrace (Noone et al., 2012). .....	27
Figure 2.14: Flux map distributions for the Gemasolar external receiver panels obtained with: (a): the reference aiming point; (b): Aiming Strategy 1; and (c): Aiming Strategy 6 (zero degrees refer to the southern direction) (Binotti et al., 2016). .....	27

Figure 2.15: Typical external tubular panel receivers that are implemented, such as: (a): the receiver design of the previously known SolarTres power plant project, but renamed the Gemasolar power plant (Lata, Rodriquez, & De Lara, 2008); and (b): the view of the four-panel external tubular receiver of the Ivanpah solar power plant (Hoffschmidt, 2014). ..... 29

Figure 2.16: Schematic diagrams of: (a): the external pyramid design mounted on top of a tower (Garbrecht, Al-Sibai, Kneer, & Wieghardt, 2012); (b): a close-up view of a section of the pyramid structure; and (c): the flow of the HTF within the pyramid structure (Garbrecht, Al-Sibai, Kneer, & Wieghardt, 2013). ..... 30

Figure 2.17: (a): The preliminary SCRAP receiver design as would be mounted on a solar tower; and (b): geometry of the internally finned tube with illustrations of air flow (Lubkoll, Von Backström, Harms, & Kröger, 2015). ..... 31

Figure 2.18: Examples of tubular panel cavity receivers with: (a): a schematic design of a cavity receiver by Li, Kong, Wang, Chang and Bai (2010); and (b): a implemented cavity receiver at the PS-10 solar plant in Seville, Spain (StateImpact, 2012). ..... 32

Figure 2.19: Examples of design concepts from the DLR: (a): a schematic illustration of the Solar-hybrid Power and Cogeneration (SOLHYCO) receiver concept (Amsbeck et al., 2008); and (b): the design of the Solugas receiver (Korzynietz, Quero, & Uhlig, 2012). ..... 33

Figure 2.20: Examples of volumetric receivers with: (a): a schematic of the performance of the HiTRec open-air volumetric receiver (Hoffschmidt et al., 2003); and (b): a concept design of the REFOS closed-loop volumetric receiver module (Buck, et al., 2002). ..... 34

Figure 2.21: The BDSTC: (a): schematic concept of plant (Kribus, Zaibel, Carey, Segal, & Karni, 1998); and (b): pilot plant constructed at the Masdar Institute of Science and Technology in Abu Dhabi (Mokhtar, 2011). ..... 35

Figure 2.22: The falling solid particle receiver system concept with an integrated storage and heat exchanger (left) and a close-up schematic design of the receiver (right) (Ho & Iverson, 2014). ..... 36

Figure 2.23: Falling, liquid film receivers for heat absorption in: (a): direct exposure, internal receivers for a surround field (Wu, Gobereit, Singer, Amsbeck, & Pitz-Paal, 2011); (b): direct exposure, external receivers for a surround field (Bohn & Green, 1989); (c): indirect exposure, internal film receivers for a surround or polar facing field (Ho & Iverson, 2014); and (d): direct exposure, internal film receivers for a polar field (Hildebrandt & Rose, 1985). ..... 38

Figure 2.24: A schematic representation of the dual receiver concept from: (a): the top view; and (b): the side view (Buck et al., 2006). ..... 39

Figure 2.25: A schematic concept design of an RPC pressurised air receiver (Hischier et al., 2009). . 40

Figure 2.26: A schematic layout of a preliminary concept of the hybrid pressurised air receiver (Kretzschmar & Gauché, 2012). ..... 41

Figure 2.27: A schematic designs of the impinging receiver developed by Wang (2015): (a): 3D model; and (b): 2D drawing. .... 42

Figure 2.28: A profile curve of the CPC (Winston & Hiterberger, 1975). ..... 44

Figure 2.29: (a): An illustration of clusters of receivers and their corresponding secondary concentrators (Schmitz et al., 2006); and (b): a schematic of a central receiver with a CPC “fly eye” second-stage collector (Rabl, 1976). ..... 45

Figure 2.30: A schematic illustration of a jet impingement on a flat surface, remodelled from Uddin (2008). ..... 48

Figure 2.31: A radial distribution of the Nusselt number at the surface for  $H/D = 2$  (Uddin, 2008). 48

Figure 2.32: The proposed novel receiver concept: (a): displayed in 3D; and (b): displayed from a side view with the basic workings illustrated. .... 50

Figure 2.33: A close-up view of the absorber structure with the one element shown with a sectioned view. The blue zone illustrates the HTF region and the green the absorber shell. .... 51

Figure 3.1: A graphic representation of: (a): the zenith angles ( $\theta$ ); and (b): the azimuth ( $\psi$ ) angles for the 1<sup>st</sup> and 180<sup>th</sup> Julian days, comparing the Iqbal model to NREL’s MIDC SPA (NREL, 2018). The error of the Iqbal model compared to the SPA is displayed in (c). ..... 54

Figure 3.2: (a): Comparison of different orders of discrete trigonometric approximations to approximate the averaged data of the relative humidity; and (b): the maximum and minimum temperatures..... 58

Figure 3.3: The fourth-order discrete trigonometric approximation of the averaged maximum and minimum temperature, as well as the annual fluctuations in relative humidity for Seville, Spain. .... 59

Figure 3.4: The Iqbal clear sky direct-insolation parameterisation model C is graphically displayed for: (a): a day period, with a winter’s and summer’s day compared to SOLERGY generated data, defined in the legend as actual data (Romero et al., 2000); and (b): a year cycle for different hours of the day. The zenith angle limit was set at 85°. ..... 60

Figure 3.5: The coordinates of the position of the PS-10 heliostats relative to the tower, with north representing the positive vertical axis, and east representing the positive horizontal axis (coordinates extracted from Noone et al., 2012). ..... 62

Figure 3.6: A histogram distribution of the heliostat distance from the receiver..... 62

Figure 4.1: A schematic illustration of the conversion of a computational mesh (shown as quadrilaterals) to circular elements to be used in SolTrace (Craig et al., 2016). ..... 65

Figure 4.2: A visual representation of the conversion from an ANSYS geometry to primitive elements simulated in SolTrace: (a): a sphere modelled in ANSYS v.19.0 SpaceClaim to use as an example; (b): the sphere meshed in ANSYS v.19.0 Meshing using tetrahedrons as type of mesh, with a sample element highlighted in yellow; and (c): the mesh simulated as a collection of primitive irregular triangles in SolTrace v.3.0.0, again with the sample element highlighted in yellow..... 66

Figure 4.3: Schematic illustration of: (a): the test case validation model (Martinek & Weimer, 2013); and (b): the model used by the author for the approach where smooth surfaces are discretised for analysis using the MCRT approach. The displayed dimensions are given in centimetres. .... 67

Figure 4.4: A normalised energy flux distribution incident on: (a): the cavity wall surface; and (b): the absorber tube surface for rays in the range of 5 000 to 10<sup>7</sup> rays. .... 68

Figure 4.5: A graphic representation of the percentage error obtained on the averaged cavity wall flux and absorber tube flux..... 69

Figure 4.6: The meshed outer cavity wall surface of the biomass solar cavity receiver test case model for element sizes: (a): 0.2 m; (b): 0.1 m; (c): 0.09 m; and (d): 0.08 m. .... 70

Figure 4.7: The normalised energy flux distribution that is incident on: (a): the cavity wall surface; and (b): the absorber tube surface for discretised or meshed geometries of the validation test case model using 10<sup>7</sup> rays..... 71

Figure 4.8: The percentage error obtained on: (a): the average cavity wall flux; and (b): the average absorber tube flux for different mesh element sizes across the range of rays generated. .... 71

Figure 4.9: A SolTrace simulation of the validation model constructed using: (a): primitive geometries; and (b): discretised elements with an element size of 0.2 m, both displaying the same generated ray path in the receiver..... 72

Figure 4.10: The percentage error on the averaged cavity wall flux and absorber tube flux as a function of the different mesh element sizes for 10<sup>7</sup> rays generated..... 73

Figure 4.11: (a): A schematic diagram of the flat plate jet impingement setup; and (b): the computational domain of the jet impingement numerical analysis constructed in ANSYS SpaceClaim (axisymmetric). ..... 75

Figure 4.12: A mesh structure of the flat plate jet impingement computational domain for a coarse mesh. .... 75

Figure 4.13: A mesh independence study for the flat plate round jet impingement study, using the area-weighted average Nusselt number over the entire simulated flat plate as a parameter..... 76

Figure 4.14: The Nusselt number as a function of the dimensionless radius for various turbulence models. Results were compared to results from ERCOFTAC (1992), Yan and Saniei (1998), Baughn, Hechanova and Yan (1991) and Lee and Lee (1999). ..... 77

Figure 4.15: (a): A schematic diagram of the concave surface jet impingement setup; and (b): the computational domain of the jet impingement numerical analysis constructed in ANSYS SpaceClaim (axisymmetric), the displayed image (b) showing the  $d/D = 0.089$  geometry. .... 79

Figure 4.16: A mesh structure of the concave surface jet impingement computational domain for a coarse mesh. .... 80

Figure 4.17: A mesh independence study conducted on the  $d/D = 0.089$  concave surface geometry, with the area-weighted, averaged Nusselt number on the concave surface displayed as a function of the number of computational elements using the transitional SST turbulence model. .... 80

Figure 4.18: A comparison of CFD using transitional SST and experiments by Lee et al. (1999). The Nusselt numbers as a function of the dimensionless radius for the diameter ratios are: (a): 0.056; and (b): 0.089. .... 82

Figure 5.1: A graphic summary of the ray independence study conducted for the aperture analysis for rays generated ranging from  $5 \times 10^3$  to  $3 \times 10^7$ , with the average flux per unit area on the aperture as an output parameter. .... 85

Figure 5.2: A schematic illustration of the trigonometric setup for the aperture optimisation using the geometric approach. .... 86

Figure 5.3: The aperture flux as a function of the aperture angle is graphically displayed for different ray counts, with the maximum flux on the aperture also accentuated. A close-up of the two most accurate trends is displayed in the bottom right frame. .... 87

Figure 5.4: Graphic illustration of the actual data obtained for the average aperture flux (irradiance) for different angles on different days of the year (illustrated with dots) plotted with the response surface polynomial function approximation. .... 88

Figure 5.5: The average irradiance on the aperture throughout the year as a function of the aperture angle, as calculated using the actual data and the response surface polynomial approximation function. .... 89

Figure 5.6: The optimum aperture angle as a function of the days of the year as estimated by the response surface technique and the raw data. This is displayed with the normalised irradiance incident on the aperture plotted in the background. .... 89

Figure 5.7: Solar flux distribution on the aperture of the PS-10 heliostat field constructed in Seville, Spain, using SolTrace MCRT for the 180<sup>th</sup> Julian Day at hours: (a): 08:00 LAT; (b): 10:00 LAT; (c): 12:00 LAT; (d): 14:00 LAT; and (e): 16:00 LAT. .... 91

Figure 5.8: The average aperture flux distribution over an entire year at different times of the day, displayed with circles illustrating the percentage flux of the current PS-10 central receiver aperture that is within the circle. Plots on the side show the flux distribution at the central axes. .... 92

Figure 5.9: The percentage flux that is captured within a circular aperture as a function of the radius for the aperture analysis. .... 93

Figure 5.10: (a): The receiver design with the highlighted region displaying the part of the design that was excluded during the analyses; and (b): the original (highlighted) and the inflated receiver compared to each other. .... 94

Figure 5.11: (a): The PS-10 heliostat field with (b): the original receiver modelled in SolTrace v.3.0.0. .... 95

Figure 5.12: The ray independency study for: (a): the original receiver design; and (b): the inflated receiver design. .... 96

Figure 5.13: (a) and (b): The aperture’s flux distributions of the original and inflated receiver design; and (c) and (d): flux distributions above the absorber surface of the original and inflated receiver design. .... 97

Figure 5.14: (a): The original receiver design with a dimensional grid (units in metres), displaying the different positions of the absorber (in red) to be analysed; and (b): a graphic representation of the change in efficiency for the different positions of the absorber. .... 98

Figure 5.15: The flux distribution of the absorber for different design points for: (a) the original design; and (b): the inflated receiver design for design points 1 to 5 (displayed from top to bottom). The vertical axis represents the dimensions in the vertical direction, parallel with the tower. The axes are scaled equally. For the dimensions, refer to Figure 5.14(a) for (a) and the 9/2 the scale of the original design for (b). .... 99

Figure 5.16: The flux profile on the one side of a pyramid element situated in the centre of the absorber of the original receiver design, with: (a): the  $3.54 \times 10^9$  single element profile; and (b): the  $4.5 \times 10^9$  meshed surface profile, compared with one another. .... 100

Figure 5.17: A detailed flux distribution on the absorber surface of the receiver, with the pink triangle indicating the detailed flux distribution of the element surface that is displayed in Figure 5.16, and the green triangle indicating the flux area to be used as heat source: (a): a zoomed-in image of the flux profile at the centre; (b): the entire absorber surface area; and (c): a detailed 3D illustration of the flux distribution on the absorber surface. .... 102

Figure 5.18: (a): Detailed flux profile on the pyramid sides, indicated by the green triangle in Figure 5.17a (represented with a black triangle in this figure), generated with MCRT using  $5.91 \times 10^9$  rays; and (b): the ray independence test conducted for the flux profile. .... 103

Figure 5.19: The new optically improved receiver design with: (a): a 3D view; (b): the top view; (c): the side view; and (d): the front view. .... 104

Figure 5.20: The flux distribution at: (a): the aperture; and (b): the absorber of the author’s new proposed design. .... 105

Figure 6.1: (a): A cross-section of the design proposed by (Garbrecht et al., 2012), which shows the internal HTF flow within the pyramid design; (b): a temperature colour profile on the outer surface of the pyramid element; and (c): a colour profile of the net heat flux into the receiver element (Garbrecht et al., 2012). Images were results published by Garbrecht et al., 2012. .... 108

Figure 6.2: The proposed improvement to the hexagonal pyramid absorber design of Garbrecht et al. (2012), with the tip on the inside of the pyramid substituted with a concave impinging surface. The variables that could be altered to improve the design are indicated. .... 109

Figure 6.3: The computational model geometry of the representative hexagonal pyramid absorber: (a): displaying the domain with the solid shell displayed in green and HTF domain in grey; and (b): showing the same geometry, but with the added air domain simulated as well. .... 110

Figure 6.4: (a): A partial 2D schematic illustration of the hexagonal pyramid absorber’s boundary conditions and cell zones; and (b): a zoomed-in section of the boundary conditions and cell zones. .... 112

Figure 6.5: A comparison between: (a): the solar flux obtained in SolTrace; and (b): the flux distribution in the ANSYS Fluent environment after interpolating the flux file. .... 113

Figure 6.6: The temperature distribution: (a): in °C, on the surface of the representative hexagonal pyramid; and (b): the symmetry wall of the computational model. .... 115

Figure 6.7: The contour plot of the efficiency at which the flux incident on the surface of the hexagonal pyramid absorber is extracted or utilised. .... 116

Figure 6.8: A graphic representation of the effect of the inlet velocity on the outlet temperature and average surface temperature. .... 117

Figure 6.9: A graphic representation of the thermal loss percentage and pressure loss as a function of the fluid inlet velocity. Displayed with the grey line is the optimisation curve illustrating the non-dimensional adding of the two variables..... 118

Figure 6.10: The contour plots of: (a): the temperature distribution; and (b): the efficiency at which the flux incident on the surface of the hexagonal pyramid absorber is extracted or utilised. .... 119

Figure A.1: A graphic representation of the eccentricity of time ( $E_t$ ) as a function of Julian days. ... 144

Figure A.2: A schematic illustration of a celestial sphere showing the sun's apparent path around the earth (Iqbal, 1983)..... 145

Figure A.3: A schematic illustration of the celestial sphere and sun's coordinates relative to a fixed point on earth at point O (Iqbal, 1983)..... 146

Figure B.1: The transformation of a mesh element to a SolTrace primitive irregular triangle illustrated with the image on the left: (a): displaying the translation to the origin and the picture on the right; and (b): displaying the rotation around the origin. .... 151

Figure C.1: A flow chart description of the processes followed during the optical and thermal analyses. .... 155

Figure C.2: The GUI that was developed by the author allows the user to set up an analysis on a central platform..... 156

Figure E.1: The outlet boundary length sensitivity study, with the outlet boundary distance being 0  $d$ , 1.54  $d$  and 3.08  $d$  from the concave surface end. .... 158

Figure E.2: The inlet profiles of a 10  $d$  vs 58  $d$  tube length compared for: (a): the flat plate; (b):  $d/D = 0.056$ ; and (c):  $d/D = 0.089$  concave wall surface impingement models. .... 160

Figure E.3: A comparison of the heat transfer effect of the different turbulence kinetic energy values ( $k$ ) on a concave surface, using the setup of Lee et al. (1999) as a test case for  $d/D = 0.056$ . .... 161

Figure E.4: A comparison of the heat transfer effect of the different turbulence kinetic energy values ( $k$ ) on a concave surface, using the setup of Lee et al. (1999) as a test case for  $d/D = 0.056$ . .... 162

Figure E.5: A comparison between constant fluid properties and temperature-dependent fluid properties for the test case of Lee et al. (1999) with a diameter ratio of  $d/D = 0.089$  and  $Re = 50\ 000$ . .... 163

## List of tables

Table 2.1: A summary of central receiver pilot and experimental electric power plants (Romero, Buck, & Pacheco, 2002; Lovegrove & Stein, 2012; Mills, 2004).....	17
Table 2.2: Summary of commercial central receiver power plants (Lovegrove & Stein, 2012; Tian & Zhao, 2013).....	18
Table 2.3: Summary of receiver designs as extracted from Ho & Iversion (2014) .....	43
Table 2.4:A comparison of turbulence models for jet impingement (Zuckerman & Lior, 2006).....	49
Table 3.1: Maximum errors (%) produced by the different orders of trigonometric approximations for the relative humidity, and maximum and minimum temperatures .....	57
Table 3.2: Coefficients calculated using the discrete trigonometric approximations theorem for the relative humidity, and maximum and minimum temperatures approximations.....	58
Table 3.3: PS-10 solar power plant heliostat field design parameters (Eddhibi et al., 2015; Noone et al., 2012; Osuna et al., 2006) .....	61
Table 5.1: Optical properties of the absorptive and reflective surfaces of the proposed receiver .....	95
Table 6.1: Material properties of the hexagonal pyramid absorber computational model, with the expressions as function of temperature, $T$ (K) .....	110
Table 6.2: Piecewise-linear values for the thermal conductivity of carbon steel (Morrell, 2017).....	111
Table 6.3: Summary of the results obtained from the inlet flow sensitivity study conducted .....	118
Table 6.4: A summary of the results of the original test case compared to the current case where the P1 channel thickness parameter was reduced .....	119
Table 7.1: Summary of the performance values (in percentages) for the different stages of the central receiver system.....	122
Table D.1: A summary of the norm of the difference between the polynomial response surface approximation and the actual data for different orders .....	157



## Nomenclature

### Symbols

$a$	Constant coefficient
$A$	Area (m <sup>2</sup> )
$b$	Constant coefficient
$B$	Lapse rate (K/m)
$C_p$	Specific heat (J/kg·K)
$CR$	Concentration Ratio
$d$	Pipe inner diameter (m)
$D$	Diameter (m)
$dA$	Area differential (m <sup>2</sup> )
$d_n$	Julian Day (days)
$ds$	Path length differential (m)
$dt$	Time differential (s)
$dz$	Zenith direction differential (m)
$E_0$	Eccentricity correction factor
$E_t$	Equation of time (minutes)
$G$	Irradiance (W)
$g$	Gravity acceleration constant (m/s <sup>2</sup> )
$h$	Convection heat transfer coefficient (W/m <sup>2</sup> ·K)
$h$	Height (m)
$H$	Nozzle-to-wall distance (m)
$H'$	Hour variable (hours)
$I_n$	Direct normal irradiance (W/m <sup>2</sup> )
$I_{sc}$	Solar constant (W/m <sup>2</sup> )
$k$	Counter
$k$	Thermal conductivity (W/m·K)
$\mathbf{k}$	Extreme accepted ray or direction cosine vector
$k$	Turbulent kinetic energy (m <sup>2</sup> /s <sup>2</sup> )
$l$	Vertical ozone layer thickness (cm)
$L$	Nozzle-to-concave-surface distance (m)
LAT	Local apparent time (hour)
$L_e$	Local longitude (°)
$L_s$	Standard longitude (°)
LST	Local standard time (hour)
$m$	Mass (kg)
$m$	Half the number of data points
$m_a$	Relative optical air mass
$m_{act}$	Optical mass
$m_r$	Relative optical mass
$n$	Order
$N$	North
$N_d$	Day length (hour)
$Nu$	Nusselt number
$P$	Pressure (kPa)
$P_0$	Standard sea level air pressure (kPa)
$p_s$	Partial pressure of water vapour in saturated air



$\dot{Q}$	Heat transfer (W)
$r$	Radius (m)
$r$	Radial direction
$R$	Gas constant ( $\text{m}^2/\text{s}^2\cdot\text{K}$ )
$R$	Rotation matrix
$Re$	Reynolds number
$s$	Path length (m)
$S$	South
$S_n$	Approximated function variable
$t$	Time (s)
$T$	Temperature (K)
TST	True solar time (hour)
$U_1$	Pressure-corrected relative optical path length (cm)
$U_3$	Ozone-relative optical path length (cm)
$v$	Velocity (m/s)
$\vec{v}$	Normal vector
$Vis$	Visibility (km)
$w$	Reduced precipitable water (cm)
$x$	Axis direction
$x$	Data variable
$x$	Axis position
$y$	Axis direction
$y$	Data variable
$y$	Day constant
$z$	Axis direction
$Z_{alt}$	Altitude above sea level

## Greek symbols

$\alpha$	Solar altitude/elevation ( $^\circ$ )
$\alpha$	Average particle size in the atmosphere
$\alpha_o$	Absorptance of direct irradiance by ozone
$\alpha_w$	Absorptance of direct irradiance by water vapour
$\beta$	Ångström's turbidity
$\delta$	Solar declination ( $^\circ$ )
$\varepsilon$	Surface emissivity
$\theta$	Zenith angle ( $^\circ$ )
$\theta$	Acceptance angle ( $^\circ$ )
$\theta$	Polar angle (discrete ordinate (DO) radiation)
$\theta_{aperture}$	Aperture angle ( $^\circ$ )
$\eta$	Efficiency
$\mu$	Dynamic viscosity ( $\text{kg}/\text{m}\cdot\text{s}$ )
$\nu$	Pitch rotation
$\zeta$	Distance from nozzle outlet (m)
$\rho$	Density ( $\text{kg}/\text{m}^3$ )
$\sigma$	Stefan-Boltzmann constant
$\tau_a$	Transmittance to direct irradiance due to attenuation by aerosols



$\tau_g$	Transmittance to direct irradiance due to absorption by uniformly mixed gases
$\tau_o$	Transmittance to direct irradiance due to absorption by ozone
$\tau_r$	Transmittance to direct irradiance due to Rayleigh scattering effects of air molecules
$\tau_w$	Transmittance to direct irradiance due to absorption by water vapour
$\phi$	Geographical latitude ( $^{\circ}$ )
$\phi$	Azimuthal angle (DO radiation)
$\phi$	Roll rotation
$\phi$	Parameterisation angle ( $^{\circ}$ )
$\phi_r$	Relative humidity
$\psi$	Solar azimuth ( $^{\circ}$ )
$\psi$	Yaw rotation
$\omega$	Hour angle (hours)
$\Gamma$	Day angle (radians)

## Subscripts

<i>0</i>	Reference
<i>a</i>	Air
<i>act</i>	Actual
<i>alt</i>	Altitude above sea level
<i>ambient</i>	Ambient
<i>amp</i>	Amplitude
<i>aperture</i>	Aperture
<i>avg</i>	Average
<i>conv</i>	Convection
<i>converted</i>	Converted
<i>corner</i>	Corner
<i>d</i>	Day
<i>e</i>	Local
<i>heliostat</i>	Heliostat
<i>incident</i>	Incident
<i>input</i>	Input
<i>j</i>	Counter
<i>jet</i>	Jet
<i>losses</i>	Losses
<i>max</i>	Maximum
<i>min</i>	Minimum
<i>n</i>	Order counter
<i>normal</i>	Normal direction
<i>o</i>	Ozone
<i>opt</i>	Optimal
<i>r</i>	Relative
<i>rad</i>	Radiation
<i>rec</i>	Receiver
<i>ref</i>	Reference
<i>s</i>	Standard
<i>sunrise</i>	Sunrise



<i>sunset</i>	Sunset
<i>t</i>	Time
<i>thermal</i>	Thermal
<i>tot</i>	Total
<i>tower</i>	Tower
<i>transform</i>	Transform
<i>translate</i>	Translate
<i>wall</i>	Wall

## List of abbreviations

2D	Two-dimensional
3D	Three-dimensional
AFOLU	Agriculture, forestry and other land use
AIP	American Institute of Physics
ARDC	Air Research and Development Command
ASHRAE	American Society of Heating, Refrigerating and Air-conditioning
ASME	American Society of Mechanical Engineers
BC	Before Christ
BDSTC	Beam-down solar thermal concentrator
C	Carbon
CC	Combined cycle
CERG	Clean Energy Research Group
CFD	Computational Fluid Dynamics
CO <sub>2</sub>	Carbon dioxide
CPC	Compound parabolic collector
CPV	Concentrating photovoltaic
CPVT	Concentrating photovoltaic thermal
CSIRO	Commonwealth Scientific and Industrial Research Organisation
CSP	Concentrating Solar Power
CST	Concentrating Solar Thermal
DAR	Direct-absorption receiver
DLR	German Aerospace Centre
DNI	Direct normal irradiance
DNS	Direct numerical simulation
DO	Discrete ordinates
DOF	Degree of freedom
EASAC	European Academies' Science Advisory Council
ERCOFTAC	European Research Community on Flow, Turbulence and Combustion
ESTELA	European Solar Thermal Electricity Association
EU	European Union
GRES	Global Renewable Energy Scenario
GUI	Graphical User Interface
HiTRec	High-Temperature Receiver
HTF	Heat transfer fluid
IEA	International Energy Agency
IPCC	Intergovernmental Panel on Climate Change
LAT	Local Apparent Time
LEC	Levelised electricity cost



LES	Large eddy simulation
LFC	Linear Fresnel collector
LST	Local Standard Time
MAD	Multiple aperture design
MCRT	Monte Carlo ray tracing
MENA	Middle East and North Africa
MIDC	Measurements and Instrumentation Data Centre
Mn	Manganese
MSEE	Molten Salt and Electric Experiment
NaNO <sub>3</sub> -KNO <sub>3</sub>	Solar salt
NREL	National Renewable Energy Laboratory
NTP	Normal temperature and surface pressure
NRF	National Research Foundation
O&M	Operations and maintenance
PS-10	Planta Solar 10
PS-20	Planta Solar 20
PTC	Parabolic trough collector
PTWG	Particle technology working group
PV	Photovoltaic
RANS	Reynolds Averaged Navier-Stokes
REFOS	Receiver for solar-hybrid gas turbine and CC systems
REmap	Renewable energy roadmap
RPC	Reticulate porous ceramic
S2S	Surface-to-surface
SA	Spalart-Allmaras
SAD	Single aperture design
SASEC	Southern African Solar Energy Conference
SCRAP	Spiky central receiver air pre-heater
SEGS	Solar electric generating system
SHS	Solar heating station
SiC	Silicon carbon
SIMPLE	Semi-implicit method for pressure-linked equations
SolarPACES	Solar power and chemical energy systems
SOLHYCO	Solar-hybrid power and cogeneration
SPA	Solar position algorithm
SPSR	Solid particle solar receiver
SSPS	Small solar power systems
SST	Shear stress transport
STERG	Solar Thermal Energy Research Group, Stellenbosch University
TES	Thermal energy storage
TST	True solar time
UDF	User-defined function
UDM	User-defined memory
UDP	User-defined profile
UDS	User-defined scalar
UNEP	United Nations Environment Programme
UNFCCC	United Nations Framework Convention on Climate Change
USA	United States of America



WMO  
WSTC

World Meteorological Organisation  
Water-Splitting Thermo-Chemical

## Chapter 1 Introduction

### 1.1 Background

A major concern in the modern era is the increase in the global mean surface air and ocean temperature, commonly referred to as global warming. The growing crisis of the ever-increasing temperature has led to a change in weather patterns, which includes an increase in weather extremities such as droughts and floods, also called climate change (Le Houérou, 1996; Meehl et al., 2000), and other changes that include polar and glacier melting (Calvert, 1982; Hock, 2005), increasing sea levels (Nicholls & Cazenave, 2010) and the destruction of ecosystems such as coral reefs (Hoegh-Guldberg, 1999).

It has already been widely researched and is common knowledge in recent times that the increase in mean temperatures is predominantly due to human activities. Although Svante Arrhenius first noted and theorised in 1896 that carbon dioxide (CO<sub>2</sub>) could have an effect on the environment, specifically the earth's climate by means of the greenhouse effect, it was only from the 1950s that a revitalised interest was sparked by the growing concern of the impact of burning fossil fuels and analytical methods. The greenhouse effect is the process whereby radiation from a planet's atmosphere warms the planet's surface to a temperature above that which it would be without its atmosphere. Studies have been showing correlations between global warming and anthropogenic emissions of greenhouse gases, which include CO<sub>2</sub>.

International concern escalated to the point where organisations such as the World Meteorological Organisation (WMO) and the United Nations Environment Programme (UNEP) started investigating the effect that CO<sub>2</sub> and other emissions had on the environment. The growing concern and interest led to the establishment of the Intergovernmental Panel on Climate Change (IPCC) in 1988 and the United Nations Framework Convention on Climate Change (UNFCCC) in 1994 in an attempt to put pressure on countries to take responsibility to limit their output of greenhouse gases (Höök & Xu, 2013). This led to agreements such as the Kyoto Protocol (adopted in 1997 and set into force in 2005) and the Paris Agreement (United Nations, 2015), both having the focus of putting limits on greenhouse gas emissions to an extent that would prevent anthropogenic interference with climate change to “dangerous” levels. The most recent limit was agreed upon in the Paris Agreement. Countries agreed to pursue efforts to restrict warming to 1.5 °C in global mean annual surface temperature relative to pre-industrial levels. This was agreed upon after assessments showed that a 2 °C warming, which was adopted by the European Union (EU) in 1996 and the UNFCCC in 2010, was too risky (James, Washington, Schleussner, Rogelj, & Conway, 2017). The agreement recognised the limited availability of information and therefore concluded that the aim would be to hold the increase in global mean surface air temperature to well below 2 °C relative to pre-industrial levels and to pursue efforts to limit it to 1.5 °C (James et al., 2017).

To achieve these set targets, limiting the emission of greenhouse gases and therefore combatting fossil fuel consumption is inevitable and of paramount importance. However, preventing an increase in global mean temperatures is not the only challenge. An increase in the global population at a staggering rate of 2 billion in just one generation and development initiatives that drive the energy demand to ever-increasing levels have sparked concerns about a global energy crisis (Kannan & Vakeesan, 2016). The electricity and heat production sector is the largest contributor to greenhouse gas emissions (25%). This is evident from the breakdown of anthropogenic greenhouse gas emissions by economic sector illustrated in Figure 1.1. The pressure on the energy sector to use alternative, cleaner methods, while maintaining growth in energy production, is a frustrating challenge.

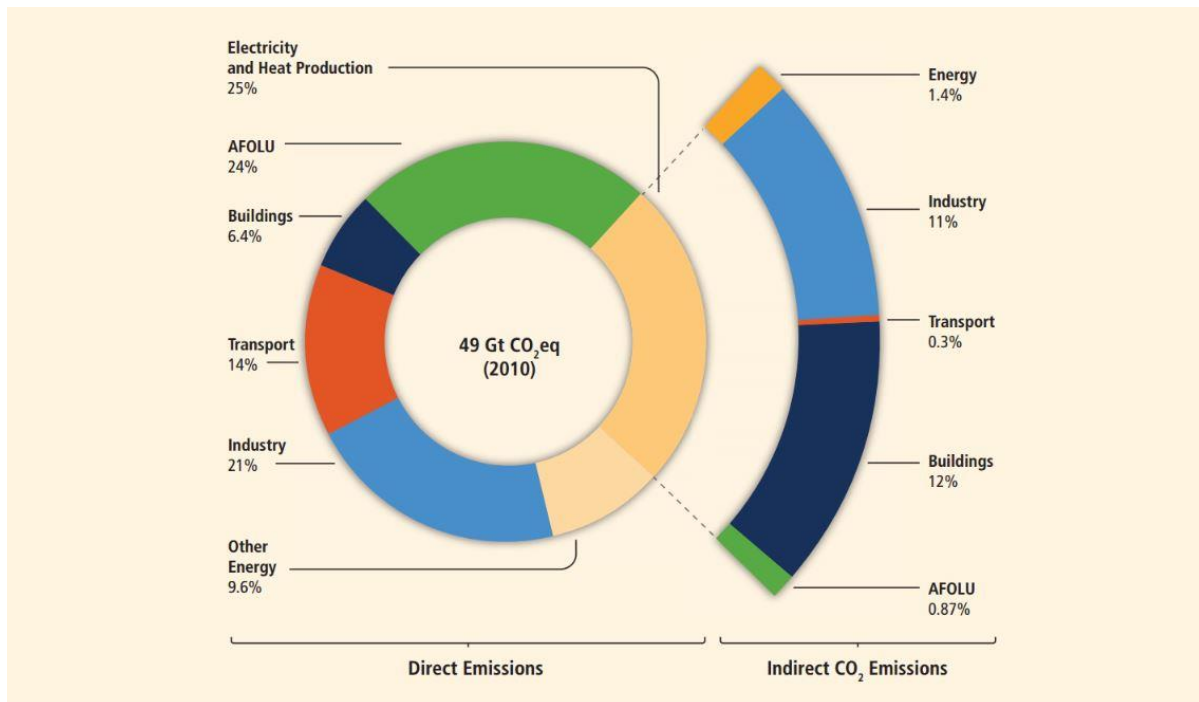


**Figure 1.1:** The total anthropogenic greenhouse gas emissions by economic sector (Merz, 2015). A graphic representation of the anthropogenic greenhouse gas emissions divided into its separate sector. The inner circle depicts the greenhouse gas emission shares that are emitted directly (as a percentage of the total greenhouse gas emissions) of the five sectors (results from 2010). The indirect CO<sub>2</sub> emission shares are shown on the right. “Other energy” refers to all greenhouse gas emission sources in the energy sector that exclude heat and electricity production. The data obtained from the agriculture, forestry and other land use (AFOLU) sector includes CO<sub>2</sub> emissions from decay and fires. The emissions are converted into CO<sub>2</sub>-equivalents based on the IPCC Second Assessment Report’s GWP1006 (Alley et al., 2004).

It is therefore vital to pursue eco-friendly energy sources for the betterment of the future world (Alanne & Saari, 2006). Sources such as solar, wind, hydropower and geothermal energy would be considered critically important, since these sources are considered eco-friendly (Herzog, Lipman, Edwards, & Kammen, 2001). Of all these sources mentioned, solar energy could be one of the better options for the future for several reasons. Firstly, with the earth intercepting approximately  $1.8 \times 10^{14}$  kW of the  $3.8 \times 10^{23}$  kW of the sun’s emitted energy, solar energy is the most abundant of all available renewable energy sources (Panwar, Kaushik, & Kothari, 2011). Studies revealed that global energy demand can be fulfilled satisfactorily with solar energy as it is abundant in nature and freely available without cost (Lewis, 2007). Secondly, this energy source is inexhaustible, giving solid and increasing output efficiencies compared to other sources of energy (Nozik, 1978). Thirdly, the utilisation and harvesting of solar energy in no way affects the natural balance of ecosystems. Finally, solar systems are versatile over a wide range of systems, from off-the-grid and modular systems to industrial operations, making it applicable and affordable.

With all the advantages mentioned above, the REmap (Renewable Energy Roadmap) case model (IRENA, 2018) has predicted that the solar industry will play a substantial role in the energy mix of the future (see the graphic model in Figure 1.2). The REmap programme is developed by IRENA, and determines the potential for countries, regions and the world to scale up renewables. REmap assesses renewable energy potential assembled from the bottom-up, starting with country analyses done in collaboration with country experts, and then aggregating these results to arrive at a global picture.

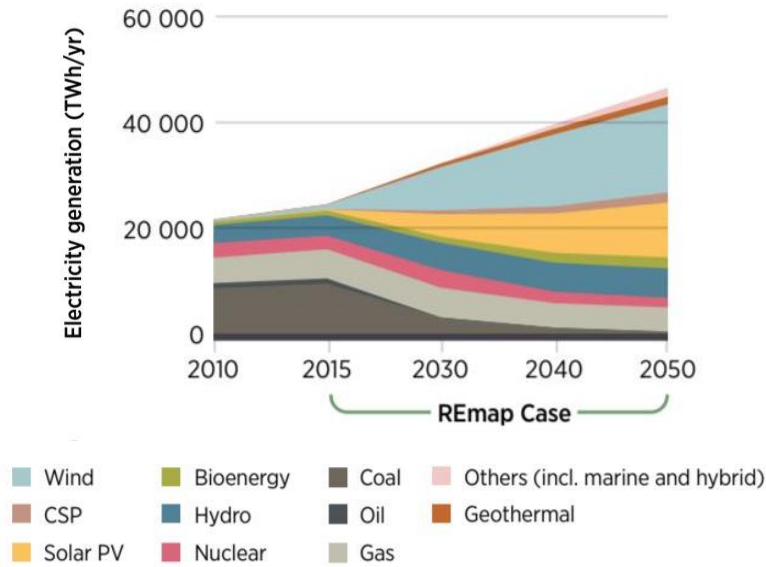


**Figure 1.2: An example of the development of the world energy supply, from the current situation to the global renewable energy scenario predicted for 2050 (IRENA, 2018).**

With the solar industry showing promising signs for future development and growth, it is worth considering the different available technologies, and developing and researching new ideas to harvest the sun’s energy. Concentrating solar power (CSP) technologies may provide such opportunities, although the contribution is predicted to be limited.

Trieb, Schillings, O’Sullivan, Pregger, and Hoyer-Klick (2009) investigated the global potential of CSP technologies. It was found that the global technical potential was almost  $3 \times 10^6$  TWh/a, which hugely exceeded the world electricity consumption at that stage, which was approximately  $18 \times 10^3$  TWh/a (Moghimi, 2017). There are, however, locations of preference for these technologies. CSP systems are only driven by the direct component of solar rays reaching the earth, also known as direct normal irradiance (DNI), so these technologies will benefit locations where there is a high and reliable DNI flux. Figure 1.3 shows the world map of the long-term averaged DNI of the sun, which could provide an easy visual illustration of the locations where CSP systems could be especially beneficial.

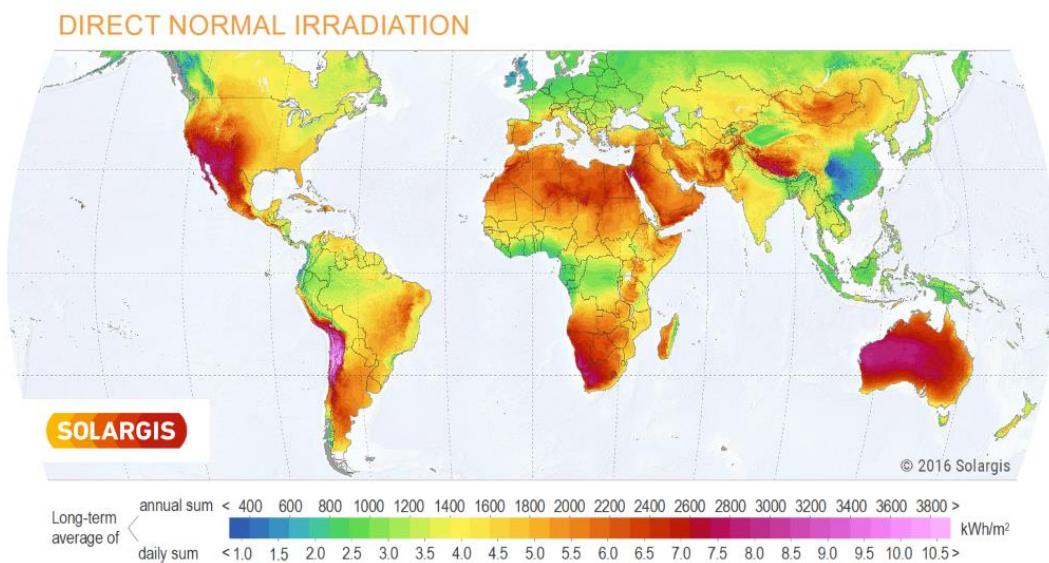


**Figure 1.3: World map of the long-term average of solar DNI (Solargis, 2016).**

From an environmental perspective, the installation of a 1 MW CSP plant could, for instance, avoid the emission of 688 t of CO<sub>2</sub> compared to a combined cycle system and 1 360 t of CO<sub>2</sub> compared to a coal or steam cycle plant (Behar, Khellaf, & Mohammedi, 2013). Unfortunately, CSP electricity generation technologies usually generate electricity at a levelised electricity cost (LEC) of 16 to 26 cents\$/kWh for recent technologies (Pitz-Paal et al., 2005; Zhang, Baeyens, Degrève, & Gacères, 2013; European Academies' Science Advisory Council (EASAC), 2011).

There is, however, an improved LEC of 7 to 12 cents\$/kWh being witnessed for current to near future technologies being developed (Craig, Brent, & Dinter, 2017) (Lilliestam & Pitz-Paal, 2018). These techno-economic optimisation of CSP technologies development make CSP technology competitive with other base-load, fossil-based generation. Especially solar tower CSP plants show great potential for improvements, with many published works predicting this technology to be the most competitive of all CSP in the energy market of the future.

## 1.2 Motivation

Technology currently available to directly harvest the sun's energy either works with a photovoltaic (PV) effect or by using the thermal component of the sun with solar thermal systems or with CSP, which could be utilised for thermal processes, heating or electricity generation. The ability of CSP to store the generated thermal energy and the possibility of scaling up renewable energy at the utility level, as well as other lesser reasons, make this conversion method an important study.

CSP technologies utilise the energy of the sun by transferring energy from the direct sunlight emitted by the sun as heat via reflectors to the heat transfer fluid (HTF), which circulates through the receiver or absorber. The HTF acts as the working fluid, depending on the system's configuration. CSP technologies can be loosely categorised into concentrating solar thermal (CST) and concentrating PV (CPV). There are also hybrid technologies in the field that combine these two technologies. These are the so-called concentrated PV thermal (CPVT) technologies. CST is more generally referred to as CSP, while CPV and CPVT technologies are referred to specifically. The study will henceforth refer to CST as CSP.

CSP systems that currently exist or are investigated can be classified into the following categories: parabolic trough collectors (PTCs), linear Fresnel collectors (LFCs), parabolic solar dishes and central receivers, also commonly referred to as solar tower receivers. The surveyed case study in this research is applied to central receivers.

As stated in Chapter 1.1, the field of CSP technology still has a great margin for improvement and cost reduction. With PTC systems starting to reach the stages of maturity in terms of development and research, the focus is on central receiver systems (Chaanaoui, Vaudreuil, & Bounahmidi, 2016). A few of the reasons are the following:

1. According to the policy report of the European Academies' Science Advisory Council (EASAC) (2011), which examines the relative increase in efficiency predicted for the different technologies available, PTC systems show the least growth with a mere 20% increase, followed by LFC systems and parabolic dishes that are predicted to have an increase of 25% efficiency. Central receiver systems are expected to increase in efficiency by a staggering 40% to 65%. This increase in efficiency is expected, with expectations that there is major room for improvement in the concentrating system (heliostat field optimisation and tracking), solar receiver, heat exchangers, as well as thermal energy storage (TES) (Pitz-Paal et al., 2005; European Solar Thermal Electricity Association (ESTELA), 2010). Although these sources are outdated, they still provide an idea of the technology that benefits the most from research and development.

2. As solar energy conversion takes place at a single fixed region (the receiver), costly energy transport networks are avoided. This allows for more cost-effective and efficient receiver designs.
3. As central receiver heliostats are able to cover a substantial area, aiming solar rays at a concentration point results in higher concentration and hence higher temperatures compared to other solar systems. This improves the Carnot efficiency of power production.
4. The technology has the potential for high annual capacity factors for the generation of electricity by using TES and is easily integrated into fossil fuel plants for hybrid operations in a wide variety of options, although the latter statement is debatable, with no CSP collector successfully being retrofitted into a fossil fuel plant (International Renewable Energy Agency (IRENA), 2012; Behar et al., 2013). There are, however, a small number of showcase projects that demonstrate new-build hybridization, such as the Shams 1 parabolic trough project in Abu Dhabi.
5. According to Ernst & Young and the Fraunhofer Institute for Solar Energy Systems (Fraunhofer) (2011), solar tower developments can offer more local opportunities (such as job creation and local economic development) than PTC systems.

Central tower receivers generally consist of an array of heliostats or tracking mirrors, which are spaced in such a way to avoid mechanical or optical interference, with the goal to reflect solar radiation to an elevated central receiver or secondary optical reflector. An HTF circulates through the receiver or absorber, therefore absorbing solar energy by heating. The absorbed energy is applied to power generation or delivered as process heat. This is illustrated in Figure 1.4.

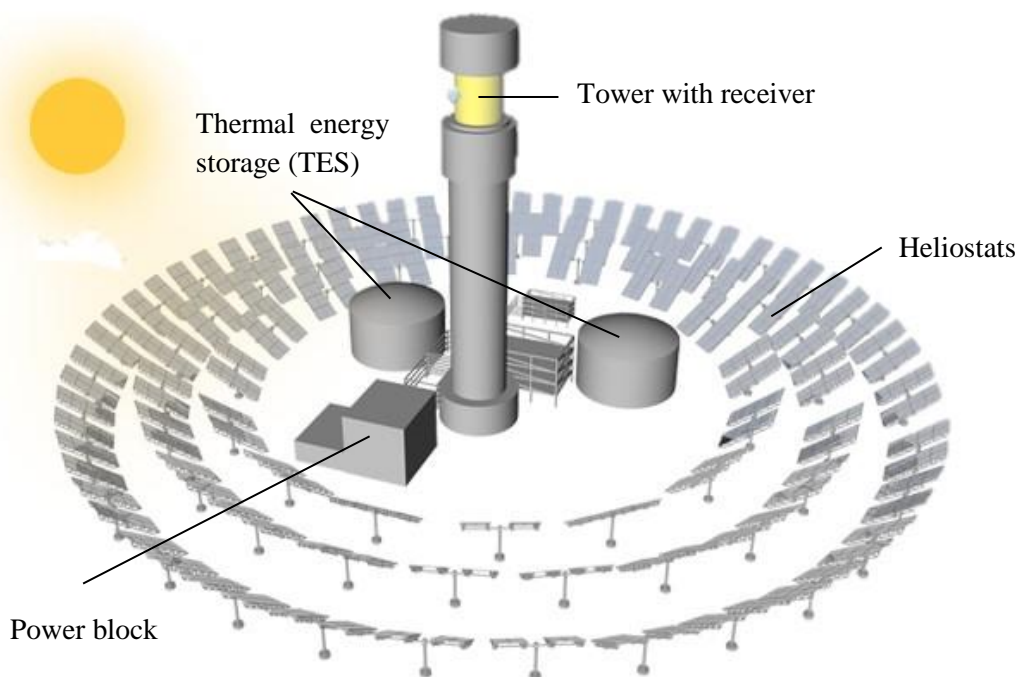


**Figure 1.4: An example of the layout of a simplified central receiver CSP plant (SQM, 2018).**

The aim of the research is to improve the current central receiver technology to ensure that solar energy can be utilised more efficiently and more cost effectively. Referring to the EASAC report (European Academies' Science Advisory Council (EASAC), 2011), there is a great margin for improvement to increase the efficiency of the receivers by approximately 40% to 60% (European Academies' Science Advisory Council (EASAC), 2011). Of all technologies analysed, the solar receiver seems to show the highest expected increase in efficiency.

Research and development for the receiver, in particular, would drastically improve the performance of the entire system. This would tempt industry and governments to invest in this source of energy and help with the shift in energy consumption from fossil fuels to solar energy.

### **1.3 Problem statement**

The aim of CSP systems is to capture solar energy by transferring the direct solar irradiance from the sun through the CSP technology to a working fluid. The process of capturing and transferring the energy to the working fluid is accompanied by thermal and optical losses. These losses in the system have a great influence on plant performance, since they can greatly affect the amount of energy that is harvested from the sun, and therefore hinder the performance of the thermodynamic cycle that follows. To ensure that CSP plants become more competitive with other energy source technologies, it is of utmost importance to develop this technology to generate a final energy product that is affordable and reliable. Higher efficiencies can help reduce the costs of generation. As mentioned in Chapter 1.2, the technology with the highest margin for improvement is the solar tower receiver. Minimising the optical and thermal losses of a receiver design while considering realistic parameters, which include convective and radiative losses, could increase the efficiency of the overall plant, which positively affects the plant's output. These efforts would make the technology more attractive for future energy investment considerations.

### **1.4 Objective**

Solar receivers or absorbers obtain their heat by the concentrated solar radiation from the mirror field or collector, depending on the setup. As mentioned briefly in Chapter 1.3, the efficiencies of these receivers are governed by their losses. The total thermal losses can be expressed as the sum of the contributions of re-radiation, convection and conduction losses, while optical losses may include the spillage of capturable focused light and the reflection of light due to material surface properties. It is therefore important to consider these losses and find innovative ways to minimise them to increase efficiency.

In this research, a novel solar cavity molten salt receiver is proposed for a central receiver CSP system. The design is introduced in detail in Chapter 2.6. The overall objective of the work is to develop, validate and demonstrate this novel design numerically and computationally while applying preliminary optimisation on certain parameters of the design through sensitivity studies. The analysis will be done using different optical and thermal models.

### **1.5 Methodology**

In order to achieve the objectives of this work, the author has applied the following methodology:

- A numerical test case central receiver heliostat field was constructed. This was done by selecting and applying the specifications of an existing heliostat field, the PS-10 central receiver heliostat field in Seville, Spain.
- To ensure realistic conditions for the proposed design, a solar tracking model working in conjunction with a DNI numerical model was developed to provide realistic solar conditions for testing at different times of the year throughout the day.
- The optical analysis was done using the Monte Carlo ray tracing software SolTrace, where the heliostat field was simulated together with the receiver. SolTrace only provides the user with primitive shapes to construct a given object, and since the proposed receiver is complex, a method was devised to overcome this problem without compromising the method's accuracy.

- The method that was developed to simulate complex shapes in the SolTrace environment was validated to ensure that the results obtained were of reasonable accuracy.
- A numerical conjugate heat transfer model, based on the boundary conditions of the solar flux obtained with the optical analysis, was used for studying the detailed thermal performance of the impinging absorber and validating it by comparing it to different impingement heat transfer studies.
- A full technical evaluation was then done to provide the study with a performance benchmark.

## **1.6 Layout of the thesis**

A literature study of the history, development and working of CSP technology in general, as well as an in-depth literature study on central receivers, followed by an introduction to numerical models that could be implemented for analysis, is conducted in Chapter 2. The focus of this chapter is the different receiver designs of currently available or proposed central receivers and how this technology's performance is affected. Chapter 3 and Chapter 4 discuss the setup and the optical and thermal models that are implemented for testing the proposed receiver design. Some of these models are tested and validated. Chapter 5 provides a broad optical analysis, breaking it down by first analysing the aperture and then analysing the receiver. Chapter 6 continues with the thermal analysis of the receiver and, more specifically, the receiver's absorber. Chapter 7 finalises the thesis with a full technical evaluation of the receiver's performance, concluding remarks and recommendations. Several addenda contain supporting information with further details to complement the body of the thesis.

## Chapter 2 Literature study

### 2.1 Introduction

Since the 1970s, there has been a surge in the development of solar technology, which included CSP technology. PTC is among the simplest form of CSP technology and has therefore developed the most over the past decades. There has been a greater interest in the development of central receiver power plants, with good prospects of high efficiencies in electricity generation and low costs at utility scale. These solar tower system developments and the prospects of substantial margins for the optimisation and improvement of this technology and the lowering of costs made it an interesting research topic.

The objective of this chapter is to conduct a literature study to identify the past and current research that has been conducted on central receiver technology, with the focus on solar tower receivers, and how these investigations have been approached. This chapter begins with a brief discussion of CSP systems in general and central receivers in particular, followed by the different research studies that are currently being conducted on central receivers. An in-depth survey of the different central receiver designs will be conducted with a quick glimpse of some dish receivers, as they provide an overlap of the technology developed for central receivers. Furthermore, a brief introduction of Monte Carlo ray tracing (MCRT) is given, since this approach will be followed for the optical analysis. CFD will be used for the thermal analysis. The focus will be on the heat transfer mechanics of jet impingement and how jet impingement is accurately modelled numerically. The literature concludes with the introduction of the proposed receiver design to be analysed.

### 2.2 Concentrating solar power

CSP systems use a combination of mirrors or lenses to concentrate direct beam solar radiation to produce forms of useful energy such as heat, electricity and, in some instances, even fuel by various downstream technologies (Lovegrove & Stein, 2012). As mentioned in Chapter 1.2, in this study, CSP will refer to the thermal branch associated with CSP. Essentially, in CSP, the energy of the concentrated direct solar radiation is reflected by the mirror field to a receiver, absorber or collector, depending on the configuration, with the purpose of heating a thermal energy carrier in the primary circuit, whether it is a working fluid (for direct use) or an HTF. A secondary circuit could utilise the heat for other processes, generally to power a turbine for electricity generation (Zhang et al., 2013).

CSP technology systems host a range of advantages, the most obvious being that, like the PV technology branch of solar energy harvesting, CSP is a means of exploiting the world's largest source of energy, the sun. Secondly, the solar-to-heat conversion step provides the possibility for TES, making the technology a dispatchable, renewable energy source. It also allows the technology to deliver energy with more consistency than its other solar technology counterpart. Since many other energy-generation technologies use heat as a primary energy source to generate electricity, such as the combustion of fossil fuels, CSP can provide the means of being hybridised in existing thermal generation processes. This compelling feature provides renewable alternatives to existing developments, and the co-existence gives stability to the solar technology during periods of low solar insolation (Miller et al., 2015).

It unfortunately also has its shortcomings, with CSP technology only being able to exploit direct solar radiation, mostly referred to as DNI. PV technology, in contrast, can generate electricity from both direct and scattered sunlight. As a result, weather conditions such as cloud cover and hazy skies affect the output of CSP plants. Another disadvantage for CSP is its sensitivity to scale. The efficiency and cost of these plants only reach their techno-economic optimum when constructed at utility scale, which affects the confidence of investment and the development of these technologies.

CSP systems also require vast tracts of land and consume large amounts of water compared to other electricity-generation technologies (Miller et al., 2015). Much research has, however, been done to decrease the consumption of water, while maintaining high efficiencies of electricity generation.

CSP technology in its simplest form has been in development for centuries. Records as old as 212 BC have reported on the works of Archimedes, in which mirrors were used to concentrate the sun's rays, although in recent years these reports get considered with more scepticism. Many centuries later, innovations such as a solar-powered motor using lenses by Caux (1615), a solar steam machine for a printing press by Mouchot (1882) (Pifre, 1882) and a parabolic dish concentrator connected to an engine exhibited at the World Fair in Paris (1878) (Frank, 2003) attempted to use CSP technology. Although a parabolic trough collector was installed at Al Meadi, Egypt, in 1913 to drive a pump for irrigation purposes (Duffie & Beckman, 1991), actual interest in the development of CSP technology started with the global oil and energy crisis from 1973 to 1979 (Ross, 2013). This crisis led to support for scientific work to develop alternative sources of energy. The support for the development of alternative technologies was short-lived, and once the oil crisis was over the funding disappeared. It was not until the pressing matter of global warming and climate change arrived in the late 1990s and early 2000s, which led to the signing of treaties such as the Kyoto Protocol (1997) and the Paris Agreement (2015) as discussed in Chapter 1.1, that a renewed interest in CSP technology became apparent. Now countries focus more on renewable energy, including CSP technology, to reduce their carbon footprint, which opens new doors for the advancement of CSP technologies.

The development of solar thermal technology has led to the introduction of the following four main CSP technologies: PTCs, LFCs, parabolic dishes and central receivers, also known as solar towers.

### **2.2.1 Parabolic trough collector**

Nowadays, parabolic trough CSP systems are the most widely implemented solar thermal plants, with the most research also being conducted in the field of CSP systems and technology. PTCs are linear-focused solar collectors with – as the name implies – a concentrator shaped like a parabolic trough that reflects direct solar rays onto a tubular receiver located at the focal line of the parabola. The large parabolic collector area, with lengths of 100 m or more and a curved aperture of up to 6 m, captures the solar radiation and reflects it onto the much smaller surface of the tube receiver. A single-axis tracking mechanism is used to orientate the solar collector and the heat receiver towards the sun (AT Kearney, 2010). The reflected radiation on the tube heats the HTF that circulates through the tubes to a temperature that is suitable for its application, whether for heat applications or electricity generation (Lovegrove & Stein, 2012). A standard illustration of a typical PTC is shown in Figure 2.1.

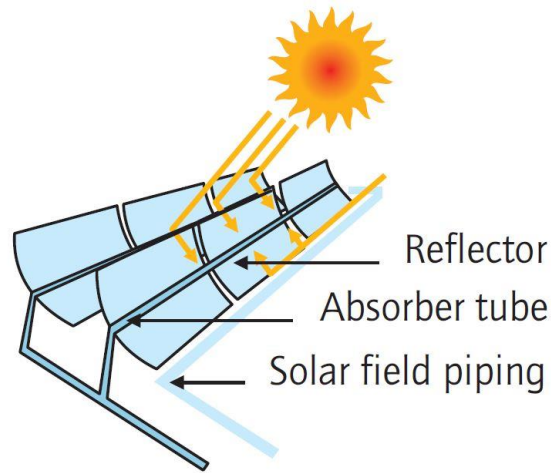


**Figure 2.1: A schematic illustration of PTC (International Energy Agency (IEA), 2010).**

The first commercially installed PTC plant was the Solar Electric Generating Systems (SEGS) plant in the USA in 1984, with the first installation generating 13.8 MW<sub>e</sub>. With extensions, it has grown to 354 MW<sub>e</sub>. PTCs are considered the most mature technology, with the parabolic trough technology accounting for most of the total installed CSP capacity (96.3%) (Zhang et al., 2013), which gives the technology the most commercial operating experience (Turchi, Mehos, Ho, & Kolb, 2010). PTC systems have been applied to many industries, including air heating, refrigeration, desalination and the food industry (Jebasingh & Herbert, 2016).

The technology currently holds a peak solar-to-electricity conversion efficiency of 23% to 27% and an annual solar-to-electricity efficiency of 15% to 16%, with an expected relative increase in efficiency of 20% (International Energy Agency (IEA), 2010; European Academies' Science Advisory Council (EASAC), 2011). The concentration ratios captured by PTC technology vary between 30 and 100 (Bennett, 2007; Geyer et al., 2002). For this study, the concentration ratio refers to the ratio of the irradiance at the receiver surface ( $G_{receiver}$ ) to the incident solar irradiance ( $G$ ), or:

$$CR = \frac{G_{receiver}}{G} \quad (2-1)$$

The advantages are substantial for PTC technology. This is evident with the dominance this technology has over the CSP industry. An advantage is the design of the continuous parabolic mirror, which gives it an almost geometrically ideal line focus concentration on the receiver. With the aperture following the position of the sun to get a normal solar ray incidence on the collector, the cosine losses are reduced to the axis of rotation direction. This contributes to higher efficiencies. These systems have their drawbacks, with the most prominent being the high operations and maintenance (O&M) costs compared to LFC (discussed in Chapter 2.2.2). They are also more expensive in terms of resources (such as needing demineralised water to wash the mirrors) (Morin, Dersch, Platzer, Eck, & Häberle, 2012). The structure of PTC systems also needs strong and stiff structures to withstand wind forces, while maintaining accurate solar projection (Arasu & Sornakumar, 2007). The current dominant HTF that is used with this technology is also limited to temperatures up to 391 °C.

## **2.2.2 Linear Fresnel collector**

Within the CSP technology family, there are two viable line-focus CSP technologies. These are the PTC (which was discussed in Chapter 2.2.1) and the LFC (Price et al., 2002). LFCs utilise an array of low-

profile, flat or nearly flat primary reflectors and a fixed receiver assembly that includes one or more linear receiver tubes screened by an optional second reflector. The primary reflectors collectively reflect the solar rays by tracking the sun onto the fixed receiver, which is usually mounted on a tower structure (Zhu, Wendelin, Wagner, & Kutscher, 2014). Figure 2.2 shows a standard illustration of a typical LFC.

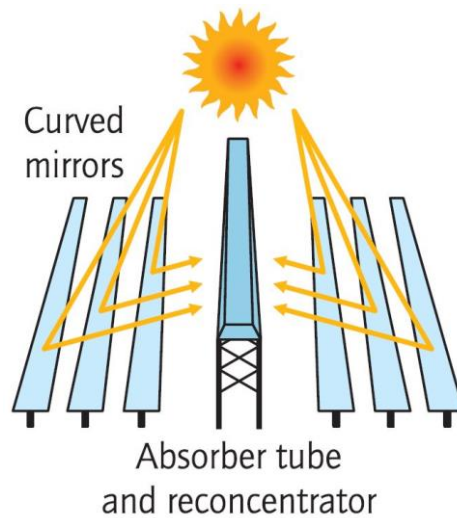


**Figure 2.2: A schematic illustration of an LFC (International Energy Agency (IEA), 2010).**

LFCs currently hold a peak solar-to-electricity conversion efficiency of 18% to 22% and an annual solar-to-electricity efficiency of 8% to 10%, with an expected relative increase in efficiency of 25% (International Energy Agency (IEA), 2010; European Academies' Science Advisory Council (EASAC), 2011). The concentration ratios captured by LFC technology vary between 10 and 30, as reported by various researchers (Goswami, Negi, Sehgal, & Sootha, 1990; Mathur, Kandpal, & Negi, 1991; Mazumder, Kandpal, & Mullick, 1987; Negi, Mathur, & Kandpal, 1989; Choudhury & Sehgal, 1986).

LFCs are still in their early stages of development, especially if one compares this technology to other groups in the field of CSP. This is evident in a study of the German Aerospace Centre (DLR) that rates the technology as immature with unknown reliability and still being developed in the pre-commercial phase (German Aerospace Centre (DLR), 2007). In recent times there have been substantial developments in LFCs, with Novatec Solar and Areva Solar reported leaders in LFC technology development, with the PE1, PE2 (Novatec Solar) and Kimberlina (Areva Solar) large-scale power station projects being developed and constructed around the world (Zhu et al., 2014). The LFC design can differ substantially from individual mirror dimensions to overall arrangements. In addition, the fixed nature of the receiver assembly provides considerable design freedom. LFC reflectors do not reflect sunlight at a normal incidence. Therefore, the system is affected by cosine losses that affect its efficiency, especially when comparing it to its line-focus counterpart (Munoz, Martinez-Val, & Ramos, 2011). However, the advantages of the design include the lower cost due to the simplicity of the production of the parts and the construction of the setup (Morin et al., 2012) and the lower wind loads on the reflectors. The O&M expenses are also less due to the design providing ease of reach (Zhu et al., 2014).

### 2.2.3 Parabolic dish

Parabolic dish CSP systems are one of the two forms of point-focusing CSP technology. The reflector is designed to use the geometrically ideal concentrator for point concentration, which is the paraboloidal-shaped design. This dish-shaped reflector is connected to a two-axis tracking system, which concentrates the incoming solar radiation throughout the day onto the focal point, where the

receiver is positioned, to generate electricity using a Stirling engine (Hafez, Soliman, El-Metwally, & Ismail, 2016; Wu, Xiao, Cao, & Li, 2010; Kleih, 1991). On a smaller scale, it is used for cooking or heating purposes (Balzar, Stumpf, Eckhoff, Ackermann, & Grupp, 1996; Mohammad, 2012). A simplistic illustration of a parabolic dish is displayed in Figure 2.3.

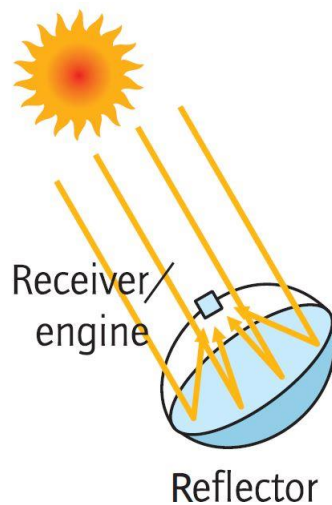


**Figure 2.3: A schematic illustration of a parabolic dish (International Energy Agency (IEA), 2010).**

Parabolic dish technology is expected to attain the highest efficiencies of all CSP technologies, with parabolic reflector design being continuous, and point focus increasing the concentration ratio. The current peak solar-to-electricity conversion efficiencies of parabolic dishes range from 20% to 29.4%, while the annual solar-to-electricity efficiency is around 18% to 24% (Mills, 2004). It is expected that the technology will grow with a relative increase of 25% (International Energy Agency (IEA), 2010; European Academies' Science Advisory Council (EASAC), 2011). The concentration ratio, as expected, is the highest of all CSP technologies, with the values usually being above 2 000, which is higher than the central receivers of the other point-focus CSP technologies that will be discussed next.

Since the parabolic dish provides the highest optical and overall conversion efficiencies, as well as the highest concentration ratios of all CSP technologies, it provides the opportunity to utilise small areas for high-efficiency energy conversion. Despite the high-efficiency conversion, the technology is applied to small capacity applications due to the size and weight of available Stirling engine-generator units, and the wind load effects on the dish reflector (Hafez et al., 2016). This technology, however, is not only limited to Stirling engine-generator units, since Brayton cycles could also be applied. The dual-axis solar tracking puts additional complications on the design, with lubrication and mechanical design being the greatest factors (Giostri & Macchi, 2016). However, research has been conducted to investigate the feasibility of applying this technology as a modular technology, which would give the advantages of utility-scale electricity generation, as well as a reduction of costs if the technology were to be mass produced (Lovegrove et al., 2007).

#### **2.2.4 Central receiver**

Central receiver CSP systems, also known as solar towers, are part of point-focus CSP technologies, just like the parabolic dish. Central receiver systems consist of a centralised elevated structure with a receiver (usually) mounted on top of it, surrounded by an array of dual-axis tracking mirrors called heliostats, which are spaced in such a way to avoid mechanical or optical interference, with the goal to reflect solar radiation to the elevated receiver or secondary optical reflector (Vant-Hull & Hildebrandt, 1976; Walzel, Lipps, & Vant-Hull, 1977). Figure 2.4 illustrates the basic workings of such a system.

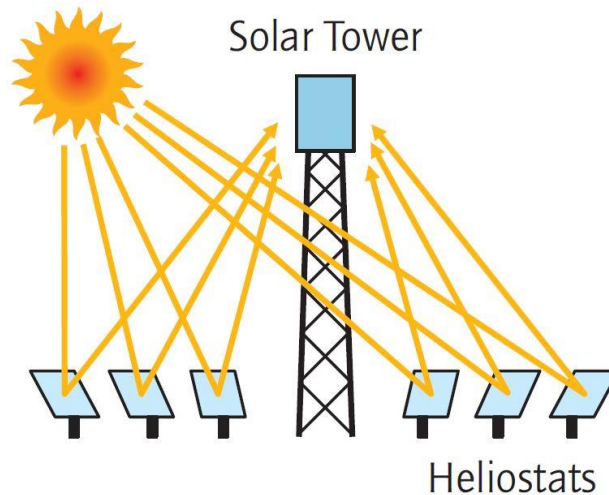


**Figure 2.4:** A schematic illustration of a central receiver system (International Energy Agency (IEA), 2010).

With central receiver technology being the point focus type of CSP technology, the temperatures that can be reached at the receiver are much higher compared to line-focus technologies, which help with increasing the system's efficiencies. Currently, this system holds a peak solar-to-electricity conversion efficiency of 20% to 27% and an annual solar-to-electricity efficiency of 15% to 17%, with an expected relative increase in efficiency of 40% to 65% (International Energy Agency (IEA), 2010; European Academies' Science Advisory Council (EASAC), 2011). The concentration ratios of this technology typically range between 200 and 1 600 (Ho & Iverson, 2014; Schmitz, Schwarzbözl, Buck, & Pitz-Paal, 2006; Romero & Steinfeld, 2012). It should be noted, however, that there have been substantial improvements in developments of this technology since these reports were published, although it provides a good perspective of the need for the research and development of this technology.

Solar tower systems provide numerous advantages compared to the other CSP technologies. Solar energy conversion takes place at a single fixed region, such as the receiver. This avoids costly energy transport networks and allows for more cost-effective and efficient receiver designs. A vast area can also be covered to capture the solar rays and focus it to a single point, which improves efficiency (Zhang, Baeyens, Degrève, & Gacères, 2013). The current focus of this technology is usually only on utility applications when considering the techno-economics of scaling and the higher efficiencies of power block systems for larger scaled systems. It is clear that if one compares the expected relative increase in efficiency of this technology with other CSP technologies, there is still much space for innovation. The design and development for central receivers are complex owing to the number of variables that need to be considered. The size, configuration, shape and number of heliostats are only a few of the variables that need to be considered on the heliostat's design to give an idea of the system's complexity. The central receiver systems will be discussed in greater detail in Chapter 2.3.

## 2.3 Central receiver systems

### 2.3.1 History and development

#### 2.3.1.1 Early developments

Although the concept of CSP was of interest for centuries, as mentioned at the beginning of Chapter 2.2, the idea that would eventually develop into central receiver or solar tower systems was only discussed in the late 1940s, and it took even longer for this technology to mature into a commercially competitive energy utility technology.

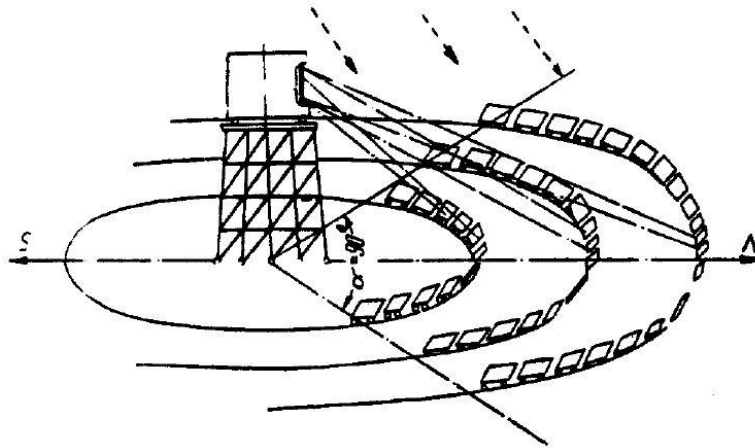


**Figure 2.5: The SHS concept developed by VA Baum et al. (Baum, Aparasi, & Garf, 1956).**

NV Lenitski proposed the first concept of what was then called a solar heating station (SHS), which was later given the name central receiver or solar tower system in Moscow in 1949. The proposed design was described as a set of flat mirrors (each of which must be adjusted separately) that reflects the sunlight onto a stationary boiler (now called a receiver) to be placed in an elevated position above the mirrors. VA Baum and colleagues from Russia (1956) later developed this concept (Baum, Aparasi, & Garf, 1956). A heliostat consisting of a  $3 \times 5$  m reflecting surface that comprised 28 mirrors, each assembled on a standard metal frame, was situated on a carriage. Some 1 293 of these carriages would be attached to each other to form 23 separate trains that would move on (or near) concentric rails with equal angular velocity around the 40 m high boiler. The azimuthal motion would therefore be controlled by the trains' movement, starting positioned in the west and gradually moving around the northern side to the east, while the zenithal movement would be controlled by electrical motors on the carriages (refer to Chapter 3.2 for more information regarding solar position terminology). The concept is illustrated in Figure 2.5.

In 1957, Felix Trombe published a paper in France (Trombe, 1957) on the construction of a novel solar furnace. The design consisted of a heliostat field placed on a steep hillside, which gave the benefit of less optical obstruction from other heliostats, aiming towards a  $40 \times 54$  m paraboloidal concentrator consisting of 3 500 mirrors and a furnace positioned at the focal point of the concentrator. The 62 heliostats of  $6 \times 7$  m were arranged as shown in Figure 2.6 and photoelectric solar tracking cells assisted the hydraulic arms that controlled the heliostats in tracking the sun. This 1 000 kW solar surface provided the first "commercial" heliostat field ever constructed (Lovegrove & Stein, 2012).

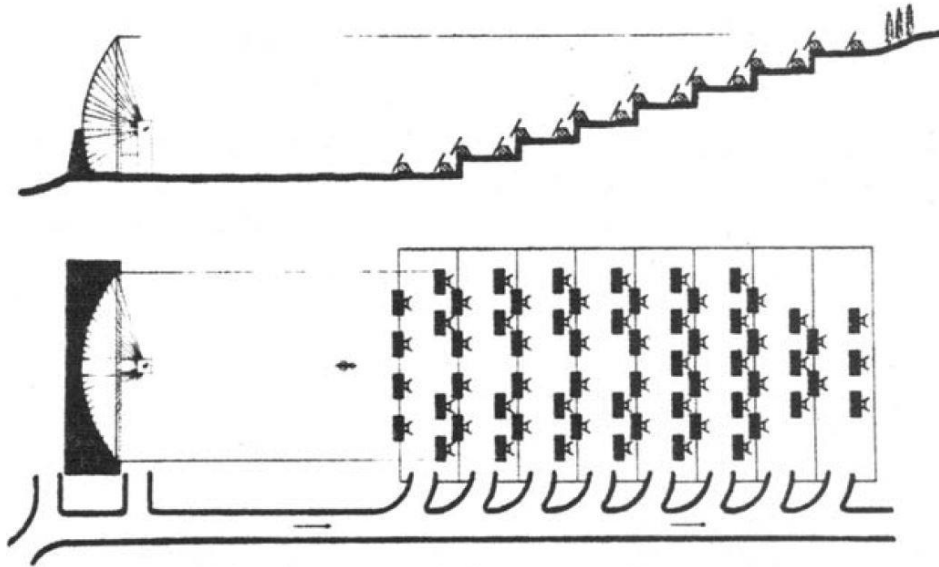
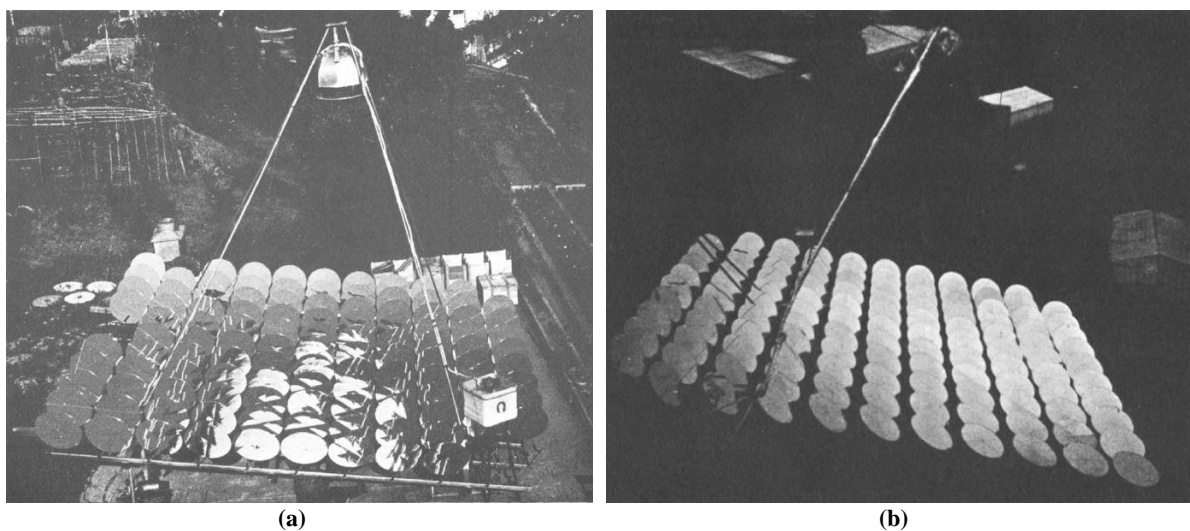
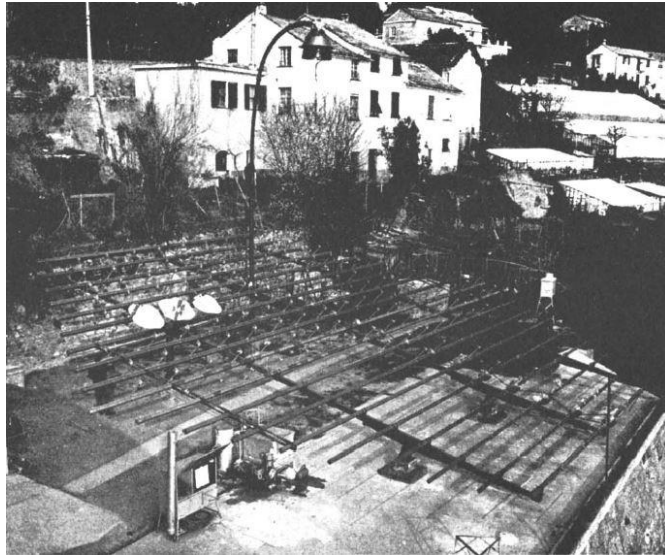


Figure 2.6: A schematic design of the 1 000 kW Montlouis solar furnace constructed in 1957 (Trombe, 1957).

In 1965, the Genoa University Istituto di Meccanica Applicata alle Macchine, headed by Prof A Capocaccia, built a point focus solar unit for steam at 150 atm, superheated at more than 450 °C. The heliostat field consisted of 121 round mirrors, 58 cm in diameter, arranged as a chess-board for a total surface area of 30 m<sup>2</sup>. The mirrors tracked the sun with a specially developed kinematic motion device. The receiver comprised a monotubular boiler that was situated 3 m over the mirror field. The boiler consisted of a 60 m blackened steel tube wound as a coil or spiral. Later that year, the heliostat field was improved with larger mirrors (74 cm in diameter) with a total working surface area of 52 m<sup>2</sup>. A third plant was constructed. This time, the 271 newly developed kinematic motions supported bevelled squared mirrors for a total working surface area of a little more than 200 m<sup>2</sup>. The pattern of the field was also changed to a hexagonal honeycomb pattern (Francia, 1968). The three plants that were constructed are shown in Figure 2.7.

Hildebrand, Haas, Jenkins and Colaco (1972) published a new design for a central hemispherical or cylindrical receiver on top of a 450 m tower surrounded by a carefully positioned heliostat field. This concept was expected to produce 565 MW<sub>th</sub> at 1 000 to 2 000 K (Hildebrandt et al., 1972; Lovegrove & Stein, 2012). This proposed design looked very similar to the modern central receivers.





(c)

Figure 2.7: St Ilario-Nervi, Genoa: (a): Solar plant No. 1; (b): solar plant No. 2; and (c): solar plant No. 3 under construction (Francia, 1968).

### 2.3.1.2 Test facilities and pilot plants

The oil crisis that persisted in the 1970s (as discussed in Chapter 2.2) created an urgency to find alternative energy solutions, and with CSP a viable energy solution, many development incentives were invested in testing the feasibility of these technologies. This led to the construction of numerous testing facilities and pilot plants around the world during the 1980s. This is evident if one looks at the summary of the pilot plants and test facilities in Table 2.1.

The research on CSP technologies, and therefore central receiver technologies, gradually stopped due to a lack of funding, as investors and governments lost interest when the oil crisis ended in 1979. This is evident with the development of research plants that were halted in the mid-1990s. It was not until the mid-2000s that treaties such as the Kyoto Protocol and Paris Agreement put pressure on governments to release resources to renewable technology research and development. This led to new research facilities such as the Jülich Solar Tower research facility to be established in Germany and the construction of the first commercial plants, which will be discussed in the following section.

**Table 2.1: A summary of central receiver pilot and experimental electric power plants (Romero, Buck, & Pacheco, 2002; Lovegrove & Stein, 2012; Mills, 2004)**

Project	Country	Year	Net electrical output (MWe)	Heat transfer fluid	Field area (ha)	Number of heliostats	Heliostat aperture area (m <sup>2</sup> )	Tower height (m)	Receiver	Temperature (°C) (inlet-outlet)	Type	Reference	
IEA/SSPS	Spain	1981	0.517	Liquid sodium	4	93	39.3	43	Cavity with octagonal aperture External panels with parallel tubes	270-530	Experimental	(CSP World, 2015b; Kesselring & Selvage, 1986)	
EURELIOS	Italy	1981	1.2	Steam (60 atm.)	3.5	112 and 70	23 and 52	55	Cavity	510	Experimental	(Hofmann & Gretz, 1980)	
SUNSHINE	Japan	1981	1	Saturated steams	~2		16	69	Semi-cavity with cone-shaped and cylindrical membranous walls	-	Pilot plant	(Mukai, Horigome, Ikeda, & Sakamoto, 1985)	
Solar One	USA	1982	10	Water/steam	29.1	1818	39.1	90.8	External cylinder	516	Pilot plant	(Pacheco, et al., 2002; Stine & Geyer, 2014)	
CESA-1 (PSA)	Spain	1982	1.2	Superheated steam (100 bar)	8.25	300	39.6	80	Cavity	520 *	Experimental	(CSP World, 2015a)	
MSEE/CRTF-SNL	USA	1983	0.75	Nitrate salt		218	37	61	Cavity		Experimental		
THEMIS	France	1983	2	Molten salts (Hitec) - KNO <sub>3</sub> (53%), NaNO <sub>2</sub> (40%), NaNO <sub>3</sub> (7%)	~2	201	53.7	104	Cavity (lined with cooling tubes)	250-450	Experimental	(CSP World, 2015c)	
SPP-5/SES-5	USSR	1986	5	Steam (40 atm.)	-	40,000 m <sup>2</sup> total heliostat surface area		60	External	250	Experimental	(Shpilrain, 1991)	
TSA	Spain	1993	1	Air		160-180		40	86	Volumetric receiver	150-700	Pilot plant	(Tyner, et al., 1996)
Solar Two	USA	1996	10	Molten nitrate salt (60 % NaNO <sub>3</sub> and 40% KNO <sub>3</sub> )	29.1	1818 and 108	39.1 and 95	90.8	External Cylinder	290-565	Pilot Plant	(Pacheco, et al., 2002)	
Jülich	Germany	2008	1.5	Air		2153	8.2	60	Open volumetric	680	Experimental	(NREL, 2013)	

**Table 2.2: Summary of commercial central receiver power plants (Lovegrove & Stein, 2012; Tian & Zhao, 2013)**

Project	Country	Year	Net electrical output (MWe)	Heat transfer fluid	Field area (ha)	Number of heliostats	Heliostat aperture area (m <sup>2</sup> )	Tower height (m)	Receiver	Temperature (°C) (inlet-outlet)	Company	Reference
PS-10	Spain	2007	11	Water/steam	55	624	120	115	Cavity	250-300	Abengoa Solar	(European Union, 2007; Solúcar, 2006; NREL, Planta Solar 10, 2017c)
PS-20	Spain	2009	20	Water/steam	80	1255	120	165	Cavity	250-300	Abengoa Solar	(NREL, Planta Solar 20, 2017d)
Sierra SunTower	USA	2009	5	Water/steam	8	24360	1.136	55	Dual-cavity receiver and tubular external receiver	218-440	eSolar	(NREL, Sierra Sun Tower, 2014c)
Gemasolar	Spain	2011	19.9	Molten salts	195	2650	120	140	External - cylindrical	290-565	Torresol Energy	(NREL, Gemasolar thermosolar plant, 2017a)
Chevron	USA	2011	29 **	Saturated steam	40.5	3822	100	100	-	-	BrightSource Energy	(BrightSource, 2018)
Ivanpah	USA	2014	392	Water/steam	142	173500	15	140	4 Plane external	250-565	BrightSource Energy	(NREL, Ivanpah solar electric-generating system, 2014b; BrightSource, 2014)
Crescent Dunes	USA	2015	110	Molten salts	650	10347	115.7	195	External - cylindrical	290-565	SolarReserve, LLC	(NREL, Crescent Dunes Solar Energy Project, 2016b)
ACME (Bikaner)	India	2014	2.5	Steam (60 bar)	5	14280	1.136	46		218-440	ACME Group, eSolar	(CSP World, 2018) (NREL, 2014a)
Khi Solar One	South Africa	2016	50	Superheated steam	57.68	4120	140	205	3 Cavity receivers	530	Abengoa Solar - IDC	(Abengoa Solar, 2018; New Energy Update: CSP, 2013; NREL, 2016c)
Ashalim Plot B	Israel	2018*	121	Water/steam	315	50600	20.8	250	-	-	BrightSource Energy (25%), General Electric	(General Electric Renewable Energy, 2016; NREL, Ashalim Plot B, 2016a)

Project	Country	Year	Net electrical output (MWe)	Heat transfer fluid	Field area (ha)	Number of heliostats	Heliostat aperture area (m <sup>2</sup> )	Tower height (m)	Receiver	Temperature (°C) (inlet-outlet)	Company	Reference
Cerro Dominador	Chile	2018*	110	Molten salts	700	10600	140	243	-	300-550	(25%), NOY (50%) Abengoa Solar	(NREL, Atacama-1, 2015)
Noor III	Morocco	2018*	134	Molten salts	750	-	-	-	-	290-565	ACWA	(NREL, NOOR III, 2017b)

\* Solar plants still under construction, therefore the estimated year of completion

\*\*Thermal energy power generation

The facilities that were constructed, especially the developments in the 1980s that lay the foundation for the commercial power plant era, provided much experience with various types of heliostats and HTFs, which included water or steam, molten salt and sodium. Many lessons were learnt from these facilities concerning control systems, heliostats, pumps, valves, receivers and working fluids. (Lovegrove & Stein, 2012)

Take note that the summary in Table 2.2 only shows the central receiver development that focuses on electricity production, and excludes any research facility that generated less than 1 MW of electricity after the 2000s. These research facilities include the Hohai University (2005) in China that only generates 70 kW of electricity (**Jun, Yaoming, Deyou, & Su, 2008**), the National Solar Energy Centre of the Commonwealth Scientific and Industrial Research Organisation (CSIRO) in Australia that generates 500 kW, or any central receiver that generates thermal energy or utilises the concentration power for solar furnace applications. Many of the research institutions have since also upgraded their test facilities (like the Solar One project that was upgraded to become the Solar Two plant), and use various other technologies not described in the summary. These technologies may include HTFs, receiver technologies or heliostat designs. Refer to Li, Ceventry, Bader, Pye and Lipiński (2016) for a more comprehensive list. The omission of these plants, however, does not mean that the author has not considered the these projects.

### ***2.3.1.3 Commercial power plants***

As with CSP in general, 2005 marked a change in activity for central receivers and the beginning of the contemporary period of industry expansion. By 2010, there were at least five commercial companies actively focusing on developing large-scale commercial utility central receiver projects. These companies are Abengoa Solar and Torresol Energy in Spain and eSolar, Brightsource and SolarReserve in the USA. Other companies such as SENER, Aalborg and ACWA Power in Saudi Arabia have recently stepped into the commercial utility central receiver market, with the NOOR III project currently under construction and expected to be operational by October 2018 (SolarPACES, 2018). These companies all had different approaches to commercialisation, which is evident in the different designs for the heliostat and field configuration (which will be discussed in Chapter 2.3.2), receiver designs (discussed in Chapter 2.3.3), working fluids, storage methodology and plant sizes. A summary of the commercial plants currently operational or under construction is presented in Table 2.2. Take note that there may be other solar tower projects, such as the developments in countries such as Australia and China, that have not been listed.

Abengoa Solar, a Spanish company with a vast amount of prior knowledge in the field of commercial parabolic trough production, was the first to construct a commercial solar tower facility with the Planta Solar 10 (PS-10) near Seville, Spain, in 2007. Although this plant was meant as a test facility for Abengoa Solar, it also served as a demonstration plant for the feasibility of future larger commercial projects. The PS-10 plant was followed by a second plant, Planta Solar 20 (PS-20), which essentially used the same configuration as the PS-10, but with improvements in receiver efficiency. The commercial operation for this plant started in 2009.

Although Abengoa Solar opted for heliostats with larger aperture sizes (and therefore fewer heliostats), eSolar took an entirely different approach by designing a tightly packed solar field with heliostats of smaller aperture sizes, and a comparably lower solar tower, as was done with its Sierra SunTower project. This is just an example of how companies use trade-offs in the design to find the most efficient and affordable design. Figure 2.8 displays the different heliostat designs and configurations of these two companies.

Companies such as Abengoa Solar have become less competitive in solar tower development in recent times, with eSolar reportedly to have ceased operating.



Figure 2.8: (a): A comparison is made between the heliostat design and field of the PS-10 power plant in Seville, Spain, developed by Abengoa Solar (Eco-friendly-world, 2018); and (b): the Sierra SunTower power plant in Lancaster, USA, developed by eSolar (Infaimon, 2016).

## 2.3.2 Heliostat field design

The heliostat field, also frequently called the solar field, consists of a large number of tracking mirrors, usually referred to as heliostats. These fields are responsible for the collection of solar rays and focusing them onto the elevated central receiver. Central receiver systems vary quite significantly in design when it comes to the heliostat as well as the field. The different designs, as well as the issues involved with them, will be discussed briefly in this sub-section.

### 2.3.2.1 Heliostat design

A heliostat is an apparatus that (usually) includes a slightly-curved mirror that turns to keep the sunlight reflecting towards a predetermined target, which is the receiver or secondary reflector on top of the tower in central receiver systems (Wikipedia, 2018). This device is an important component of the

central receiver system design, especially since a group of these devices, collectively called the heliostat field, is responsible for capturing the sun's rays and projecting them towards the intended object with the highest efficiency possible. They also form about 50% of the total investment cost (Kolb, 2007). This study does not focus on heliostat design, hence only an overview of the factors that influence the design of a heliostat, as well as the types currently available, will be discussed. The following requirements are paramount for the design of any heliostat used in a central receiver system (Spellning, 2012; Björkman, 2014):

- High reflectivity
- High optical precision
- High tracking accuracy
- Resistant structure

Considering these requirements, there are certain design factors that need to be taken into account to reduce the cost, according to Coventry & Pye (2014). These design factors are the following:

- Heliostat manufacturing and assembly
- Heliostat size
- Wind loads

Different types of heliostats have been developed over the years. These heliostats can be divided into three categories: serial, parallel and wire heliostats. A short description of each type of heliostat will be given (Björkman, 2014).

**Serial type:** The most established heliostat, in its most common design, is a single-point-mounted pedestal. The motor module is on top of the pedestal and the torque tube (long steel tube) is mounted onto this motor module. The torque tube contains both an azimuth drive and an elevation drive (displayed in Figure 2.9a).

**Parallel type:** This type of design has the following concepts:

- *Universal solar tracker:*  
It consists of two linear actuators and five universal joints. The actuators are fixed in a tilted plane so that the joints form a triangle. A modelled design is shown in Figure 2.9b.
- *Octahedral hexapod:*  
This is also called a Stewart-Gough platform. It is a six degree-of-freedom (DOF) parallel manipulator. The octahedral hexapod design has the main benefit of being very stable. An example of this design is shown in Figure 2.9c.
- *Google wire heliostat:*  
This design was proposed by the Google Corporation. It is a heliostat actuated by two wires wound by worm gear motors (the design is shown in Figure 2.9d).
- *Liquid ballasted heliostat:*  
This design is shaped like a hemispherical ball with numerous internal chambers. The heliostat is directed by pumping water in between the chambers, therefore changing the centre of gravity.

**Wire heliostat:** Ultra-light heliostats can be developed by using wires instead of beam grids. The design uses the properties of tension and compression, rather than bending.

The concept can be seen in Figure 2.9e. This could reduce the weight of the design by 65%.



Figure 2.9: The different types of heliostats (starting from the top left): (a): a serial type heliostat shown from the back used in the PS-10 heliostat field in Seville, Spain (Solúcar, 2006); (b): a universal solar tracker shown at different angles (Orshan, 2010); (c): an octahedral hexapod concept (Wikipedia, 2018); (d): a Google wire heliostat designed by Google Corporation (Google.org, 2011); and (e): a wire heliostat developed by Solaflect Energy (Solaflect Energy, 2018).

### 2.3.2.2 Heliostat field layout configuration

To obtain high efficiencies in central receiver systems, the optical design and optimisation of the heliostat field is essential. The three main factors that account for the loss of performance in a heliostat field are shading, blocking and atmospheric attenuation. According to Li et al. (2016), the general design procedure for a heliostat field with a predetermined heliostat design and receiver type is as follows:

- i. Determine the basic configuration or heliostat field type, as well as the location of the heliostat field and the receiver within the field.
- ii. Generate and optimise the field layout through a simplified optical analysis.
- iii. Iteratively obtain a high-fidelity heliostat field through detailed optical or thermal models by coupling the field system with the predetermined receiver.

Heliostat fields can be classified in their most basic configuration as either a polar or a surround field. A polar field provides a one-sided, highly asymmetric irradiation, while the surround field allows for a

more circumferential irradiation. A surround field can collect solar irradiation at lower solar azimuth angle values with the heliostats positioned in the east and the west.

These fields do not need towers that are as high for a given power level, compared to polar fields, which have advantages in terms of losses, construction material and other costs. Since surround field heliostats are positioned closer to the target than polar fields, there are fewer atmospheric attenuation losses. Polar field heliostats, on the other hand, are positioned on the polar side (north or south field configuration for plants located in the northern or southern hemisphere, respectively), and will therefore operate with lower cosine losses. Polar fields are generally used for cavity receivers with high-temperature applications (Li et al., 2016). Examples of real-life applications of both these fields can be seen in Figure 2.10.



**Figure 2.10:** (a): The PS-20 north-facing heliostat polar field in Seville, Spain, is on the left (Wordpress.com, 2013); and (b): the Crescent Dunes surround field constructed near Tonopah, USA, on the right (Proud Green Building, 2017).

With the basic configuration decided on, one can decide on the arrangement or layout of these heliostats within the configuration. The general categories are as follows (Li et al., 2016; Lal, 2017):

- Radial cornfield
- Radially staggered field
- North-south cornfield
- North-south staggered field
- Biomimetic field

The radially staggered field layout is used in the majority of applications and research due to its superior performance over the other patterns, although the biomimetic field layout has shown better optical efficiencies and ground coverage than the radially staggered pattern (Noone, Torrilhon, & Mitsos, 2012). The basic heliostat pattern is then applied to the basic configuration and optimised. Many heliostat field generators and optimisation tools have been developed, and these codes provide substantially different fields, each with its own benefit. A study conducted by Mutuberria, Pascual, Guisado and Mallor (2015) illustrated the different layouts that were produced by comparing the dense radially staggered method, Campo code, graphical method, DELSOL method and biomimetic pattern with each other, and seeing how the different layouts affect the power plant's efficiency. The different layouts that were produced during that study are displayed in Figure 2.11.

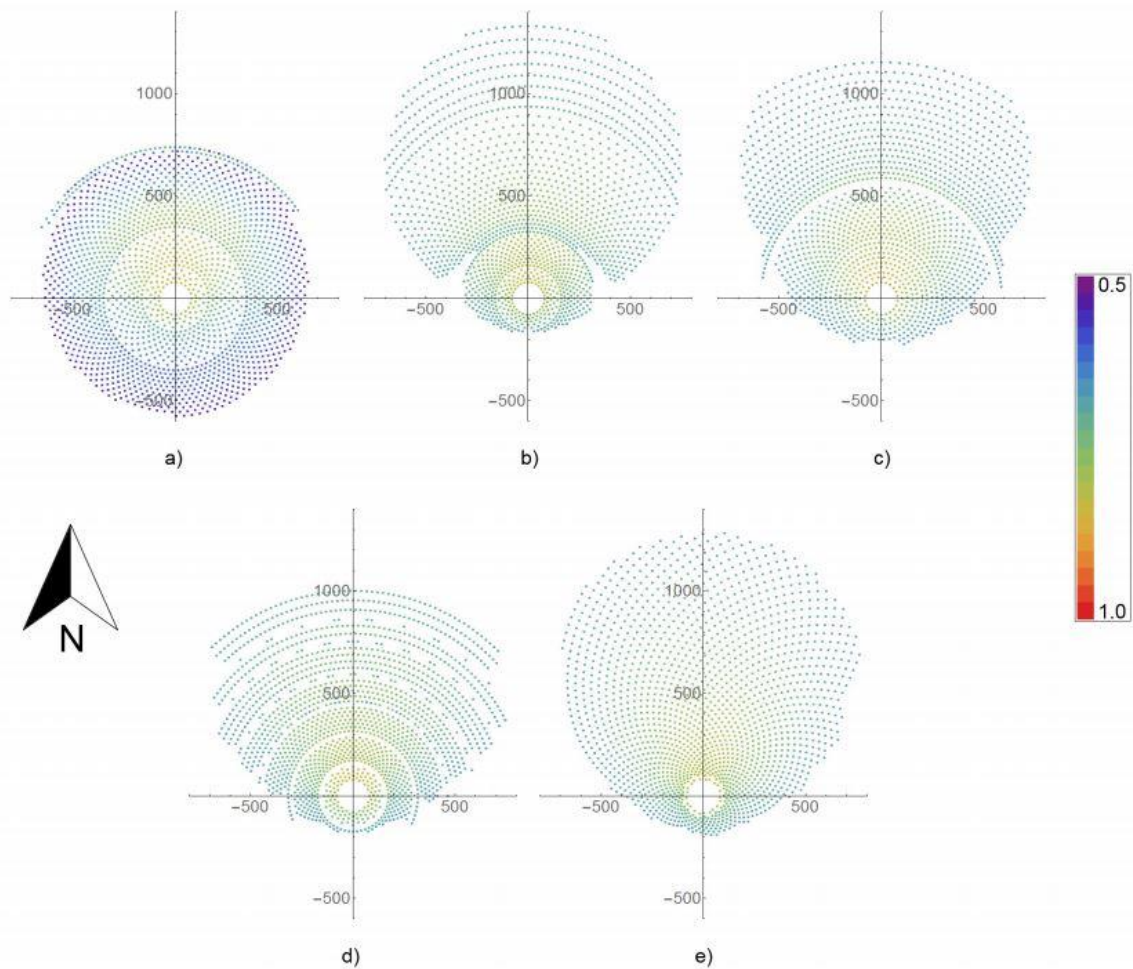


**Figure 2.11: Heliostat field layouts developed with different approaches: (a): dense radially staggered method; (b): Campo code; (c): graphical method; (d) DELSOL method; and (e): biomimetic pattern.**

Although surround-field layout optimisation dominates, there are also interesting developments and applications for polar field development, especially when considering cavity receivers. There has to be some innovative solution to reduce the drawbacks that were mentioned to make polar field layouts competitive. Studies conducted by researchers such as Schmitz et al. (2006) and Ramos and Ramos (2012) proposed fields with multiple apertures, thereby dividing one north-oriented (northern hemisphere) polar heliostat field into multiple sub-fields, all spaced around the central receiver tower. This has shown to increase the heliostat field efficiency compared to the single aperture field configuration. An example of the multiple sub-field commercial application is the Khi Solar One project in South Africa (refer to Table 2.2).

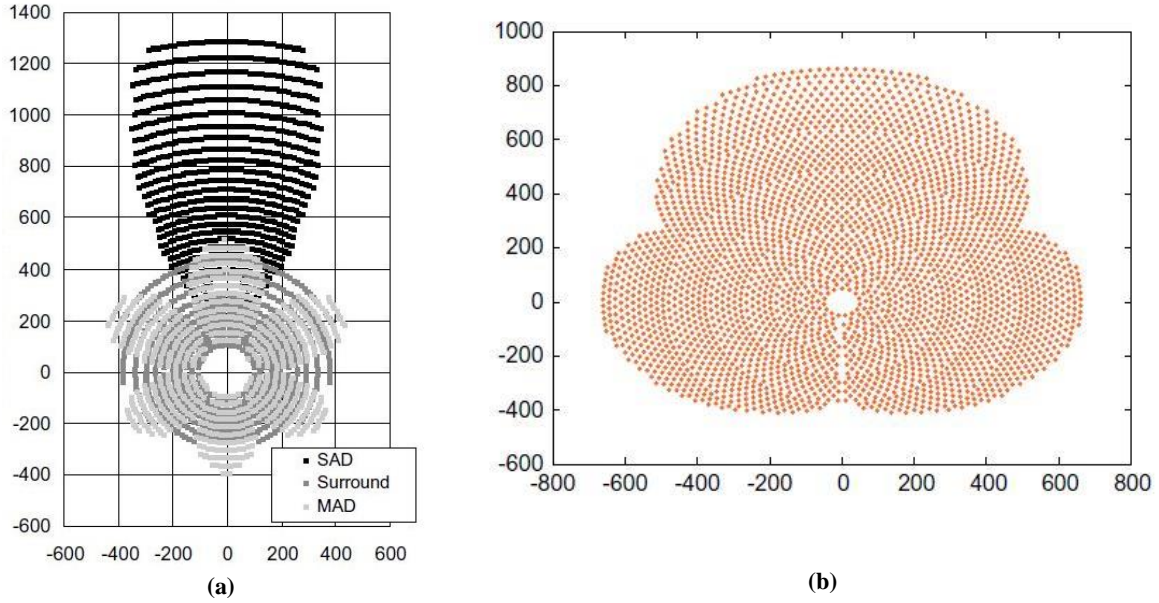


**Figure 2.12: (a): Multiple aperture field studies conducted by Schmitz et al. (2006) with multiple (six in this case) aperture design (MAD) compared to single aperture design (SAD) and surround field; and (b): Three polar fields spaced at 120° (Ramos & Ramos, 2012).**

### 2.3.3 Receiver design

The solar receiver for a central receiver system, or any other CSP system for that matter, is the heat exchanger where the concentrated solar radiation from the heliostat field is absorbed and transformed into thermal energy. It is then transported by means of an HTF to the desired destination of use or conversion. A great hindrance to central receiver development is the many variables that need to be considered, which affect the performance, efficiency and development of the system, since parametric studies of variables, as well as optimisation of the entire system, are resource intensive. This is no different when considering the receiver design of solar towers. Solar tower receivers differ in many aspects: from the type of HTFs they use, the geometrical configuration and the absorber material used, to the orientation of these receivers. There are no definite classification criteria for solar receivers. In this literature study, the classification of receivers will be conducted as follows: external receivers, cavity receivers, volumetric receivers, beam-down solar thermal concentrators, solid particle receivers, falling-film receivers and various other designs.

The main factors accounting for a receiver's loss of performance are due to thermal losses, as well as aperture spillage losses at the focal region due to aperture constraints. The receiver's efficiency is the ratio of energy that is usefully converted ( $\dot{Q}_{converted}$ ) to the amount of energy concentrated onto the receiver ( $\dot{Q}_{input}$ ), or (Lovegrove & Stein, 2012):

$$\eta_{rec} = \frac{\dot{Q}_{converted}}{\dot{Q}_{input}} = \frac{\dot{Q}_{input} - \dot{Q}_{losses}}{\dot{Q}_{input}} \quad (2-2)$$

The amount of energy concentrated onto the receiver can be analytically stated as follows:

$$\dot{Q}_{input} = \int_{time} \int_{aperture} G_{incident}(t) dA dt \quad (2-3)$$

Should the receiver not use any of the energy radiated onto it, it will heat up to the point where the losses balance out the incident radiation. The temperature to which it heats up is generally called the stagnation temperature.

The focal region flux distribution is of substantial importance, since it will determine the shape and size of an optimal receiver. A typical point focus distribution is displayed in Figure 2.13. An increase in the receiver aperture area is needed to capture all of the rays directed onto it. On the other hand, increasing the area of a receiver will result in large radiative and convective losses. These trade-offs should thus be considered when designing a receiver.

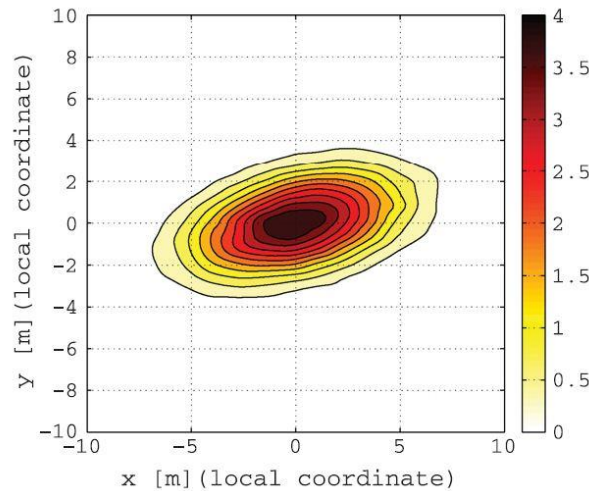


**Figure 2.13: Single heliostat spot size aperture flux distribution of the PS-10 heliostat field using SolTrace (Noone et al., 2012).**

Unlike parabolic dishes, where the system is limited to a single focal region flux distribution, central receiver systems have the freedom of applying different aiming strategies by assigning different zones of the heliostat field to different regions on the aperture, therefore providing different solar flux distributions. These altering aiming strategies could provide flexibility in terms of receiver design or optimise the flux absorption of an existing design. The study of Binotti, De Giorgi, Sanchez and Manzolini (2016) is an example of a study that was conducted on aiming strategies for central receiver systems, where different strategies were compared with one another for cavity and external receivers. An example of how different aiming strategies change the flux distribution is clearly visible in Figure 2.14.

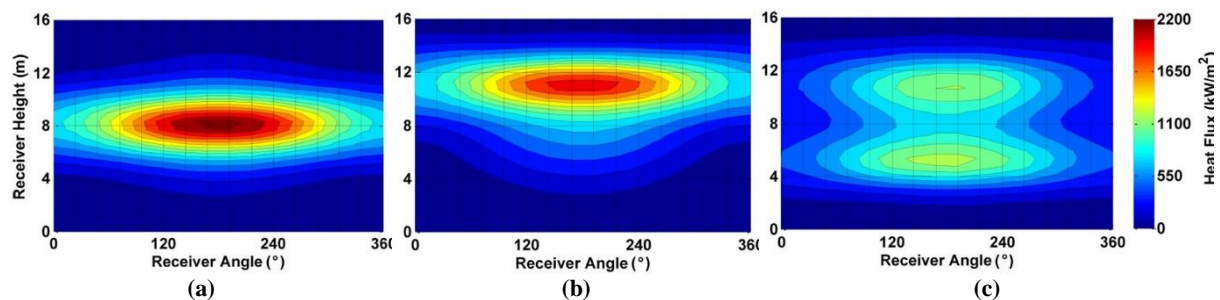


**Figure 2.14: Flux map distributions for the Gemasolar external receiver panels obtained with: (a): the reference aiming point; (b): Aiming Strategy 1; and (c): Aiming Strategy 6 (zero degrees refer to the southern direction) (Binotti et al., 2016).**

Receivers obtain their thermal energy from the concentrated solar radiation of the concentrators. It is this energy, or rather the thermal losses as mentioned earlier, that plays a significant role in receiver performance, and is the dominating factor when one looks at receiver efficiency. Other factors that would affect the receiver’s performance would include optical losses such as spillage and reflectivity. The thermal losses will be the sum of the conduction, convection and radiation losses that are experienced by the receiver. The conduction losses (heat transfer through the receiver structure) do not

usually play a major role when compared to the other losses and are therefore generally not a great focus in the optimisation of receivers.

The losses obtained from receivers due to radiation include the reflection of some of the incident radiation on the receiver as well as the net emitted radiation from the receiver because of its temperature. The surface of an object (such as a receiver) will emit radiation in proportion to the fourth power of temperature at a rate given by the black body emissive power multiplied by its emissivity, or as follows (Cengel & Ghajar, 2015):

$$\dot{Q}_{rad} = \sigma A \varepsilon (T_{rec}^4 - T_{ambient}^4) \quad (2-4)$$

with:

- $\sigma$  - Stefan-Boltzmann constant ( $\sigma = 5.670 \times 10^{-8} \text{ W/m}^2 \cdot \text{K}^4$ )
- $A$  - Area of surface of radiating object
- $\varepsilon$  - Emmissivity of a surface,  $0 \leq \varepsilon \leq 1$
- $T$  - Temperature measured in Kelvin

Some fraction of the incident radiation is reflected from any surface on which it is incident. This fraction depends on the geometry and its surface properties, more specifically its reflectivity. Another surface on the receiver, especially in designs such as cavity receivers, sometimes intercepts the reflected radiation and radiation emitted due to the surface temperature. Cavity receivers are especially relevant in receiver designs for high-temperature central receiver systems due to the radiation losses factor being coupled to the fourth power of temperature, since the view factor to the external environment is smaller, thereby limiting the radiation losses.

The other major thermal loss factor is the effect of convection. Convection losses are the losses that arise in solar receivers when air moves over the hot receiver surfaces. These convection losses can be further divided into forced convection losses due to wind and natural convection losses as a result of the buoyancy effects of heated air.

These losses are minimised by placing glass covers over receiver surfaces and/or by orientating the receiver to capture the buoyant hot air. Many other designs are also available to withstand these losses, as will be discussed in the following sections. Convection losses are difficult to measure directly, and empirical results are usually obtained by subtracting other losses from the overall energy balance. Once the average convection heat transfer coefficient ( $h$ ) is obtained, one can calculate the convective losses as follows (Cengel & Ghajar, 2015):

$$\dot{Q}_{conv} = hA(T_{rec} - T_{ambient}) \quad (2-5)$$

A review will follow on solar tower receiver designs that have been implemented, receivers that are still being developed and proposed designs.

### 2.3.3.1 External receivers

External receivers are situated externally, as the name implies. To be more specific, these receivers are open to the surroundings (and therefore have a large view factor) with the aim of being as exposed to the heliostat fields as possible. Although other external receiver designs have been proposed, one type of external receiver has been applied in practice and has therefore been researched the most. This is the external tubular panel receiver.

External receivers have the advantage of being visible for heliostats at all angles around the receiver, but this is also one of their disadvantages. If the receiver is heated by solar radiation, it loses a large

amount of thermal energy due to radiation losses because of the increased temperature (higher operating temperatures will result in higher surface temperatures, which again results in increased thermal emissions and convective losses) and increased view factor. Convection losses occur due to the receiver area being exposed to air flow passing unopposed across the surface of the receiver.

### 2.3.3.1.1 External tubular panel receivers

Together with the cavity receiver, external receivers that are equipped with panels of parallel-aligned tubes are among the earliest and most common receivers to have been implemented in central receiver systems. Research conducted on these types of receivers in the 1970s led to the eventual first implementation at the Solar One and Solar Two demonstration plants (Stine & Geyer, 2014; Pacheco et al., 2002). The conventional tubular receiver usually consists of a multitude of panels with an array of thin-walled tubes that are typically arranged to provide the HTF with optimal heat absorption. The many thin-walled tubes act as a mechanism to enhance heat transfer due to the increased surface area that the tubes provide to absorb the incident flux. Examples of these receivers are displayed in Figure 2.15.

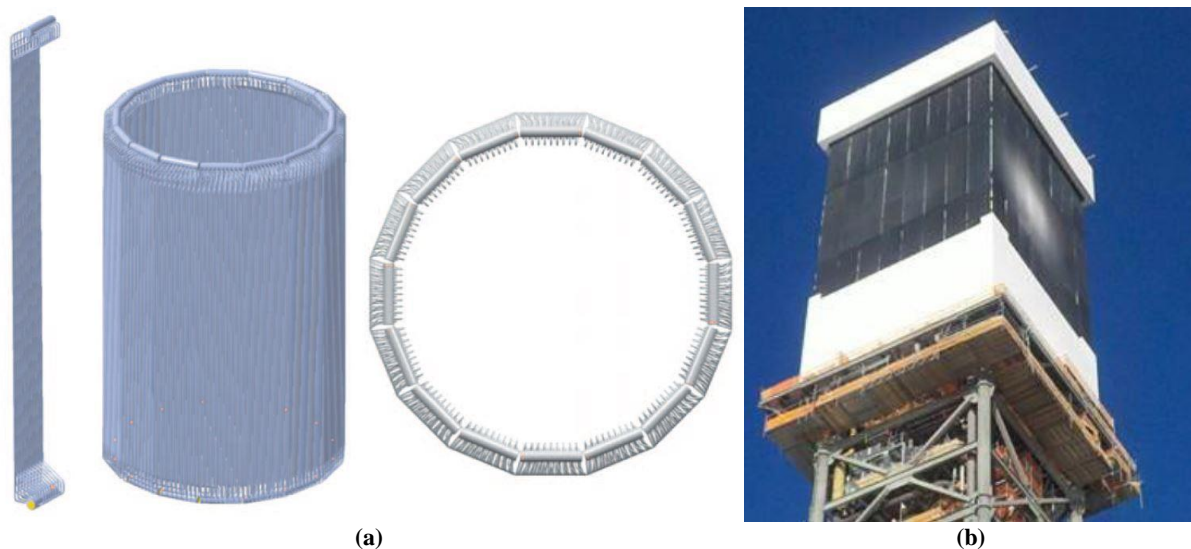


Figure 2.15: Typical external tubular panel receivers that are implemented, such as: (a): the receiver design of the previously known SolarTres power plant project, but renamed the Gemasolar power plant (Lata, Rodriguez, & De Lara, 2008); and (b): the view of the four-panel external tubular receiver of the Ivanpah solar power plant (Hoffschmidt, 2014).

The simplistic design that the tubular receiver provides makes it possible to be manufactured and assembled easily. It also provides the freedom to easily adjust the design to accommodate a wide variety of HTFs. This is evident with the different HTFs that have been implemented and tested with the tubular panel. These include water or steam, nitrate salt (Ortega, Burgaleta, & Téllez, 2008; Dunn, Hearsps, & Wright, 2012) and sodium, although sodium was never implemented commercially due to its high combustibility when in contact with water, which would require extra precautionary measures (Boerema, Morrison, Taylor, & Rosengarten, 2012). Recent reports prove otherwise, with commercial prototyping and development currently being done by Vast Solar (Vast Solar, 2019). Other fluids are also being considered for external tubular receivers, such as alternative liquid metals (Pacio & Wetzel, 2013), fluoride salts (Forsberg, Peterson, & Zhao, 2007), carbonate salts (Ho & Iverson, 2014) and chloride salts (Singer, Buck, Pitz-Paal, & Müller-Steinhagen, 2010) to improve the efficiency of the receiver with the superior properties the fluids hold. Liquid fluids are considered better HTFs compared to gaseous fluids due to the generally higher heat transfer rates and specific heat properties. High thermal conductivity is also preferred to reduce the temperature difference between the front (flux side) and back, which reduces the thermal stresses involved. Apart from the HTF being selected for the

external tubular receiver design, a lot of research is being conducted to optimise the dimensions of the receiver (such as the overall cylinder diameter, number of tubes, tube diameter and thickness, and fluid velocity) for different heliostat fields (Lata et al., 2008; Rodríguez-Sánchez, Sánchez-González, Marugán-Cruz, & Santana, 2014; Rodríguez-Sánchez, Sánchez-González, Acosta-Iborra, & Santana, 2017).

Research also focuses on analysing and minimising the thermal losses (including emissive, convective, reflective and conductive losses) (Rodríguez-Sánchez, Soria-Verdugo, Almendros-Ibáñez, Acosta-Iborra, & Santana, 2014; Rodríguez-Sánchez, Marugan-Cruz, Acosta-Iborra, & Santana, 2014; Pye, Zheng, Asselineau, & Coventry, 2014), coating materials (Joly et al., 2013) and aiming strategies for optimal flux distributions on the receiver (Binotti et al., 2016; Sanchez-Gonzalez & Santana, 2015).

### 2.3.3.1.2 External pyramid receiver

As was mentioned earlier, a significant disadvantage of external receivers is the losses experienced by re-radiation and convection. To mitigate these losses, different innovative designs have been proposed. The Institute of Heat and Mass Transfer in Aachen, Germany, proposed a concept to overcome these losses. This innovative design consists of many hexagonal pyramid-shaped elements that are arranged in a honeycomb structure, their apexes pointing outwards in the direction of the heliostat field. Figure 2.16a displays the pyramid design as it would be installed on top of a tower. Figure 2.16b shows a schematic of the structure of the outside geometry for a section of the receiver.

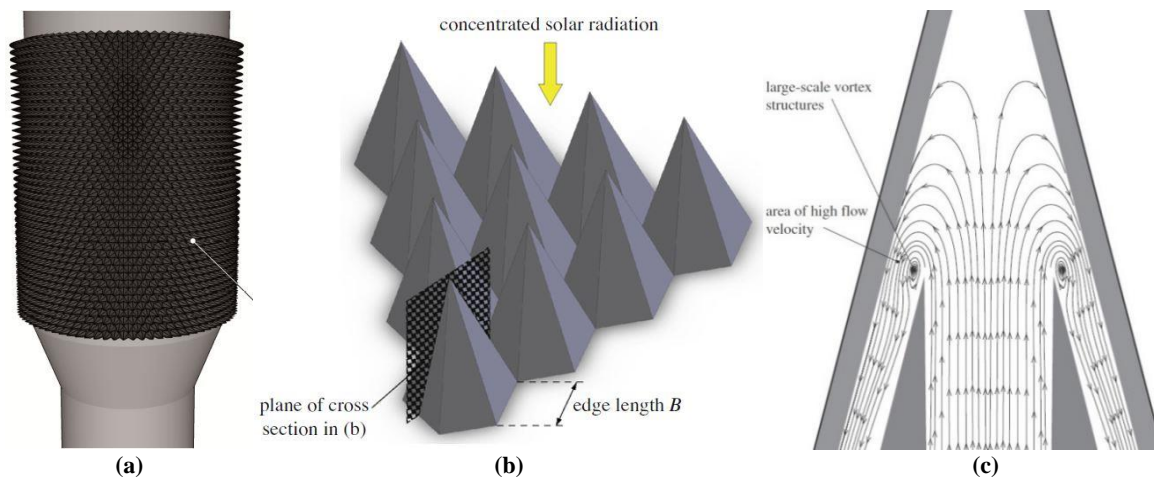


Figure 2.16: Schematic diagrams of: (a): the external pyramid design mounted on top of a tower (Garbrecht, Al-Sibai, Kneer, & Wiegardt, 2012); (b): a close-up view of a section of the pyramid structure; and (c): the flow of the HTF within the pyramid structure (Garbrecht, Al-Sibai, Kneer, & Wiegardt, 2013).

Figure 2.16c illustrates the HTF flow. This concept was specifically designed for molten salts. As can be seen in the image, the cold HTF enters the bottom of a central pipe, after which it flows next to the inner surface of the pyramid, where the HTF is heated due to the incident radiation until it eventually exits at the fringes of the pyramid's base. Each pyramid consists of two nested components: an outer and an inner pyramid. The outer pyramid absorbs all the radiation and keeps the flow from escaping to the environment. The outer pyramid is also stacked with fins, therefore increasing the heat transfer to the HTF. The inner pyramid consists of the central pipe that channels the flow to the tip of the pyramid.

The design has the advantage of creating a large surface area, therefore reducing thermal stresses that are witnessed at other receivers. The honeycomb layout of the structure also reduces natural or forced convection created by winds, since the hexagonal elements cause “valleys” to bifurcate after each edge, which reduces the wind speed. Reportedly, the problem of radiation losses is also limited with this design. Whether it is incident light reflecting, or radiation due to increased temperature, the pyramid

shape ensures that when radiation is emitted from its body, the lost energy will at least be partially captured by a neighbouring pyramid. The argument can be countered with the statement that an increase in irregular surfaces results in an increased surface area, which in turn results in an increase in losses. This design's structure counters these losses by distributing the high temperatures to low view factor areas.

With cool HTF entering through the central pipe, it is injected at the tip of the pyramid. Having the coolest HTF at the tip ensures less loss at the tip, which is beneficial since the heat losses at the tip of the pyramid structure are those losses that are least likely to be captured, while the high temperature regions in the “trenches” of the design experience lower view factors. The impinging flow also gives the receiver superior heat transfer capabilities (Garbrecht et al., 2013).

### 2.3.3.1.3 Spiky central receiver air pre-heater receiver

The spiky central receiver air pre-heater (SCRAP) is another innovative external receiver design proposed by the Solar Thermal Energy Research Group (STERG) of the Stellenbosch University, South Africa. This receiver's goal is similar to the goal of the pyramid's external receiver: to have the advantages of external receivers without the excessive radiation and convection losses associated with them. The receiver can be described as a collection of tubular absorber assemblies or spikes concentrically distributed to form a “porcupine” effect, where the spike density increases as one approaches the centre of the receiver. The design is illustrated in Figure 2.17a.

Intended for solarised gas turbine applications, “cold” air enters through an inner chamber, where it is directed through a multitude of circular tubes into the absorber assemblies. The spike consists of two concentric tubes, with the inner tube supplying the cold air to the tip of the spike, where it impinges and returns via the outer tube back to the centre of the receiver. The heat transfer is enhanced by adding internal, helical fins. Figure 2.17 schematically illustrates the geometry and design of the tube.

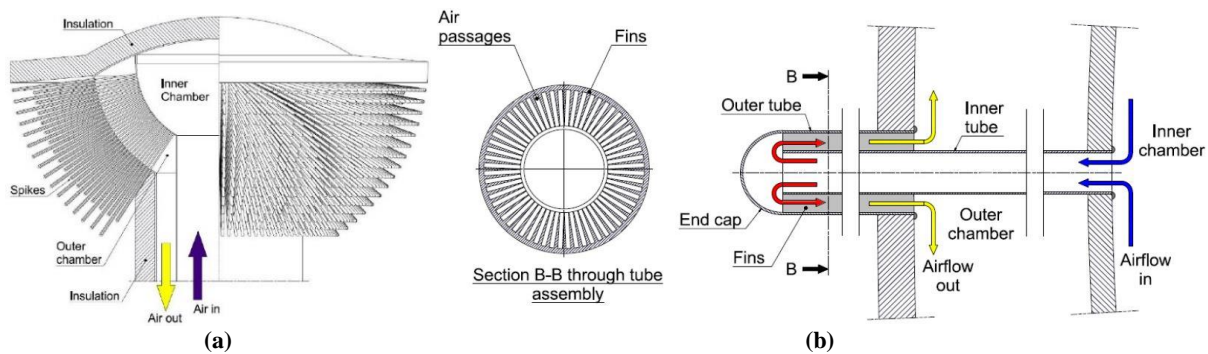


Figure 2.17: (a): The preliminary SCRAP receiver design as would be mounted on a solar tower; and (b): geometry of the internally finned tube with illustrations of air flow (Lubkoll, Von Backström, Harms, & Kröger, 2015).

The concept of the SCRAP receiver is similar to the pyramid external receiver, where the cold fluid is impinged at the tip to prevent overheating, as well as to limit radiation losses. As the air flows from the spike tip to the centre, the temperature increases, which causes radiation losses. Other spikes capture these losses as the spike density increases towards the centre. A similar pattern is also introduced (hexagonal) for the structure of the spikes. As was explained under the heading ‘External pyramid receiver’, the pattern reduces convection losses due to the bifurcation of flow streams (Lubkoll et al., 2015).

### 2.3.3.2 Cavity receivers

The cavity receiver is designed and developed to limit the thermal losses that are evident at external receivers. The heating element or absorbing material is designed to be situated inside a cavity, where

the receiver is not exposed to the elements, and with some designs even limiting major radiation losses. Although these designs pose the advantage of limiting convection and radiation losses, they have the disadvantage of only being able to capture a limited acceptance angle of incoming rays. Unlike the external receiver that can usually absorb incident radiation from any angle or direction, the cavity receiver is limited to acceptance angles of  $60^\circ$  to  $120^\circ$  (Battleson, 1981). Hence, this restriction is a vital piece of information when designing a central receiver system, since it influences the heliostat solar field pattern and position because all heliostats need to be within the receiver's designed angle. There are innovative ways of overcoming this restriction with special heliostat field designs, as was discussed in Chapter 2.3.2 under the sub-section 'Heliostat field layout configuration'.

### 2.3.3.2.1 Tubular panel cavity receiver

As mentioned earlier, together with the external counterpart, cavity receivers with parallel-aligned tubes nested within the cavity are the most common receiver in central receiver systems. It is the simplistic design of panels consisting of tubes, which were explained in the sub-section 'External tubular panel receivers', that provides an alternative to the external design. It also provides the added benefit of having a smaller view factor, which limits the radiative losses, and since it is enclosed, also restricts the convective losses. In small-scale developments, a central receiver system with a polar field provides the obvious choice for a cavity receiver due to its simplicity in design. For this reason, the first central receiver test systems were developed with cavity receivers, such as the IEA/SSPS in Spain (Kesselring & Selvage, 1986) and the EURELIOS solar system in Italy (Hofmann & Gretz, 1980). Examples of cavity receivers with tubular panels are displayed in Figure 2.18.

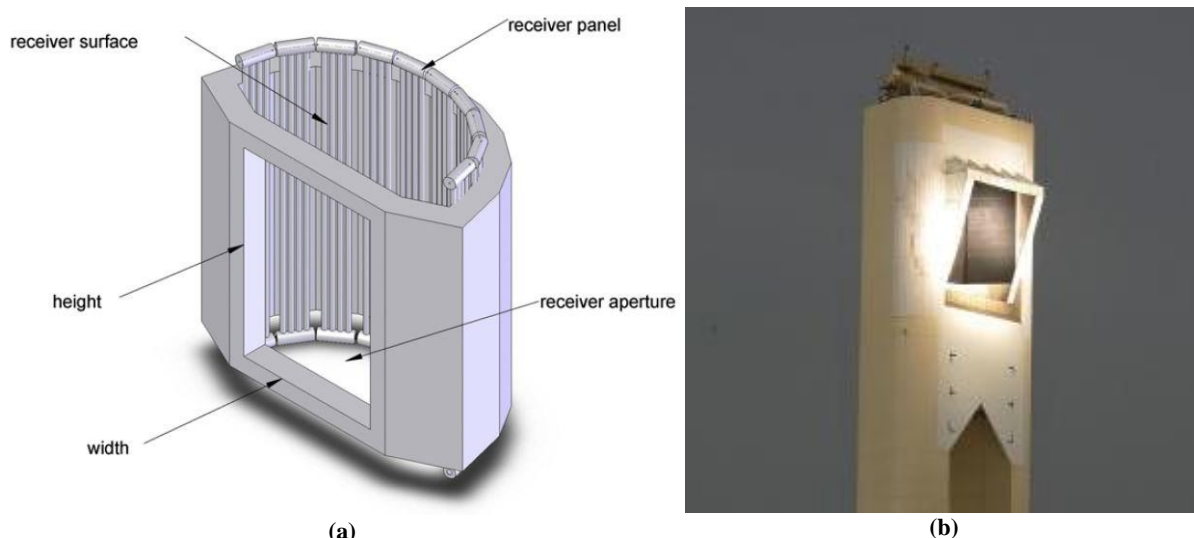


**Figure 2.18: Examples of tubular panel cavity receivers with: (a): a schematic design of a cavity receiver by Li, Kong, Wang, Chang and Bai (2010); and (b): a implemented cavity receiver at the PS-10 solar plant in Seville, Spain (StateImpact, 2012).**

The panel design of cavity receivers is similar. Therefore, much research that was conducted on tubular panels for external tubular receivers could apply to the cavity receiver. This is especially true for design parameters such as the selection of HTF and coating materials. The main purpose for cavity receiver implementation is to mitigate losses for high-temperature processes. Therefore, a lot of research has been conducted on the effect that factors such as natural convection (Clausing, 1981; Gonzalez, Palafox, & Estrada, 2012), forced convection by winds (Fang, Wei, Dong, & Wang, 2011) and radiation have on the performance of the receiver (Yu, Wang, & Xu, 2012), and how these factors could be limited (Chang, Li, Xu, Chang, & Wang, 2014; Li et al., 2010). In addition, research to enhance heat transfer is a much-researched topic (Montes, Rovira, Martínez-Val, & Ramos, 2012), with researchers such as Liao and Faghri (2016) proposing innovative designs to improve the cavity receiver's performance.

### 2.3.3.2 Tubular gas receiver

Some receiver designs use gas as a medium for tubular receivers since it has the benefit of high-temperature solar thermal cycles for air-Brayton cycles. The most basic prototype for air is the use of tubes, although the design differs substantially from the liquid HTF medium tubular designs. Since gas receivers are only practical at high temperatures, it only makes sense to have a design that minimises the effect of re-radiation, hence a cavity design. Early receiver designs for air tubular gas receivers were conducted for parabolic dish systems (Bienert, Rind, & Wolf, 1979), although tubular gas receiver prototype developments for central receivers are done independently nowadays. The DLR recently conducted designs and tests for a solar-hybrid microturbine system for applications to the order of 100 kW to 1 MW (Heller et al., 2006; Amsbeck, Buck, Heller, Jedamski, & Uhlig, 2008). Examples of tubular gas receiver designs are displayed in Figure 2.19.

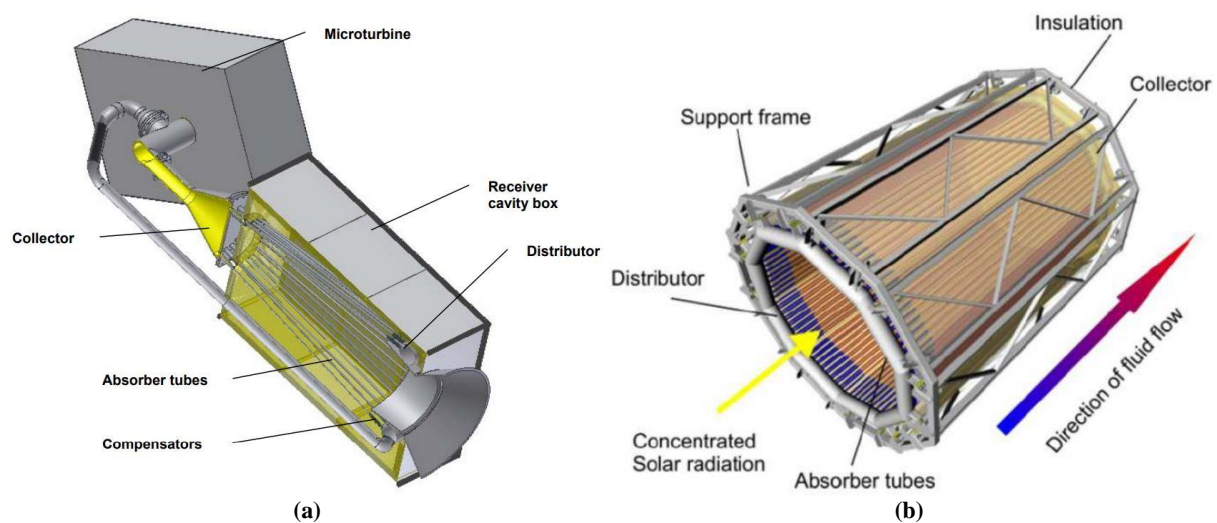


**Figure 2.19:** Examples of design concepts from the DLR: (a): a schematic illustration of the Solar-hybrid Power and Cogeneration (SOLHYCO) receiver concept (Amsbeck et al., 2008); and (b): the design of the Solugas receiver (Korzynietz, Quero, & Uhlig, 2012).

One of the great disadvantages of these receivers is the low heat transfer coefficient of gases in general. The high fluxes on the receiver could lead to metal tubes reaching temperatures above those needed for structural integrity, since the gases are unable to effectively absorb the incident fluxes. Designs have been proposed to increase this heat transfer. Another major issue is the rapid transient thermomechanical loads that the receivers are subject to. This can adversely affect the receiver's fatigue life.

### 2.3.3.3 Volumetric receivers

During the early developments of central receiver systems, it was noticed that the quasi-two-dimensional tube provided limited heat transfer abilities, hence the search continued for alternative heating elements. This led to the development of volumetric receivers: receivers that provided the benefit of having a smaller aperture (which resulted in smaller thermal losses due to re-radiation) and that were more flexible due to their three-dimensional (3D) configuration. The volumetric receiver has been researched extensively since the 1990s, predominantly in Europe and Israel (Avila-Marin, 2011).

Fundamentally, volumetric receivers are a multitude of porous interlocking shapes, foam, knit-wire packs or foil arrangements made of metal, ceramic or other adequate materials with a specific porosity that are installed in a space or volume inside a receiver. This volumetric porous substance absorbs the concentrated solar radiation by heating the material in the volume. While the material is heated, a working fluid such as air or carbon dioxide passes through the volume. Forced convection heats the

working fluid. Therefore, the material transforms the solar radiation to thermal energy. The schematic in Figure 2.20a illustrates this process well (Hoffschmidt, Téllez, Valverde, Fernandez, & Fernandez, 2003). A significant amount of research has been conducted on different designs using the concept of volumetric irradiance absorptance and the prospects of using solar energy for a combined cycle.

This has brought with it developments for pressurised, closed-loop volumetric receivers. Volumetric receivers can hence be classified to be either open-air volumetric receivers, as illustrated with a schematic of the performance of the HiTRec open-air volumetric receiver in Figure 2.20a, or closed-loop volumetric receivers, as illustrated in Figure 2.20b. This provides a good example of a closed-loop volumetric receiver, and gives the concept design for the receiver module of solar-hybrid gas turbine and CC systems (REFOS).

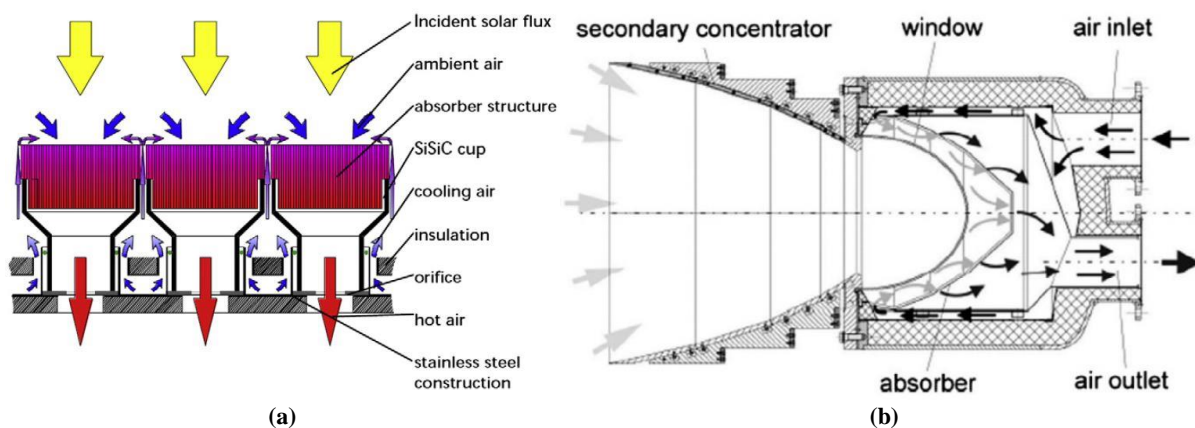


Figure 2.20: Examples of volumetric receivers with: (a): a schematic of the performance of the HiTRec open-air volumetric receiver (Hoffschmidt et al., 2003); and (b): a concept design of the REFOS closed-loop volumetric receiver module (Buck, et al., 2002).

Volumetric receivers are claimed to be more efficient than tubular receivers and are reported to can reach much higher temperatures due to their volumetric effect. This is because the thermal energy can be directly absorbed and is not subject to thermal conductivity losses through the absorber material. Another benefitting factor of volumetric receivers is the fact that cold air penetrating the porous medium keeps the frontal surface temperature at a lower temperature. This limits the radiation losses to the environment. One obvious benefit of porous-medium heat transfer is the large surface contact region between the working fluid and the absorber, enhancing heat transfer (Avila-Marin, 2011).

During the selection of volumetric receivers, the following predominant variables should be considered:

- The absorber material
- The flow stability

When considering a potential absorber material, any highly porous structure that can sustain its properties and be durable over a lengthy period under high, fluctuating temperatures would suffice as an absorber material candidate. Currently, two major materials are being used for volumetric receivers: metal and ceramic materials. Ceramics can achieve the highest temperatures and is therefore a more suitable material when temperatures exceed 800 °C. Metals are capped at an absolute maximum near 1 000 °C for super alloys, with most other metals being unable to go over 800 °C. SiSiC ceramics' range dominates above the metals range exceeding temperatures of 1 200 °C, and SiC ceramics achieve a stable state at temperatures as high as 1 500 °C (Becker, Bohmer, Meinecke, & Unger, 1989). There are also other newly emerging ceramic materials, such as aluminium ceramics, which have a melting point of about 2 000 °C. They do, however inherit the main disadvantage of being white, but this can

be averted by doping or coating the material to increase its absorptivity, while retaining its good mechanical properties (Avila-Marin, 2011).

Next to choosing a material based on its temperature stability threshold, one also needs to consider a porous sample where there is a stable mass flow density distribution across the flow area. The mass flow density is usually determined by the pressure difference created between the two sides of a sample, with the pressure difference produced by a device such as a blower. Instability in the mass flow density can cause a difference in outlet temperatures. This could lead to a variety of issues, such as design flaws due to incorrect temperature predictions or thermal stress limits due to large temperature differences (Avila-Marin, 2011).

Current volumetric receivers still have poor performance in this category. The working fluid exit temperature for temperatures above 1 000 °C has not been predicted correctly yet. As is described in the research of Kribus, Ries and Spirkel (1995), unstable gas flow through the receivers has led to local overheating, causing poor performance and local fractures, such as melting or cracking.

#### 2.3.3.4 *Beam-down solar thermal concentrator*

The beam-down solar thermal concentrator (BDSTC) concept, although not a receiver concept, still deals with optics on the tower side, and it was decided to add it to this section. The concept was proposed for the first time at the Weizmann Institute in Israel (Segal & Epstein, 1997). Although at first welcomed with scepticism from the scientific community, the interest in this system has grown to what may today be a promising way of collecting solar energy. The BDSTC system is a point-focus concentrator that uses a heliostat field as a primary reflector that concentrates the incident solar radiation towards a second secondary central reflector. This secondary reflector redirects the focused radiation to a lower focal point close to ground level, where the receiver is situated. A schematic illustration of the workings of such a plant is displayed in Figure 2.21a.

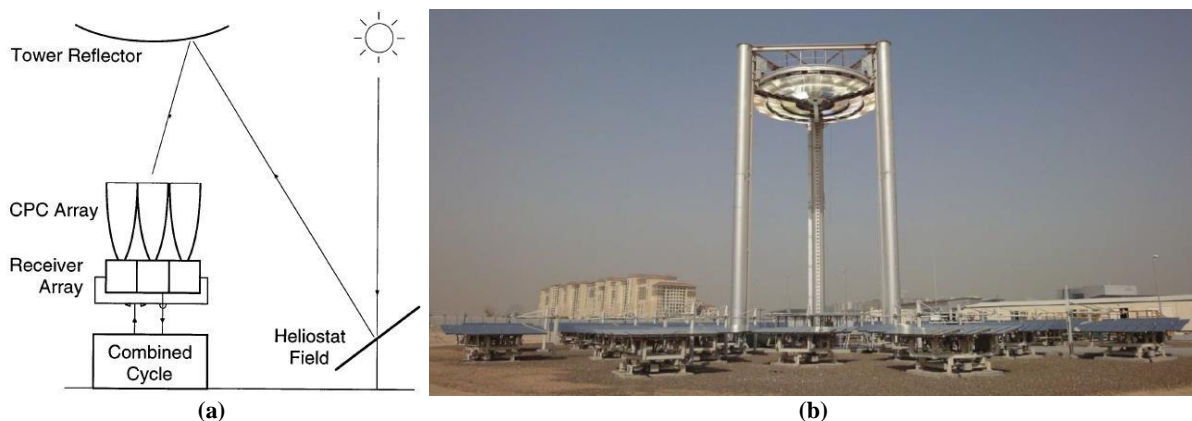


**Figure 2.21: The BDSTC: (a): schematic concept of plant (Kribus, Zaibel, Carey, Segal, & Karni, 1998); and (b): pilot plant constructed at the Masdar Institute of Science and Technology in Abu Dhabi (Mokhtar, 2011).**

The beam-down solar receiver has the main advantage of directing solar energy to a central point on ground level, rather than converting solar energy to heat at the top of the tower. At the bottom, the directed solar rays are further concentrated to a receiver by means of a secondary receiver such as a compound parabolic receiver (Kribus et al., 1998; Leonardi, 2012). This reduces losses associated with heat transport and would increase flexibility in receiver design development, with the receiver being on the ground level.

Since this is a relatively new concept in the world of CSP systems, not much research has been conducted on it. Therefore, there is not a variety of mentionable design concepts available. An example

of a prototype is the 100 kW<sub>th</sub> beam-down solar receiver pilot plant erected in Masdar City, Abu Dhabi (Mokhtar, 2011), while other prototypes include the Magaldi system in Italy and the prototype at the University of Miyazaki (Kodama, et al., 2014). This pilot plant of Masdar City is displayed in Figure 2.21b. A study conducted by Vant-Hull (2013) presented issues on this concept, with limitations regarding the constraints of the boundary of the heliostat field, costs associated with the production exceeding the elements that would be eliminated, as well as less than half of the optimum power to be generated compared to typical tower top receivers.

### 2.3.3.5 Solid particle receivers

In the 1980s, falling solid particle receivers were proposed as a means of reaching outlet temperatures of over 1 000 °C, with the advantage of using them as thermal storage by insulating these heated particles in insulated containers (Falcone, Noring, & Hruby, 1985). The solid particle solar receiver (SPSR) is a direct-absorption solar receiver that uses solid particles, mostly sand-like ceramic particles, which are enclosed in a cavity receiver to absorb the concentrated solar radiation. After the heating process, these particles are stored in an insulated tank for storage and used later or used by passing them through a secondary working-fluid-like steam, CO<sub>2</sub> and air for a power cycle. Figure 2.22 shows a design concept of such a solid particle receiver.

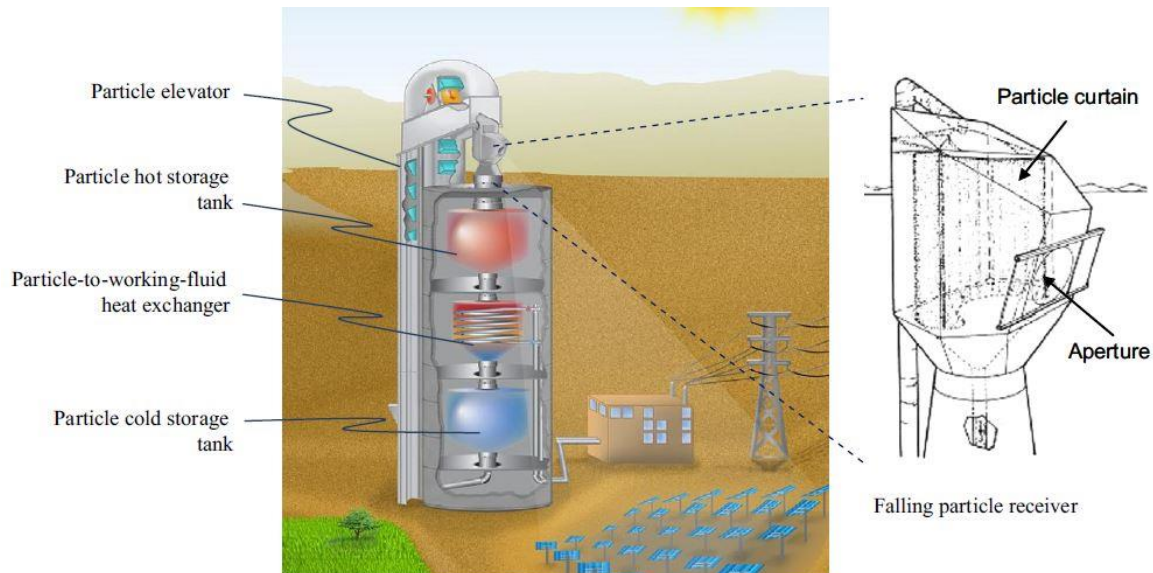


**Figure 2.22: The falling solid particle receiver system concept with an integrated storage and heat exchanger (left) and a close-up schematic design of the receiver (right) (Ho & Iverson, 2014).**

The most prominent research is currently done for the application of solid particle receiver technology on thermo-chemical hydrogen production processes. Water-splitting thermo-chemical (WSTC) processes require minimum temperatures of 700 °C and with current predictions to estimate solid particle receivers that obtain output temperatures of 1 000 °C and higher, it is a promising field to incorporate the technology (Tan & Chen, 2010).

SPSRs can pose great advantages. The WSTC process to produce hydrogen is a good alternative to provide transportable fuel for other industries. Solid particles also provide the advantage of being the medium that can be used to store heat, therefore eliminating inefficient heat exchangers for solar thermal storage. Solar thermal storage systems are also much cheaper to manufacture than the current commercial thermal storage systems that are implemented at other CSP plants, since the problems related to piping and heat exchanger designs, as well problems posed by using molten salts (freezing problem), air or steam (poor heat transfer) are absent when using solid particles. Furthermore, there are

no excessive thermal stresses on the plant components, since the particles absorb the heat instead of heating pipes or cavities (Tan & Chen, 2010).

Falling solid particle receivers, however, also have their disadvantages. Wind and convection losses greatly affect solid particles, even though they are positioned within a cavity-type receiver. With the particles falling, any wind can influence the particles' movement and position within the receiver, making the receiver inconsistent during the heating of the elements. (Tan & Chen, 2010)

Much analytical and numerical research has been conducted to overcome these challenges. There is also currently one on-sun prototype that has been constructed. Research has been conducted on the following topics:

- Particle materials with respect to their optical characteristics, structural stability, dynamics and heat exchange properties (Hruby & Burolla, 1984; Stahl, Griffin, Matson, & Pettit, 1986; Rightley, Matthews, & Mulholland, 1992)
- The receiver's internal fluid dynamics and heat transfer (Evans, Houf, Grief, & Growe, 1985; Meier, 1999; Chen, Chen, Hsieh, & Siegel, 2007; Kim, Moujaes, & Kolb, 2010; Tan, Chen, Chen, Siegel, & Kolb, 2009)
- The performance of a solar falling particle reactor (Meier, 1999; Chen, Chen, Hsieh, & Siegel, 2007; Röger, Amsbeck, Gobereit, & Buck, 2011)

Current developments also suggest that high-temperature, solar-thermal particle technologies have great potential. The Particle Technology Working Group (PTWG) has been established to collaborate on the acceleration of technology development. (Forty researchers from 13 countries are part of the PTWG.) Research needs and opportunities for particle technology include research on particle receivers, storage, heat exchangers, conveyance, systems analysis, modelling and research on the particles themselves. With this study not considering solar-thermal particle research, refer to Ho (2018) for further developments in high-temperature, solar-thermal particle research.

#### ***2.3.3.6 Falling-film receivers***

Falling-film receivers are characterised by the gravity-driven fluid motion in the receiver. The heat transfer medium enters the receiver at the top with a predetermined mass flow. The receiver contains a liquid film with free surface forms on an inclined absorber wall caused by gravity as it is being heated by concentrated solar radiation, either directly or indirectly, through the absorber wall, depending on whether the radiation is projected directly onto the fluid or onto the absorber wall. A major advantage of this type of receiver is the reduction of pumping requirements. The research community has proposed four different concepts so far (see Figure 2.23).

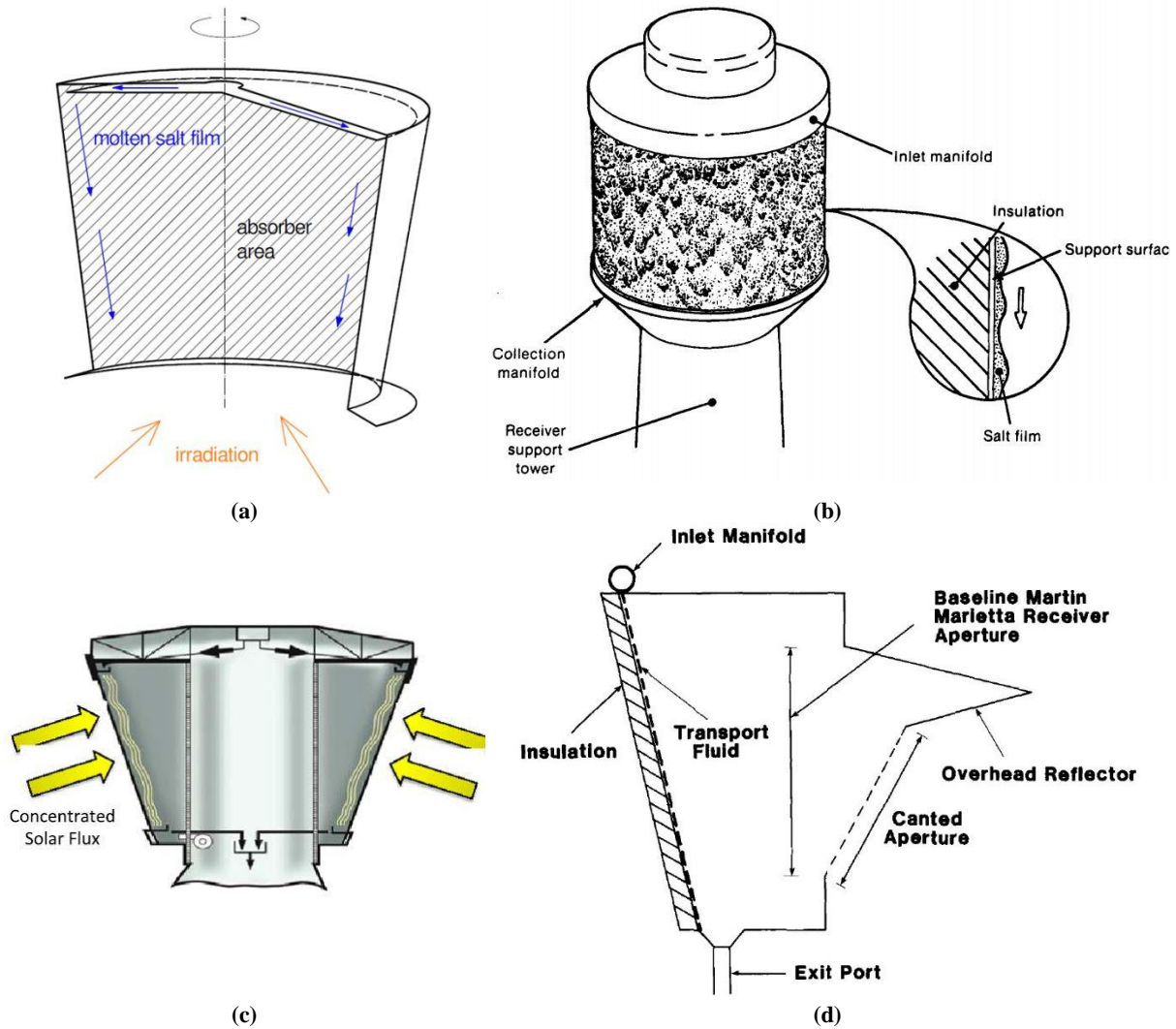


**Figure 2.23: Falling, liquid film receivers for heat absorption in: (a): direct exposure, internal receivers for a surround field (Wu, Gobereit, Singer, Amsbeck, & Pitz-Paal, 2011); (b): direct exposure, external receivers for a surround field (Bohn & Green, 1989); (c): indirect exposure, internal film receivers for a surround or polar facing field (Ho & Iverson, 2014); and (d): direct exposure, internal film receivers for a polar field (Hildebrandt & Rose, 1985).**

As noted in Figure 2.23, these receivers can have either direct or indirect exposure to radiation, irrespective of whether they have an external or cavity configuration. Direct-absorption receivers (DAR), the name given to receivers that have direct exposure to solar radiation, have the advantage of having a lower thermal resistance. Figure 2.23b shows a direct exposure external DAR. This receiver has an HTF that flows down its exterior as concentrated solar rays radiate from the receiver. One of the most predominant factors with this design, as well as with the other designs, is fluid flow control. The simplest way of increasing flow control is to increase the panel tilt as it has a strong effect on controlling fluid loss. It does, however, increase the receiver surface height as well (Bohn & Green, 1989).

Figure 2.23a and Figure 2.23d both illustrate internal DARs, meaning that the curtain of the falling liquid flows along the internal wall of the receiver as the solar flux is incident on it. These designs provide the benefit of cavity receivers: they drastically reduce convection and radiation losses, and benefit from the impact of wind on the fluid flow. The design also has the benefit of having a lower thermal resistance due to the design being a DAR. When one considers Figure 2.23a, the solar radiation enters the face-down aperture at the bottom of the receiver. The fluid is semi-transparent. Therefore, the radiation also heats up the wall of the enclosure. The receiver's efficiency can be increased by including the receiver's rotation and inclined absorber walls. Inclined walls drastically reduce reflection

losses, while rotation provides film stability, mass flow control, HTF overheating and excessive temperature variation mitigation (Wu et al., 2011). DAR designs' main concern is, however, that the molten salt HTF could contaminate the environment through film instability and wind exposure.

The indirect exposure internal film receiver (see Figure 2.23c) avoids the weaknesses of direct absorption techniques, such as environmental contamination. With this design, the external wall is heated by the concentrated solar ray incidence, while the film absorbs the heat while flowing onto the internal wall. The main advantage of this design over the external tubular panel receiver is its design and assembly simplicity, as well as the material and manufacturing cost reduction by replacing tube panels with a thin plate, as well as a smaller pump, which is required to reduce pressure losses (Ho & Iverson, 2014).

### 2.3.3.7 Other receiver designs

#### 2.3.3.7.1 Dual receiver

The dual receiver concept is assumed to be a combination of a tubular receiver and a volumetric receiver. The tube flow drives the evaporation of water, while the volumetric receiver heats up the air. The receiver is configured so that the tubes are placed in front the volumetric receiver facing the focal point. The tubes' purpose is primarily to cool down the front of the volumetric area and to restrict radiation and convection losses associated with great temperature difference at surfaces. This concept can be configured radially to capture a wide angle as was proposed by Buck, Barth, Eck and Steinmann (2006), but it does not have to be restricted to such designs. Figure 2.24 shows the schematic representation of the dual receiver concept.

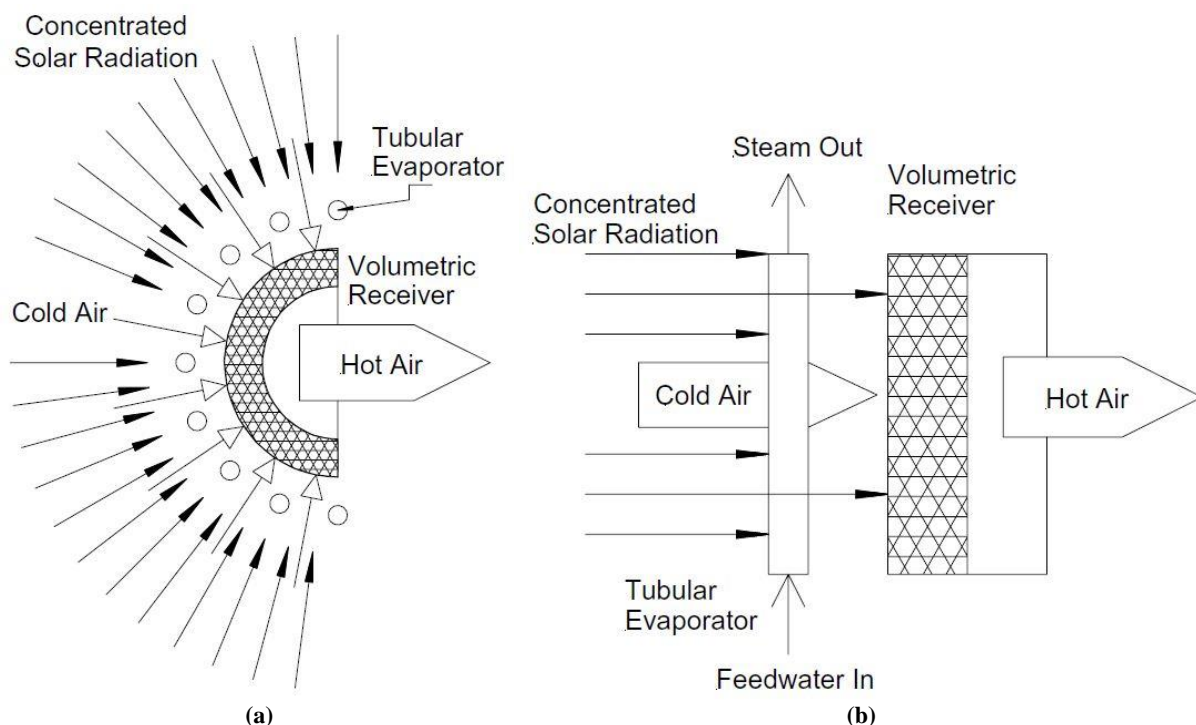


Figure 2.24: A schematic representation of the dual receiver concept from: (a): the top view; and (b): the side view (Buck et al., 2006).

#### 2.3.3.7.2 Reticulate porous ceramic pressurised air receiver

Pressurised air is needed for increased efficiencies in power generation cycles. Most volumetric receivers absorb air from the environment at the receiver. Therefore, the air is not heated at high pressures. Numerous designs have been available for closed-loop volumetric receivers, where the

receiver is closed off with a quartz window. This, however, puts other strains on the design, since the window is under high pressure, while it has to deal with thermal stresses as well.

The reticulate porous ceramic (RPC) pressurised air receiver proposed by Hischier, Hess, Lipinski, Modest and Steinfeld (2009) is a more robust and less complex design, which can neglect the quartz window while retaining pressurised air. The design consists of two concentric cylinders, with an annular RPC foam bound in between them. The smaller cylinder has a small aperture that lets in concentrated solar rays. It has a cavity configuration. Therefore, it efficiently captures the incoming light. A 3D compound parabolic collector (CPC) is incorporated at the aperture, boosting the solar concentration ratio and reducing re-radiation losses. The outer cylinder is insulated with a non-porous insulation material that can keep the air under high pressure.

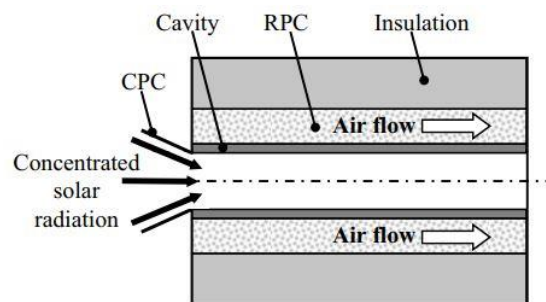


**Figure 2.25:** A schematic concept design of an RPC pressurised air receiver (Hischier et al., 2009).

The receiver's design provides it with several advantages, which include the following:

- High apparent absorptivity due to cavity-type geometry
- High convective heat transfer from the RPC to the air
- Homogenous and monotonous increasing temperature profile
- Uniform compressive load on cavity
- Reduced re-radiation losses due to cold air entering at aperture

### 2.3.3.7.3 Hybrid pressurised air receiver

Hybrid system concepts have also been proposed in recent years to take advantage of the benefits that different designs provide. The hybrid pressurised air receiver design was proposed by Kretschmar & Gauché (2012) at the Southern African Solar Energy Conference (SASEC). This design was inspired by the design concepts of the dual receiver and the RPC pressurised air receiver. The concept consists of three zones: the cavity, the secondary counter flow heat exchanger and the CPC secondary concentrator (which is optional in the design). The cavity's aperture consists of a transparent window (glass panes or louvres) and an array of tubular receivers.

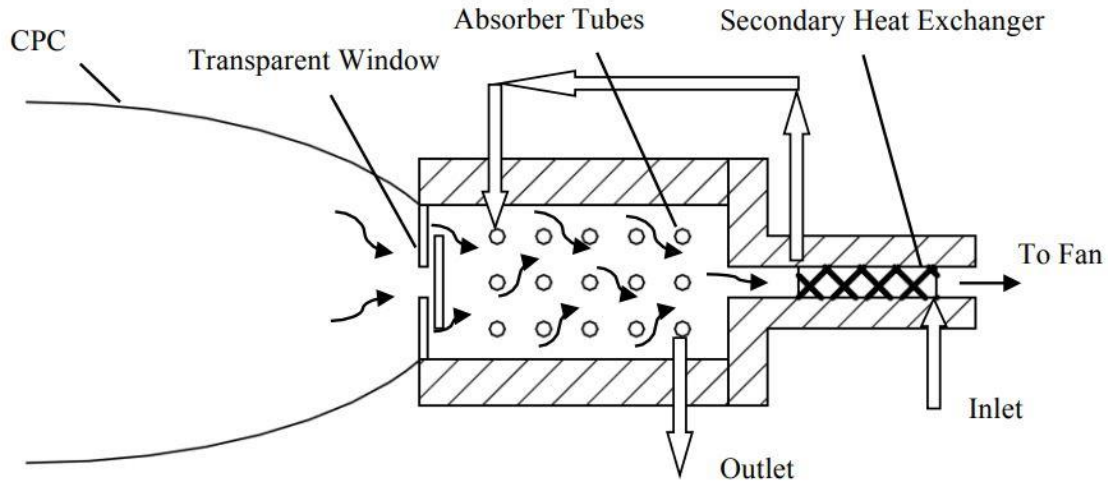


Figure 2.26: A schematic layout of a preliminary concept of the hybrid pressurised air receiver (Kretzschmar & Gauché, 2012).

The receiver's thermodynamic cycle can be divided into two separated loops: the pressurised and the unpressurised loop. Within the pressurised loop, the unpressurised air loop preheats the compressed air and enters the receiver cavity. It is then further heated by the indirectly irradiated tube bundles to the final maximum outlet temperature. The unpressurised cycle follows a typical volumetric receiver concept where ambient air is sucked into the receiver and heated by the volumetric absorber. Figure 2.26 shows this concept.

This design provides numerous benefits. Irradiated tubes that are cooled by the incoming air have the advantage of higher solar flux densities focused onto the receiver. If higher solar fluxes are allowed, the a smaller receiver may be needed, which will reduce the cost price. The incoming air distributes the temperature along the tubes, reducing thermal stresses. The transparent window at the aperture captures re-radiated infrared radiation emitted by the tubes.

There are also some disadvantages to this design, such as the concept using tubes instead of a porous absorber material, therefore making the heat transfer less efficient. It will less likely have higher temperatures compared to a volumetric receiver. In addition, the tubes will most likely be made of super-alloys, which cannot handle as temperatures that are as high as SiC foam in volumetric receivers can.

#### 2.3.3.7.4 Impinging receiver for dish Brayton system

This impinging receiver is designed and tested for parabolic dish systems, but was a design of interest for the literature study because of its jet-impinging design. For receivers that make use of air or any other gas, the low-heat conductivity of the air hinders the convective heat transfer between the cavity wall and the medium. This is usually mitigated by designing complex fin structures to increase the heat transfer. The low rate of heat transfer also limits the flux onto the receiver or requires expensive ceramic materials to increase the absorber's allowable working temperature. Another problem that occurs is the local peak temperatures that occur on a surface. The new concept that was proposed by Wang (2015) uses the advanced heat transfer capabilities of impinging jet flow. Jet impingement increases the local heat transfer at both the contact region and the direct circumferential region. It also has the added benefit of smoothing out the temperature distribution on a surface, which is beneficial to prevent local spikes in temperature. An illustration of the developed concept is displayed in Figure 2.27.

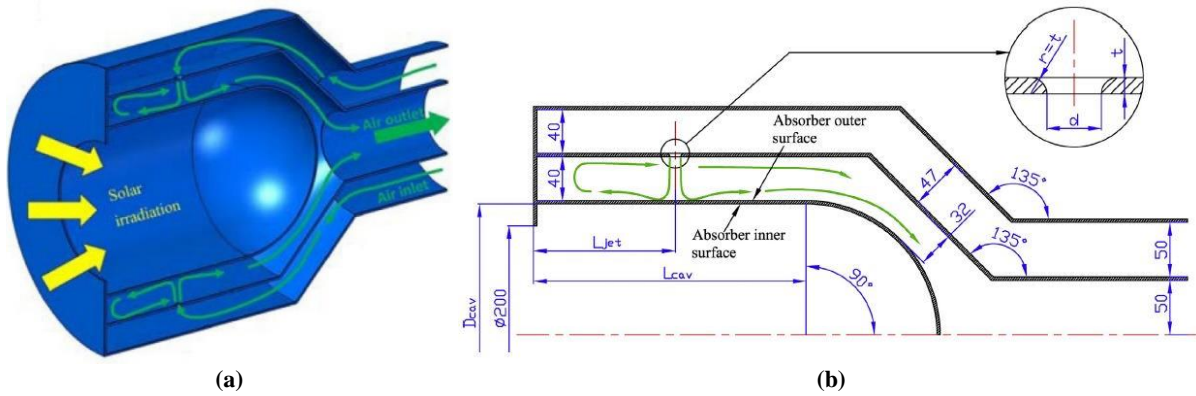


Figure 2.27: A schematic designs of the impinging receiver developed by Wang (2015): (a): 3D model; and (b): 2D drawing.

### 2.3.3.8 Receiver designs summary

It is clear that there is still a great deal of uncertainty as to which design would result in the most efficient and cost effective design for the required application. Table 2.3 provides a summary of the receiver designs, their benefits and challenges associated with them or research that still needs to be conducted.

**Table 2.3: Summary of receiver designs as extracted from Ho & Iversion (2014)**

Receiver design	Outlet temperature	Thermal efficiency	Benefits	Challenges or research needed
<b>Gas receivers</b>				
Volumetric air receiver	> 700 °C	~50% to 60%	Can achieve high temperatures, simple and flexible construction	Material durability, flow instability, radiative heat losses, low thermal efficiency, long-term storage
Small particle air receiver	> 700 °C	~80% to 90%	Can achieve high temperatures, volumetric absorption of energy	Required window for pressurised receivers, solid-gas suspension system to maintain desired particle concentration and temperature, long-term storage
Tubular gas receiver	> 800 °C	~80% to 85% (theoretical) ~40% (prototype test)	Can achieve high temperatures and pressures, heat pipes provide compact and effective heat transfer	High radiative and convective losses; , low thermal efficiency, heat transfer improvement from tubes to gas, material durability, long-term storage
<b>Liquid receivers</b>				
Tubular liquid receiver	> 600 °C	~80% to 90%	Liquid contained, demonstrated technology, can accommodate high pressures	Thermal expansion, material compatibility, increased pressure requirements to manage pressure drop across receiver panel, potential of solidification in tube
Falling-film receiver (direct exposure)	> 600 °C	~80% to 90% (external DAR, experimental) ~94% (internal DAR, theoretical)	Higher receiver outlet temperatures, reduced thermal resistance and start-up time, lower pumping losses	Film stability, complexity of rotating body, fluid impurities and integrity in exposed environments, absorber wall flatness during thermal expansion
Falling-film receiver (indirect exposure)	> 600 °C	>80% (theoretical)	Lower pumping losses, quick start-up time, operates with less insolation, simplicity of fabrication, no need for fluid doping	Film stability, shape integrity during thermal expansion, flow distribution across illuminated surfaces to match incident flux, efficiency improvement
<b>Solid particle receivers</b>				
Falling particle receiver	> 800 °C	~80% to 90% (simulations) ~50% (prototype)	Can achieve high temperatures, direct irradiance reduces flux limitations, particles can be stored at high temperatures, particles can be cheaper than molten salt	Reduces radiative and convective losses, higher concentration ratios, lower particle attrition, great solar absorptance, lower thermal emittance, increased particle residence time, more effective particle/fluid heat exchangers

### 2.3.4 Secondary concentrator

For receivers that are designed to have the concentrated solar rays directed at a single aperture opening or flat surface, it is of utmost importance to have high accuracy aiming strategies to ensure that most of the energy is captured. High accuracy usually means more expensive designs and aiming strategies on the heliostat side of the development. This can be overcome by implementing a secondary concentrator at the receiver aperture, which could capture a larger area of concentrated solar rays.

Several designs can be implemented as secondary concentrators, although the most common secondary concentrator currently being used in designs and applications is the CPC. The design was proposed in 1965 by Winston and Hinterberger (Rabl, 1976). Although the initial idea of the design was to be implemented to line-concentrating solar applications (Winston & Hiterberger, 1975), the principles can be used for point focus technologies as well. Many receiver designs have been proposed with CPC receivers, as shown in the subsection ‘Receiver design’.

The design of a CPC, as described by Winston and Hiterberger (1975), is as follows:

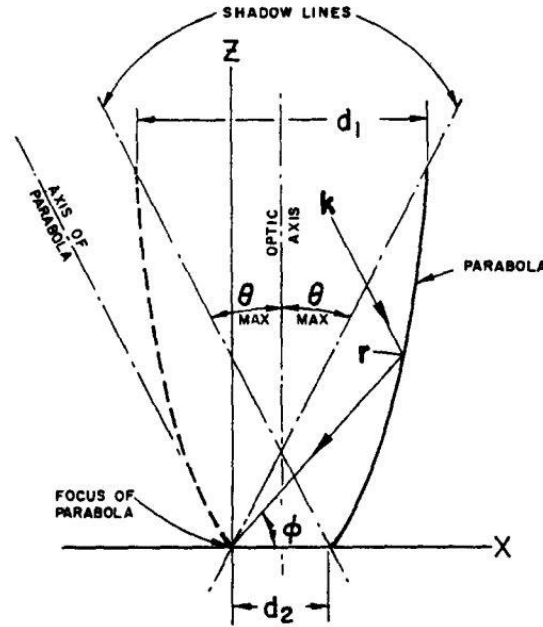


Figure 2.28: A profile curve of the CPC (Winston & Hiterberger, 1975).

With the axis origin placed at the edge of the exit aperture, the extreme accepted ray or direction cosines are denoted by the following:

$$\mathbf{k} = [\sin \theta_{max}, 0, -\cos \theta_{max}] \quad (2-6)$$

The shadow lines (displayed in Figure 2.28 as dashed lines) intersect the edges of the exit aperture and are inclined at angle  $\theta_{max}$  to the optic axis. The intention of the curve  $r(\phi)$  is to reflect the extreme ray into the origin. Therefore:

$$\frac{dr}{d\phi} = -\left(\frac{dr}{d\theta}\right) \cdot \mathbf{k}, \quad (2-7)$$

where the angle  $\phi$  parameterises the profile curve. The curve extends to the point where it turns parallel with the optic axis and intersects the shadow lines. Integrating equation (2-7), the following is obtained:

$$(\mathbf{r}_1 - \mathbf{r}_2) = -(\mathbf{r}_1 - \mathbf{r}_2) \cdot \mathbf{k} \quad (2-8)$$

From the geometry in Figure 2.28, the following equations are derived:

$$r_1 = d_1 \sin \theta_{max} - (\mathbf{r}_1 - \mathbf{r}_2) \cdot \mathbf{k} \quad (2-9)$$

$$r_1 = d_2 \quad (2-10)$$

and therefore,

$$d_2 = d_1 \sin \theta_{max} \quad (2-11)$$

Research done by Timinger, SpirkI, Kribus and Ries (2000) presented secondary concentrators with non-regular shapes to increase the concentration of the radiation from a given field of heliostats, which were well suited for portioning the receiver into several units arranged side by side. Through optimisation techniques, the best results were obtained for concentrators based on rectangular entrance and exit apertures, with the concentration increasing by a factor of 2.3 and an optical efficiency of 90%.

Secondary receivers have been proposed for most single-receiver designs, although other ideas have been presented. Such is the idea of clustering receivers together to form a large aperture of multiple secondary collectors, as can be seen in Figure 2.29a. A similar concept, labelled the CPC “fly eye” secondary-stage concentrator, uses CPC mirrors at the point where a designated part of a heliostat field concentrates a narrow acceptance angle in a given collector, as displayed in Figure 2.29b.

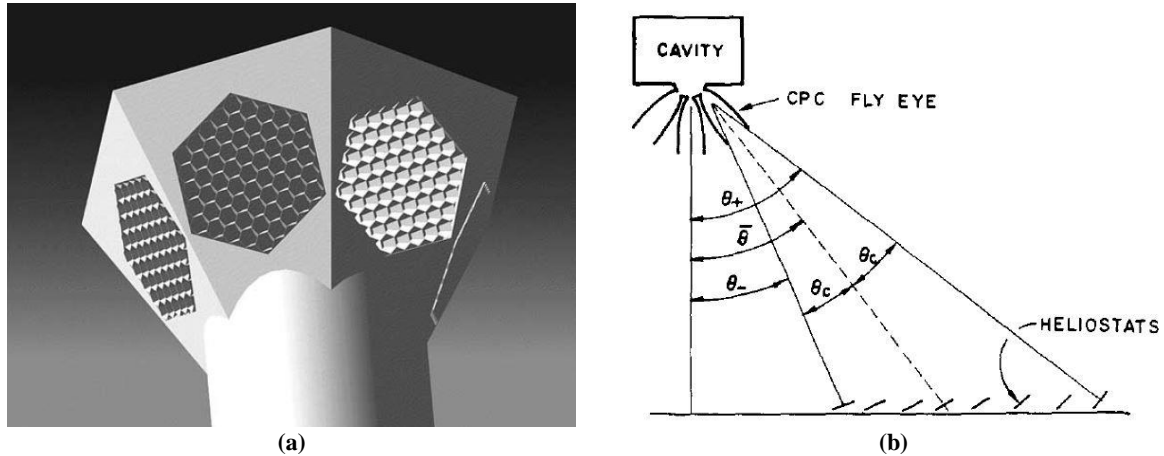


Figure 2.29: (a): An illustration of clusters of receivers and their corresponding secondary concentrators (Schmitz et al., 2006); and (b): a schematic of a central receiver with a CPC “fly eye” second-stage collector (Rabl, 1976).

## 2.4 Monte Carlo ray tracing

With a numerical analysis of central receiver technology, it is important to determine the optical performances of such systems accurately. This means that the optical performance of the heliostat field and receiver must be simulated accurately by considering the sun angle, concentration ratio, blocking and shading, reflectivity and absorptivity, and reflective surface error properties. One way of analysing the optical performance of systems is by using the MCRT approach.

Monte Carlo refers to the statistical numerical method that can be used over a wide variety of fields to estimate or calculate a prediction or outcome of a certain event. By using a Markov chain, which is a sequence of events with the condition that the probability of each succeeding event is not influenced by prior events, one could obtain a probability distribution by repeating these events a great number of

times. The accuracy of this method is therefore restricted to the number of times these events are repeated, and how varied these events are within the restrictions that have been given, namely the randomness of these events. Because solutions obtained by the Monte Carlo method are averages over results that were obtained from individual samples, they contain fluctuations of a mean value. The mean can therefore be obtained more accurately by increasing the number of samples.

The Monte Carlo method of numerical predictions can be applied to radiative heat transfer by assigning a discrete amount of energy to a single ray. The local energy flux can then be easily calculated as the number of rays reaching a location per unit area at a set time, and multiplying the number of rays with the energy per ray. One could simulate numerical models by generating a large number of rays and ensuring that these rays interact with surfaces that have predefined boundary properties that would determine whether a ray would be reflected, absorbed or transmitted through statistical relationships. These rays can be generated by giving an appropriate probability density function, such as a defined sun shape in the case of solar technology modelling. For more details, such as the mathematics involved in this method and its application, refer to sources such as Howell, Siegel and Mengüç (2010).

Using a probabilistic model of radiative exchange and applying Monte Carlo techniques is preferable over other methods such as finite volume techniques, where difficulties can occur when formulating integral equations, especially for complex problems. It is for this reason that this method is so popular among researchers who analyse CSP solar plants, which also led to different commercial and public ray tracing codes being developed by various research institutes and companies (Wendelin, Dobos, & Lewandowski, 2013; Blanco, Amieva, & Mancillas, 2005; Leary & Hankins, 1979; Vittitoe & Biggs, 1977; Belhomme, Pitz-Paal, Schwarzbozl, & Ulmer, 2009).

SolTrace is one of the freely available ray tracing software tools and was developed by the National Renewable Energy Laboratory (NREL) to model CSP systems and analyse their optical performance, although it is not limited to solar applications. A major restriction of this software is its inability to simulate complex geometries, since the software only enables the user to build a model using primitive geometries such as planar elements, tubes and dishes. The lack of online resources or proper documentation on the workings of SolTrace for matters that are not discussed in the Help section can also be seen as a drawback. SolTrace does, however, provide the advantage of simulating optical systems inexpensively, and the scripting abilities that the software provides allows the user to incorporate other software, while also allowing automation to be implemented.

## **2.5 Computational fluid dynamics thermal analysis**

An accurate and cost-effective method of simulating the heat transfer of the flux incident on the absorber needs to be implemented to analyse the thermal performance of the receiver. The most popular approach for thermal simulation of solar plants is by using computational fluid dynamics (CFD), which has been widely used by previous researchers. CFD also provides the added benefit of better understanding the flow physics involved, which in the past was understood through conventional analytical and experimental techniques.

Turbulent flow is a flow phenomenon that is hard to predict accurately. CFD broadly offers the following three approaches for the analysis of this problem:

- Direct numerical simulation (DNS)
- Large eddy simulation (LES)
- Reynolds-averaged Navier-Stokes (RANS) equations

DNS simulates the complete flow and it has to do so up to the smallest scale of the flow, which demands high computational resources. LES provides an alternative to DNS by simulating the large scale while the small scales are being modelled. This approach to flow simulation provides a less expensive alternative, although it is still costly compared to RANS turbulence models, since the LES, such as DNS, gives the instantaneous flow field and should therefore be statistically averaged to get the mean flow field. In RANS, the complete flow field is modelled. Therefore it boils down to the type of turbulence model that is used. With RANS, the flow is statistically averaged and therefore only the mean flow is computed. This provides low-order statistics, but with the main advantage of cost-effective modelling. RANS modelling thus provides the best approach to CFD thermal modelling, depending on whether it provides a model to accurately predict the heat flow at the absorber.

In general, CSP plants use tubes or ducts to navigate the flow during heat transfer. The new proposed design has an absorber that impinges flow onto a concave surface inside a pyramid-like structure to enhance the heat transfer (refer to Chapter 2.6 for more information on the layout of the receiver design). Modelling the flow of jet impingement has been a topic of several studies and is generally seen as a test case for turbulence models, since it contains many complex flow features like free shear flow, near wall flow, flow stagnation, boundary layer acceleration and deceleration. The flow mechanics involved in jet impingement will be discussed next to better understand and model the receiver's impingement flow.

### 2.5.1 Jet impingement

Jet impingement is a complex flow problem that has entertained the minds of many researchers. Fluid flow in jet impingement can be categorised into different flow regimes, depending on the Reynolds number ( $Re = v_{jet}D_{jet}\rho/\mu$ ). According to Viskanta (1993), the flow regimes are as follows:

- Dissipated laminar flow ( $Re < 300$ )
- Fully laminar flow ( $300 < Re < 1000$ )
- Transitional flow ( $1000 < Re < 3000$ )
- Fully turbulent flow ( $Re > 3000$ )

This study will only be considering the fully developed turbulent flow that leaves the nozzle exit.

Literature defines the impinging jet structure by dividing it into the following zones (see Figure 2.30):

- Free jet zone
- Impingement zone
- Radial wall jet zone

As the jet exits the nozzle, a fast-moving flow is met with a slow-moving surrounding flow. This causes instabilities, also known as Kelvin Helmholtz instability mechanisms, which form vortices around the round jet. From the exit of the nozzle, the free jet develops and is structured according to its behaviour. The free jet may consist of a potential core region ( $\xi/D_{jet} \approx 4-5$ ), a flow development region ( $\xi/D_{jet} \approx 5-8$ ) and a fully developed region ( $\xi/D_{jet} > 8$ ), depending on the distance from the jet outlet. These structures may not always be present during impingement, depending on the distance of the nozzle from the impingement surface. As the jet approaches the impinging surface, the static pressure increases and the momentum decreases, after which the flow deflects and spreads radially. The wall jet region comprises a very thin accelerating boundary layer. Although the flow is not parallel to the surface, the turbulence levels in a wall jet zone are much higher than the parallel flows (Uddin, 2008).

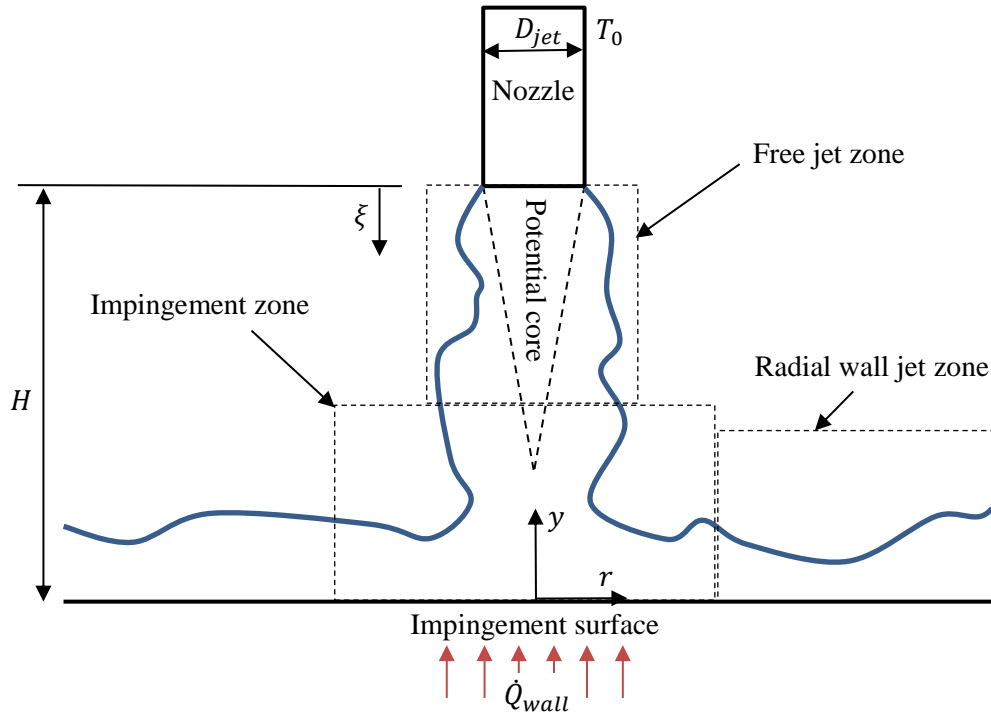


Figure 2.30: A schematic illustration of a jet impingement on a flat surface, remodelled from Uddin (2008).

The heat transfer effects of an impinging flow can be investigated through the surface heat transfer coefficient, which is incorporated in the non-dimensional Nusselt number, a function of the jet diameter and temperature, as seen in Equation (2-12):

$$Nu = \frac{hD}{k} = \frac{\dot{Q}_{wall}D_{jet}}{(T_{wall} - T_0)k} \quad (2-12)$$

Research conducted in the field of jet impingement heat transfer has produced interesting surface Nusselt number distributions (see Figure 2.31).

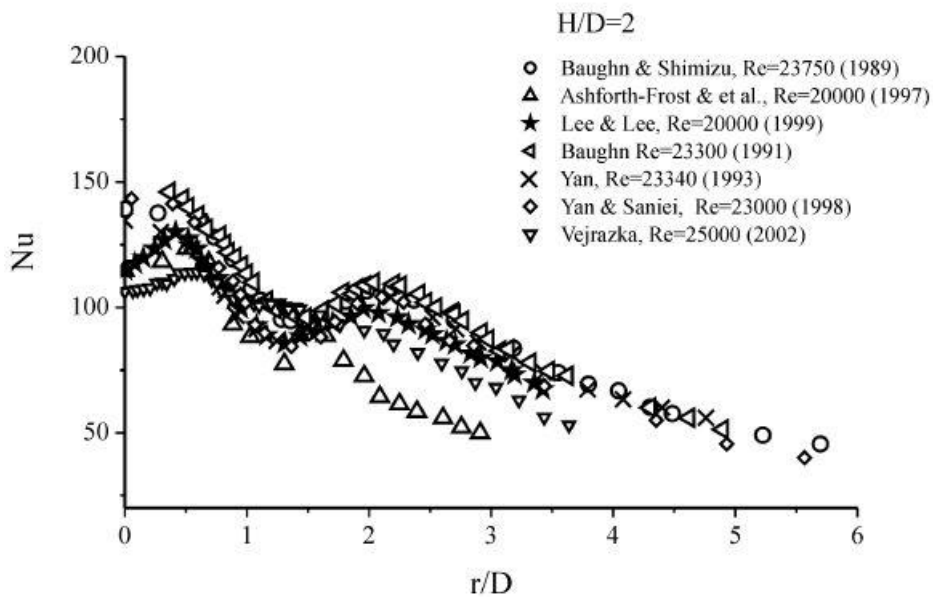


Figure 2.31: A radial distribution of the Nusselt number at the surface for  $H/D = 2$  (Uddin, 2008).

The distribution shape and magnitude of the heat transfer of an impinging jet is greatly affected by the nozzle-to-wall distance ( $H$ ). The distribution, as seen in Figure 2.31, shows two prominent peaks in heat transfer. These peaks remain prominent up to  $H/D_{jet} \approx 4$ . According to Sakakibara and Hishida (1997), the amplification of vorticity in the stagnation region is the main reason for the enhancement of the heat transfer in plane impingement jets. From the stagnation point, the flow accelerates radially, and as the flow speeds up, it transitions from laminar to turbulent flow again.

The second peak witnessed in the Nusselt number radial distribution is a well-known phenomenon, although there is no consensus on the physical explanation. What is known is the fact that the occurrence of the second peak not only depends on the distance of the nozzle to the plate, but also on the turbulence levels in the jet. Suggestions for an explanation of the phenomenon include the local thinning of the boundary layer at that region (Gardon & Akfirat, 1965), the flow transition in the wall jet region (Hoogendoorn, 1977) and the higher turbulence in the boundary layer due to flow acceleration and intense shear between the radially ejecting jet and the stagnant ambient temperature (Lytle & Webb, 1994; Behnia, Parneix, & Durbin, 1998). Viskanta (1993) proposed that the ring-shaped wall eddies are responsible for this secondary peak, which is induced by the large-scale toroidal vortices hitting the plate.

## 2.5.2 Numerical investigations

For jet impingement, many numerical studies have been conducted, with the earlier studies focusing on laminar impingement flow, but with industrial jets generally being turbulent, and the focus shifting towards turbulent flow simulations. Reviews have been conducted by Polat, Huang, Mujumdar and Douglas (1989), Zuckerman and Lior (2006) and Coussirat et al. (2005). The review conducted by Zuckermann and Lior (2006) included an interesting comparison of the summarised numerical models and is reproduced in Table 2.4.

**Table 2.4:A comparison of turbulence models for jet impingement (Zuckerman & Lior, 2006)**

Turbulence model	Computational cost	Nu-prediction/ anticipated percentage error	Prediction of secondary peaks
k- $\epsilon$	Low ****	Poor/15–60 *	Poor *
k- $\omega$	Low-medium ****	Poor-fair/10–30 **	Fair **
Realisable k- $\epsilon$	Low ****	Poor-fair/15–30 **	Poor-fair **
Algebraic stress model	Low ****	Poor-fair/10–30 **	Poor *
Reynolds stress model	Moderate-high **	Poor/25–100 *	Fair **
SST	Low-moderate ***	Good/20–40 ***	Fair **
$v^2 - f$	Moderate ***	Excellent/2–30 ****	Excellent ****
DNS/LES	Extremely high *	Good-excellent ****	Good-excellent ****

**Note:** Fair indicates the incorrect prediction of location or magnitude.

\* Undesirable model characteristics

\*\*\*\* Excellent model characteristics

Polat et al. (1989) pointed out that the only way to verify the validity of the results of a numerical simulation in the case of the turbulent impinging jets is to compare them to the results of experiments where the boundary conditions of the flow domain are the same as those of the numerical study. It is therefore very important to choose the correct boundary conditions.

## 2.6 Proposed new central receiver concept

As was presented throughout the literature study, there is a great need to increase the efficiencies and decrease the costs of central receiver CSP systems. One of the main obstacles in the effort to increase efficiencies is the thermal losses obtained at the receiver itself. Many receivers have been proposed, tested and implemented. Each has been motivated by a valid argument or reason for being proposed. However, there is currently no single design that provides exceptional efficiencies at reasonable costs. There is hence a great need for a design that would overcome these challenges.

M da Silva, a student under the supervision of Prof KJ Craig of the Clean Energy Research Group (CERG) in the Department of Mechanical and Aeronautical Engineering at the University of Pretoria, proposed a novel receiver design for a central receiver polar field system. The main goal of the design was to limit the incident rays that entered the aperture from escaping, as well as limiting the re-radiation and convective thermal losses. The design was inspired by the work of Garbrecht et al. (2013) and Lubkoll et al. (2015) that used jet impingement heat transfer at the absorber. The idea of Buck et al. (2002) to use secondary concentrators to direct the incident flux into a cavity also played a role in the new design. The concept design of the receiver is displayed in Figure 2.32.

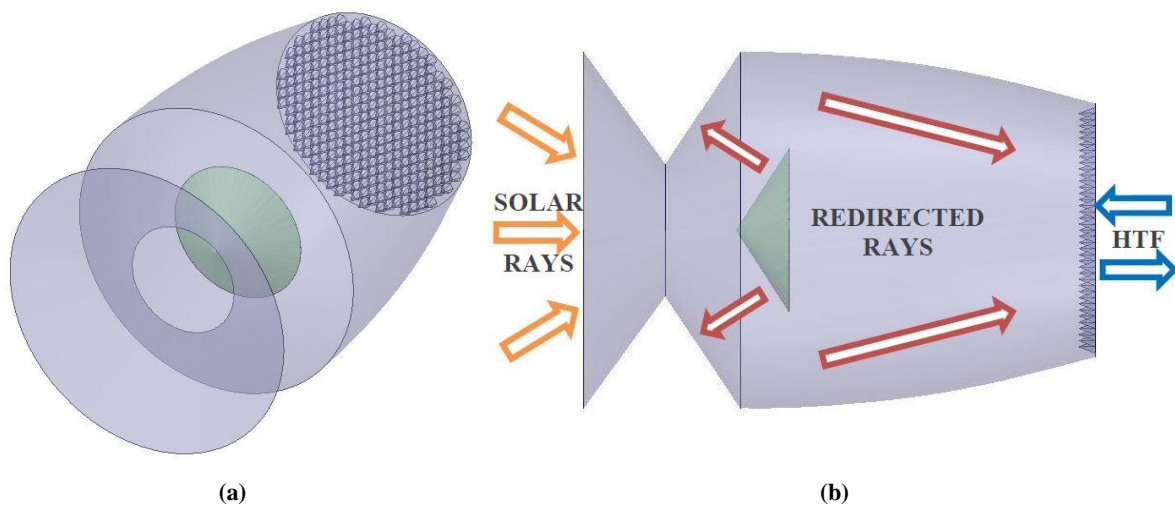


**Figure 2.32: The proposed novel receiver concept: (a): displayed in 3D; and (b): displayed from a side view with the basic workings illustrated.**

As illustrated in Figure 2.32, the rays that enter the aperture of the receiver are reflected to the cavity area of the receiver. The rays are deflected to the point where they reach the absorber area of the receiver. The absorber consists of a multitude of hexagonal pyramid-shaped elements arranged in a honeycomb structure. Their apexes point in the direction of the aperture. It is within these pyramid elements that the HTF absorbs the incident radiation.

The purpose of the receiver cavity is predominantly to limit the effects of convection losses on receiver performance. In addition, it stops the reflection and re-radiation of energy, while the multiple hexagonal pyramid-shaped matrix absorber design minimises the re-radiation effects, since the pyramid areas capture the neighbouring radiative losses, and maximise the heat transfer by making use of jet impingement, which provides superior heat transfer capabilities. The structure of the pyramid element

is displayed in Figure 2.33. With the cool HTF entering through the central pipe inside the pyramid (represented by the blue arrow), it is injected at the tip of the pyramid. Having the coolest HTF at the tip ensures less heat loss at the tip, which is beneficial, since the heat losses at the tip of the pyramid structure are least likely to be captured by neighbouring pyramids.

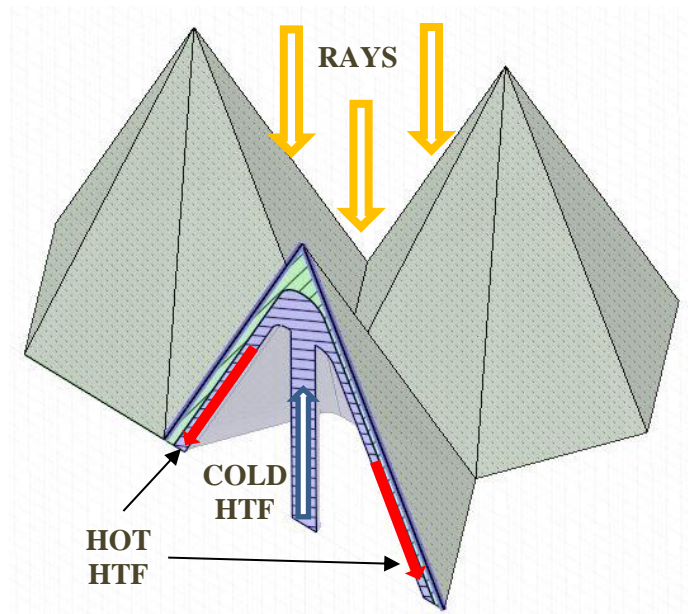


**Figure 2.33:** A close-up view of the absorber structure with the one element shown with a sectioned view. The blue zone illustrates the HTF region and the green the absorber shell.

As mentioned in the objective in Chapter 1.4, this novel receiver design needs to be developed, validated and demonstrated to determine its performance, while the design would undergo optimisation on some selected parameters with the hope of significantly improving the proposed design's performance. The original receiver design drawings are attached in Appendix F.

## 2.7 Summary and conclusion

This chapter reported on the background required to understand the current developments in the world of CSP, and why there is currently a need to research and develop the technologies associated with central receiver systems. This was done by comparing the four branches of CSP with one another. An in-depth study was conducted on the historic development of the central receiver to get an idea of what challenges were faced in the progress of development towards commercial implementation. With the main elements of a central receiver system design identified, the study presented the challenges of the heliostat field design, heliostats and receivers. With studies estimating the greatest improvements to be made in receiver design in terms of efficiency improvements (40% to 65%) (European Academies' Science Advisory Council (EASAC), 2011), a review was conducted of all current implemented and proposed receiver designs, with a summary of their advantages and disadvantages, as well as their limitations. Subsections of parabolic dish systems and secondary concentrators were also discussed. This provided the author with the necessary understanding of the challenges experienced in receiver development, as well as some possible solutions.

This background was followed by an introduction to approaches and engineering techniques for optical and thermal performance analyses on a new proposed central receiver concept. The MCRT approach was presented as a possibility to analyse the optical performance, while the concept of jet impingement and the solving capabilities of the heat transfer in the CFD environment were also introduced. This was necessary to develop the proposed receiver design that was introduced in Chapter 2.6.

From the literature study conducted, there seems to be much development in the field of CSP, with this literature's focus put on the development of central receiver systems. A lot of effort is being put into improving performances of these systems, as well as making them more cost-effective and to competitive against other energy production technologies, especially base-load utility electricity providers. Innovation plays a central role in overcoming many of these challenges, although not all prove to be successful, with trade-offs between simplicity and efficiency being a major factor in the development of central receiver technologies, especially the receiver designs. The author recognises that not all relevant literature was considered. However, the presented literature does give a good background of the developments and principles.

The introduction of different numerical techniques such as the MCRT approach and CFD provides the benefits of testing and developing receiver technologies with limited resources, and gives a method for analysing the performance of the newly proposed receiver design concept.

## Chapter 3 Solar tracking, DNI and heliostat field numerical modelling

### 3.1 Introduction

A new receiver design was introduced in Chapter 2.6 with the goal to limit the thermal losses that are usually associated with solar tower receivers. The main objective of this study is to numerically analyse the thermal performance of the proposed receiver design. In the process of numerically analysing the design, a new approach is proposed to analyse the solar tower receiver design.

In general, a simplified approach is followed by which the flux incident on the receiver is approximated by for example assuming a constant flux incident on the receiver or modelling a flat surface approximated distribution of the flux on the surface of the receiver. The new proposed approach takes into consideration the sun for a given location and time, as well as the heliostat field to more accurately approximate the flux incident on the modelled receiver.

The work introduced in this chapter proposes an alternative approach to analyse a solar tower receiver design, by considering the variables that gets mentioned, which hopes to provide more realistic, and therefore more applicable results.

To approximate the sun, a model is considered that takes into consideration the location (solar tracking), the angular intensity of light across its disk (referred to as the sun shape), as well as its DNI for different times of the year. The approximation of these models is of significant importance, since any errors associated with approximating the sun can have a trickle-down effect to all other models that are analysed.

In this section, the models that are implemented to track the sun, as well as the sun's interaction with the heliostat field, are described. This will include the solar tracking model, the DNI approximation model and the heliostat field description to be used as reference field in this study. The sun shape is assumed to be a pillbox distribution with a half-angle width of 4.65 mrad.

### 3.2 Solar tracking numerical model

Much research has been done on solar tracking and how to approximate it by defining it numerically or analytically. Proposed models are those of Cooper (1969) and Swift (1976). According to literature, the model proposed by Iqbal is sufficient (Starks, Norman, Blad, Walter-Shea, & Walthall, 1991; Reda & Andreas, 2004). For a more complex, but more accurate solar vector model, the solar position algorithm (SPA) should be implemented (Blanco-Muriel, Alarcon-Padilla, Lopez-Moratalla, & Lara-Coira, 2001).

The solar position model of Iqbal, which is presented in Appendix A, is the model that is applied to the analysis of the performance of the receiver in subsequent chapters.

Compared to NREL's Measurements and Instrumentation Data Centre (MIDC) SPA (NREL, 2018), which is based on work done by Reda and Andreas (2004), with results displayed graphically in Figure 3.1, the results provide assurance that the Iqbal solar position model is adequate for realistic analysis from a solar position perspective.

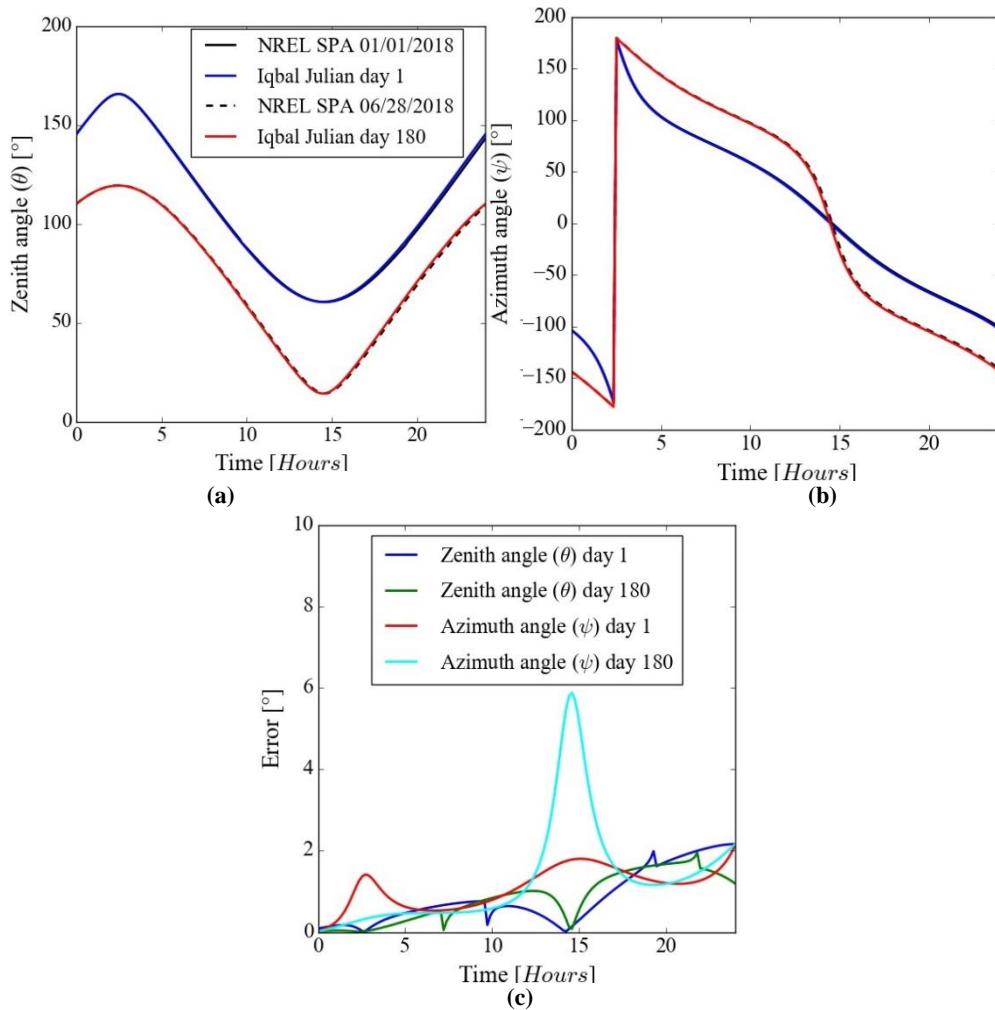


**Figure 3.1:** A graphic representation of: (a): the zenith angles ( $\theta$ ); and (b): the azimuth ( $\psi$ ) angles for the 1<sup>st</sup> and 180<sup>th</sup> Julian days, comparing the Iqbal model to NREL’s MIDC SPA (NREL, 2018). The error of the Iqbal model compared to the SPA is displayed in (c).

### 3.3 Direct normal irradiance model

The challenge of numerically modelling a DNI model for any given location is immense, since the DNI is subject to many variables, some of which are almost impossible to express in analytical or numerical terms. The weather plays a significant role in the DNI values, and since it does not display a typical trend on an annual cycle, one must make certain assumptions that will make the modelling less complex, without failing to calculate realistic DNI values.

One assumption one could make is to assume a cloudless sky atmosphere model. This assumption makes sense if one considers the purpose for which this model is constructed. CSP plants are only functional during times when there is a level of radiation above a certain threshold level. Clouds only hinder such analyses. The drawback of a cloudless sky DNI model would be that it fails to simulate the moments of cloud interferences, which has a significant effect on the performance of a CSP plant. Due to the already comprehensive scope of this study, cloud interferences are not considered.

Different DNI models have been proposed in literature. A review by Iqbal included a summary of the clear sky direct insolation models presented by Bird and Hulstrom (1981). This compared different models, including what was described as parameterisation models A, B and C, as well as the American Society of Heating, Refrigerating and Air-conditioning (ASHRAE) algorithm. It was concluded that parameterisation model C produced the most accurate results, and was hence chosen as the model that would be used to simulate the DNI.

Parameterisation models are designed in a manner that permits, in this instance, the atmospheric parameters to be varied independently. This allows one to find good correlations for specific variables that have already been studied in other fields. With DNI parameterisation models, the overall spectrally integrated transmittance for each atmospheric constituent is employed to compute the total transmittance of the atmosphere. Simply stated, the atmospheric transmittance is a function of selected variables. The variables for the model to be employed are as follows:

- Transmittance to direct irradiance due to Rayleigh scattering effects of air molecules,  $\tau_r$
- Transmittance to direct irradiance due to absorption by ozone,  $\tau_o$
- Transmittance to direct irradiance due to absorption by uniformly mixed gases,  $\tau_g$
- Transmittance to direct irradiance due to absorption by water vapour,  $\tau_w$
- Transmittance to direct irradiance due to attenuation by aerosols,  $\tau_a$

The DNI is also a function of the distance of the sun from the earth. The model can be constructed using the eccentricity correction factor, which is described and expressed in Equation (A-1).

The model can then be constructed by weighing these variables to a constant. This constant is called the solar constant,  $I_{sc}$ . The solar constant is the rate of total solar energy at all wavelengths incident on a unit area exposed normally to rays of the sun at one astronomical unit (the mean distance between the sun and the earth, which is approximately  $1.496 \times 10^8$  km). Although called a constant, it fluctuates slightly in reality. With the model, the fluctuations are assumed to be negligible. From 1969 to 1980, Fröhlich and colleagues (Frohlich & Wehrli, 1981; Frohlich & Brusa, 1981) recorded eight solar constant measurements. They subsequently recommended the revised value:

$$I_{sc} = 1367 \text{ W/m}^2$$

Iqbal notes that accurate measurements of the constant have been one of the biggest challenges in radiometry, and a final value of the constant remains elusive.

From this model, the DNI is then given by:

$$I_n = 0.9751 E_0 I_{sc} \tau_r \tau_o \tau_g \tau_w \tau_a \quad (3-1)$$

The multiplying factor 0.9751 in this equation was proposed by Iqbal, and was adjusted from the original sources (Frohlich & Wehrli, 1981) to conform to the proposed solar constant and its spectral distribution.

The different transmittance parameters, as discussed and proposed by Iqbal, is presented in Appendix A. Due to a lack of accurate models to predict relative humidity and temperature on a global scale, the option that remained was to obtain actual annual data or tables from the region to be analysed or by making correlations from simple information. This provides an extra dimension to the existing model that in essence synthesises DNI data from weather data. The modelling of the temperature and relative humidity is therefore presented next.

### 3.3.1 Temperature and relative humidity modelling

For temperature, a study by Reicosky and colleagues (Reicosky, Winkelman, Baker, & Baker, 1989) compared different ways of approximating hourly temperatures for a particular location and time of the year. With only minimum and maximum temperatures needed, different models were set up and compared with actual temperature fluctuations. The wave subroutine initially presented by De Wit, Goudriaan and Van Laar (1978) turned out to be the most accurate. The method divides the day into

two segments, from sunrise to 14:00 and from 14:00 to sunrise the next day. These equations are as follows:

For  $0 \leq LAT < t_{sunrise}$  and  $14 < LAT \leq 24$ :

$$T = T_{avg} + T_{amp} \cos\left(\frac{\pi H'}{10 + t_{sunrise}}\right) \quad (3-2)$$

$t_{sunrise} \leq LAT \leq 14$ :

$$T = T_{avg} - T_{amp} \cos\left(\frac{\pi(LAT - t_{sunrise})}{14 + t_{sunrise}}\right) \quad (3-3)$$

where:

$$\begin{aligned} H' &= LAT + 10 && \text{if } LAT < t_{sunrise} \\ H' &= 14 && \text{if } LAT > 14 \end{aligned}$$

and

$$T_{avg} = \frac{T_{min} + T_{max}}{2} \quad (3-4)$$

$$T_{amp} = \frac{T_{min} - T_{max}}{2} \quad (3-5)$$

To obtain the minimum and maximum temperature values over an annual period, the author took the monthly averaged minimum and maximum temperature values of the place of interest, which is Seville, Spain, in this case over a time span of eight years (WorldWeatherOnline.com, 2018), and approximated the data by applying a function of best fit to the data set. It was decided to use the discrete trigonometric approximation to approximate the data. The data shows sine and cosine trends, and since the discrete trigonometric approximation uses a series of sine and cosine functions to represent arbitrary functions, a low-order trigonometric function would hopefully give a sufficient approximation. The same method was applied to obtain an approximation for the relative humidity, since the data gives similar trends.

The discrete trigonometric approximation is constructed using a collection of  $2m$  paired data points  $\{(x_j, y_j)\}_{j=0}^{2m-1}$ , with the interval transformed linearly to fit the interval  $[-\pi, \pi]$ . This can be done as follows:

$$x_{transform} = \pi \left( \frac{x}{365/2} - 1 \right) \quad (3-6)$$

The approximated function ( $S_n$ ) is constructed using the following equation:

$$S_n(x) = \frac{a_0}{2} + a_n \cos nx + \sum_{k=1}^{n-1} (a_k \cos kx + b_k \sin kx) \quad (3-7)$$

With the constants being calculated as follows:

$$a_k = \frac{1}{m} \sum_{j=0}^{2m-1} y_j \cos kx_j \quad (3-8)$$

for  $k = 0, 1, \dots, n$ ,

and

$$b_k = \frac{1}{m} \sum_{j=0}^{2m-1} y_j \sin kx_j \quad (3-9)$$

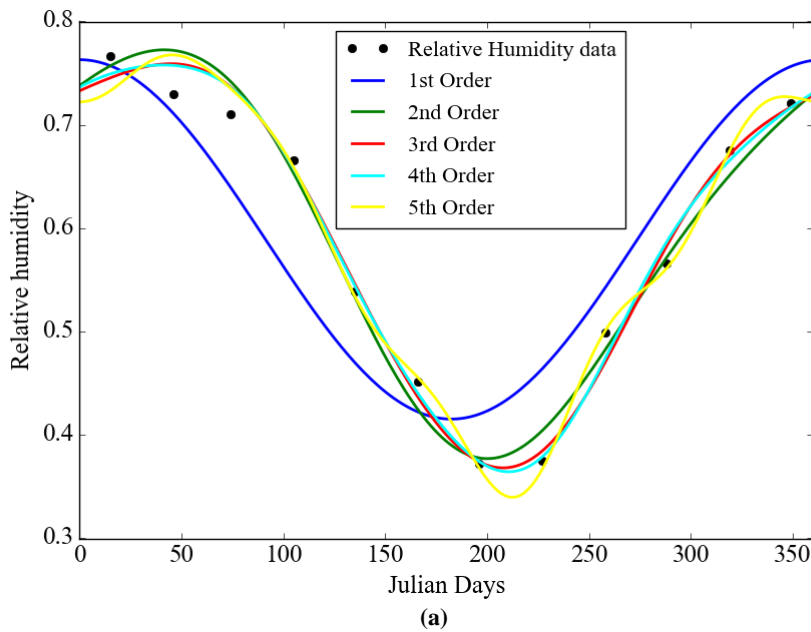
for  $k = 1, 2, \dots, n - 1$ ,

where  $n$  represents the order chosen to approximate the data (Burden & Faires, 2011).

One first needs to determine the order of the trigonometric approximation equation. To do this, the orders are compared to the actual data. The various order functions, ranging from 1 to 5, are plotted on the averaged data of the maximum and minimum temperatures and the relative humidity of Seville, Spain. This is shown in Figure 3.2. The maximum errors for the different orders are also given in Table 3.1.

**Table 3.1: Maximum errors (%) produced by the different orders of trigonometric approximations for the relative humidity, and maximum and minimum temperatures**

	$n = 1$	$n = 2$	$n = 3$	$n = 4$	$n = 5$
Relative humidity ( $\phi_r$ )	23.730	7.780	5.629	4.902	5.166
Maximum temperature ( $T_{max}$ )	20.166	9.237	5.328	3.986	3.637
Minimum temperature ( $T_{min}$ )	58.346	9.772	6.212	3.662	3.523



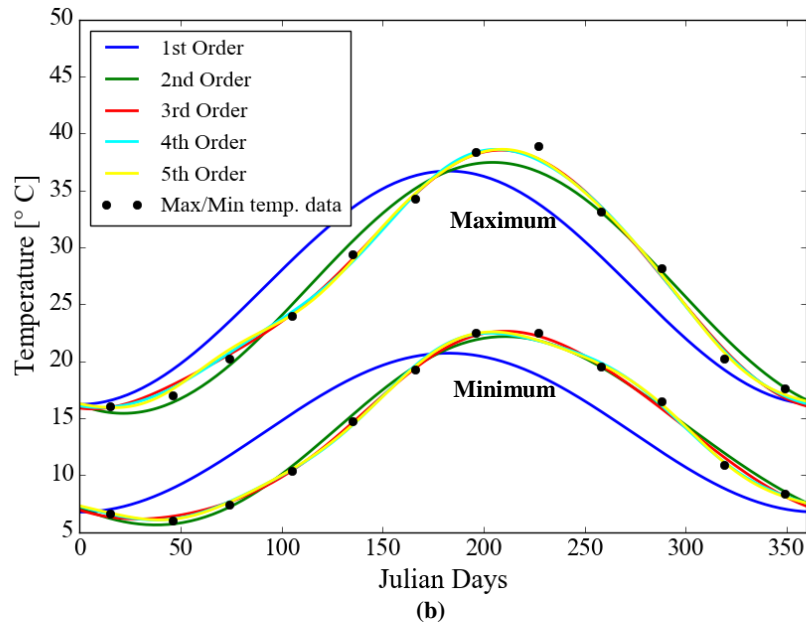


Figure 3.2: (a): Comparison of different orders of discrete trigonometric approximations to approximate the averaged data of the relative humidity; and (b): the maximum and minimum temperatures.

From the graphs in Figure 3.2 it is evident that, in general, the trends converge for orders of 3 and higher. If the orders become too high, unwanted fluctuations take place, as can be seen with the order of 5 approximation in Figure 3.2a.

It is also evident that an increase in the order results in a decrease in the maximum error that is produced between the approximation and the actual data, as can be seen in Table 3.1. In the case of the approximation of the relative humidity data, there is an increase in the maximum error. It is hence also clear in the category of evaluating the maximum error that using a high-order approximation is not the ideal case.

It has been decided to opt for the fourth-order approximation, which is the most accurate in terms of trend approximation and low error. It is not necessary to have a highly accurate approximation for the data given, though, since the data used is an averaged value of weather patterns that fluctuate annually. The coefficients calculated for the fourth-order approximations of the relative humidity and maximum and minimum temperatures are presented in Table 3.2.

Table 3.2: Coefficients calculated using the discrete trigonometric approximations theorem for the relative humidity, and maximum and minimum temperatures approximations

	$a_0$	$a_1$	$a_2$	$a_3$	$a_4$	$b_1$	$b_2$	$b_3$
$\phi_r$	1.18	-0.174	-0.0254	0.00484	0.00357	-0.0849	-0.0165	-0.00285
$T_{max}$	52.9	10.2	-0.0147	0.303	0.188	4.05	1.33	0.0971
$T_{min}$	27.4	6.97	0.389	0.201	0.320	4.389	0.532	-0.138

The values presented in Table 3.2 are given for up to three significant figures. The final approximated temperatures and relative humidity annual fluctuation models are displayed with the actual data in Figure 3.3.

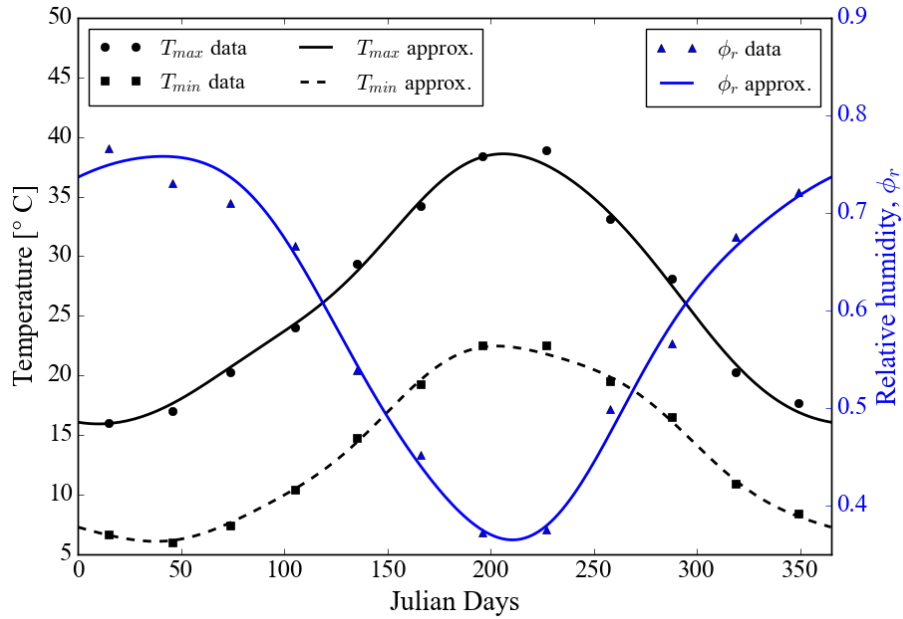
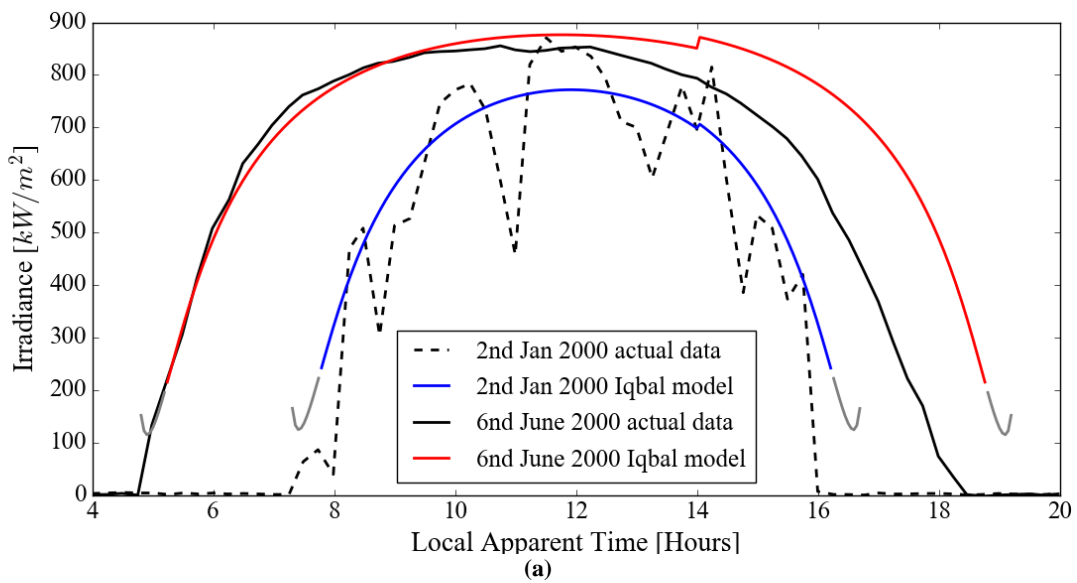
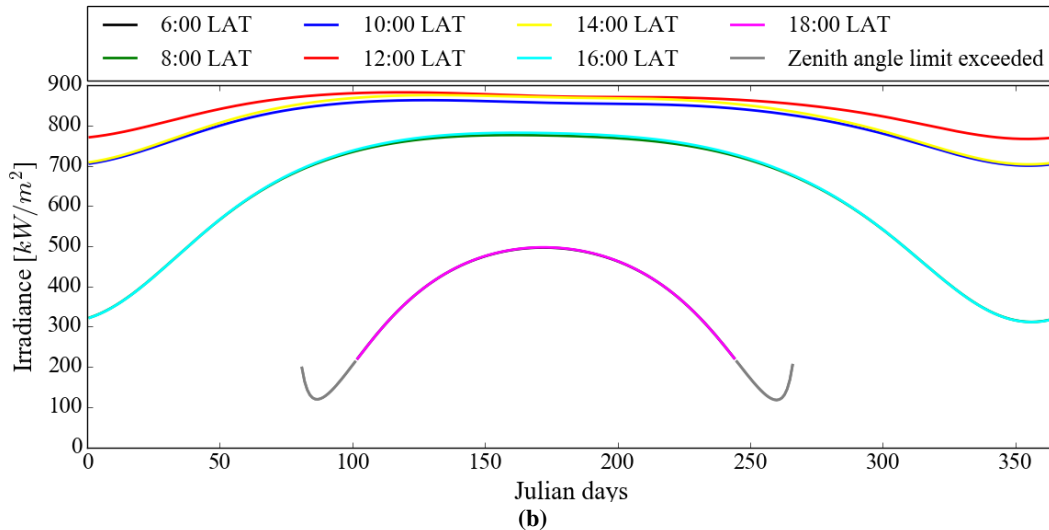


Figure 3.3: The fourth-order discrete trigonometric approximation of the averaged maximum and minimum temperature, as well as the annual fluctuations in relative humidity for Seville, Spain.

### 3.3.2 DNI model results

By applying all these equations and models in the clear sky DNI parametrisation model (Equation (3-1)) to the location of reference, which is Seville, Spain, one can obtain an approximated estimate of the DNI fluctuations over a day as well as over a year cycle. The day cycles were compared to SOLERGY generated data (an interpolated derivative of weather data) for two different times of the year, chosen to be 2 January and 6 June (Romero, Marcos, Osuna, & Fernandez, 2000), while the year cycles were presented for different hours of the day. It should be noted that the author has put a limit of  $85^\circ$  on the zenith angle so as to differentiate between the results that the model deems fit and the DNI, which is inaccurate. These models are presented in Figure 3.4.





**Figure 3.4:** The Iqbal clear sky direct-insolation parameterisation model C is graphically displayed for: (a): a day period, with a winter’s and summer’s day compared to SOLERGY generated data, defined in the legend as actual data (Romero et al., 2000); and (b): a year cycle for different hours of the day. The zenith angle limit was set at  $85^\circ$ .

From the graph in Figure 3.4a, it is clear that, although the model follows the trend of the actual weather data, it does not accurately predict the DNI for all times of the day. This is to be expected, since the model is based on the clear sky assumption, meaning that clouds or other weather interferences are not included in the model. It is also for this reason that the actual data, especially the data representing 2 January, displays a non-smooth fluctuation throughout the day. The purpose of the DNI model in the research conducted is not to accurately predict the DNI throughout the year, but rather to give realistic DNI fluctuations that can be used to test CSP technologies accurately in a numerical environment. The model has shown to provide exactly that. It should be noted that the DNI validation only takes into consideration two arbitrarily chosen days with which it was compared. For a more comprehensive validation, a full year’s weather data should be considered. As was mentioned previously, the model is constructed mainly for approximation purposes rather than for accurately predicting the DNI for a given time and location.

With the zenith angle limit set at  $85^\circ$ , but the values still being displayed on the graph, it is interesting to see how the model presents an upward curve when the sun’s position is low on the horizon. This is also evident in Figure 3.4b, and is clearly wrong, which is the reason these values are omitted. Figure 3.4b displays the DNI fluctuations throughout the year and, as expected, the values are the highest during the summer months. The opposite is found for the winter months.

### 3.4 Heliostat field test case layout

A central receiver system comprises two major subsystems: the heliostat field and the receiver design. The optical efficiency of these systems depends on a variety of different factors for both the heliostat field and the receiver. Only the heliostat field design factors could range as widely as the type of field, its size, configuration, as well as the individual heliostat type, size, and other properties. For more information regarding heliostats and field design factors, refer to Chapter 2.3.2 (‘Heliostat field design’). It is therefore of utmost importance to define the heliostat field completely before doing tests and analyses on the proposed receiver.

To decide on a heliostat field, one should also consider the receiver. As was mentioned in Chapter 2.3.2 (‘Heliostat field design’), an external receiver or receiver that is designed to receive incident fluxes from a wide angle (typically in excess of a receiver acceptance angle of  $120^\circ$ ) makes use of a surround heliostat field, while a receiver design with a flat aperture inlet or narrow acceptance angle, a category

under which cavity and volumetric receivers fall, is usually implemented with a polar field, or a set of these fields. The currently investigated receiver falls under the latter, which narrows the options available for heliostat field test case design.

A solar power plant that has undergone an extensive amount of research on several aspects of central receiver design development is the Planta Solar 11 MW central receiver solar power plant (PS-10) situated near Seville, Spain (Wei et al., 2010; Mustafa, Abdelhady, & Elweteedy, 2012; Noone, Torrilhon, & Mitsos, 2012; Eddhibi, Ben Amara, Balghouthi, & Guizani, 2015). This power plant also hosts a polar field, making it a viable option as a reference test case heliostat field to do tests on the proposed receiver. The multitude of research papers published on research regarding the PS-10 solar power plant makes it easier to obtain the specifications of the solar plant. Since the model will be optically modelled in the SolTrace MCRT software environment (for more information regarding the setup and modelling within SolTrace, refer to Appendix C and Appendix H), the parameters displayed in Table 3.3 provide a summary of the dimensions and properties needed to simulate the heliostat field in SolTrace.

**Table 3.3: PS-10 solar power plant heliostat field design parameters (Eddhibi et al., 2015; Noone et al., 2012; Osuna et al., 2006)**

<b>Location</b>	Latitude (°)	37.44 (North)
	Longitude (°)	6.25 (West)
	Altitude (m)*	7
	Greenwich Mean Time (GMT) (hours)**	+2
<b>Tower</b>	Height (m)	115
<b>Aperture</b>	Angle (°)	11.5/12.5
	Width (m)	13.78
	Height (m)	12
<b>Heliostat</b>	Type	Sanlúcar 120
	Width (m)	12.84
	Height (m)	9.45
	Reflectivity	0.88
	Transmissivity	0
	Slope error	0.71
	Specularity error	0.14
	Error type	Gaussian

\* Since Seville, Spain, is situated in the Central European Time (CET) zone, the value changes to +1 during the northern hemisphere winter months.

\*\* Inspection was done after the study was commenced, and it was noted that the plant is situated in a region outside Seville with an elevation of between 63 m and 76 m. This change is assumed to make a negligible difference.

Although the parameters displayed in Table 3.3 do not indicate the exact figures of some dimensions and properties, they give a close resemblance of the values that the field might have. This is verified with sources such as Eddhibi et al. (2015), Noone et al. (2012) and Osuna et al. (2006). For more accurate values, one would need to contact the solar plant and the manufacturers of the implemented technologies. Figure 3.5 is a cartographic display of the location of each of the 624 heliostats relative to the solar tower, which is positioned at the origin.

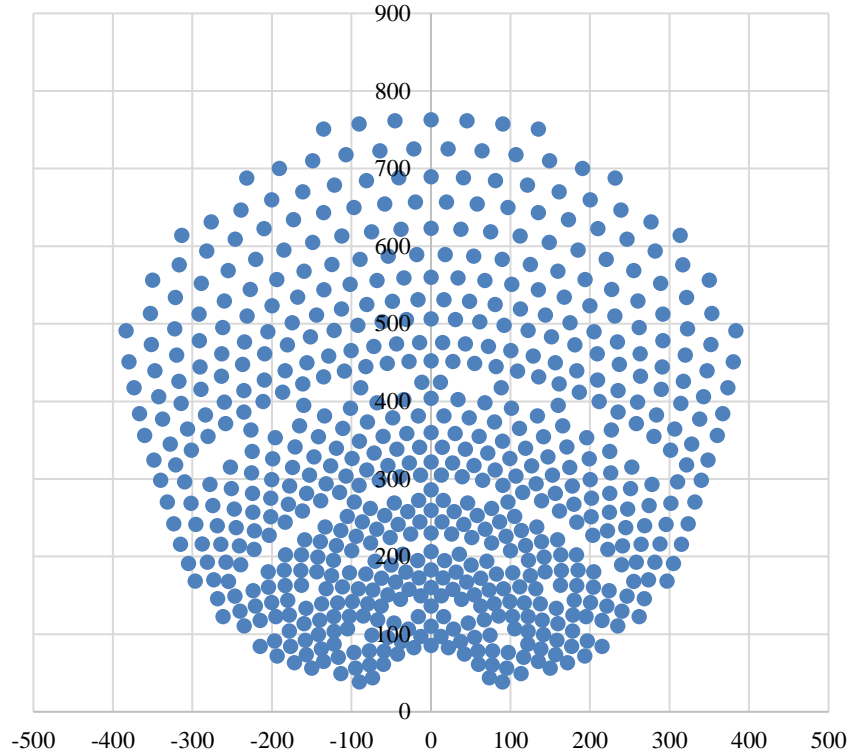


**Figure 3.5:** The coordinates of the position of the PS-10 heliostats relative to the tower, with north representing the positive vertical axis, and east representing the positive horizontal axis (coordinates extracted from Noone et al., 2012).

The focal length of the heliostat field was one of the parameter design values that the author was unable to obtain. To resolve this issue, the assumption was made that all the heliostats were identical. The distance of each heliostat from its individual location to the receiver on top of the tower was then calculated. The average was calculated to be 400.9 m, and the median 377.9 m. Since these two values corresponded closely to one another, an approximate average of these two values (approximately 390 m) was taken as the focal length of each heliostat. A histogram distribution of the distance of these heliostats from the receiver is displayed in Figure 3.6.

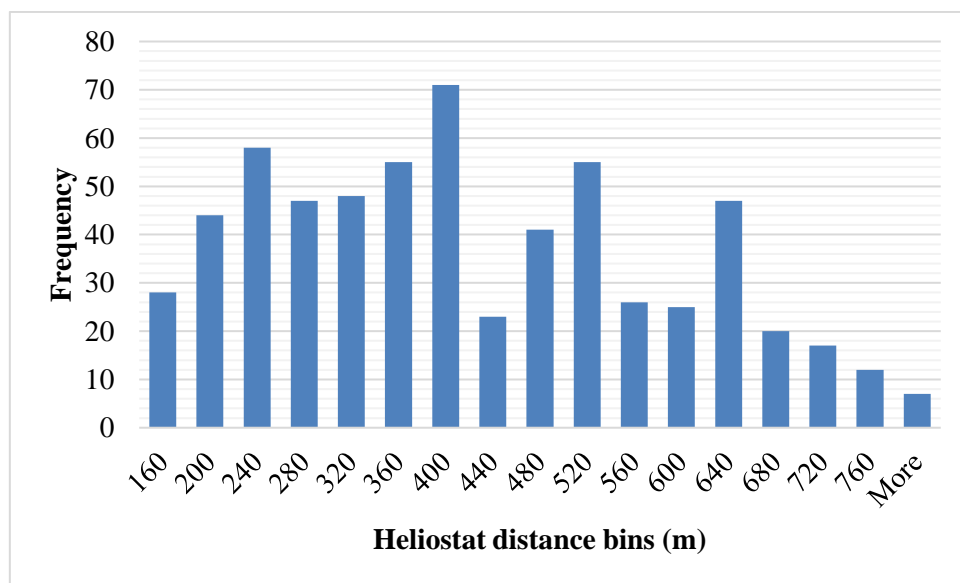


**Figure 3.6:** A histogram distribution of the heliostat distance from the receiver.

Take note that the focal point determined is an approximation, and the author is aware that the focal points differ for heliostats based on their location.

### 3.5 Summary and conclusion

In this chapter, the models to track the sun and the sun's interaction with the heliostat field selected were presented, with the main models of focus being the solar tracking model, the DNI approximation model and the heliostat field description that would be used as reference field for the research that follows.

For the implementation of the solar tracking model, it was decided to use the model proposed by Iqbal (1983), which was developed by Spencer (1971). The results of the equations that were implemented were compared to NREL's SPA model, using the location of the reference field. The equations showed great accuracy, with the equation of time showing a difference of less than a minute. The greatest error for calculating the zenith ( $\theta$ ) and azimuth ( $\psi$ ) angles resulted in maximum errors of  $\pm 2^\circ$  and  $\pm 6^\circ$  respectively, with the predominant errors being less than  $2^\circ$ .

The DNI approximation model that was implemented was the parameterisation model C summarised by Iqbal (1983) and presented by Bird and Hulstrom (1981). This model considers the effects of a Rayleigh scattering of air molecules, the attenuation of aerosols and the absorption by ozone, uniformly mixed gases and water vapour. To obtain accurate temperatures and humidity levels for the region to implement the model, approximation functions of the variables were developed. The implementation of the model gave results that were compared to the weather data of the region, which showed that the model provided realistic DNI fluctuations.

This chapter also presented a summary of the heliostat field, which is the PS-10 heliostat field located near Seville, Spain. The parameters that would be needed to implement the model within the SolTrace environment for the optical analysis include the location, as well as the tower, aperture and heliostat specifications. The coordinates of the position of the heliostats within the field were also presented.

From this chapter can be concluded that it is straightforward to analytically model the solar position with good accuracy. DNI, on the other hand, is more comprehensive and complex, and, although the results were adequate, the DNI model obtained lacks the realistic effects of cloud passage. This only emphasises the complexity of weather modelling, and that there fails to be an accurate substitute for raw weather data or derivatives thereof.

Modelling the PS10 field required some assumptions, such as assuming the focal length for all the heliostats were equal, and not considering atmospheric attenuation. The author takes note that especially the assumption of equal focal length will have a significant effect on the results that will be obtained.

## Chapter 4 Solar receiver setup and numerical modelling

### 4.1 Introduction

Chapter 3 presented the models that were of importance in simulating a central receiver field to provide the receiver with a realistic approximate flux for a given day and time at a specific location. Once the flux reaches the receiver's aperture area, other models need to be implemented to simulate the performance of the receiver, both optically and thermally. These models would include a proposed way of simulating complex geometries within the SolTrace MCRT environment and using the flux generated within the CFD environment to analyse the receiver's thermal performance.

This chapter starts with the introduction of a new approach to model complex geometries in SolTrace, followed by a validation of this approach on an existing, tested geometry using the same solving method (MCRT). After testing the accuracy and applicability of this proposed approach, the discussion shifts to the thermal modelling of the receiver, which, for the proposed receiver to be tested, involves heat transfer by using impingement flow onto a heated surface. By analysing both flat and concave surfaces on which the fluid impinges, the study concludes which computational model is most suited for the thermal analysis of the receiver absorber.

### 4.2 Receiver optical setup

The proposed receiver design is a complex structure, which consists of different shapes that combine to form an intricate design that is intended to "trap" the incident solar rays. These designs, however, provide problems in terms of optical analyses in the SolTrace environment, the MCRT software in which the optical analyses will be conducted. This is due to the fact that SolTrace only provides the user the possibility of constructing designs using the provided suite of standard or primitive geometries such as flat circles, triangles and rectangles, or curved shapes like cylinders, cones and dishes, to name a few. Ideally, one would like to be able to have the exact model or at least a good approximation of it to analyse the optical performance of the geometry.

#### 4.2.1 New approach to model complex geometries in SolTrace

An American Institute of Physics (AIP) SolarPACES 2015 conference proceedings paper authored by Craig, Marsberg and Meyer (2016) suggested an approach where the model to be analysed is meshed in the CFD software environment ANSYS Meshing. The \*.msh file that is generated by the software, which contains the information of each cell of the mesh, is then converted to information such as the cell centroid, cell area and aim vector that could be used to generate elements in the SolTrace environment. This method was limited to converting these cells to overlapping circular discs. This limitation could pose challenges, such as compromising the fidelity of the original discretised geometry due to a poor or coarse mesh. Overlapping elements could cause blocking and shading. A schematic illustration of this method is presented in Figure 4.1.

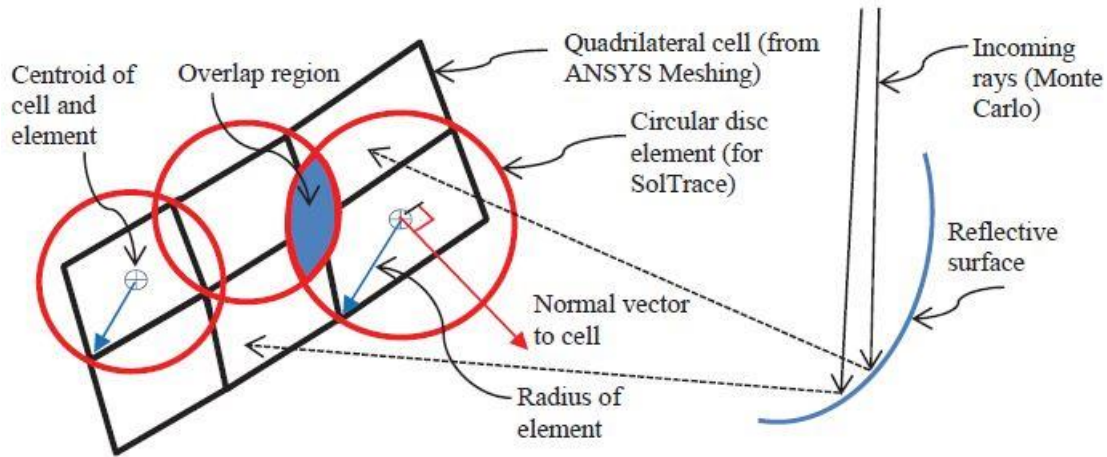


**Figure 4.1: A schematic illustration of the conversion of a computational mesh (shown as quadrilaterals) to circular elements to be used in SolTrace (Craig et al., 2016).**

The new approach that is proposed uses the same method as was described by Craig et al. (2016), but instead of using circular discs to replace the cell, the shape of the cell is replicated by using irregular triangles as primitive geometry to replace the area of the cell. The method used to achieve this is summarised by the following steps:

- The geometry modelled is meshed in the software ANSYS Meshing. The meshing is preferably done using tetrahedrons, but one is not limited to this. The reason this is preferred has to do with the fact that these cells break up into triangles. It is therefore more efficient in terms of computational power to provide the model with a surface that is divided into triangles.
- Since only the surface will be analysed in SolTrace, one only needs to export the surface mesh file in its \*.msh format (the mesh generated in the volume is redundant). To convert the mesh file, the format needs to be changed from binary to ASCII.
- A mesh file presents the user with information regarding the meshed component, such as geometry dimensions, cell or face trees (which provides information on the hierarchy of the cells or faces) or information regarding the nodes, cell or faces. For this process, one is only interested in the node locations for the selected walls that were defined in ANSYS Meshing, as well as the face information of these cell walls (for example, which nodes belong to which cell and what name allocation was given to them). This information is extracted from the mesh file using a script run in Python 3.5.
- With the information sorted in terms of nodes, faces and boundary names, the information is processed further by selecting the boundaries that need to be simulated, and assigning surface properties to these boundaries. All cells that fall under these boundaries are assigned the same optical properties.
- The coordinates of each cell are transformed and rotated to the format that is needed in SolTrace to obtain the same position and orientation as it was originally. For an irregular triangle to be modelled in SolTrace, the reference position of the element (typically given as the centroid of the element), its aim vector and the transformed coordinates of the triangle corners are required. Refer to Appendix A for more information on the cell node transformation.
- By using the scripting possibility provided in SolTrace, the coordinates of the receiver elements are simulated.

Figure 4.2 gives an example of how a geometry that is modelled in ANSYS is converted to primitive elements in SolTrace. For demonstration purposes, a sphere, divided and labelled in the named selection

as “front” and “back”, is modelled in ANSYS v.19.0 SpaceClaim, as shown in Figure 4.2a. The geometry is then meshed, in this case using tetrahedrons as the type of mesh, using ANSYS v.19.0 Meshing (Figure 4.2). A surface mesh of the meshed geometry is exported, containing all the information on the elements. The yellow element in Figure 4.2b and Figure 4.2c displays one of these elements that has been converted from the mesh file to SolTrace. A Python script extracts and converts the mesh file information to import the primitive irregular triangle elements into SolTrace. With the script allowing the user to select which boundaries to simulate, the user may opt to simulate only the front part of the sphere by selecting “front”. SolTrace then simulates the chosen boundary as a collection of primitive elements that is like the meshed geometry. The converted elements in SolTrace v3.0.0 are displayed in Figure 4.2c, with the sample element highlighted in yellow.

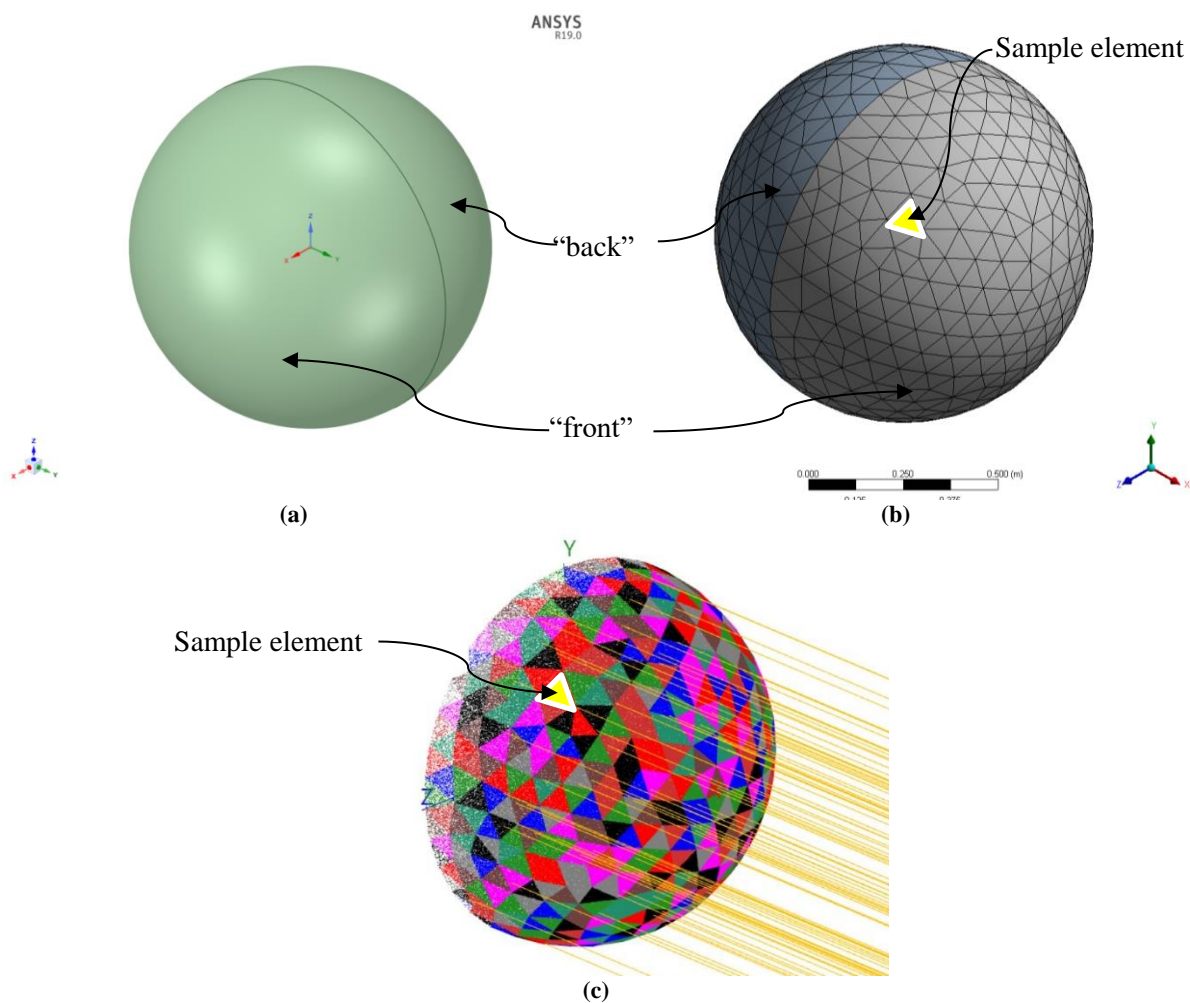


**Figure 4.2:** A visual representation of the conversion from an ANSYS geometry to primitive elements simulated in SolTrace: (a): a sphere modelled in ANSYS v.19.0 SpaceClaim to use as an example; (b): the sphere meshed in ANSYS v.19.0 Meshing using tetrahedrons as type of mesh, with a sample element highlighted in yellow; and (c): the mesh simulated as a collection of primitive irregular triangles in SolTrace v.3.0.0, again with the sample element highlighted in yellow.

To use the incident flux on the elements that represent the complex geometry as the boundary condition or heat source for thermal analyses, the heat flux on an individual element is averaged and given a location of the local heat source equal to the centroid of the primitive element. The flux and location per element are summarised in an interpolation file, after which it can be used in the ANSYS Fluent environment as heat source in the intended model.

#### 4.2.2 Validation of the new approach

The new approach to simulate geometries in SolTrace with the MCRT method simplifies complex problems. There is, however, a chance that the discretisation of a smooth surface may alter the results significantly. It is therefore necessary to validate this approach with a test case that provides the necessary complexity in terms of surface curvature, although simple enough to compare it with primitive geometries.

The test case reported by Martinek and Weimer (2012) provides a model of a biomass solar thermal cavity receiver configuration. The design consists of a circular cavity enclosure and a flat aperture surface. Centred in the cavity is a single tube geometry, which represents the absorber tube. A schematic of the design to be simulated is illustrated with dimensions in Figure 4.3.

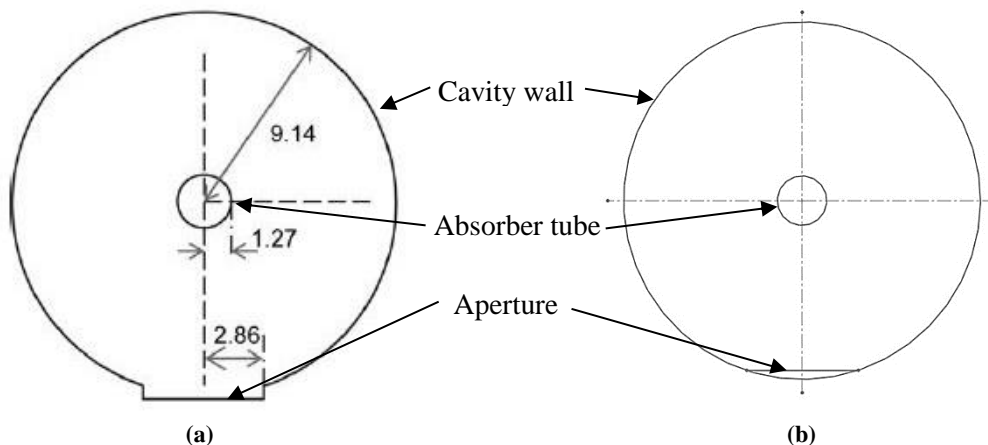


**Figure 4.3:** Schematic illustration of: (a): the test case validation model (Martinek & Weimer, 2013); and (b): the model used by the author for the approach where smooth surfaces are discretised for analysis using the MCRT approach. The displayed dimensions are given in centimetres.

The assumptions and boundary conditions for the test case presented here as validation are the same as assumed by Martinek and Weimer (2013). The cavity medium is assumed to be non-participating, which is necessary if one conducts MCRT-based analyses. The boundary conditions of the setup are summarised as follows:

- A collimated uniform radiative heat flux enters normally through the semi-transparent wall at the aperture at a normalised flux of  $1 \text{ W/m}^2$ . The front of the aperture is completely transmissive (transmissivity of 1.0), while the back of the aperture is given a reflectivity of 1.0. The slope error was given a value of 0.95 and the specularity error was given a value of 0.2.
- The cavity wall is seen as a realistic reflective surface with a uniform reflectivity across the surface of 0.9.
- The absorber tube in the centre's surface reflectivity is assumed to be minimal, with a realistic reflectivity value of 0.04 or rather an absorptivity of 0.96.

Since the model is to be simulated in SolTrace, where simple geometries are generally used to construct the model, the test case was altered slightly to accommodate this restriction. The aperture inlet was shifted to the inside of the cavity wall, as illustrated in Figure 4.3b, and an absorber plate with the exact dimensions of the inlet aperture was positioned directly in front of the inlet, or below the inlet if one refers to the image in Figure 4.3b. All reflected rays that bounce back onto the aperture would therefore be absorbed, which is similar to the rays reflecting from the cavity.

Before conducting the test, a ray independence study is done to ensure that the number of rays used during the test is sufficient not to have a significant impact on the results. The model was constructed using primitive geometries built into the SolTrace software. The number of ray intersections generated for the test ranged from  $5\,000$  to  $10^7$ , and the average flux that hit the cavity wall, as well as the absorber tube, was used as a comparative results check against the results obtained by Martinek and Weimer (2013). To check whether the flux distribution on the cavity wall and absorber tube was similar to that obtained by Martinek and Weimer (2013), these flux distributions were plotted next to each other, as shown in Figure 4.4.

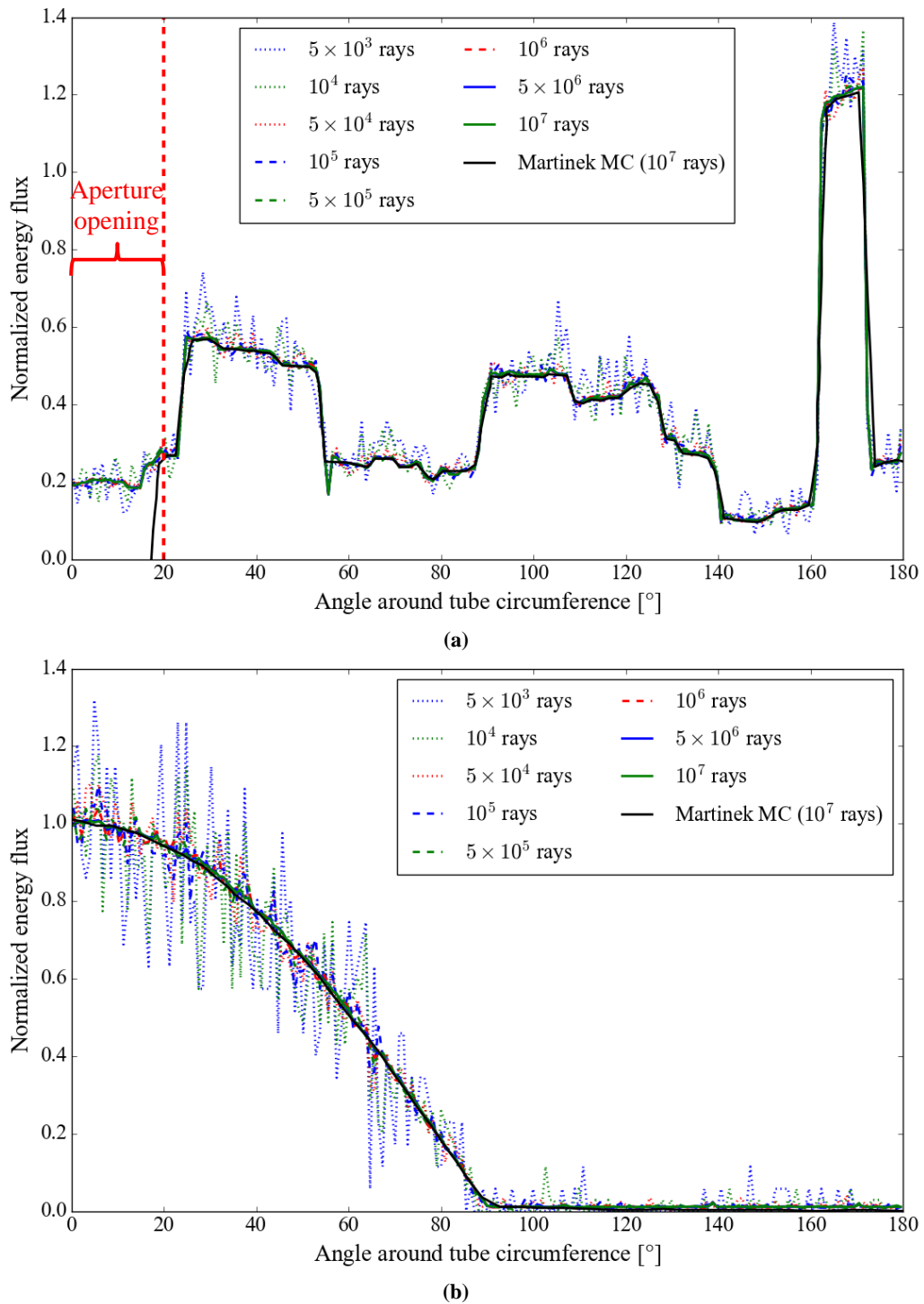
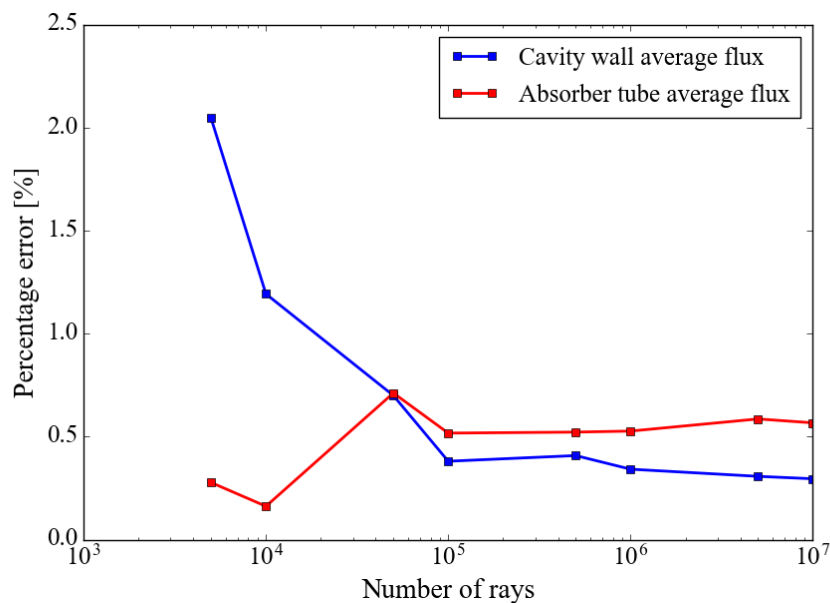


Figure 4.4: A normalised energy flux distribution incident on: (a): the cavity wall surface; and (b): the absorber tube surface for rays in the range of  $5\,000$  to  $10^7$  rays.

Take note that the flux distribution provided by Martinek and Weimer (2013) in Figure 4.4 represents the number of hits of the simulated rays on the surface of the cavity wall and absorber tube surface, rather than the energy absorbed by a surface. The higher concentration of ray hits would therefore result in a higher normalised energy flux for a specific location on the surface.

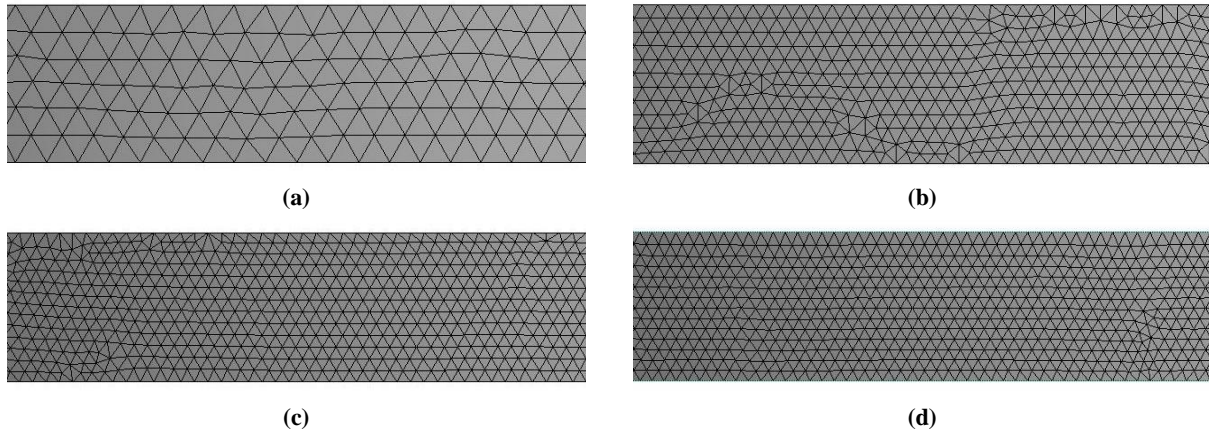
The results displayed in Figure 4.4 show the phenomenon that is typical of Monte Carlo. Since the results obtained are averages over individual samples (or rays in the case of ray tracing), they contain fluctuations about a mean value. This is evident with the lower order rays that were generated showing major fluctuations around the mean curve trend. As the rays generated increase, the fluctuations around the mean decrease up to the point where they are not evident. When comparing the results with the results of Martinek and Weimer (2013), they seem to follow the trend almost perfectly, especially in the highest orders of ray numbers tested. The results displayed in Figure 4.4a show a diversion from the compared results from an angle of  $0^\circ$  to  $20^\circ$ . This is because the tested results plotted include the absorber plate at the aperture's flux incident on it, while the model of Martinek and Weimer (2013) does not have a surface at those angles. The author can therefore neglect the results obtained at the aperture. To check whether the results obtained fell within a 1% margin of accuracy, the averages of the cavity wall flux (excluding the data in the range of  $0^\circ$  to  $20^\circ$ ), as well as the absorber tube flux, were calculated for the range of rays that was generated. A summary of the results is displayed graphically in Figure 4.5.



**Figure 4.5: A graphic representation of the percentage error obtained on the averaged cavity wall flux and absorber tube flux.**

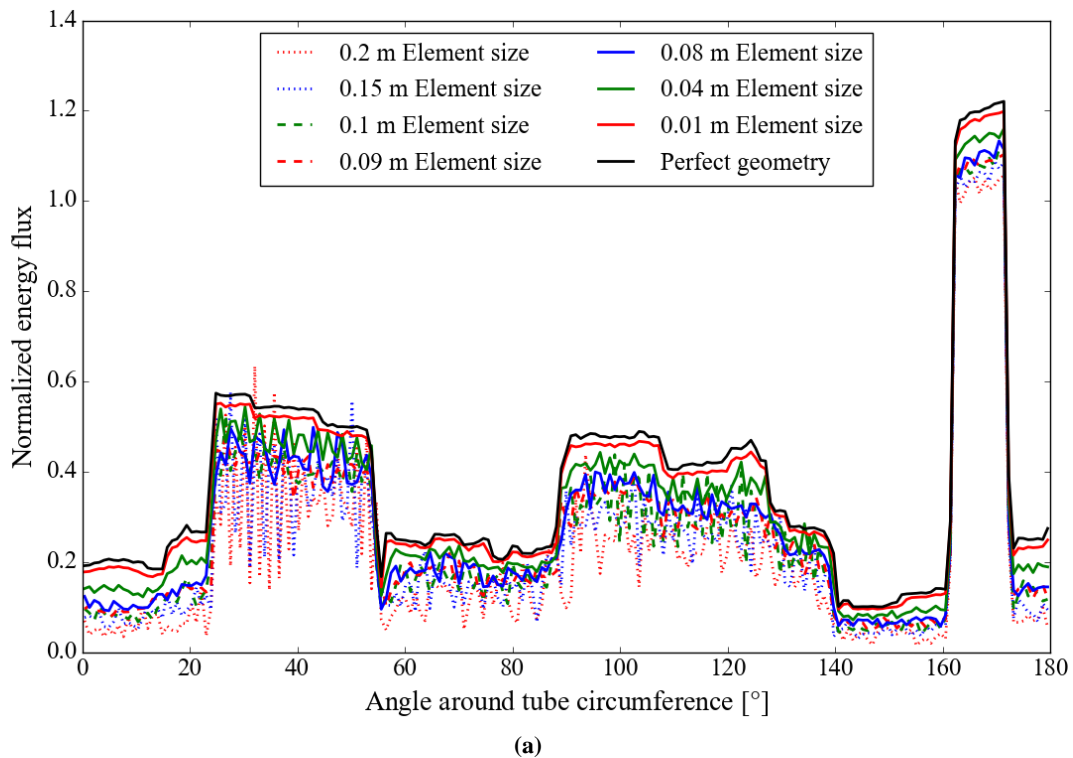
From the results displayed in Figure 4.5, it is clear that the model reaches ray independence at around  $10^5$  ray intersections generated, with the percentage difference in results dipping below 1% from this number and remaining relatively stable onwards. It is therefore not a bad assumption to make that good tests can be conducted with ray intersections generated at  $10^6$  upwards. Martinek and Weimer (2013) conducted their tests with  $10^7$  rays. Hence, for consistency, the author did the same. The source of the 0.5% discrepancy that is visible with the ray independence plot (Figure 4.5) is most likely due to a combination of converting the available data of Martinek and Weimer (2013) to a digital format, as well as the number of divisions used to represent the surface of the model numerically. It is likely that the author used a smaller interval between data points, among inspecting the graph of Figure 4.4a. This discrepancy, however, is of no concern.

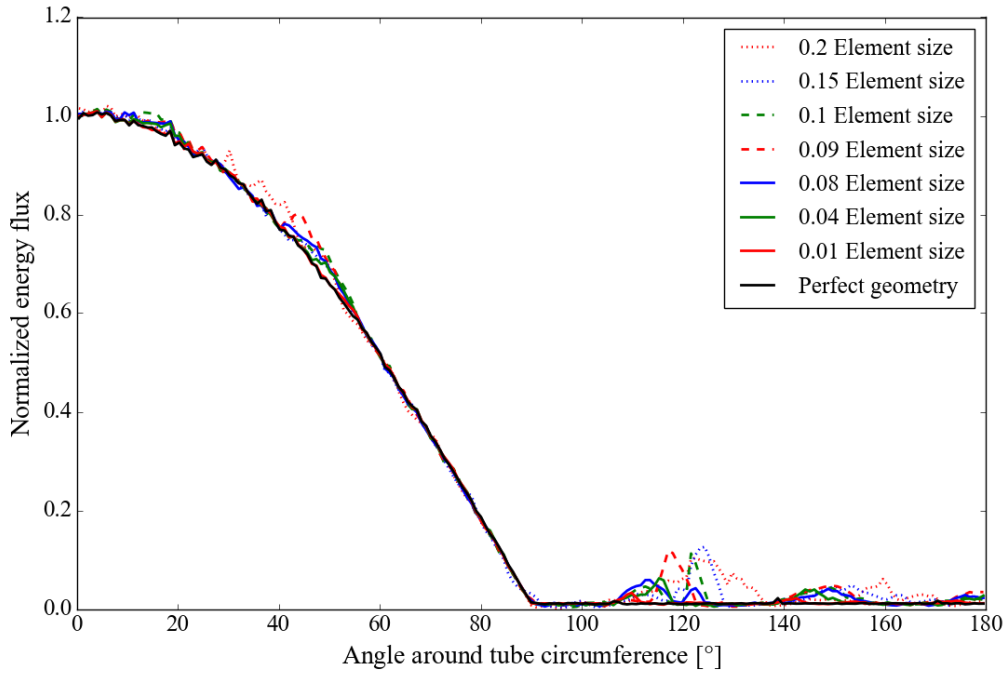
To determine the effects that the discretisation of a smooth surface have on the results, the test case model is meshed to different element sizes. Once these cases have been modelled and simulated in SolTrace, they are compared to the smooth surface primitive geometry model simulation results, since the results obtained with the geometry compared well with those of Martinek and Weimer (2013). A side view of the cavity wall for the different element size mesh surfaces is displayed in Figure 4.6.



**Figure 4.6: The meshed outer cavity wall surface of the biomass solar cavity receiver test case model for element sizes: (a): 0.2 m; (b): 0.1 m; (c): 0.09 m; and (d): 0.08 m.**

The results obtained have been plotted with the results of the primitive geometry that were previously analysed for both the cavity wall and the absorber tube. These results are displayed in Figure 4.7.

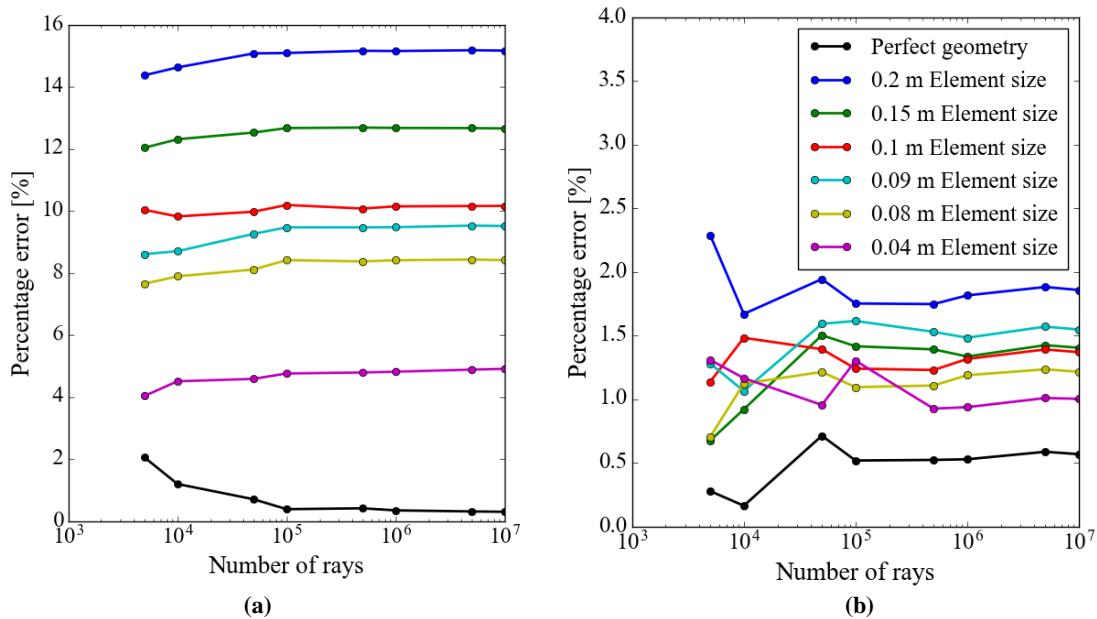




(b)

**Figure 4.7: The normalised energy flux distribution that is incident on: (a): the cavity wall surface; and (b): the absorber tube surface for discretised or meshed geometries of the validation test case model using  $10^7$  rays.**

From the first observation, one could observe that a decrease in the element size decreases the fluctuations of the flux distribution. This could be explained by the fact that a smooth curvature is discretised by a certain amount of small, flat surfaces. The smaller the element size value (this is therefore also applicable to flat surface areas), the “smoother” these surfaces are represented. Another interesting occurrence is the fact that the results obtained on the surface of the absorber tube (Figure 4.7b) seem to represent the actual data quite well right from the coarse mesh, while the cavity wall (Figure 4.7a) seems to show a considerable gap for most of the element sizes tested. This is even more evident when one compares the errors of the average flux on the cavity wall with the errors of the average flux on the absorber tube surface, which are graphically displayed in Figure 4.8.



(a)

(b)

**Figure 4.8: The percentage error obtained on: (a): the average cavity wall flux; and (b): the average absorber tube flux for different mesh element sizes across the range of rays generated.**

If one compares the 0.2 m element size model for the error on the average flux on the cavity wall with the absorber tube's average flux error, one can see that the error is more than seven times greater on the cavity wall than on the absorber tube surface. This trend remains the same to a relative extent as the element size decreases. This is explained by considering how the rays travel within the receiver geometry. To illustrate the difference, the rays travelling in the receiver constructed with primitive geometries are compared with the receiver discretised with an element size of 0.2 m. This is shown in Figure 4.9.

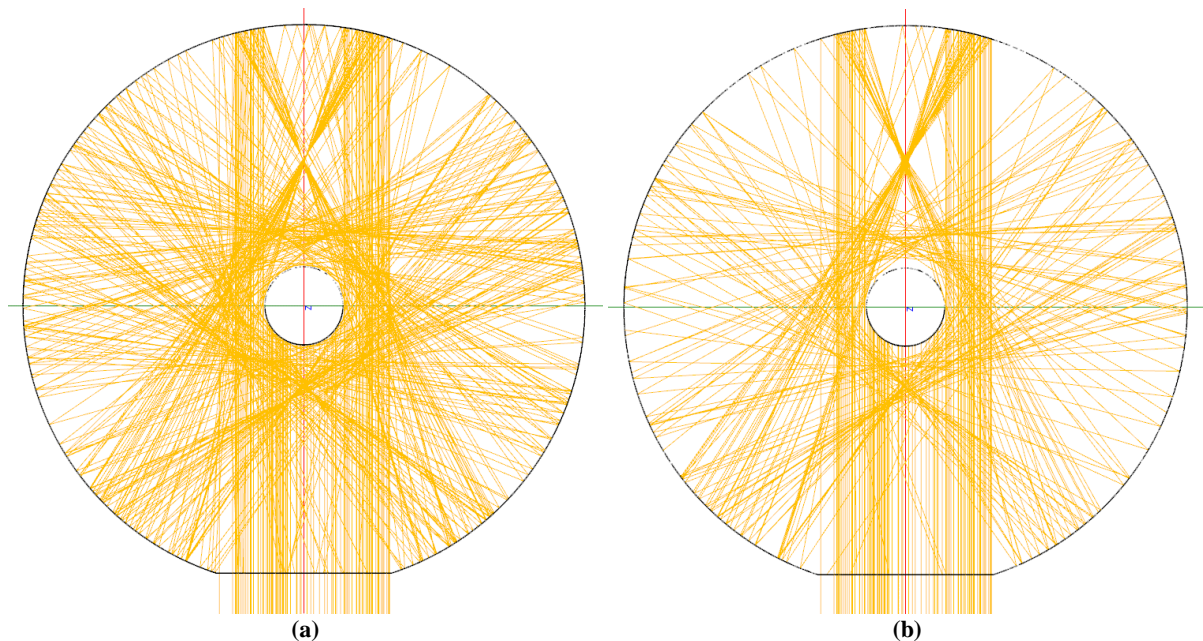


**Figure 4.9:** A SolTrace simulation of the validation model constructed using: (a): primitive geometries; and (b): discretised elements with an element size of 0.2 m, both displaying the same generated ray path in the receiver.

The rays that enter the aperture are either absorbed directly by the absorber tube, or are reflected at the back of the cavity wall, which is also evident in the sharp spike in the flux incident on the cavity wall in Figure 4.4a and Figure 4.7a between the 160° and 170° range. Once they are reflected, these rays seem to “bounce” off the cavity wall a couple of times before they eventually end up at the absorber tube, or are eventually absorbed by the cavity wall. With the discretised model in Figure 4.9b, it is clear that the ray paths are less dense compared to the primitive geometry model in Figure 4.9a. The small discrepancies with the discretised model cause the rays to be reflected towards the absorber tube much sooner than with the “perfect” model. It is due to these small discrepancies that the error on the cavity wall is much greater. Multiple reflections on discretised surfaces cause the errors that are prevalent on the surface to add up with every reflection that follows.

Again, reminding the reader that the data of Martinek and Weimer (2013) refers to ray hits rather than energy absorption, the smooth surface allows much of the light to reflect off the outer reflective surface multiple times before being absorbed by the inner absorber surface. This is not the case for the course approximated surface, where the small discrepancies in inaccuracies on the reflective surface causes the light to end up much sooner at the absorber surface, therefore less hits are observed on the outer reflective surface. This explains why the course mesh approximated surface underpredicts the number of hits.

Another point of interest to consider for the graphs in Figure 4.8 is that the graph fluctuates in error values up to the number of rays generated, which is  $10^5$  upwards for every element size. This speculates that the convergence of a value as a function of the number of rays used does not depend on the element

size or at least not to a degree worth mentioning. One could therefore assume that, once convergence has been obtained with the number of rays generated, one would only need to consider the element size. To analyse the influence the element size has on the accuracy of an analysis, the model was compared to a discretised model of different element sizes, all simulated with a ray count of  $10^7$ . The results are summarised and plotted in Figure 4.10.

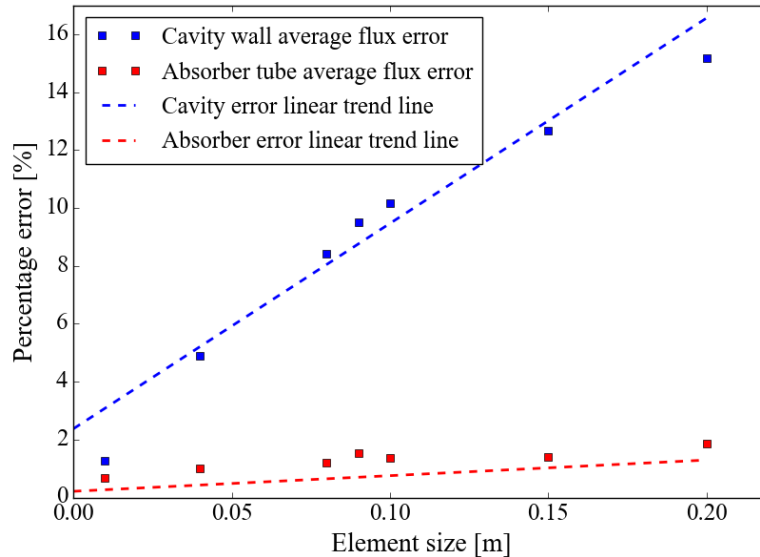


**Figure 4.10: The percentage error on the averaged cavity wall flux and absorber tube flux as a function of the different mesh element sizes for  $10^7$  rays generated.**

The graph in Figure 4.10 displays a clear correlation between the element size of the model and the error obtained with the ray tracing analysis. There seems to be an almost linear correlation between these two variables, with a reduction in the element size producing a reduction in the error obtained. This observation could be of great importance for future ray tracing analyses using the method of discretising complex models with the new approach. One would be able to predict the results of a complex model by discretising the model for different element sizes. Then, by using a trend line, one could extrapolate the results to the point where the model would be discretised to an element size of zero. The results obtained through extrapolation could then be considered a rough estimate for the model were it not discretised. This is, of course, on the assumption that the ray count has reached independence.

### 4.3 Computational fluid dynamics thermal model

To correctly model the heat transfer of the receiver, it is good practice to validate the numerical approach to comparable experimental results. The proposed receiver design consists of an absorber surface of an array of pyramid elements on which the incident flux irradiates. The converted optical to thermal energy at the surface is partially transferred to an HTF that impinges on a concave surface on the inside of these pyramid elements. In order to simulate these models, one would need to select a heat transfer model that delivers accurate results and is preferably computationally inexpensive.

CFD is a proven method and popular approach to the thermal simulation of key components and sub-systems in a solar plant. The approach has proved its applicability to the simulation of different engineering problems for years. However, the accuracy and reliability of its results are highly dependent on the considered assumptions in its simulation, the way the computational domain is structured and the type of computational model that is applied to calculate the results. It is therefore important to develop a model that correlates well with experimental results. With impingement heat transfer being

the focus for heat transfer modelling with the receiver proposed, and with much research already conducted on the heat transfer capabilities of an impinging fluid on a heated surface, a study was conducted to establish a turbulence model that correlates well with existing results and that was not computationally expensive. Only RANS-based turbulence models were considered, since DNS and LES models, although very accurate, are computationally costly. The study first conducted a test with an impinging fluid on a flat surface, followed by a concave surface test.

### **4.3.1 Vertical round jet impingement on a horizontal flat surface**

The jet impingement heat transfer on a horizontal flat surface is an extensively studied field, with a wide range of experimental and numerical studies conducted for different cases, as referred to in Chapter 2.5. The practical application of a numerical model to simulate the performance of the receiver absorber requires the validation of a turbulence model suitable for this application. Before conducting validation tests on the concave surface jet impingement test case, the simplified and more broadly studied flat plate jet impingement test case will be validated, after which the turbulence model with the best distribution will be used further.

#### **4.3.1.1 Geometry and computational domain**

Although numerous experimental and numerical studies have been conducted on horizontal flat surface jet impingement heat transfer characterisations, the author opted for the well-defined model in Case 25 of the European Research Community on Flow, Turbulence and Combustion (ERCOFTAC) (1992), with experiments conducted by Cooper, Jackson, Launder and Liao (1993) and Baughn, Yan and Masbah (1992). The model's dimensions are, however, not of great importance, since the results are presented non-dimensionally.

The setup consists of an inlet pipe with a diameter ( $d$ ) of 26 mm, positioned normally at a height of  $2d$  to the flat surface. Tests were also conducted for other heights and diameters, but the heat transfer data was only available for the given dimensions. It was suggested that the outlet plane was to be placed at a sufficiently large radial distance to have no effect on the results. The measurements were conducted up to a distance of  $r/d = 6$ , and an outer radial boundary of  $r/d = 8$  or greater was suggested. The air flows through the pipe at a fully developed turbulent flow of a Reynolds number of  $2.3 \times 10^4$  (the velocity of the air can be calculated from the Reynolds number value, the pipe diameter, and the material properties based on an inlet temperature of 300 K), with the properties of the air in the computational domain defined by a piecewise-linear approximation of the tabulated properties, as defined by Cengel and Ghajar (2015). To ensure that the flow is fully developed by the time it reaches the pipe's exit, at a length of  $10d$ , as proposed by Cengel and Ghajar (2015) for turbulent flow, it was entered into the computational domain. Sensitivity studies (refer to Appendix E) on the inlet boundary conditions showed that the proposed length was not enough for a fully developed flow, and hence the velocity, intermittency, turbulent kinetic energy ( $k$ ) and specific dissipation profile were produced from the outlet of a  $48d$  length pipe simulation and used as boundary condition, as the length of this tube corresponds to the experimental setup of Lee and Lee (1999). The computational boundary opposite the plate is situated a given distance of 20 mm before the exit of the pipe to allow the fluid to be entrained at the rate necessary to satisfy continuity in the boundary cells. The boundary condition given for the plate was an assumed uniform heat flux of  $\dot{Q} = 1\,000$  W/m, while ambient pressure was imposed as boundary condition for the exits, with the ambient temperature equal to the inlet temperature. An axisymmetric two-dimensional computational domain was constructed with the assumption that the flow is axisymmetric. The setup is schematically illustrated in Figure 4.11a, with the computational domain shown in Figure 4.11b.

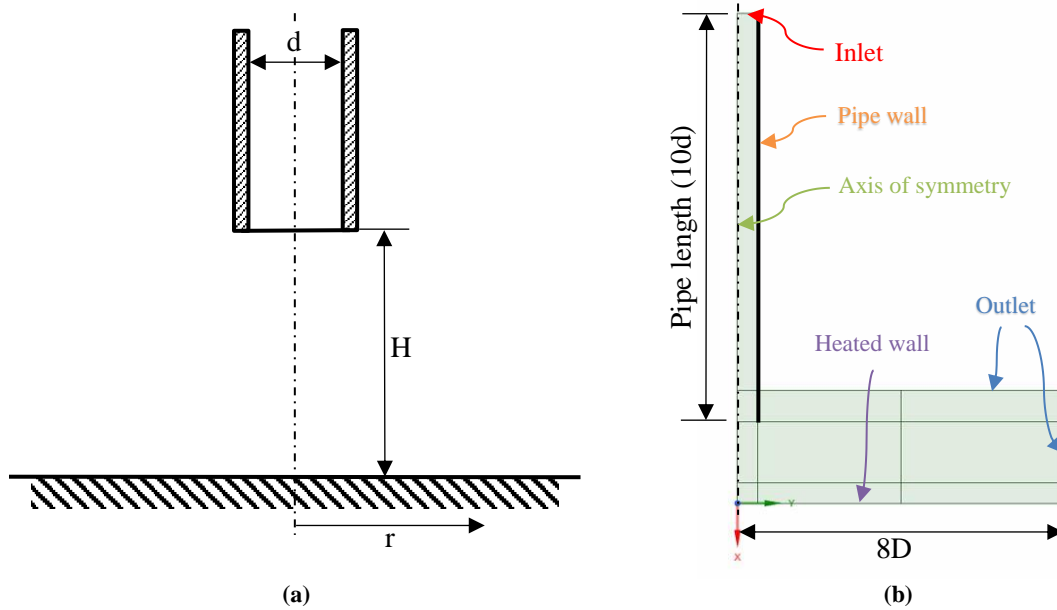


**Figure 4.11:** (a): A schematic diagram of the flat plate jet impingement setup; and (b): the computational domain of the jet impingement numerical analysis constructed in ANSYS SpaceClaim (axisymmetric).

#### 4.3.1.2 Mesh independency study

Referring to the computational domain created in SpaceClaim (shown in Figure 4.11b), the geometry plane is divided into segments that assist with the meshing of the computational domain. Fine meshing was constructed near the surface onto which the fluid impinges, while a coarser mesh was constructed near the exit boundaries. Figure 4.12 gives a depiction of the meshing structure for one of the coarser meshes, although it clearly shows how the finer mesh is constructed near the impinging region.



**Figure 4.12:** A mesh structure of the flat plate jet impingement computational domain for a coarse mesh.

A mesh independence study was conducted to conclude whether the mesh density would be sufficient for computing the results. A coarse mesh was constructed and the results computed using the transitional Menter’s shear stress transport (SST) and the Spalart-Allmaras (SA) turbulence models. The coarse mesh’s density was then increased and the computation repeated. This was done for up to 10 design points. The results’ area-weighted average of the Nusselt number on the surface of the impinged plate was used as a parameter with which to check the mesh convergence. The Nusselt number was used as convergence parameter due to it being the focus of the investigation, although initial analyses also have indicated overall convergence if the Nusselt number variable converges. A graph with the results of the mesh independence study is plotted in Figure 4.13.

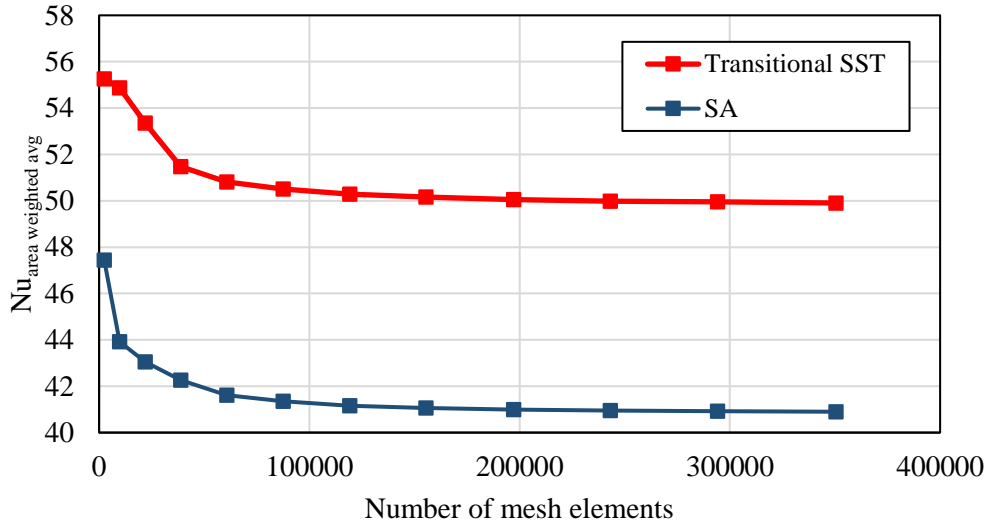


**Figure 4.13:** A mesh independence study for the flat plate round jet impingement study, using the area-weighted average Nusselt number over the entire simulated flat plate as a parameter.

From the graph shown in Figure 4.13, one can see that mesh independence is reached as the curve gradually moves to an asymptotic value. It is therefore safe to say that mesh independence has been reached at about the 7<sup>th</sup> and 8<sup>th</sup> design point. Although the mesh independence study showed independence at the given design point stated earlier, the author decided on doing the turbulence model analysis using the finest mesh used with the mesh independence test.

#### 4.3.1.3 Discussion of results

To compare the accuracy with which RANS turbulence models can calculate the jet impingement heat transfer, the dimensionless Nusselt number on the surface of the impinging plate is used as a reference. Different turbulence models were compared to experimental results from several sources. The turbulence models that were compared include the  $k-\epsilon$ ,  $k-\omega$  SST,  $k-kl-\omega$ , SA and the transitional SST models. To compare the results for different Reynolds numbers, the results were normalised by dividing them by  $Re^{2/3}$  (Martin, 1977). The results are shown in Figure 4.14.

It is important for the chosen turbulence model to estimate the occurrence of the second-“hump” phenomenon. All the tested models, except for the  $k-\epsilon$  turbulence model, displayed some degree of estimating the second peak in heat transfer, although the majority failed to convincingly predict the second maximum point. The  $v^2 - f$  model was not considered, due to the unavailability of the model with the software used. The SA turbulence model predicted what seems to be a second peak, although it is estimated far too early, and under-predicts the results further from the axis. The  $k-\omega$  turbulence model also displayed a second “hump”, although this is not as evident. It also over-predicts the first peak, although the results further from the axis follow the experimental results quite well. The transitional models, such as the  $k-kl-\omega$  turbulence model, but especially the transitional SST model, displayed the best results. Both accurately predict the first maximum and the results further away from the axis. Both models predict the second peak, although the transitional  $k-kl-\omega$  turbulence model fails to predict it as accurately as the transitional SST model. For all models, the impingement region heat transfer is over-predicted compared to the experimental data, although the experimental results do not agree well with each other at that point either.

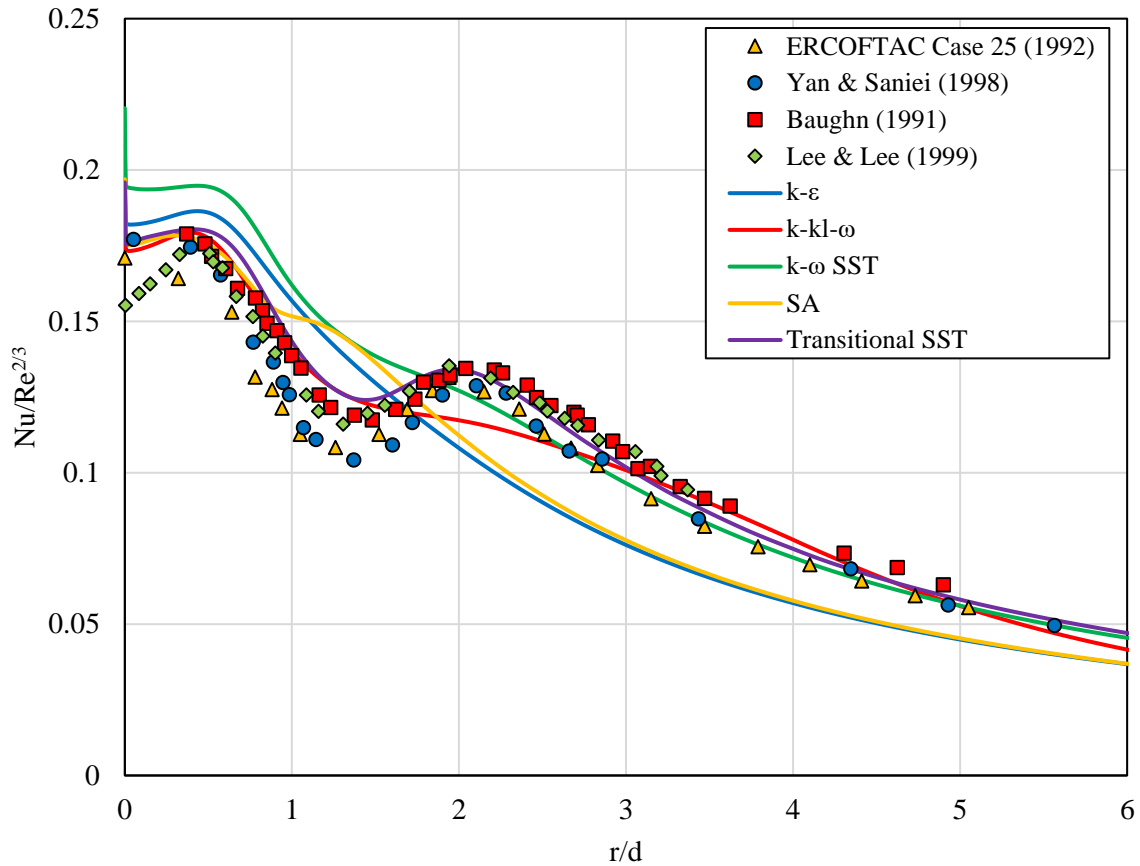


**Figure 4.14: The Nusselt number as a function of the dimensionless radius for various turbulence models. Results were compared to results from ERCOFTAC (1992), Yan and Saniei (1998), Baughn, Hechanova and Yan (1991) and Lee and Lee (1999).**

As discussed in the literature study on jet impingement heat transfer in Chapter 2.5.1, there is no consensus yet on the cause of the second peak phenomenon. The idea of the transition of flow from the stagnation point that follows from laminar to turbulent flow would be able to explain the phenomenon. After the flow reaches the stagnation point, the flow accelerates. After being laminar initially (based on the Reynolds number calculated using the radial distance from the stagnation point), the flow transition becomes turbulent.

LES numerical modelling has also been conducted, with the observation speculating that the initial acceleration and associated convection cause a high convection heat transfer zone, but since the flow is laminar, no mixing occurs, and the heat transfer rate drops at increasing radii. The turbulence flow's eddies that develop after the transition enhance the heat transfer, which leads to another local maximum zone of heat transfer, which is referred to as the second peak (Craig, Sloopweg, & Meyer, 2018).

This transition from laminar to turbulent may be the cause for the struggle to capture the local heat transfer peaks due to transition for the different turbulence models, and the reason why the transitional models seem to perform the best. The transitional SST model, for example, in addition to the  $k-\epsilon/k-\omega$  approach of the SST model, solves for two additional transport equations (those for turbulence intermittency and the Reynolds number based on the momentum thickness of the boundary layer). In this way, the surface effects of laminar, transitional and turbulent flow can be captured in a steady-state RANS setting without having to resolve the temporal turbulence domain (Craig et al., 2018).

The transitional SST model is evidently the best model of those tested for impingement heat transfer and will therefore be considered for the vertical round jet impingement on a concave surface. This validation only considers the impinging flow phenomenon, and therefore neglects the possibility with the application of this computational model the prediction of other flow patterns. This study therefore assumes that the transitional SST model adequately predicts other flow patterns. This assumption is based on the observation that this model adequately predicts a flow phenomenon that presents various flow regimes and patterns.

### **4.3.2 Vertical round jet impingement on a concave surface**

The HTF of the proposed receiver impinges on a concave surface inside the absorber's pyramid element. It is therefore not a bad assumption to make to assume that a turbulence model that correlates well with experimental data for a round jet that impinges on a concave surface is sufficient for the analysis of the receiver's absorber area. An experimental study conducted by Lee, Chung and Won (1999) examined the heat transfer effects that an impinging round jet would have on a concave surface.

#### **4.3.2.1 Geometry**

The study conducted by Lee et al. (1999) had an experimental setup that consisted of a nozzle with an outlet diameter,  $d$ , situated a distance  $L = 2$  from the point of impingement on the concave surface of a diameter ( $D$ ). The nozzle would produce a fully developed round jet on a surface with a fixed uniform heat transfer rate,  $\dot{Q}$ . All the results of the flow on the concave surface will be a function of the curve length, which is a function of  $r$ . Tests will be conducted for jet Reynolds numbers (based on the pipe diameter) of  $Re = 11\ 000$ ,  $23\ 000$  and  $50\ 000$  for jet diameter to concave diameter ratios of  $d/D = 0.056$  and  $0.089$ . The properties of the fluid (air) are defined in the same way as in the study of the vertical round jet impingement on a horizontal flat surface. The pipe length produces a fully developed flow that is also constructed to have a length of  $10\ d$  with the boundary profile of the outlet of a  $48\ d$  length tube similar to the flat plate jet impingement setup. A sensitivity analysis was conducted on the outlet boundary after the concave surface to determine whether the distance of the boundary from the exit of the concave wall has an effect on the results. The resulting boundary domain used ended up being sufficient, with no fluctuation in results from that distance onwards. For more information on the analysis, refer to Appendix E. As with the flat surface impingement study, an axisymmetric two-dimensional computational domain was constructed with the assumption that the flow is axisymmetric. A schematic diagram that graphically explains the setup, as well as the computational domain constructed in ANSYS SpaceClaim, is depicted in Figure 4.15a and Figure 4.15b, respectively.

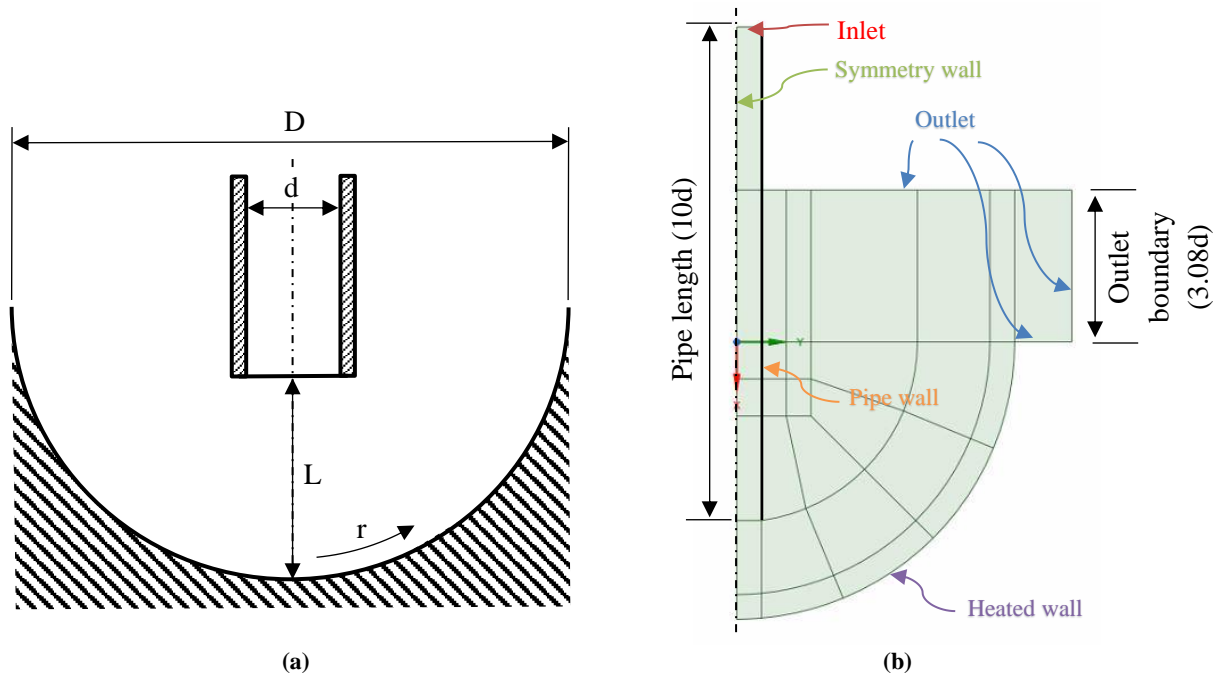
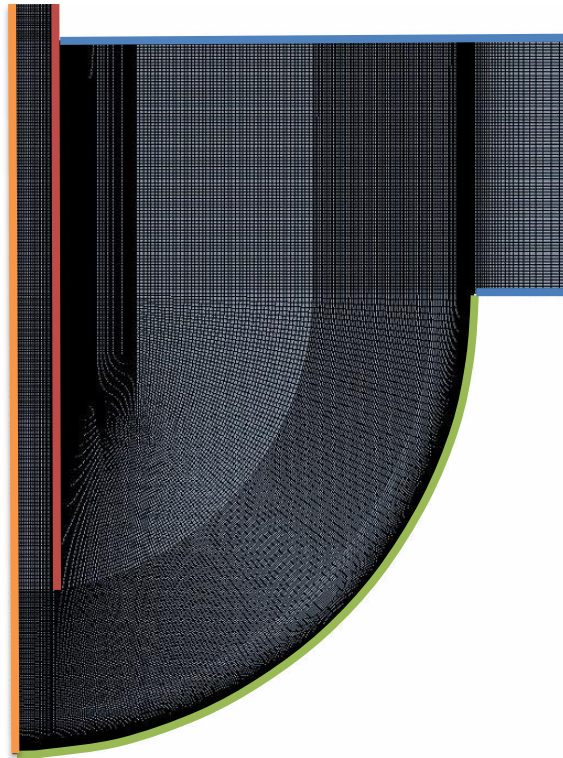


Figure 4.15: (a): A schematic diagram of the concave surface jet impingement setup; and (b): the computational domain of the jet impingement numerical analysis constructed in ANSYS SpaceClaim (axisymmetric), the displayed image (b) showing the  $d/D = 0.089$  geometry.

#### 4.3.2.2 Mesh independency study

The same procedure was conducted with the computational domain of the concave surface and the flat plate test, with a fine mesh constructed at the curved plate boundary, and especially the impinging point, to capture the heat transfer effects occurring at the surface. A coarse mesh of the  $d/D = 0.089$  model is displayed in Figure 4.16. Displayed in the figure is the pipe wall (red) and impinged concave plate surface (green), which are defined with no-slip boundary conditions. The orange line displays the axisymmetric axis, while the blue regions represent the zero-pressure outlet.



**Figure 4.16:** A mesh structure of the concave surface jet impingement computational domain for a coarse mesh.

A mesh sensitivity test was conducted to determine how fine a mesh was necessary to proceed with the analysis. The results of the mesh sensitivity study are displayed in Figure 4.17 (refer to Equation (4-1) and the ANSYS Fluent documentation (ANSYS, 2018) for the calculation of the Nusselt number and then averaging it). It is clear from the presented graph that the results flat out as the number of elements increase, with the finest mesh tested showing minimal change in value compared to the previous design point. The finest mesh tested is therefore used for the tests that are conducted on that geometry.

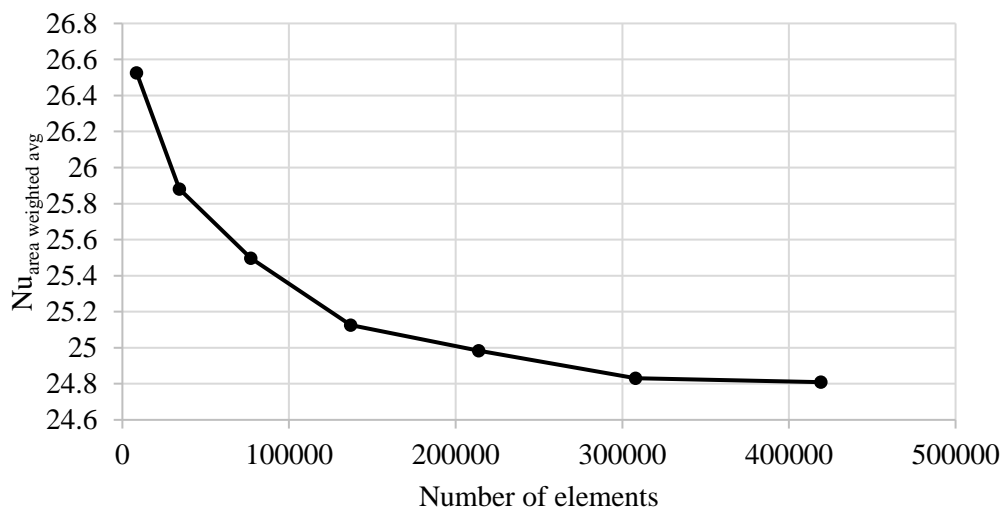


**Figure 4.17:** A mesh independence study conducted on the  $d/D = 0.089$  concave surface geometry, with the area-weighted, averaged Nusselt number on the concave surface displayed as a function of the number of computational elements using the transitional SST turbulence model.

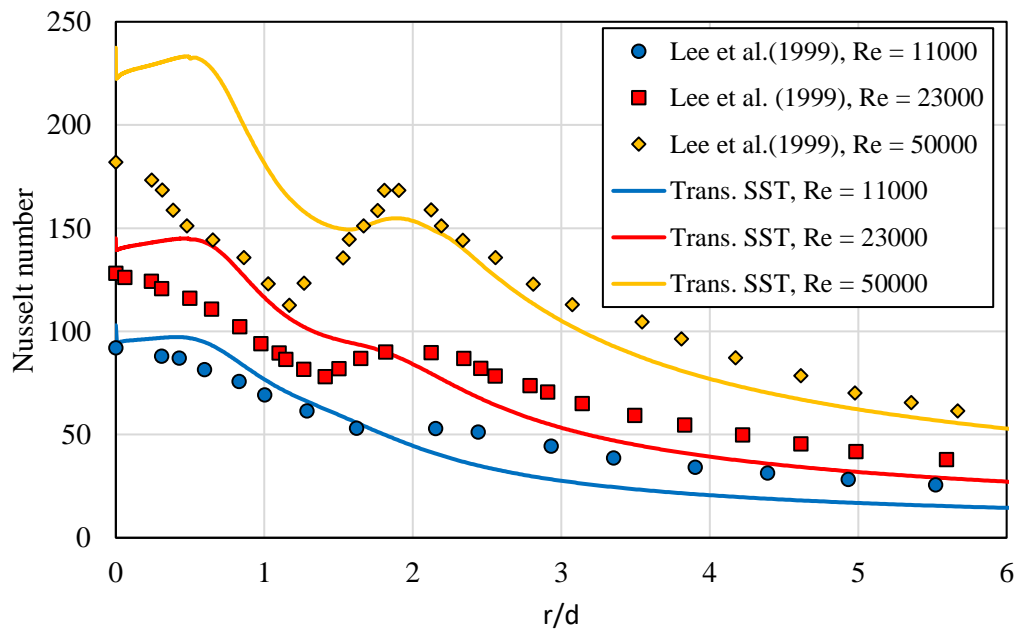
### 4.3.2.3 Discussion of results

Before a final test was conducted for the different test cases, a sensitivity study was conducted on a wide range of parameters. These include the sensitivity of the position of the outlet boundary, the velocity profiles and the turbulence kinetic energy sensitivities at the inlet, as well as a comparison between constant fluid properties and piecewise-linear temperature-dependent fluid property approximations. The results of the sensitivity studies are presented in Appendix E. The results have given insight into the sensitivity that the boundary conditions provide to the heat transfer of the model, and therefore to apply certain assumptions may have a considerable effect on the results. It was also assumed that the Nusselt number calculations were done as follows in the experiments conducted by Lee et al. (1999):

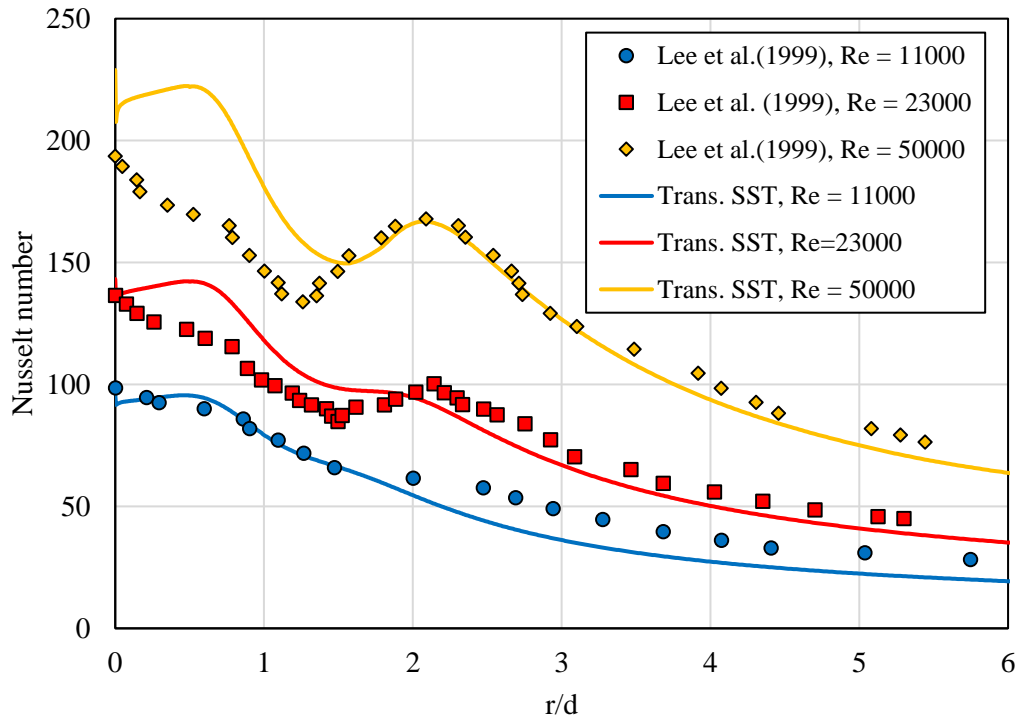
$$Nu = \frac{h(T)d}{k} = \frac{\dot{Q}d}{(T_{wall} - T_0)k(T_0)} \quad (4-1)$$

The heat transfer is therefore defined by  $\dot{Q} = 1\,000\text{ W/m}$ , with  $d$  representing the nozzle diameter and  $k$  being the thermal conductivity of the air assumed as constant by calculating the value at the inlet, which is at  $T_0 = 300\text{ K}$ . Radiative heat transfer is not considered for the analysis, and the assumption is backed up with the initial results showing minor temperature differences, therefore radiation will play a negligible role.

With the boundary conditions assumed (see Chapter 4.3.2.1 ‘Geometry’), the results displayed in Figure 4.18 are produced with Figure 4.18a displaying the results for the test case described by Lee et al. (1999) for a diameter ratio of  $d/D = 0.056$ , and Figure 4.18b displaying the results for a diameter ratio of  $d/D = 0.089$ .



(a)



(b)

**Figure 4.18:** A comparison of CFD using transitional SST and experiments by Lee et al. (1999). The Nusselt numbers as a function of the dimensionless radius for the diameter ratios are: (a): 0.056; and (b): 0.089.

The results show that the transitional SST RANS model correlates well with the experimental results for the test cases with high Reynolds numbers and diameter ratios. When considering the peaks, the model seems to capture the results less accurately. As shown in the sensitivity studies in Appendix E, the inlet velocity profiles and the low turbulence kinetic energy values could alter the magnitude of these peaks considerably. Studies by Craig et al. (2018) that compared LES with experimental results also saw a significant difference in the impingement zone's values, and ascribed the probable difference in results to the lack of information provided by Lee et al. (1999) for the profile at the exit of the nozzle. These results are preliminary, however, and more in-depth analyses should be conducted before the comments can be conclusive. It is for this reason that the LES results were not added.

#### 4.4 Conclusion

The following conclusions can be made based on the work presented in this chapter:

- The new approach for modelling complex geometries within SolTrace, using primitive irregular triangles, not only provides the great benefit of analysing a wider range of geometries using the MCRT approach, but also gives the option of analysing previous designs in more detail, since one does not have to simplify the geometry shape to a standard primitive element shape.
- With the new approach, one needs to discretise the geometry into small irregular triangles. The validation of replacing a smooth curved surface (which represents the complex surface) with the discretised approach has given a good understanding of how discretisation affects the results. The results have shown that, once a model has reached ray independence, the number of rays generated for the MCRT approach is no longer dependent on the element size. The element size, in contrast, plays a significant role in the accuracy of the results, with a smaller element size providing more accurate results. The correlation between the element size of a curved geometry and its error has been noted to be linear. One could therefore estimate the results, with a theoretical element size of

zero providing the most accurate results, which would typically resemble the curved body. Element sizes are restricted by available computational power. More elements will require more computational power.

- Impingement heat transfer is the means by which heat is removed from the surface on which the solar flux penetrates for the new receiver design. In order to model the heat transfer within the CFD environment as accurately as possible, different models have to be compared to experimental data to validate which would be the most appropriate. This was done for two cases: the flat plate and the concave wall flow impingement for heat transfer purposes. The transitional SST RANS model was the most effective, giving the most accurate results compared to experimental data for different cases compared to other RANS models, as well as being computationally inexpensive. Sensitivity studies with this model have shown that the impingement flow results are particularly sensitive to the different inlet flow variables.

## Chapter 5 Optical analysis, preliminary scoping and optimisation

### 5.1 Introduction

In the current research, the computational analysis can be divided into two categories: optical and thermal analyses. The optical analysis, preliminary scoping and optimisation will be presented in this chapter. As mentioned in the previous chapters, the optical analysis will be conducted using the MCRT approach with the SolTrace ray tracing software as the computational platform, with the numerical and geometrical models developed in Chapter 3 and Chapter 4.

The optical analysis will be conducted starting with an analysis of the solar flux on the aperture and an examination of the flux shape. This is done to determine what aperture dimensions are necessary for the field being analysed, and to optimise the angle of the aperture by comparing it with the proposed aperture angle. After the analysis, the aperture plate will be replaced by the receiver of interest, with several tests being conducted to examine the sensitivity of some mentioned parameters. Finally, a viable solar flux will be obtained on the absorber that will be used as a heat source for the thermal analysis in the chapter that follows. A new receiver design will also be proposed based on the findings and literature review, with an initial optical analysis conducted to check its feasibility.

### 5.2 Aperture analysis and optimisation

For central receiver systems, apertures may refer to different sections. For the purpose of this study, the aperture of a central receiver system is the area that represents the opening of the cavity receiver where the concentrated solar rays that are reflected from the solar heliostat field enter. For this study, it is considered the focal point of the central receiver system, although more research needs to be conducted on aiming strategies to optimise the efficiencies of this system. The aperture can be seen as the intersection between the heliostat field that collects and reflects the incident solar radiation, and the receiver that absorbs the concentrated solar energy. With an aperture defined as a window through which the solar rays should pass, it is of significant importance to analyse this area, since an understanding of the aperture solar flux could provide information on how to improve the collection of these fluxes.

All optical analyses that use a heliostat field will be conducted by applying the dimensions and specifications of the PS-10 heliostat field in Seville, Spain. This is no different to the analysis of the aperture. In addition, it is assumed that all heliostats aim the reflected solar rays towards a singular point situated at the centre of the positioned aperture. The aperture's centre point is assumed to be positioned at the top of the defined tower of the simulated central receiver field tower.

Before conducting any aperture tests, a ray independence study is performed to ensure that the results obtained in the tests are sufficiently independent not to have an impact on the results. The proposed aperture angle of  $12^\circ$  is used as a benchmark, and the time of the year is decided to be Julian Day 180 at solar noon. The ray count range that was used for the ray independence study ranged from 5 000 to  $3 \times 10^7$  rays, with the average net flux per square metre incident on the aperture of  $8 \times 8$  m used as an output parameter for the test. It was assumed that the area size would have a negligible effect on the aperture angle optimisation test. Therefore, the smaller  $8 \times 8$  m aperture area was decided on, since the results would be accentuated with an increased spillage present. Usually, a least-square assessment where the evolution of the flux map is considered would be the better approach for a ray independence study, although this would be a function of the binning criteria of the MCRT result. This output parameter was justified, since the only result that needed to be considered was the total flux that hit the aperture, rather than the aperture flux profile. This ray independence, together with the other ray independence studies, were conducted with the random number generator seeding from the same initial

value, therefore making the results comparable. The results of the independence are summarised and graphically displayed in Figure 5.1.

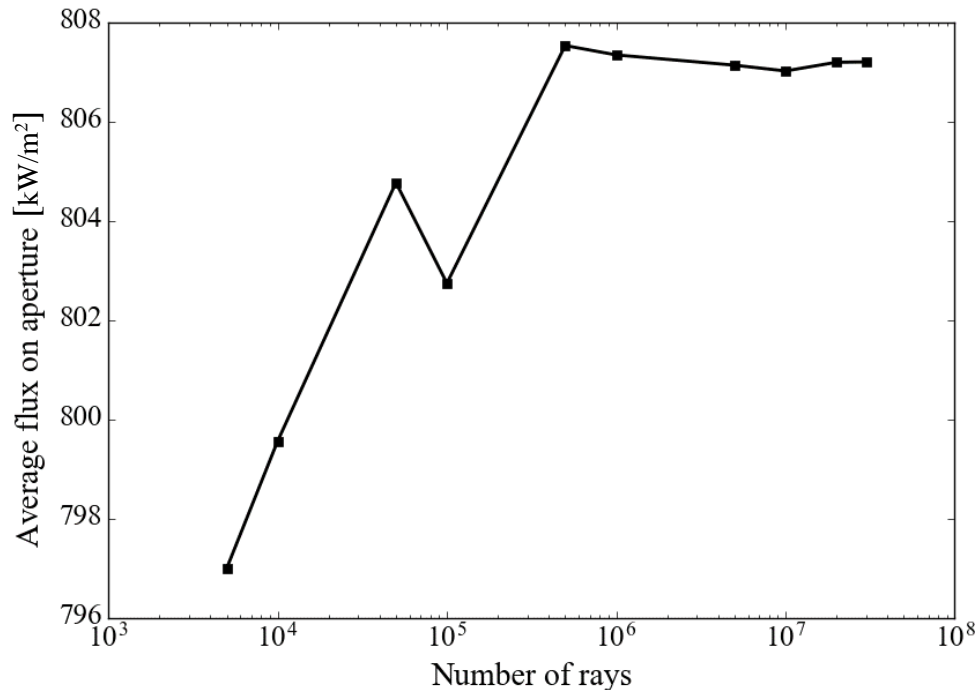


**Figure 5.1:** A graphic summary of the ray independence study conducted for the aperture analysis for rays generated ranging from  $5 \times 10^3$  to  $3 \times 10^7$ , with the average flux per unit area on the aperture as an output parameter.

If one considers the results displayed in Figure 5.1, one will note that the range of the results presented are small. This was expected, since a large aperture area, although reduced, offers little sensitivity for the number of rays. Therefore, ray independence is reached when the relative fluctuations reduce to negligible levels. One will note that there seems to be a considerable amount of fluctuation up to the point of  $5 \times 10^5$  rays, after which the results seem to stabilise at a value close to  $807 \text{ kW/m}^2$ . This would suggest that the model has reached ray independence at around this point. One would therefore assume that one could get reasonable results from the MCRT simulations with this model by using a ray count of  $5 \times 10^5$  upwards. The author decided to use a ray count of  $10^6$  for the aperture angle optimisation.

### 5.2.1 Aperture angle optimisation

With the ray independence concluded, a study is conducted to verify the proposed aperture angle by conducting an optimisation study on the aperture angle. This is done firstly with the crude geometrical approach, followed by the more sophisticated MCRT approach. Take note that this study does not fall under the main objective of analysing the proposed receiver, although variables such as the aperture angle could have an effect on the performance of the receiver.

#### 5.2.1.1 Geometrical approach

The optimal angle with which the aperture is fixed onto the tower can be estimated by taking an approach where one would assume that every single heliostat reflects the same amount of flux onto the aperture, in other words, that the contribution of every single heliostat is equal. Considering this, one can reduce the problem to a simplistic trigonometric problem. The optimal angle of the aperture would be the angle at which the aperture's face is normal to the direction of a specific heliostat. With the assumption that every heliostat makes an even contribution, one can take the average of the optimal angle of every single heliostat in the field. This approach is a first-order analysis, and does not consider any variable other than the location of the heliostat relative to the aperture. Variables such as those that

influence the focal spot of every individual heliostat is therefore not considered. For a better understanding of the approach, refer to the schematic illustration displayed in Figure 5.2.

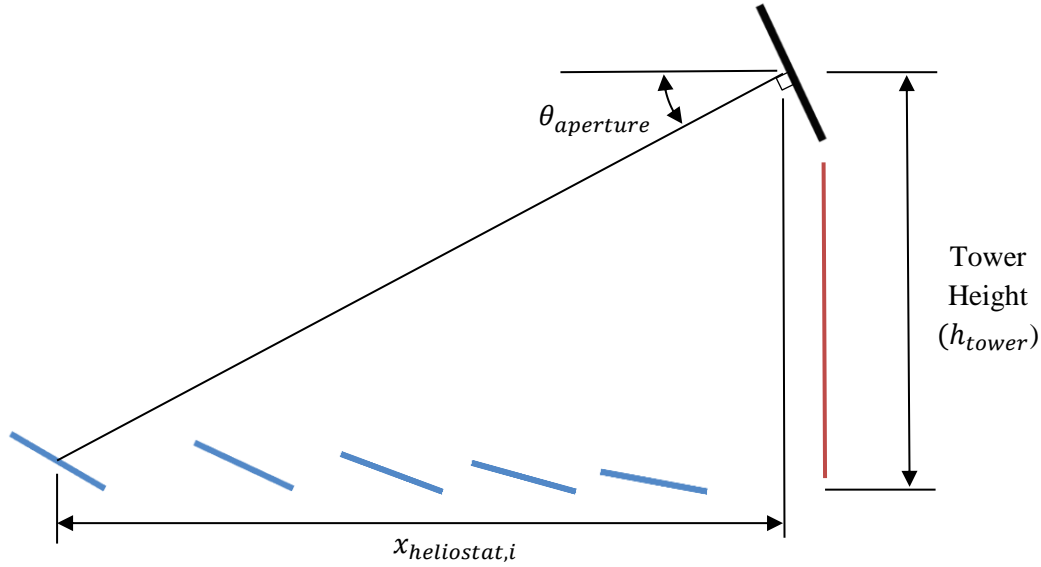


**Figure 5.2:** A schematic illustration of the trigonometric setup for the aperture optimisation using the geometric approach.

By assuming that the northern direction of the heliostat field is represented by the x-axis, only the x-component of the distance between the heliostat and the tower is considered, since only this component would have an effect on the aperture position. The tower is set as the origin to simplify the problem. The following equation was used to calculate the optimal angle:

$$\theta_{aperture,i} = 90^\circ - \tan^{-1} \left( \frac{x_{heliostat,i}}{h_{tower}} \right) \quad (5-1)$$

The optimal angle for the entire heliostat field is then the average of the optimal angle of each heliostat field or:

$$\theta_{aperture,opt} = \frac{1}{n_{heliostats}} \sum_{i=1}^{n_{heliostats}} \theta_{aperture,i} \quad (5-2)$$

with  $n_{heliostats}$  being the number of heliostats in the heliostat field and  $\theta_{aperture}$  the aperture angle.

This approach calculated the optimum angle for the PS-10 heliostat field to be  $25.19^\circ$ , a number that is more than double the proposed value of  $11.5^\circ$  to  $12.5^\circ$  used by the authors (refer to Table 3.3).

### 5.2.1.2 Monte Carlo ray tracing approach

For the aperture angle optimisation using the MCRT approach, one needs to determine the parameter range. After some initial analyses, it was noted that the optimal aperture angle would be situated in the region of between  $20^\circ$  and  $28^\circ$ . It was therefore decided to utilise the limited computational resources optimally. Aperture angles between these regions would be simulated in 40 intervals in order to obtain a reasonable degree of continuity. Due to the computational expense, the analyses were restricted to 12:00 LAT (solar noon) for five-day intervals, from Day 5 to Day 365. It has been noted that other hours of the day could have a significant effect in the results. This, however, was not considered.

An initial test was conducted for an arbitrary day (in this case Day 180) for a different number of rays to see what type of influence the rays would have on the continuity of the incident flux as a function of the aperture angle, since this would have an effect on the optimisation that would take place. Figure 5.3 shows graphic representation of this test's results.

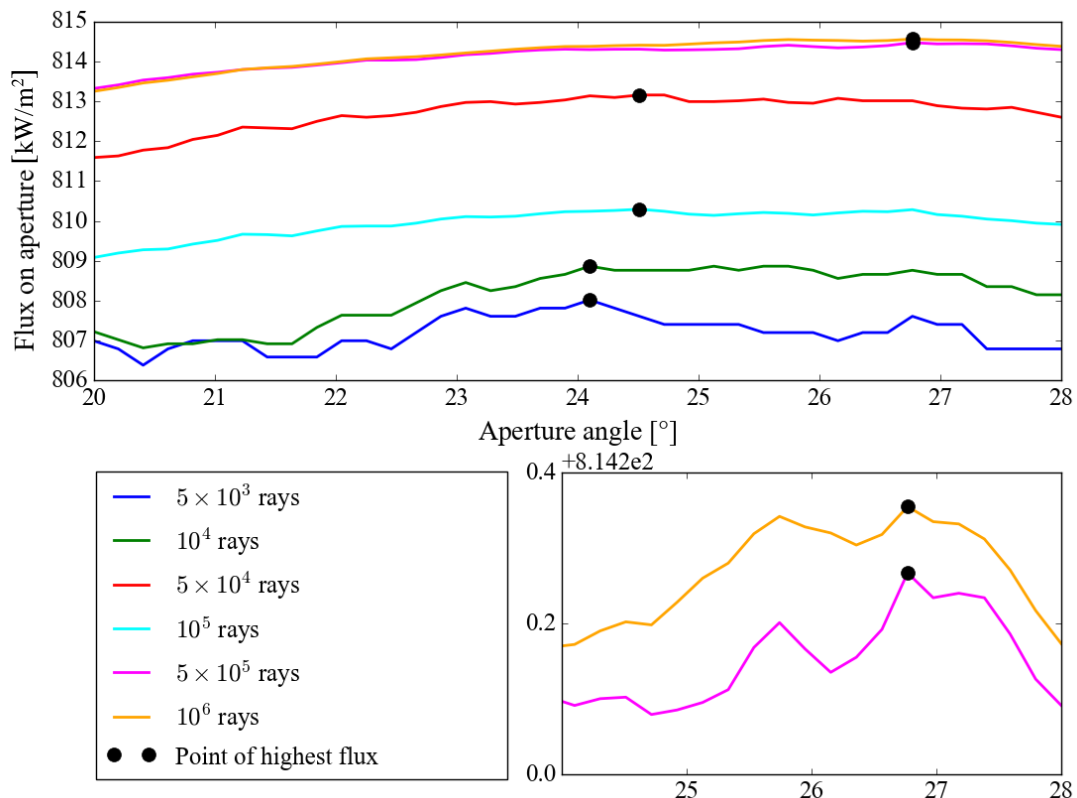


**Figure 5.3:** The aperture flux as a function of the aperture angle is graphically displayed for different ray counts, with the maximum flux on the aperture also accentuated. A close-up of the two most accurate trends is displayed in the bottom right frame.

When one considers the results displayed in the graphic representation in Figure 5.3, one can note that an increase in rays reduces the discontinuous jagged fluctuations, as noted in a previous study (refer to Chapter 4.2.2). It is also noticeable that an increase in the number of rays used converges the profile to a single line, which is especially visible with the  $5 \times 10^5$  and  $10^6$  rays' profiles. This was to be expected, since the ray independence study showed that convergence was reached from  $5 \times 10^5$  rays upwards. At first glance, one would also assume that the profile has reached a point of continuity (no jagged fluctuations) at  $10^6$  rays, but when one considers the close-up of the profile at its peak (displayed in Figure 5.3 in the bottom right frame), it becomes clear that the profile has not reached continuity. This could provide problems for the optimisation techniques, since small fluctuations could provide other local maximum points, which are clearly visible in the close-up frame with both profiles having an alternative local maximum point approximately  $1^\circ$  from the absolute maximum. The fluctuation or noise could be avoided by constructing a response surface or surrogate (a smooth approximation function of the results) and using the response surface to further obtain the optimal aperture angle.

After obtaining the simulation results, it was decided to fit a polynomial response surface through the data obtained. The polynomial orders were decided on by taking the norm of the difference between the response surface data and the actual data. For more information, refer to Appendix D. The response

surface obtained is illustrated in Figure 5.4, which is plotted against the actual data points obtained with the simulations.

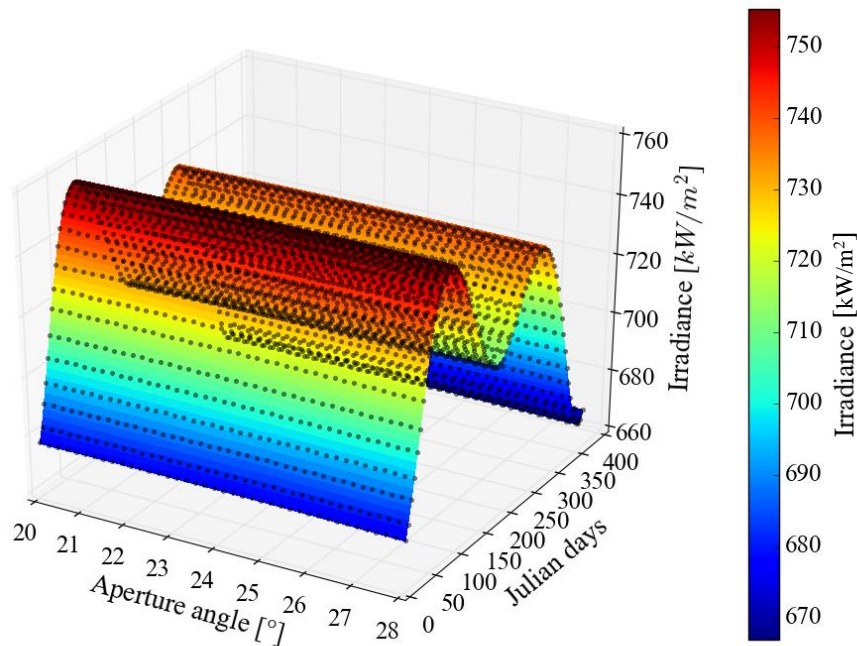


**Figure 5.4:** Graphic illustration of the actual data obtained for the average aperture flux (irradiance) for different angles on different days of the year (illustrated with dots) plotted with the response surface polynomial function approximation.

From the response surface depicted in Figure 5.4, it is clear that the irradiance influence is significantly greater on the axis that represents the days of the year than on the aperture angle axis. It is also for this reason that a good high-order approximation was needed for both axes to represent the data well on both axes. The optimisation procedure was done using both the response surface and the actual data, and then comparing them to one another. The optimum angle was calculated for a given day, giving an idea of how the optimum angle changes throughout the year. The optimum angle for the entire year was also calculated by averaging the flux on the aperture for a given angle throughout the year. The results of this test are summarised in Figure 5.5.

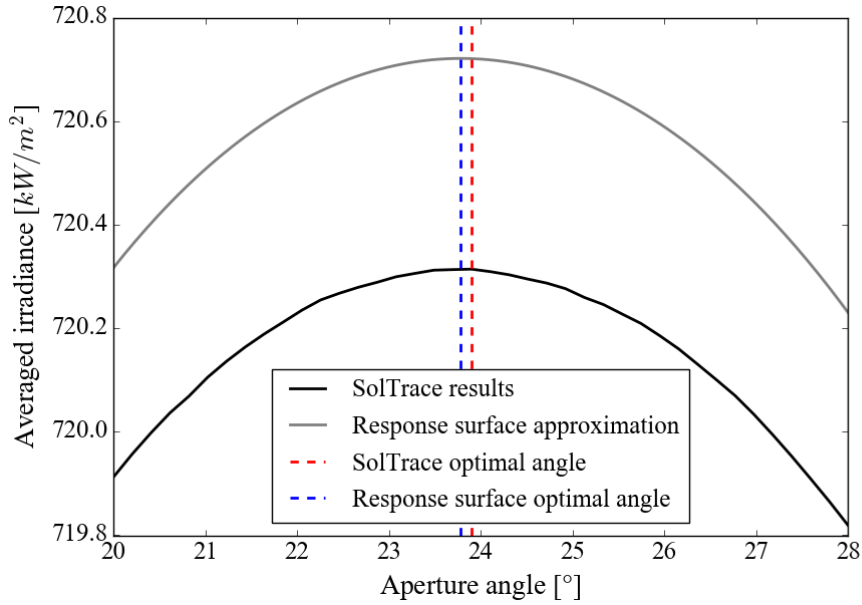


**Figure 5.5:** The average irradiance on the aperture throughout the year as a function of the aperture angle, as calculated using the actual data and the response surface polynomial approximation function.

From the results shown in Figure 5.5 it is noteworthy that the curvature of both the response surface approach and an analysis of the actual data are very similar, although the magnitude of the two approaches vary slightly. The optimal angle for both approaches is also very similar, with the response surface approach estimating the optimal angle slightly lower with a value of  $23.78^\circ$ , while the raw data approach gives a value of  $23.90^\circ$ . As mentioned earlier, the optimal angle for a given day was also calculated. This can be seen in Figure 5.6.

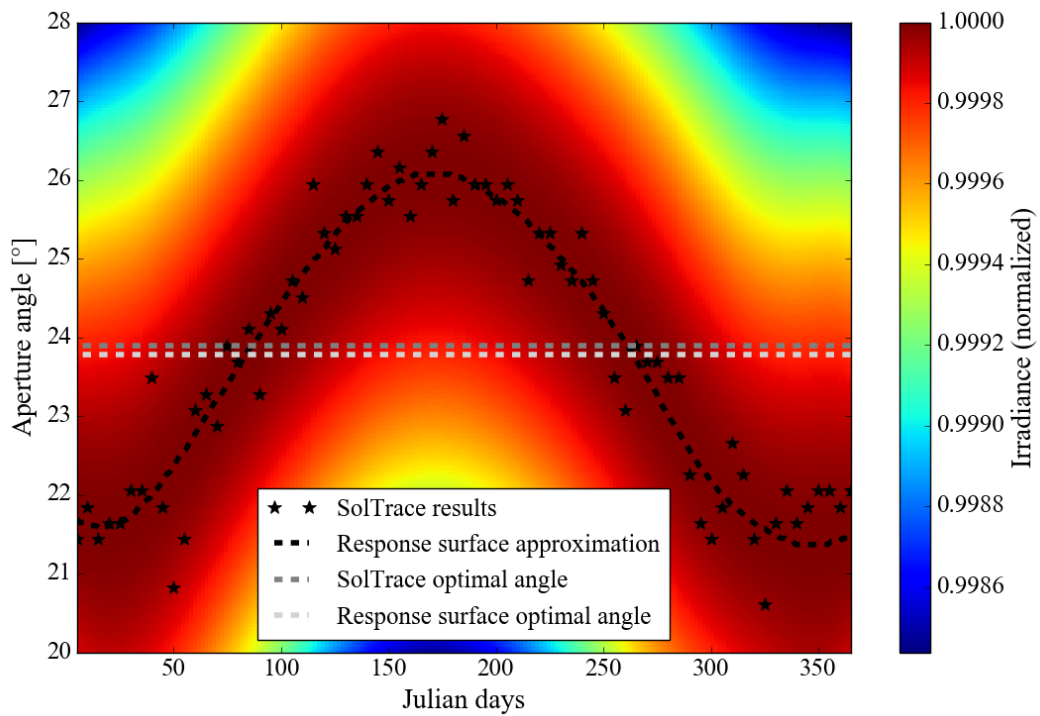


**Figure 5.6:** The optimum aperture angle as a function of the days of the year as estimated by the response surface technique and the raw data. This is displayed with the normalised irradiance incident on the aperture plotted in the background.

The results displayed in Figure 5.6 are plotted with the normalised irradiance incident on the aperture displayed in the background using a colour distribution. The irradiance was only normalised in one direction, meaning that only the maximum irradiance of a given day was used to normalise the flux of that day, therefore only illustrating the influence of the aperture angle throughout the year by excluding the daily factors such as solar positioning and DNI flux.

The results show a fluctuation of the optimum aperture angle from around 21.5° close to the winter solstice to about 26° around and on the summer solstice. If one compares the results of the raw data to the response surface results, one can see that there is a definite good correlation between the two results, although the results may differ up to almost 2° at some points. As explained earlier, this has to do with the fluctuations that the Monte Carlo method produces when a limited number of rays is used to simulate the model. It is predicted that an increase in the ray count would bring the raw data closer to the response surface optimum angle, and that the response surface would not alter significantly. This prediction can be justified by the fact that a ray independence study was conducted, which showed that the results do not change significantly when one uses a higher ray count.

As mentioned earlier, the optimal fixed angle using the MCRT approach with the response surface is 23.78°, while it is 23.90° with the actual data. This is almost double the proposed angle of 11.5° to 12.5° (refer to Table 3.3). It is, however, much closer to the geometrical optimal angle of 25.19°. The angle calculated with the MCRT approach can be assumed to be much more accurate than the first-order geometrical approach, since the MCRT approach considers many more factors than the geometrical approach. By extrapolating the response surface polynomial approximation, one can predict the results for other angles. This was done to estimate the average aperture flux for the aperture at the proposed 12°. There seems to be a 0.81% increase in the average aperture flux over an entire year cycle by changing the aperture angle from the proposed angle to the optimal angle.

### 5.2.2 Field-to-aperture analysis

With the optimal angle for the aperture obtained, it has been decided to use the optimal angle as the angle for further analyses. The receiver aperture will therefore be positioned at a rounded angle value of 24° relative to the horizon. For the aperture analysis and all other analyses on the receiver that will be conducted, the solar rays reflected by the solar field will be aimed at a singular point. An important factor to consider when analysing the receiver's performance is to consider the efficiency at which the rays are redirected from the field and captured. By again analysing every 5<sup>th</sup> day of the year for two-hour intervals from 08:00 to 16:00 LAT, the fraction of the rays hitting the solar field to the reflected rays incident on the aperture has been calculated. This results in a year-averaged field-to-aperture efficiency of 86.0%. This value was expected, as the heliostats already absorb 12% of the rays (refer to Table 3.3 'Heliostat properties'). The remaining 2% can be due to the blocking and shading of the heliostats and a small fraction of the rays being lost due to aperture spillage (although analyses have shown this to be negligible). The field-to-aperture efficiency is the ratio of irradiance incident on the field ( $G_{field}$ ) to the irradiance ending at the aperture ( $G_{aperture}$ ), or:

$$\eta_{field-to-apert.} = \frac{G_{field}}{G_{aperture}} \quad (5-3)$$

The losses involved with the field-to-aperture efficiency would mainly include the absorption, misdirection (which causes spillage), blocking or shading of the heliostats.

It has been noted that the year-averaged field-to-aperture efficiency calculated only considers solar noon for every day analysed. A big difference in efficiencies could therefore be obtained when considering

the remaining hours of incident light in a day. It has also been noted that the aperture size may also influence the result, and was also not considered. These may have brought with it misrepresented results.

### 5.2.3 Aperture analysis

It is important to analyse the distribution of the solar flux incident on the aperture since the distribution can provide perspective on how widely distributed the flux is when only concentrated on a singular point, and how the shape of the distribution can help to improve the design of receiver apertures. A quick analysis of the aperture flux distribution for different hours on different days of the year shows a significant change in the flux shape. The sensitivity of the change in shape is especially great for different times of the day compared to different days of the year. Figure 5.7 shows the aperture flux distribution for different times of the day. Although not clearly visible in the images, it shows shape change throughout the day, with the morning hours producing a flux skewed to the left. As the day progresses, the angle turns to the right. As expected, the intensity of the flux also increases until noon, after which it decreases again.

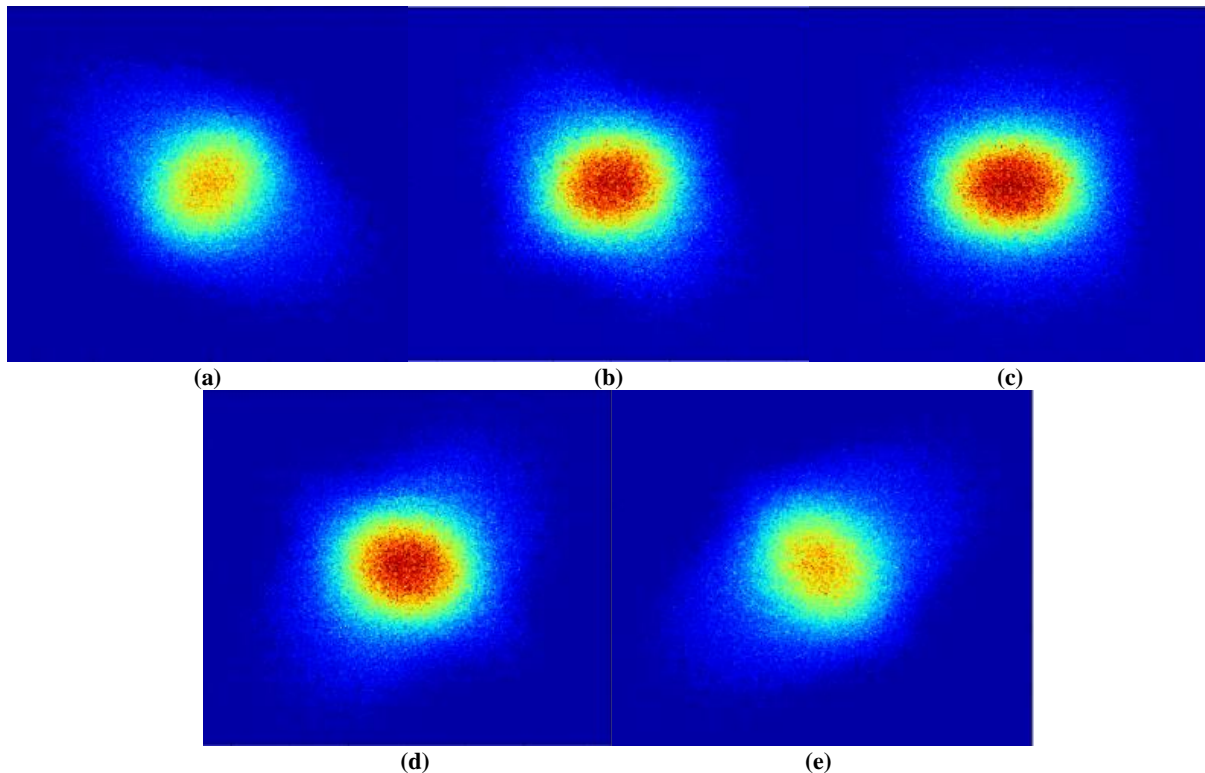


**Figure 5.7: Solar flux distribution on the aperture of the PS-10 heliostat field constructed in Seville, Spain, using SolTrace MCRT for the 180<sup>th</sup> Julian Day at hours: (a): 08:00 LAT; (b): 10:00 LAT; (c): 12:00 LAT; (d): 14:00 LAT; and (e): 16:00 LAT.**

To get the most out of a predefined heliostat field, a receiver needs to capture most of the available rays that are concentrated onto the tower. To analyse the flux shapes of different times of the year and to see what contribution a shape has on the overall flux, it was decided to analyse the aperture flux for every 5<sup>th</sup> day of the year, starting on the 5<sup>th</sup> Julian Day and ending on the 365<sup>th</sup> Julian Day (Julian description is given in Appendix A) for hours between 08:00 LAT and 16:00 LAT at two-hour intervals. The fluxes obtained would then be added together and divided by the number of contributions. One can then see the average flux throughout the year, and the shape of the flux for which the receiver can be designed. The average solar irradiance on the aperture over an entire year is illustrated with a colour map in Figure 5.8.

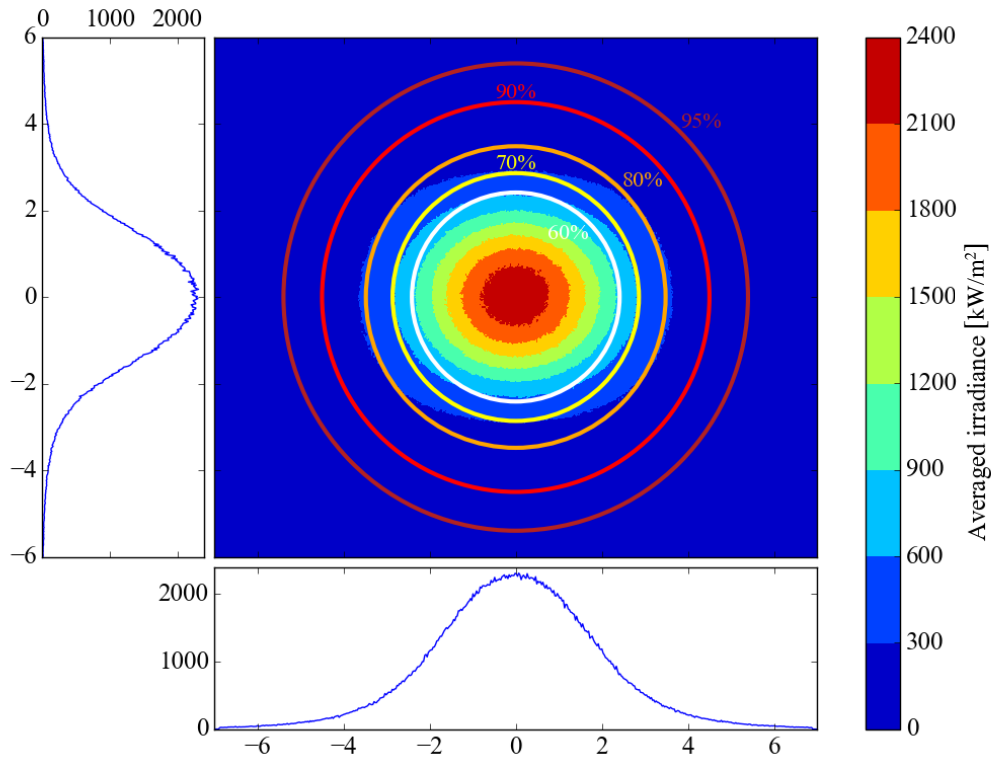


**Figure 5.8: The average aperture flux distribution over an entire year at different times of the day, displayed with circles illustrating the percentage flux of the current PS-10 central receiver aperture that is within the circle. Plots on the side show the flux distribution at the central axes.**

The aperture flux displayed in Figure 5.8 confirms the expected bell curve (almost Gaussian-like) distribution that is incident on the aperture, correlating well with the 12:00 LAT distribution. The flux distribution is not skewed in a certain direction, but is rather symmetric in all directions. The flux is, however, not entirely concentric from the centre, which is evident with the circles plotted over the flux distribution, which point this out. There seems to be more of a horizontal than a vertical flux distribution. Should one be limited to a fixed aperture area, it would make more sense to have an aperture with a larger width compared to the height of the aperture. The proposed receiver design for this research is limited to a circular aperture. Therefore, the analysis conducted will only consider the flux that falls within a circular region from the centre.

Apart from the flux distribution, Figure 5.8 also displays concentric circles from the centre of the aperture, which is also the focal point of the heliostat field. Each circle is labelled with a percentage. This percentage value is the incident irradiance that falls within the circle relative to the total flux that falls on the proposed aperture of the PS-10 central receiver system (the full aperture is the full display of the image). The relation between the percentage flux and the radius is graphically displayed in Figure 5.9.

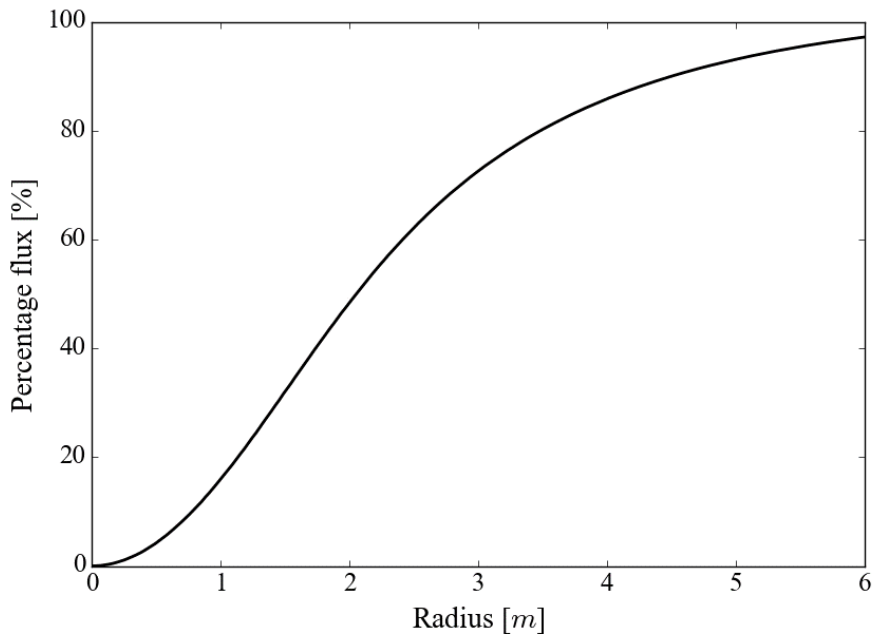


**Figure 5.9:** The percentage flux that is captured within a circular aperture as a function of the radius for the aperture analysis.

From the graph depicted in Figure 5.9, one can see a clear, smooth trend of the percentage flux as a function of the radius, showing a rapid increase in the percentage flux for small radius values, but it slowly curves along the seeming asymptote, which is the 100% mark. This indicates that if one would want to capture almost all the rays that are incident, one would have to construct an unrealistically large aperture. One would therefore need to determine what is feasible or what percentage flux one is willing to leave out. This problem can extend to apertures with different forms and sizes, as well as cost analysis versus efficiency, but that does not fall within the scope of the research conducted in the dissertation. The author decided to capture 90% of the incident radiation on the original aperture, which equals the radius of the inflated receiver aperture (discussed in the following subsection), which is roughly 4.5 m. Take note that the inflated receiver design is merely considered to provide a comparison and was not presented with trade-off evaluations.

### 5.3 Receiver optical analysis

With the aperture analyses concluded, the focus can shift towards the receiver to be tested. The original design is described in Chapter 2.6 and is displayed in Figure 2.32. It is also included, with dimensions, in Appendix F (the inflated design is not included). From the analysis done in Chapter 5.2.3, an alternative design with a 9 m aperture diameter is considered to increase the penetration of incident radiation to acceptable levels. When compared to the original design, which has an aperture diameter of about 2 m, it is clear that the original design should either be inflated to accommodate a higher flux with a bigger aperture diameter, or the fly eye concept discussed in Chapter 2.3.4 and illustrated in Figure 2.29 should be considered. The difference in dimensions between the original and the inflated receiver is illustrated in Figure 5.10b (illustrated to scale), the inflated design scaled up to 9/2 of the original design. For the analysis of the receiver, these two concepts will be considered, with both designs tested with their apertures positioned at the centre of the aiming point. Take note that the aperture refers to the smallest opening of the design, since initial analyses conducted on the design have shown that the rim around the aperture does not significantly increase the number of rays that enter the receiver. It is therefore excluded in the further analyses. The excluded rim that is described is illustrated as the highlighted region in Figure 5.10a.

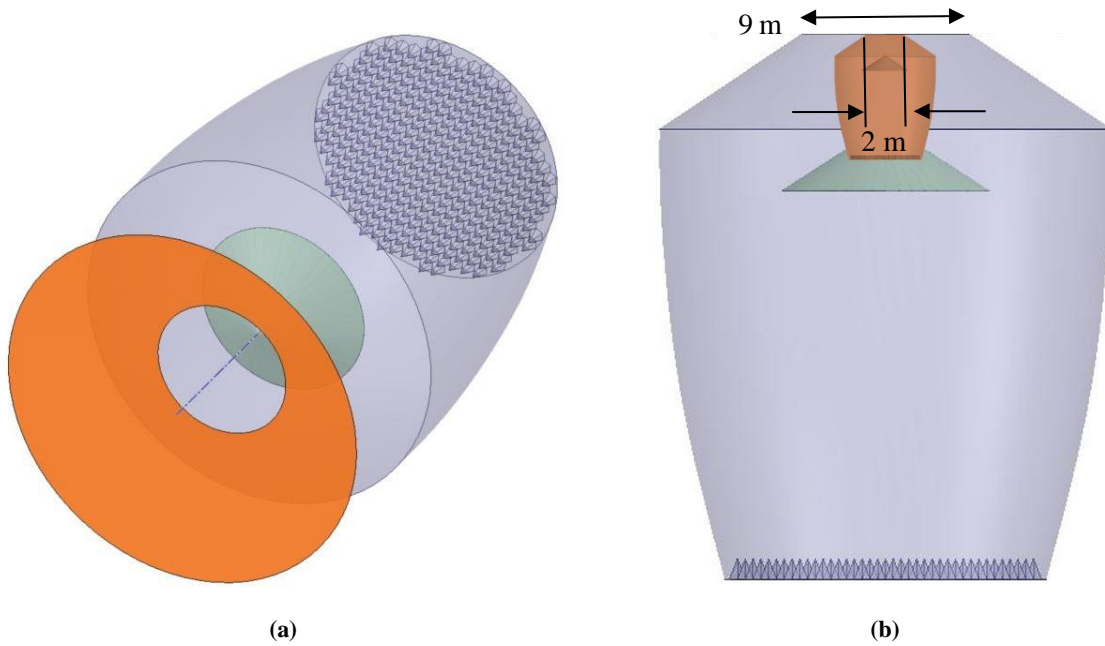
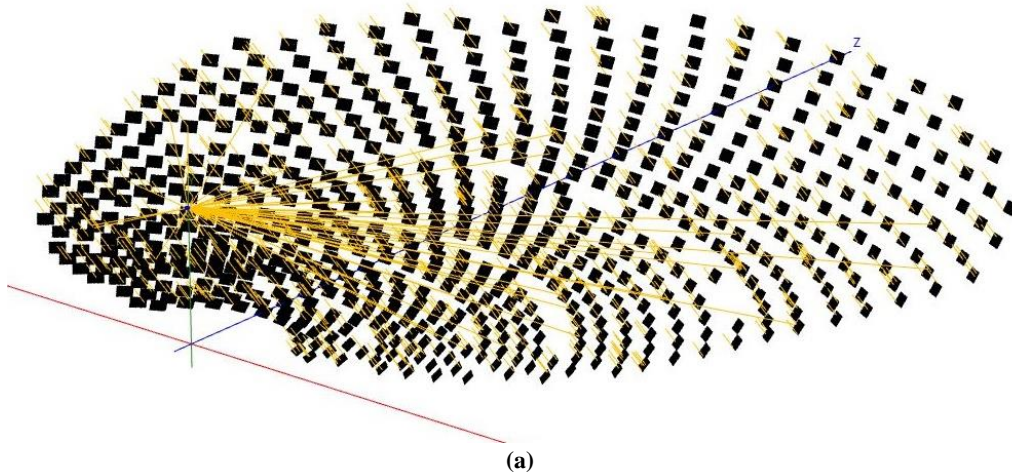


Figure 5.10: (a): The receiver design with the highlighted region displaying the part of the design that was excluded during the analyses; and (b): the original (highlighted) and the inflated receiver compared to each other.

The apertures will be tested with the same setup as for the aperture analysis. The only difference is that the time of the analysis will be fixed to 12:00 LAT during an equinox, since the average aperture flux distribution of an entire year gives a similar flux distribution as one would get on an equinox day at noon. The model, as simulated in SolTrace, is displayed in Figure 5.11.



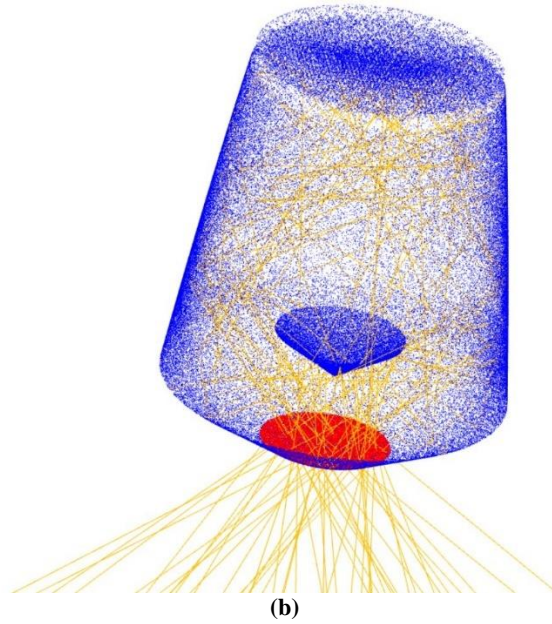


Figure 5.11: (a): The PS-10 heliostat field with (b): the original receiver modelled in SolTrace v.3.0.0.

The receiver is made up of the secondary reflector area that reflects the incident solar rays, and the absorber area that absorbs the flux. Therefore, two sets of optical properties were given for the receiver: an absorptive optical property, which was given to the absorber area that includes the pyramid array, and the neighbouring end plate on which the pyramids are mounted and a reflective optical property for the remaining surfaces. The values for the absorptive surface are similar to that of the Solar Two receiver (Pacheco et al., 2002), while the reflectivity assigned to the reflective surface is a value standard for high quality mirrors (Butel, et al., 2011). This is summarised in Table 5.1.

Table 5.1: Optical properties of the absorptive and reflective surfaces of the proposed receiver

	Reflectivity	Transmissivity	Slope error	Specularity error
<b>Absorptive</b>	0.05	0	0.95	0.2
<b>Reflective</b>	0.95	0	0.71	0.14

A ray independence study was conducted for both models. As expected, the number of rays needed for the original model was greater than for the inflated model. This is due to fewer rays entering the small aperture of the original receiver compared to the inflated receiver. Therefore, more rays need to be simulated to obtain a flux profile that is sufficient. The ray independence graphs for both models are displayed in Figure 5.12. From the ray independence study, a minimal fluctuation from the median of 0.045% is experienced in results from  $30 \times 10^6$  rays onwards for the original receiver design and a 0.021% fluctuation in results for the inflated receiver from  $20 \times 10^6$  rays onwards. These fluctuation margins are displayed by the dotted red lines in Figure 5.12.

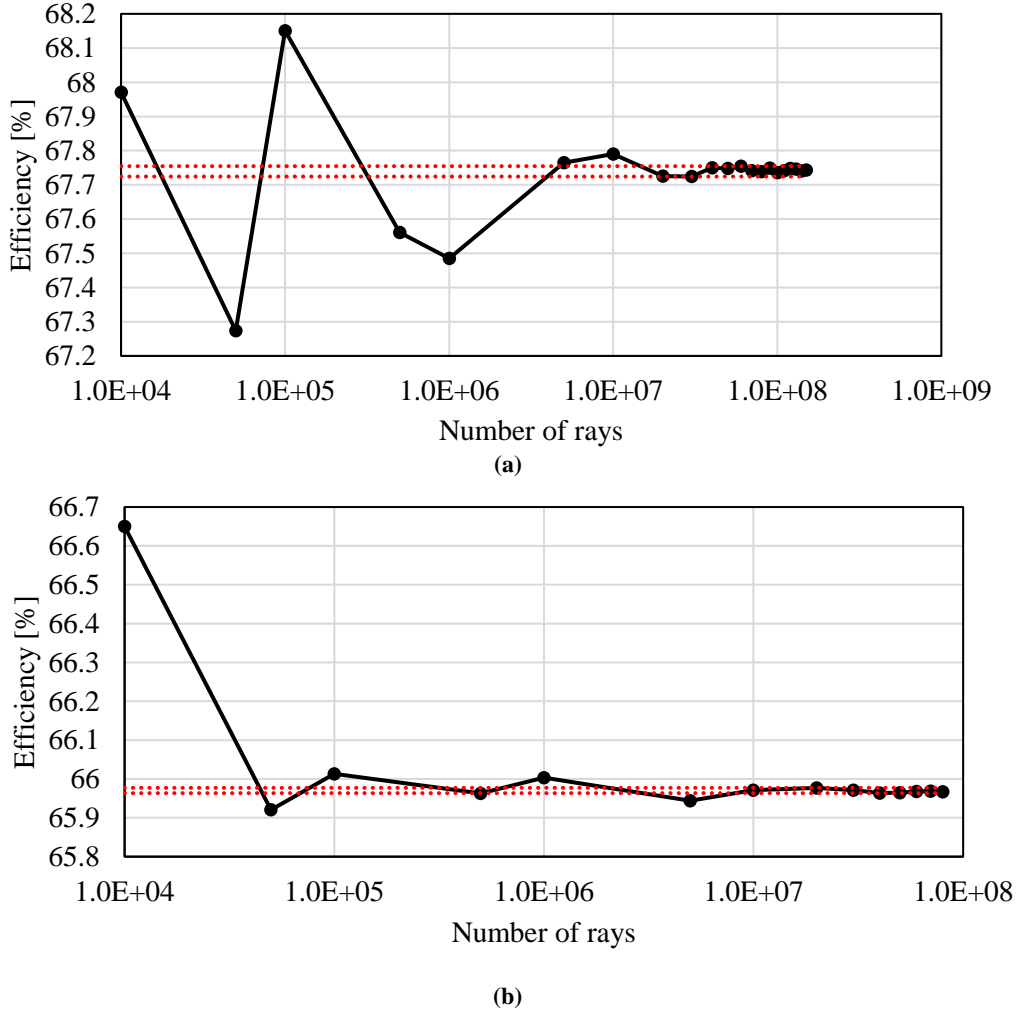


**Figure 5.12: The ray independency study for: (a): the original receiver design; and (b): the inflated receiver design.**

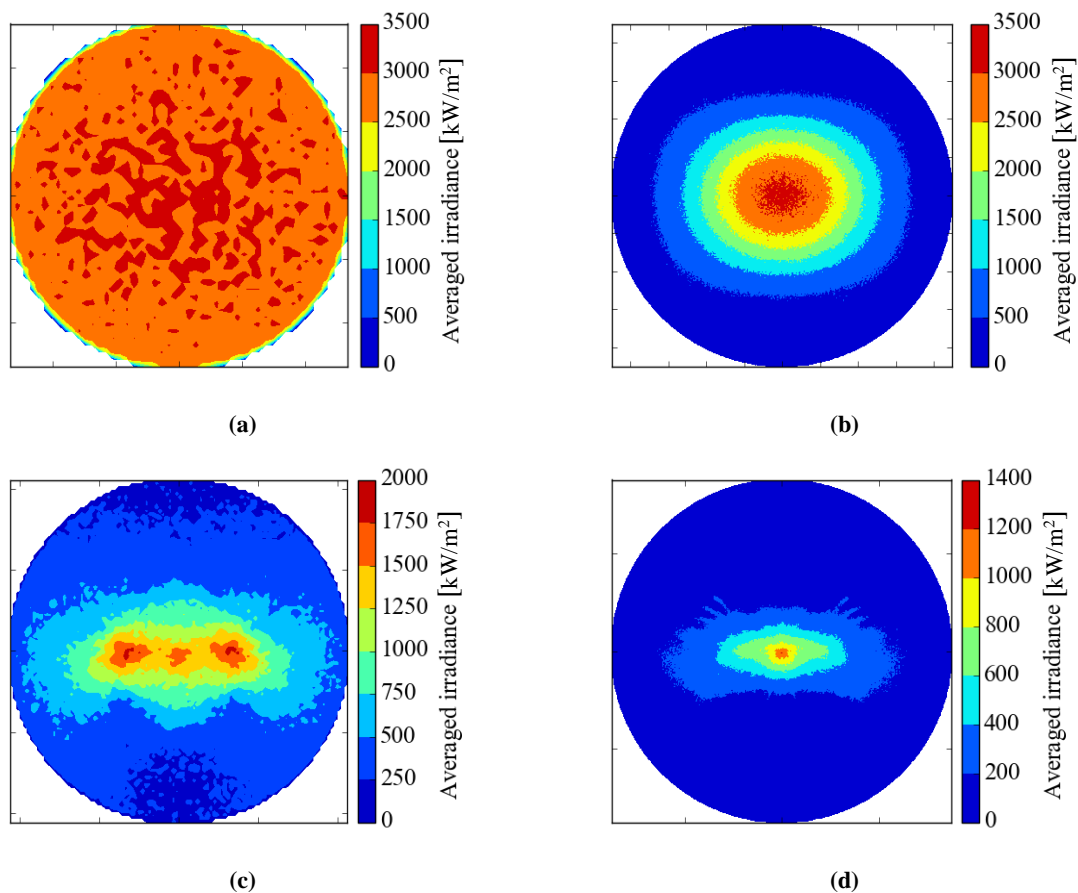
The displayed results also show that there is a minimal difference in optical aperture-to-absorber efficiency for both receivers (original receiver = 67.7%; inflated receiver = 66%), indicating that the difference in flux shape does not affect the receiver’s efficiency much. The researcher checked to see whether the collector cone situated at the opening of the receiver had a significant effect on the receiver’s performance. For the original receiver design, the aperture-to-absorber efficiency would increase to 87% if one neglected the cone. Future studies should therefore investigate the contribution that such a “cap” has on hindering the re-radiation and convection losses and how a “cap” like this cone can be designed and integrated to improve the receiver efficiencies. Take note that the aperture-to-absorber efficiency (also called the solar collection efficiency) refers to the ratio of rays that hit the absorber to the rays that enter the aperture, and is presented in the following equation.

$$\eta_{apert.-to-abs.} = \frac{\dot{Q}_{absorber}}{\dot{Q}_{aperture}} \tag{5-4}$$

The losses involved with the aperture-to-absorber efficiency would mainly include the absorption or misdirection of the secondary reflector.

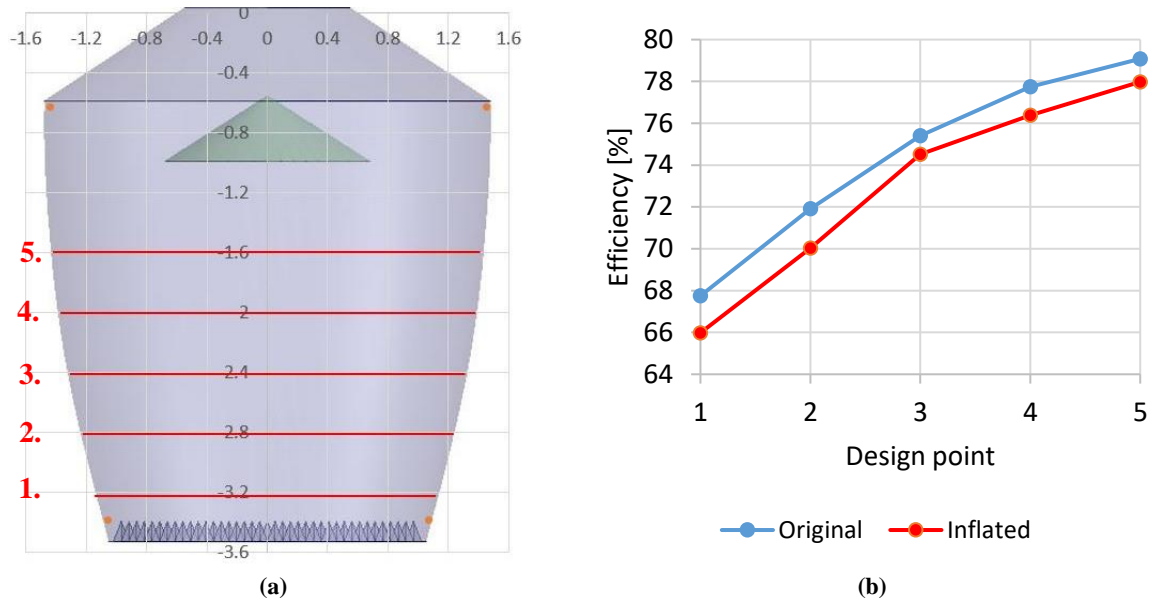
The idea of the proposed design’s shape was partly to provide a well-distributed absorber surface flux distribution. It is therefore important to analyse the flux distribution for the original design and the inflated receiver design. Depicted in Figure 5.13a and Figure 5.13b is the flux distribution on the

apertures of the two receivers. As expected, the flux distribution of the aperture on the inflated receiver looks similar to the annual average aperture flux distribution shown in Figure 5.8, while the flux distribution on the smaller original receiver is an almost evenly distributed flux that develops at the centre of the aiming point. Two very different absorber flux distributions develop from these two different aperture flux distributions (see Figure 5.13c and Figure 5.13d). Take note that these figures that are presented do not host the same plot range. The original receiver's absorber flux distribution shows a much better distributed flux compared to the inflated receiver design, although none of the two show near-perfect flux distributions, with the gradient from the high to low flux patches being too great. A study on the shape of the receiver needs to be conducted in the future to determine how it can reflect the incoming rays so as to capture the reflection better, and also to distribute the flux better onto the absorber surface.



**Figure 5.13: (a) and (b): The aperture's flux distributions of the original and inflated receiver design; and (c) and (d): flux distributions above the absorber surface of the original and inflated receiver design.**

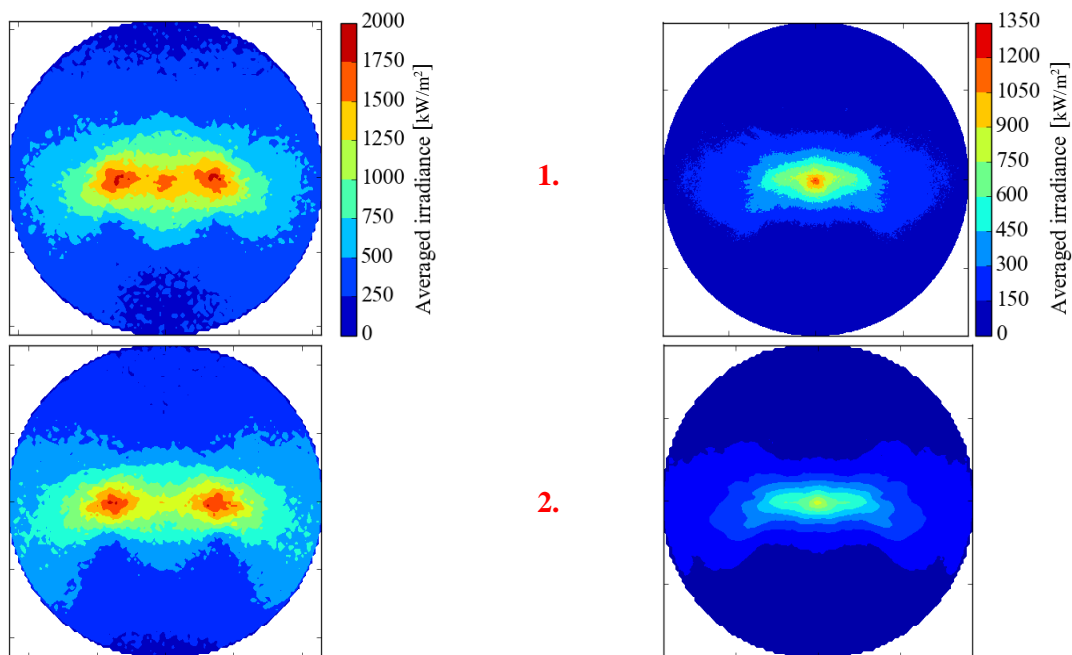
A sensitivity study was conducted to understand the effect that the position of the absorber from the aperture opening has on the absorber's flux distribution. The absorber's position was tested in fixed increments from above the position of the original absorber to near the ray-deflecting cone. The considered positions are displayed in Figure 5.14a, and were repeated for the inflated design as well.



**Figure 5.14:** (a): The original receiver design with a dimensional grid (units in metres), displaying the different positions of the absorber (in red) to be analysed; and (b): a graphic representation of the change in efficiency for the different positions of the absorber.

While conducting the study, a dramatic change in the aperture-to-absorber efficiency was noted, with the efficiency increasing as it is positioned closer to the aperture (refer to Figure 5.14b). The increase in efficiency was expected, although the magnitude of increase was surprising (an increase of 11% to 12% was recorded between design points 1 and 5). It is clear from the results obtained that a multitude of ray reflections occurs before finally reaching the absorber, since 5% (refer to Table 5.1) of the light's energy is lost for every reflection that occurs. For the design to obtain optimal efficiency, its shape should change as such to facilitate a minimal number of reflections before reaching the absorber.

As mentioned earlier, the importance of a well and equally distributed flux on the absorber cannot be understated. The absorber flux distribution was investigated for the different design points. These distributions are illustrated in Figure 5.15.



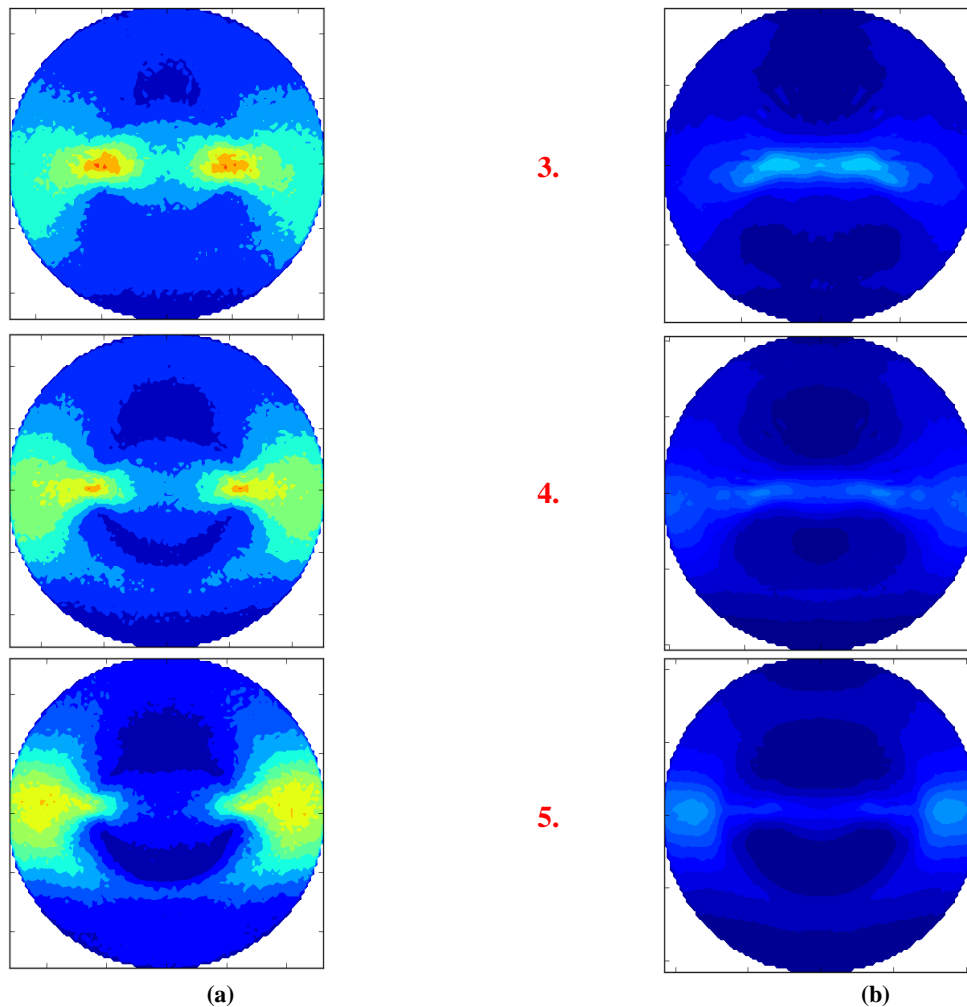


Figure 5.15: The flux distribution of the absorber for different design points for: (a) the original design; and (b): the inflated receiver design for design points 1 to 5 (displayed from top to bottom). The vertical axis represents the dimensions in the vertical direction, parallel with the tower. The axes are scaled equally. For the dimensions, refer to Figure 5.14(a) for (a) and the 9/2 the scale of the original design for (b).

The most noticeable when analysing the results displayed in Figure 5.15 is the fact that the flux per square metre decreases as the distance between the aperture and the absorber decreases. The most probable reason would be that the design's collector circumference increases closer to the aperture area, therefore an increased absorber area is obtained as the absorber gets closer to the aperture, which in return lowers the flux per square meter. There is also a slight asymmetry seen with the flux. This is the nature of MCRT, with the results being more probabilistic. This asymmetry reduces with more rays or larger bin areas. The lower irradiance is not ideal for the design, since a low flux would generally result in a lower temperature for power production, which would decrease the overall efficiency of the plant. Alternatively, the flow in the absorber can be reduced to increase the temperature, but this will reduce the rate of energy production. The increase in efficiency by shifting the absorber closer to the aperture would therefore not necessarily be beneficial for the design's efficiency.

#### 5.4 Detailed absorber flux distribution

With the flux distribution on the absorber surface analysed, it is clear that the distribution is not evenly distributed, even after some alterations were considered. It was, however, decided to consider an appropriate location that is representative for a flux on a single pyramid element in the absorber's array. The pyramid element is symmetrical in design, and the thermal analysis will use this symmetry to simplify the analysis. It is therefore preferable to choose a location that shows symmetrical flux. It is

with this line of thought that the centre of the absorber of the original receiver design (indicated with the pink and green triangle in Figure 5.17) was chosen as the location of the pyramid element that would be analysed.

#### 5.4.1 Single absorber element flux analysis

By applying the model of discretising the absorber surface that was modelled and meshed within the ANSYS environment, and then reconstructed in SolTrace by using primitive elements (for more information regarding the procedure, refer to Chapter 4.2.1), a flux is produced on the absorber surface that can be used for further thermal analysis. To ensure that a detailed flux profile is constructed with the MCRT method, the number of simulated rays was increased until a smooth flux distribution was obtained on one of the sides of the pyramid element using a single element for one side of the pyramid element's surface, with the number of rays eventually reaching  $3.54 \times 10^9$ . This number was used as a benchmark, and it was decided to compare this profile obtained from the single element with a meshed surface to check whether the number of elements used to discretise the surface would be sufficient to capture the flux profile on the pyramid. The number of rays for the meshed surface was also increased to  $4.5 \times 10^9$  to ensure ray independence. The single element profile and meshed surface profile are displayed in Figure 5.16a and Figure 5.16b, respectively.

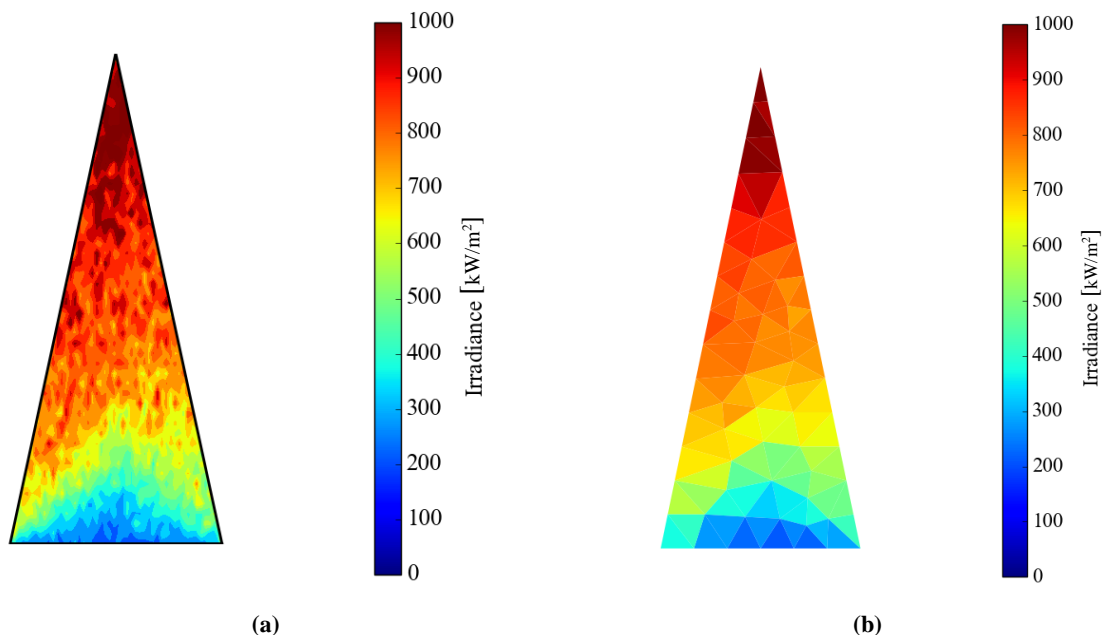


**Figure 5.16: The flux profile on the one side of a pyramid element situated in the centre of the absorber of the original receiver design, with: (a): the  $3.54 \times 10^9$  single element profile; and (b): the  $4.5 \times 10^9$  meshed surface profile, compared with one another.**

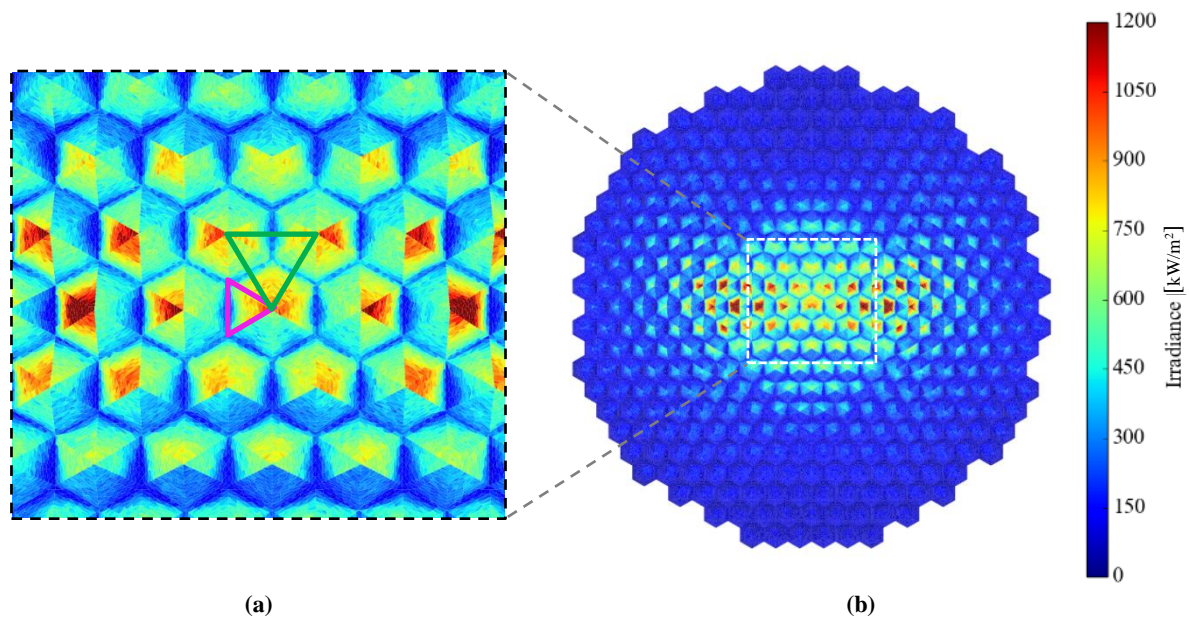
As can be seen in Figure 5.16, when comparing the two profiles with one another, the discretised profile smooths out the irregularities of the profile in Figure 5.16a, which is typical for MCRT results. It is interesting to note that, although the flux profile is relatively constant when plotted onto a flat surface situated right above the pyramid elements, the flux profile changes dramatically on the pyramid surface. It is clear that the tip captures the highest concentration of heat flux, and as one moves towards the “base” of the pyramid, the flux reduces by a factor of four compared to the tip of the pyramid element. It is evident that the majority of the rays that reach the absorber surface enter at an angle, which is captured by the tips of the pyramid elements, therefore causing less flux to reach the “valleys” between the pyramid elements. Take note that the flux profile excludes the re-radiation received from other neighbouring pyramid surfaces (to be evaluated using CFD later).

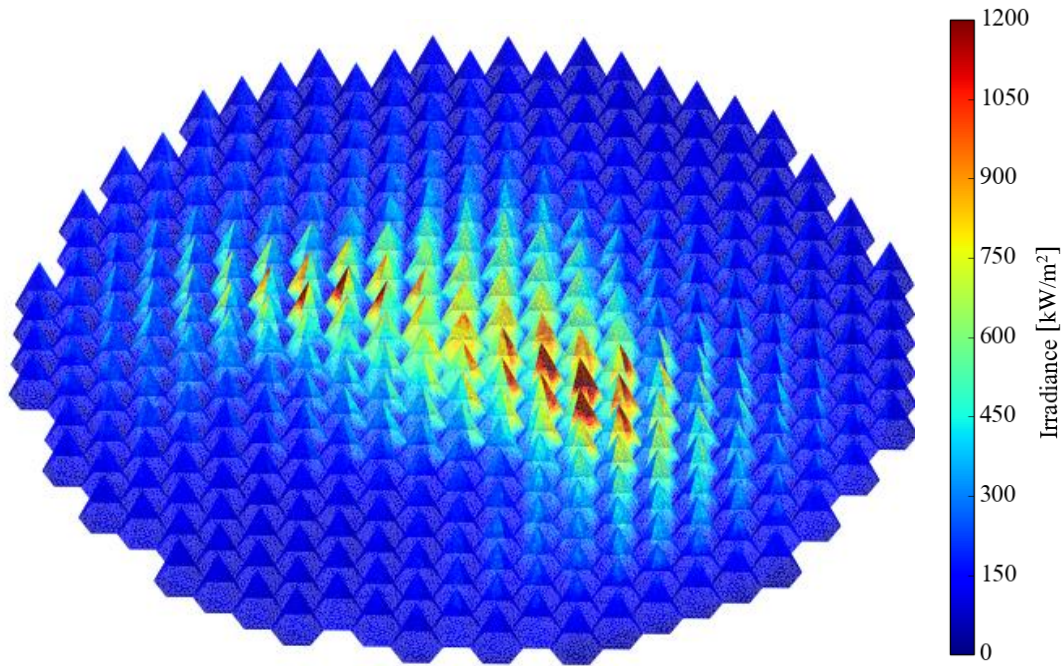
If one would like to get a more detailed profile of the flux for the thermal analysis, one would need to reduce the element size, which would cause the surface to be divided into more discretised elements that can capture more detail. This profile is, however, sufficient for the thermal analysis to be conducted. The centroid of every discretised irregular triangle (Figure 5.16b) is used as the location of the averaged flux on that triangle, which could then be used in an interpolation file for the thermal analysis.

Take note that, with the discretisation of a complex geometry method, one would usually do an element-size independency test to ensure that the element size is adequate for the accuracy of the results. This is, however, only needed for geometries with curved surfaces, since the primitive elements are flat surfaces that approximate complex curvatures. Since the proposed receiver's absorber surface consists of hexagonal pyramids with flat surfaces, it is redundant to do an element size independency study for the absorber surface. The number of triangles should also be sufficient to capture the expected flux variation that is shown in Figure 5.16 to be sufficient for the chosen element size.

### 5.4.2 Full absorber flux analysis

With an understanding of the flux on a single face of a single pyramid element, the entire absorber surface was discretised and put through the same process as the single element face. Since the model consists of a large number of discretised primitive elements and since the flux distribution on the entire absorber surface is only for illustration purposes, the number of rays used was reduced to  $0.64 \times 10^9$ . This resulted in the following flux distribution image on the absorber area of the receiver.





(c)

**Figure 5.17:** A detailed flux distribution on the absorber surface of the receiver, with the pink triangle indicating the detailed flux distribution of the element surface that is displayed in Figure 5.16, and the green triangle indicating the flux area to be used as heat source: (a): a zoomed-in image of the flux profile at the centre; (b): the entire absorber surface area; and (c): a detailed 3D illustration of the flux distribution on the absorber surface.

As was noted with the analysis of the absorber element face, high flux values are captured by the tip of the pyramid, causing low flux values at the trenches between the pyramid elements. It is also clear that the flux that strikes a pyramid in general has an asymmetric flux distribution.

The asymmetry reduces as one approaches the centre of the absorber surface, although there still seems to be a clearly visible flux asymmetry. When the flux distribution is compared with the flat absorber surface area, as was done in the previous analysis in Chapter 5.3 (refer to Figure 5.13c), the overall flux distribution shape correlates well, although it fails to predict the details such as the flux spikes at the tip of the elements, and does not provide information on how the flux enters the absorber surface area, as this information is of substantial importance when analysing the pyramid element in detail.

### 5.4.3 Flux region for heat source

With the knowledge of the flux distribution on an arbitrary pyramid side, as well as the detailed flux distribution over the entire absorber surface for the proposed receiver, one could make a better-informed decision on which pyramids could be representative for an equally distributed solar flux profile. It was decided to use the location indicated with the green triangle in Figure 5.17a, since it provides the best equally distributed flux on all three sides of the adjacent pyramids. It also provides realistic flux distributions. A detailed flux distribution of this region is displayed in Figure 5.18a. The flux is generated using  $5.91 \times 10^9$  rays. Take note that the SolTrace model involves the entire absorber, with only the provided detailed distribution meshed finer. Therefore, the number of generated rays was necessary to adequately simulate the entire absorber area, and not only the illustrated flux distribution. The number of rays used for the profile was adequate after doing a quick ray independence study using the average flux across the surface as a variable, with the results shown in the graph displayed in Figure 5.18b. The graph clearly shows minor fluctuations as it converges, which indicates that the number of rays used for the analysis is accurate enough.

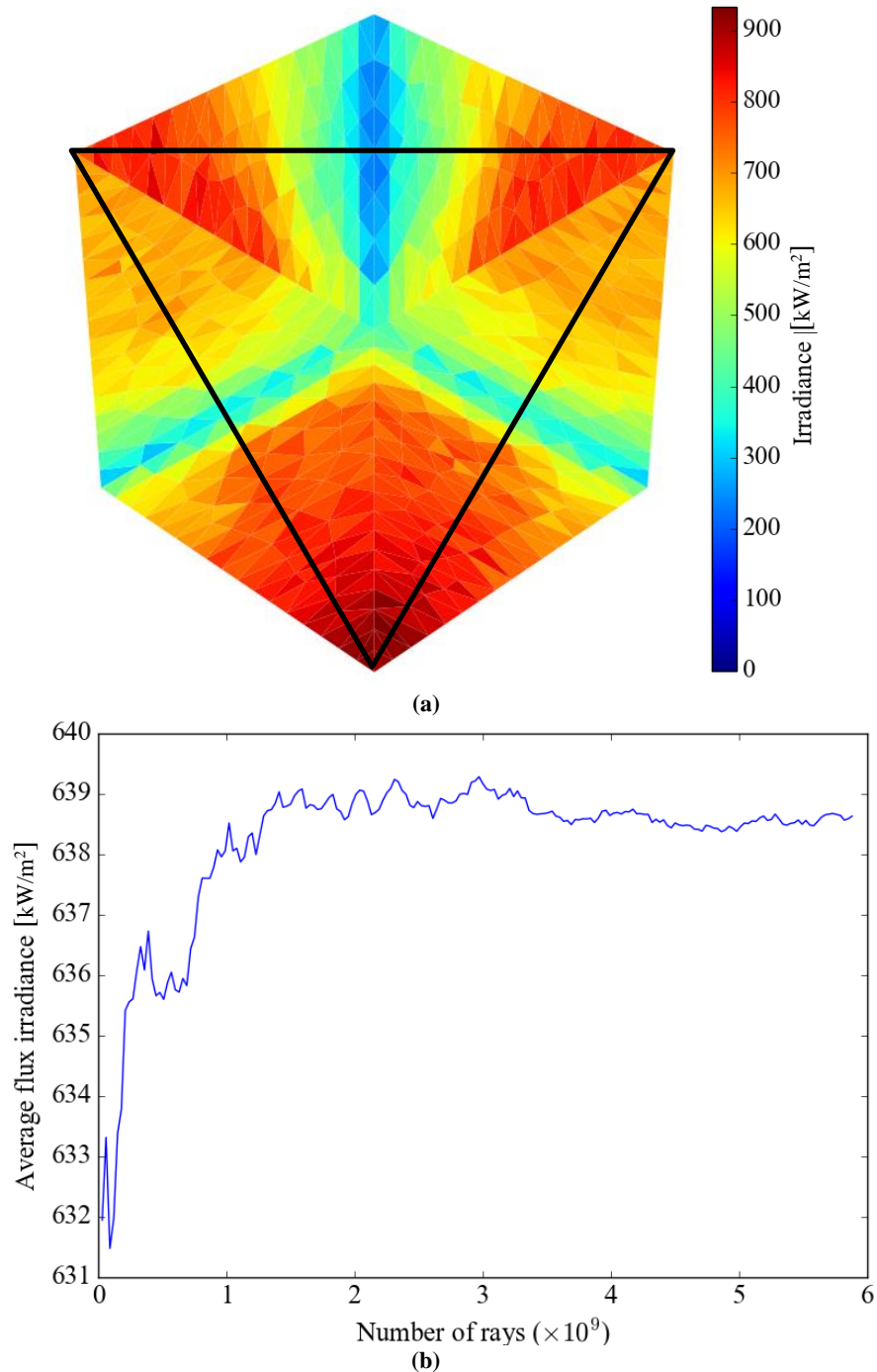


**Figure 5.18:** (a): Detailed flux profile on the pyramid sides, indicated by the green triangle in Figure 5.17a (represented with a black triangle in this figure), generated with MCRT using  $5.91 \times 10^9$  rays; and (b): the ray independence test conducted for the flux profile.

### 5.5 New proposed design for future work

As mentioned earlier, the idea of the original design that was investigated was to have a design that would minimise the losses that one usually finds on other receivers. The analysis, however, has shown that the effort to minimise these losses compromises the solar collection efficiency (aperture-to-absorber efficiency) to such an extent that it makes the original design impractical. For the design to have a better performance, improvements should be made on the optical side. With the author taking inspiration from work done by Timinger et al. (2000) and keeping the absorber surface design the same as the original design, a new design is proposed. Figure 5.19 displays the new design.

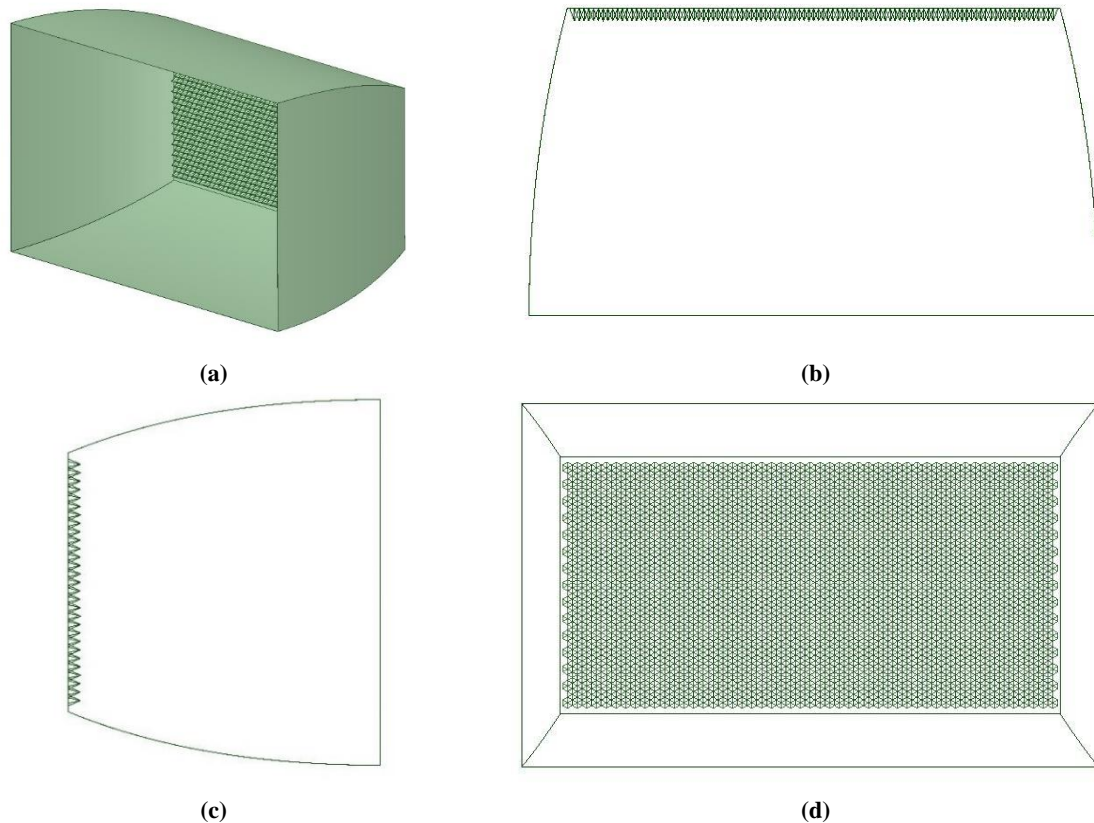


**Figure 5.19: The new optically improved receiver design with: (a): a 3D view; (b): the top view; (c): the side view; and (d): the front view.**

As mentioned by Timinger et al. (2000), secondary receivers that perform the best, according to their research, are a secondary concentrator with a rectangular aperture and a rectangular concentrator outlet, which is the absorber area in this case. By taking this knowledge and applying the curvature of a CPC in two axes, and considering that the maximum shadow line angle (refer to Chapter 2.3.4 for more information) in the vertical direction is  $45^\circ$  for the PS-10 heliostat field, it is found that most of the heliostat field can be spanned within a  $120^\circ$  acceptance angle.

With the current models developed, an optical test was conducted on this new design to determine the optical performance, and how it compares with the other design. The aperture capture efficiency value is calculated to be 79.2% (an efficiency calculated as the percentage flux captured by the aperture compared to the total flux that could be captured if the aperture were infinitely large), which is a value that could be improved on by simply inflating the dimensions of the design, therefore increasing the aperture size. The aperture-to-absorber efficiency calculated to a significantly improved 93.1% when compared with the original design (67.7%). Take note that an external receiver would provide a 100% aperture-to-absorber efficiency, although this provides the drawback of the absorber area being exposed to the elements. When one takes a look at the flux distribution on the absorber (refer to Figure 5.20), the flux is also relatively well distributed, especially when compared to the flux distribution of the original design. The most noteworthy, however, is the fact that not only is the absorber flux average more than double in the case of the new design compared to the original design, but it can also provide this flux distribution more evenly spread over an area of over 15 times larger than the original design. This design also hopes to limit convective losses to a large extent, partly with the cavity that the design provides, while keeping the original absorber surface design with its limited re-radiation losses.

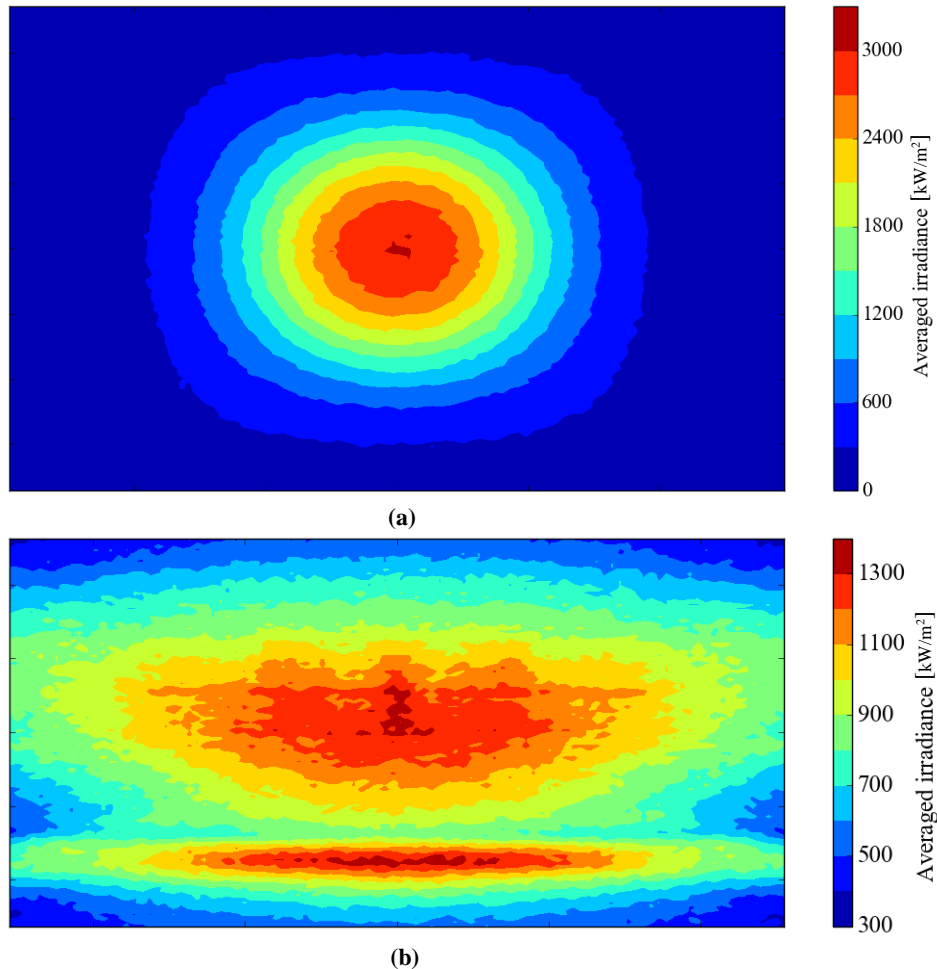


**Figure 5.20: The flux distribution at: (a): the aperture; and (b): the absorber of the author’s new proposed design.**

This new proposed design, although it shows promising preliminary results, needs to be improved in terms of its optical performance to have an even more equally distributed flux on the absorber, compared to the now two hot spots present. Take note that the testing and analysis of this new proposed design falls beyond the scope of this study and should therefore be considered for future study.

## 5.6 Conclusion

The following conclusions can be drawn from this chapter:

- The approach of optimising the aperture angle with the MCRT approach was shown to be a credible means of obtaining an optimal angle for the aperture, although there remains questions regarding the validity of only using the solar noon for the annual evaluation, since the sun’s position on a daily basis fluctuates much more, and could have a substantial contribution to the end results. Atmospheric attenuation was also neglected, which is an assumption that could have a significant influence on the results. The approach’s average result was compared to the cruder geometrical approach, which only considers the relative position of the heliostats to the receiver. The results showed a deviation of 5.4%. This result provides the author with more confidence of the results obtained, although the effect of the rest of the day should also be considered to bring substance to the conclusion. The study to find the optimal aperture angle has shown that it is a function of days, and therefore fluctuates throughout the year. The aperture angle increases to higher angle values compared to the mean, while it decreases during the winter season. This also indicates that the position of the sun plays a role, although small, on the optimal aperture angle. The sensitivity of the

aperture angle was shown to be very low, with a 0.81% improvement in solar flux capture from the original PS-10 aperture angle to the calculated optimal angle, and is therefore negligible. As discussed earlier, the sensitivity on the daily basis should have been considered. A sensitivity analysis on the weighting effect that the DNI has on the result should also have been conducted to illustrate the validity to include DNI as a variable in such analyses.

- Visual comparisons between flux distributions over a day time span compared to the average flux distribution over an entire year have shown that the solar noon flux distribution is the most comparable flux, while the equinoxes proved the best for analyses, since the average flux of the equinoxes is found at noon over an annual analysis. Therefore, to simplify analyses, one could reduce the analysis of the receivers to only one day and time, which is the equinox solar noon, to represent the average performance of an entire year. The equinox solar noon does not, however, represent the DNI flux average over an entire year, and should be incorporated in future analyses.
- The receiver optical analysis has shown the optical performance (absorber-to-aperture efficiency) of the proposed receiver to be 67.7%. When comparing this to the overall receiver efficiencies of other plants, it is clear that this result is much too low for practical applications, despite the design curbing thermal losses. The Solar Two external receiver obtains overall receiver efficiencies of 85.6% to 88% (Pacheco et al., 2002), for instance. Even increasing the size of the receiver does not improve the aperture-to-absorber efficiency. The sensitivity on the absorber position relative to the aperture showed a dramatic increase in the aperture-to-absorber efficiency, with an increase of more than 20%. This indicates that the design still has the potential to improve dramatically in terms of optical design.
- The absorber flux distribution analysis provided insight into the flux distribution on the hexagonal pyramid elements. The flux distribution on a single element has shown that the tip of the pyramid had a flux up to five times more than the bottom (valley) of the pyramid element. The flux on the pyramid's sides for most elements is also non-symmetrical. These observations are vital for further thermal analyses, since this could have a substantial impact on the thermal performance of the absorber.
- Literature and the poor performance of the current design have inspired a new receiver design, keeping the absorber surface design, but opting for a new CPC-based secondary concentrator. The new design's results have shown significant improvements in optical performance, with an aperture-to-absorber efficiency of 93.1%. The design, however, compromises some thermal advantages of the current receiver design, although the new proposed receiver provides some cover from winds, and the absorber design still provides many thermal advantages. The new proposed receiver design's aperture area is also large compared to the overall design, as well as compared to the original receiver.

## Chapter 6 Thermal analysis and optimisation

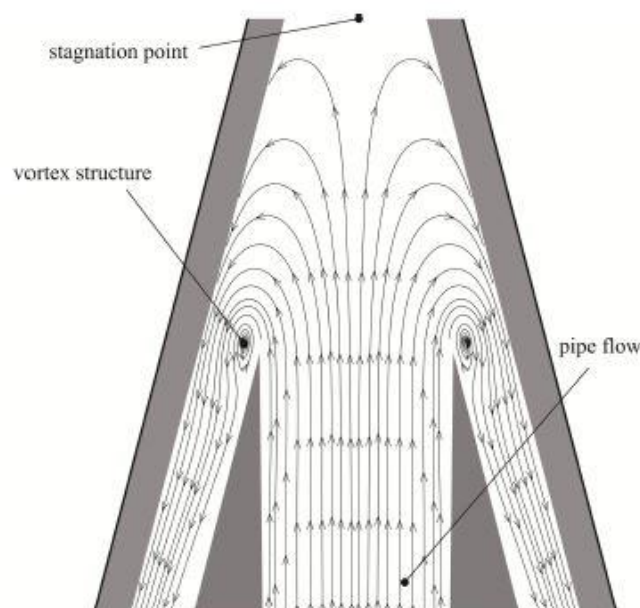
### 6.1 Introduction

The receiver's absorber consists of an array of pyramid-shaped elements, as explained and illustrated in the previous chapters. The absorber represents the boundary where the optical and thermal modelling meet, with the optical side being represented with MCRT, and the thermal modelling and heat transfer represented by CFD in this study. The flux generated with MCRT approach on the surface of the absorber is converted to a thin boundary heat source to replicate the conversion of optical to thermal energy. After doing the optical analysis to obtain the heat flux needed as input for the thermal analysis using the MCRT approach, it is time to implement the model developed in Chapter 4.3 and to apply it to the absorber element design.

The thermal analysis will be done by introducing the improvements made to the original design proposed by Garbrecht et al. (2012), followed by an evaluation of the performance by applying the model that was developed and validated in Chapter 4.3 to a heat source extracted from the optical analysis. The thermal performance of the absorber design can then be analysed, with a sensitivity analysis conducted on some parameters to get an idea of the improvements that can be made in the future.

### 6.2 Absorber design

As mentioned in the introduction of the new proposed design in Chapter 2.6, the receiver's absorber is inspired by the design introduced by Garbrecht et al. (2012). The innovative design consists of an array of hexagonal pyramids structured in a honeycomb format that impinges the HTF into the tip of this pyramid to absorb the flux incident on the outside of the pyramid. This design hosts a variety of advantages, mainly with the initial theoretical thermal efficiencies of this design going as high as 91.2%, which is significantly higher than the values obtained for receivers at plants such as Solar Two (85.6% to 88%) (Pacheco et al., 2002) and the Molten Salt Electric Experiment (MSEE) (cavity measurements ranging from 86% to 88%) (Bergan, 1986). The claimed reason for this improvement in efficiency is the design's ability to reduce the reflection and re-radiation losses by letting a neighbouring pyramid element capture the radiation. The convection losses are also estimated to decrease due to the pattern hindering convective flow.



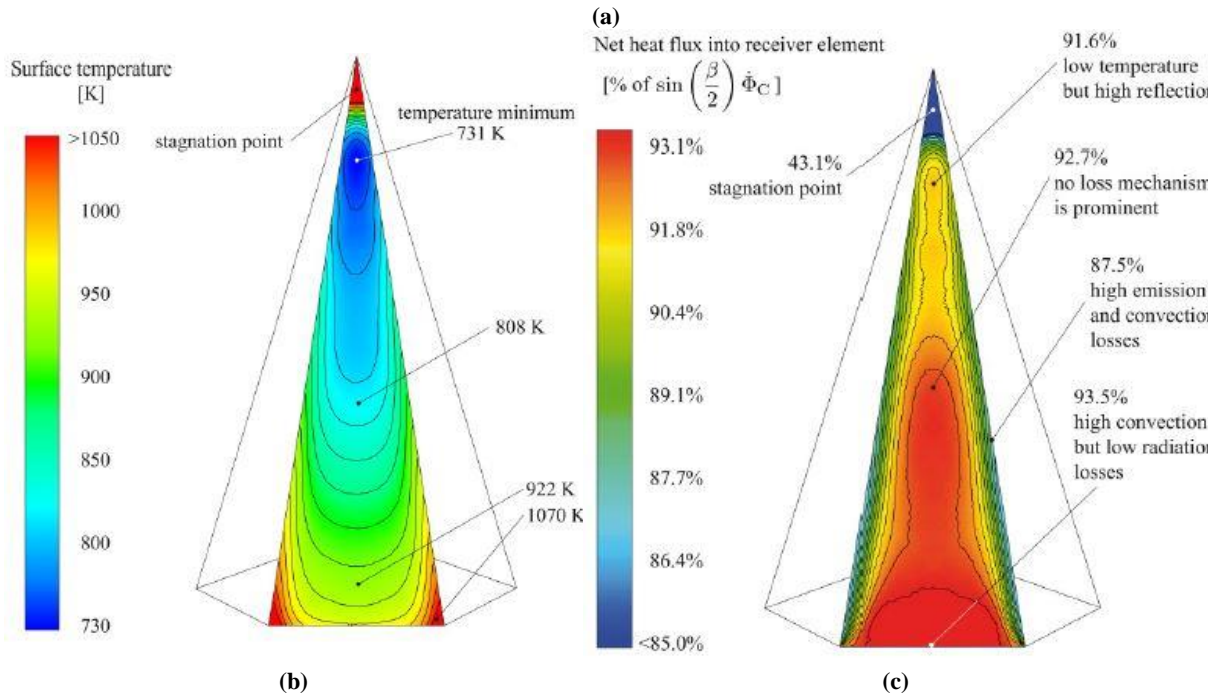


**Figure 6.1:** (a): A cross-section of the design proposed by (Garbrecht et al., 2012), which shows the internal HTF flow within the pyramid design; (b): a temperature colour profile on the outer surface of the pyramid element; and (c): a colour profile of the net heat flux into the receiver element (Garbrecht et al., 2012). Images were results published by Garbrecht et al., 2012.

Although the design of Garbrecht et al. (2012) shows promising results, it has its pitfalls. The HTF's internal flow is schematically displayed in Figure 6.1a. As can be noted, the streamlines are narrowly spaced next to the nozzle outlet, showing a high velocity flow of the fluid around the edges. This causes a high heat transfer rate, which is evident in the temperature profile in Figure 6.1b, with a low surface temperature region displayed in blue. The tip of the pyramid, however, causes the flow to stagnate and in its inability to transfer the heat incident on the tip of the pyramid, the tip heats up. This results in an excessively high temperature in the tip, which causes a low heat transfer rate at the tip (43.1% as displayed in Figure 6.1c) due to re-radiation and convective losses. It may compromise the structure's integrity at the tip, which could produce leakages and ruptures.

The proposed improvement that will be implemented and tested in the new design focuses on this problem. The new absorber design will take on a similar shape to the design of Garbrecht et al. (2012), but to overcome the stagnating flow in the tip, the tip of the pyramid element will be concave on the inside, which would provide an impinging flow on the surface. This is a heat transfer method that has proven to increase heat transfer (refer to Chapter 2.5.1). The heat will therefore be transferred with the much higher thermal conductive shell material up to the point of the impingement zone, where the fluid will absorb the heat and flow along the same route parallel to the surface of the pyramid to the outlet, as with the design of Garbrecht et al. (2012). This design is illustrated in Figure 6.2.

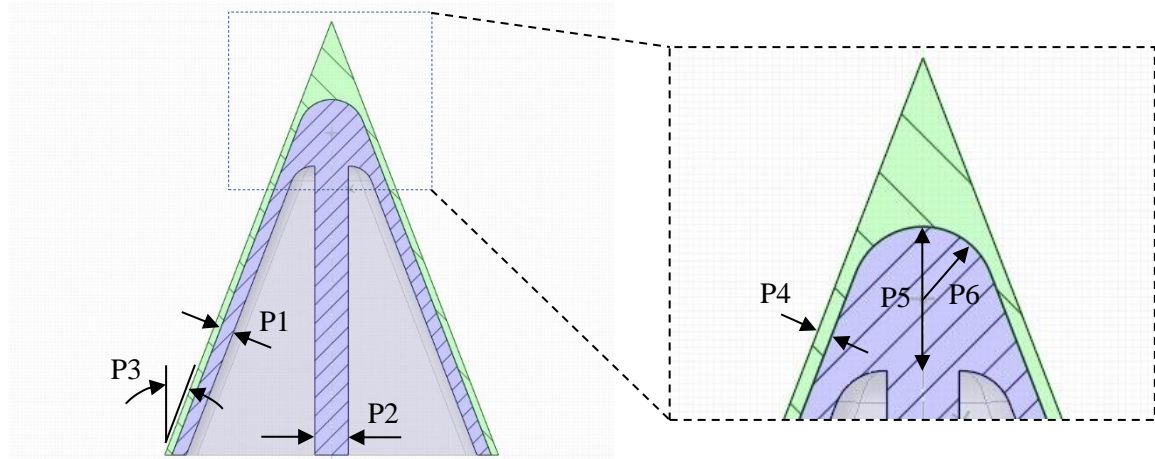


Figure 6.2: The proposed improvement to the hexagonal pyramid absorber design of Garbrecht et al. (2012), with the tip on the inside of the pyramid substituted with a concave impinging surface. The variables that could be altered to improve the design are indicated.

The design of Garbrecht et al. (2012) inserted heat transfer fins in the channels prior to the outlet of the internal flow to counteract the effect that the increased flow cross-section has on the heat transfer capabilities as the flow approaches the outlet. The internal fins were neglected for the model that will be tested. Refer to Garbrecht et al. (2012) for a more detailed description of how internal fins could be introduced into this design.

The parameters indicated in Figure 6.2 are parameters that indicate the variables that should be considered for an improved design. For this study, the changing of variables lies outside the scope of this study and was therefore not considered. A crude sensitivity study on parameter P1, however, was conducted, to indicate the possibility of improvements.

### 6.3 Absorber thermal analysis

For the absorber thermal analysis, a representative section of the whole absorber will be used for the analysis, therefore assuming that this section provides significant insight into the performance of the absorber heat transfer, as well as the receiver's performance as a whole. This sub-section will take the approach of conveying the model setup, followed by the results and a discussion of these results. This is followed by a sensitivity study for the two parameters, inlet flow velocity and outlet channel thickness.

#### 6.3.1 Geometry and computational model setup

For the design illustrated in Figure 6.2, a 3D hexagonal pyramid geometry is constructed with two adjacent replicas of the geometry. These pyramids are cut in such a manner that the geometry can apply symmetrical boundaries to resemble the entire hexagonal pyramid. The geometry is displayed in Figure 6.3, with Figure 6.3a displaying the sectioned hexagonal pyramids without the air domain, and Figure 6.3b showing the air domain as well. The geometry is divided into different sections to facilitate the meshing of its computational domain.

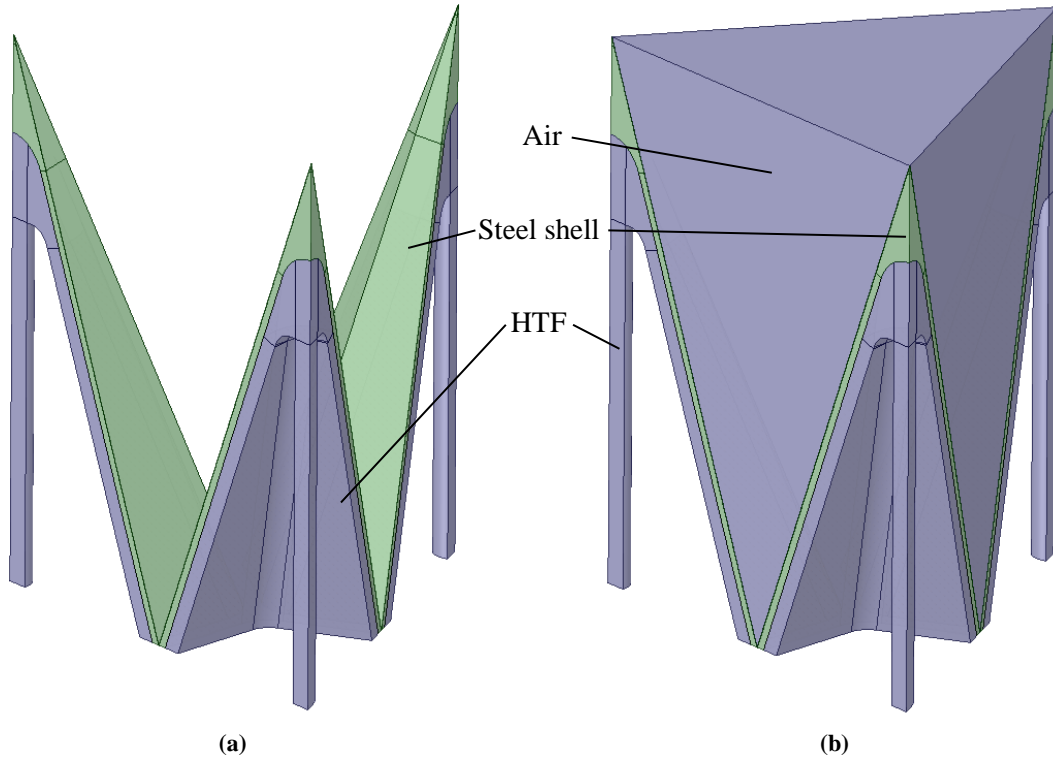


Figure 6.3: The computational model geometry of the representative hexagonal pyramid absorber: (a): displaying the domain with the solid shell displayed in green and HTF domain in grey; and (b): showing the same geometry, but with the added air domain simulated as well.

### 6.3.1.1 Material properties

For the computational setup, three material properties were defined: molten salt in the form of solar salt ( $\text{NaNO}_3\text{-KNO}_3$ ), carbon steel (0.08 C, 0.3 Mn) and air. For the property values, refer to Table 6.1 and Table 6.2. Since natural convective heat transfer is a complex heat transfer phenomenon to solve numerically, and not considered for this study at the surface between the pyramid surface and the air, the air was set as a transparent solid, hence the dynamic viscosity was not added. The assumption of neglecting natural convection is further justified with the knowledge that the absorber is situated in a downward-pointing cavity. The solar salt properties were given to the HTF (and it was also the only fluid in the model), while the carbon steel properties were given to the pyramid shell, and the air property was given to the remaining domain outside the pyramid shell, as indicated in Figure 6.3.

Table 6.1: Material properties of the hexagonal pyramid absorber computational model, with the expressions as function of temperature,  $T$  (K)

	Density, $\rho$ ( $\text{kg/m}^3$ )	Specific heat, $C_p$ ( $\text{J/kg}\cdot\text{K}$ )	Thermal conductivity, $k$ ( $\text{W/m}\cdot\text{K}$ )	Dynamic viscosity, $\mu$ ( $\text{kg/m}\cdot\text{s}$ )	Reference
<b>Solar salt</b>	2263.641 $- 0.636T$	1396.044 $+ 0.172T$	0.45	0.07543937 $- 2.77 \times 10^{-4}T$ $+ 3.49 \times 10^{-7}T^2$ $- 1.47 \times 10^{-10}T^3$	(Serrano- López, Fradera, & Cuesta-López, 2013)
<b>Carbon steel</b>	8030	502.48	Piecewise- linear function (refer to Table 6.2)	-	(Morrell, 2017; ANSYS, 2018)

**Air**                      1.225                      1006.43                      0.0242                      -                      (ANSYS, 2018)

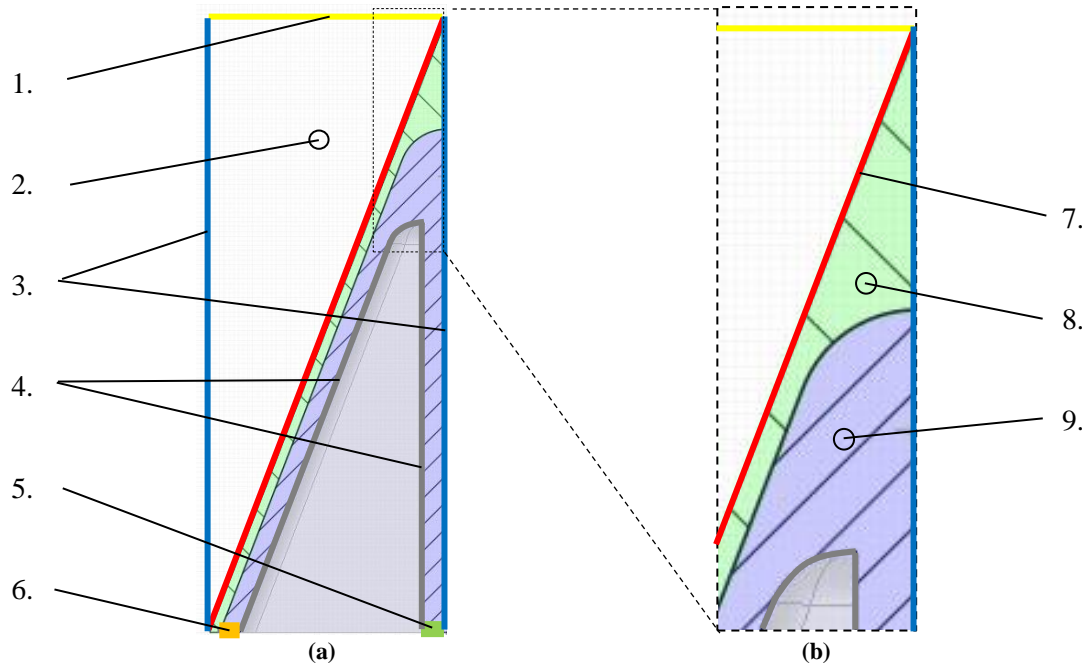
**Table 6.2: Piecewise-linear values for the thermal conductivity of carbon steel (Morrell, 2017)**

Temperature (K)	Thermal conductivity, $k$ (W/m·K)
273	59
373	58
573	49
773	40
973	32
1 273	28

### 6.3.1.2 Boundary conditions and cell zone specifications

The computational model geometry displayed in Figure 6.3 is the model that is being investigated. For demonstration purposes, however, the boundary conditions and cell zones will be considered with a 2D illustration presented in Figure 6.4. As mentioned earlier, the hexagonal pyramid absorber geometry is divided on some symmetry planes to provide a computational domain that looks like the image presented in Figure 6.3. The boundary conditions for these symmetry planes are, as expected, symmetry boundary conditions, and are illustrated in blue (and indicated as no. 3) in Figure 6.4. Confusion may arise when comparing the 2D illustration with the 3D geometry, especially with the symmetry planes. This confusion may be averted by taking in mind that the symmetry planes represent the flat planes on the side of the pyramids, which, if applied, constructs a hexagonal pyramid. Since the computational model geometry represents three independent pyramid structures, asymmetric results may still arise. The walls' heat conducted on the inside of the pyramid (shown in grey and indicated as no. 4) is assumed to stay in the system. It is also assumed that this region is well insulated. Therefore, the walls are assumed to be adiabatic. The green boundary (indicated as no. 5) is the inlet boundary, with the assumption of a constant velocity profile with an inlet temperature of 290 °C, while the outlet boundary is assumed to be a zero-pressure outlet (shown in orange and indicated as no. 6) with an outlet temperature requirement of 565 °C. The velocity at the inlet is therefore iterated to obtain the given outlet temperature. The top boundary that caps the air zone (discussed later), shown in yellow (indicated as no. 1), is assumed to be semi-transparent with a diffuse fraction of 1. The effects of radiation from other hot bodies such as the secondary reflector, the diverter cone and other bodies not mentioned is not considered for this study, although the author is aware of the possible contributions these components could have to the result of the absorber performance.

The computational domain consists of four zones: the air outside the absorber (no. 2), the steel shell structure of the absorber (no. 8), the molten salt HTF (no. 9) and the heat source region. Of all these regions, the air is the only zone that participates in radiation to simplify the simulation process. This region is also given the solid air properties listed in Table 6.1. All the shell boundaries neighbouring the air zone were given an internal emissivity of 0.95, with Kirchhoff's law of thermal radiation assumed stating that the absorption coefficient is equal to the emissivity if the surface emits diffusely. The heat source zone, which is sandwiched in between the air zone and the steel structure, is a region that is given the same properties as the steel shell structure, but is separated to provide the heat source for the simulations. An energy source or power density term is applied to this zone, on which the solar heat source is interpolated. For more information, see Chapter 6.3.1.3.



**Legend**

- |                         |                       |                           |
|-------------------------|-----------------------|---------------------------|
| 1. Transparent boundary | 4. Adiabatic boundary | 7. Heat source zone       |
| 2. Air (solid) zone     | 5. Inlet boundary     | 8. Steel shell zone       |
| 3. Symmetry boundary    | 6. Outlet boundary    | 9. HTF (molten salt) zone |

**Figure 6.4:** (a): A partial 2D schematic illustration of the hexagonal pyramid absorber’s boundary conditions and cell zones; and (b): a zoomed-in section of the boundary conditions and cell zones.

**6.3.1.3 Heat source interpolation and application**

As explained earlier, the heat source zone is given a heat-generation term based on the solar heat flux obtained with the MCRT approach (refer to Chapter 5.4.3). This is done with the aid of an interpolation file (\*.ip extension) in the ANSYS Fluent environment. For more information about implementing the interpolation file as a heat source within ANSYS Fluent, refer to the work done by Craig, Harkness, Kritzinger and Hoffmann (2010) and Moghimi (2017) or refer to Appendix G. The issue that arises with the transition from the flux obtained in SolTrace to ANSYS Fluent is with the units, with the former being a flux in  $W/m^2$  and the latter being a power density in  $W/m^3$ . The heat source zone is given a set depth (in this case  $10^{-4}$  m) to resolve this issue. The flux distribution obtained in SolTrace is then divided by this value, thereby changing the surface heat flux to a volumetric heat source. Since the heat source region is so thin, it acts as a boundary condition at the surface of the absorber, but provides the benefit of simulating this “boundary condition” within the computational domain and allows the heat source to conduct heat into the solid, while simultaneously radiating (and potentially convecting) heat to the air.

By applying the interpolation file in ANSYS Fluent of the flux computed in SolTrace (Figure 6.5a), the flux distribution seen in Figure 6.5b is generated. From a visual comparison, the flux as heat source translated well, being almost identical in terms of flux distribution. The integrated heat of the source and target were compared to one another to check whether this was true. The initial flux generated 7 705 W worth of heat, compared to the imported interpolated file, which generated a heat value of 7 778 W, which gives a percentage difference of 0.95%. This negligible difference provided the assurance that the interpolation was done adequately. It also proves the concept that it is possible to use a flux distribution generated using MCRT within a CFD environment.

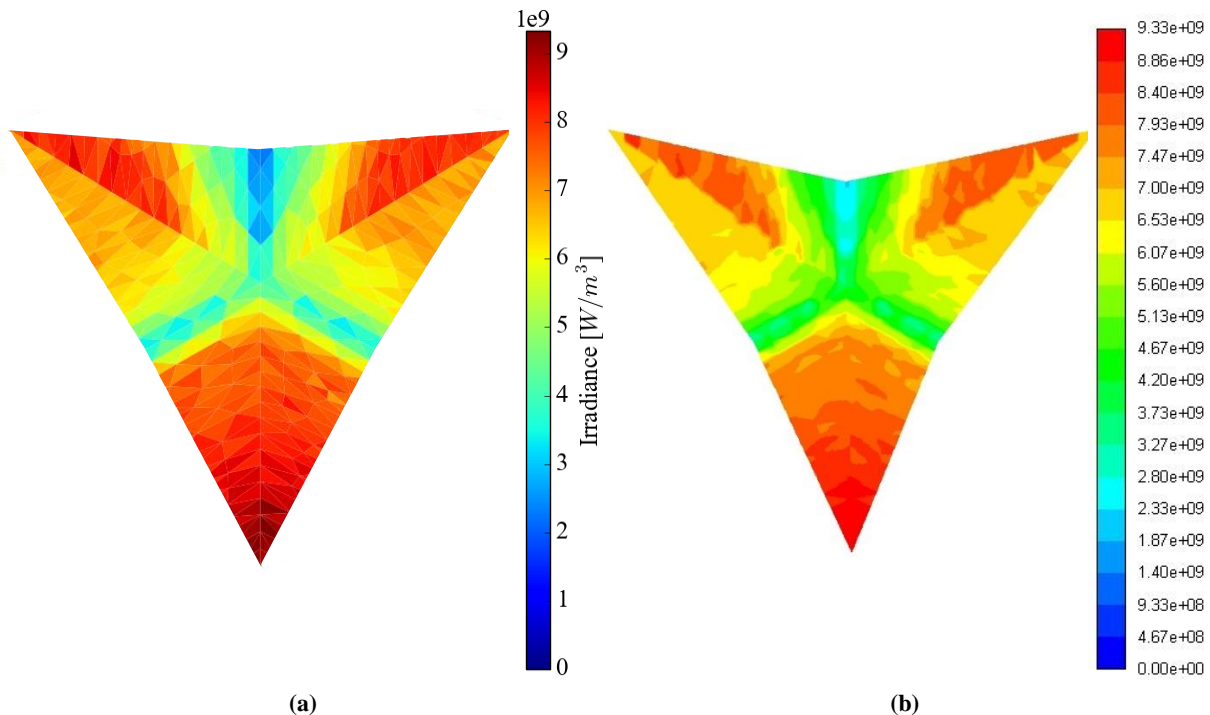


**Figure 6.5: A comparison between: (a): the solar flux obtained in SolTrace; and (b): the flux distribution in the ANSYS Fluent environment after interpolating the flux file.**

#### 6.3.1.4 Mesh generation

As mentioned earlier, the computational domain was divided into segments to simplify the process of generating a quality mesh domain (see Figure 6.3). Since solving fluid dynamics is more sensitive to mesh quality than heat transfer through solids, the focus was set on the fluid domain. The central pipe was given a radius edge sizing division of 10 elements, with an inflation bias of 4 with the smallest elements at the wall of the pipe to capture the flow gradient at the wall. The same was done with the outlet channel, except that a 20-element division was set with a bias inflation from both walls. The impingement zone was given an inflation layer with a growth rate of 1.2 and a maximum of five layers. The element size was also set at a value of  $5 \times 10^{-4}$  m to provide the fine mesh structure needed for the complex flow resulting at this point. All other mesh generation values were set to provide a smooth transition from the fluid environment to the air zone, which was given an element size value of  $2 \times 10^{-3}$  m and resulted in a high-quality mesh. Approximately  $2.75 \times 10^6$  elements were generated for this computational domain.

#### 6.3.1.5 CFD model settings

The 3D model was set up in the ANSYS Fluent v.19.1 environment. The activated models included the energy, viscous and radiation models. For the viscous model, it was already shown in Chapter 4.3.2 that, for the simulation of impinging flow heat transfer on a concave surface, the transitional SST model performed the best of the studied RANS models, and is therefore considered for this model as well. For the transitional SST model, the production Kato-Launder and production Limiter options were selected, identical to the model that was applied to the validation cases in Chapter 4.3. All other values were left at the default settings.

The selected radiation model was the discrete ordinates (DO) method. In each quadrant, the polar ( $\theta$ ) and azimuthal ( $\phi$ ) angles were divided into three sections as control angles with three subdivisions (pixels) for each angular discretisation, respectively. This implies that 72 ( $8 \times 3 \times 3$ ) extra equations can be solved, in addition to the mass, three times momentum, energy and four times turbulence model equations. The DO equations are only solved in the transparent, solid air, as mentioned before, with no

flow or turbulence being solved in this region. All the radiation emitted was also assumed to be diffused. The surface-to-surface (S2S) model could have also been selected, although this was not considered.

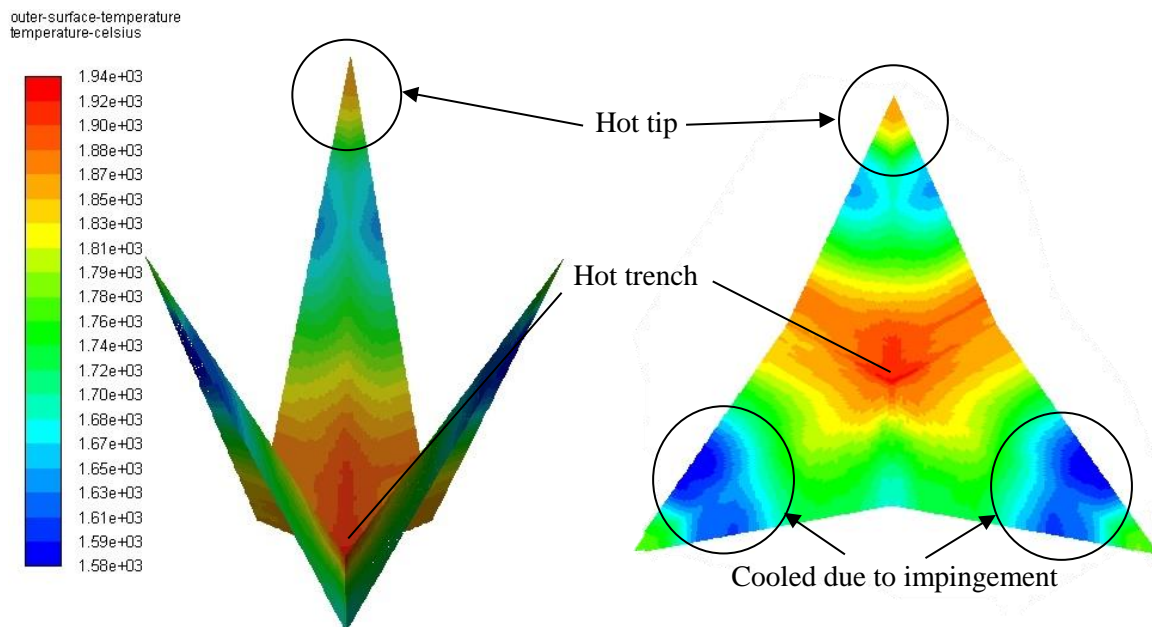
For the solution methods, the Semi-implicit Method for Pressure-linked Equations (SIMPLE) scheme was implemented for the pressure-velocity coupling. The options selected for the spatial discretisation were as follows: for solving the gradient, the least squares cell-based method was selected; for solving the pressure, the second-order approach was chosen; and for computing all the other variables (such as momentum and turbulent kinetic energy), the second-order upwind scheme was selected.

### 6.3.2 Results

The current model was simulated and converged after less than 750 iterations, with the continuity residual being less than  $10^{-7}$ ; the energy residual being less than  $10^{-8}$ ; and the DO-intensity residual dropping to below  $10^{-9}$ . These values gave the author the assurance that the results converged satisfactorily with the built computational domain.

As mentioned in Chapter 6.3.1.2, the velocity was iterated until the outlet temperature converged to within 1 °C of the set outlet boundary condition, which ended up being an inlet flow velocity of 0.085 m/s.

The absorber design originated with the idea of using the impingement flow to cool the tip of the pyramid where the view factor is the biggest, hence limiting major radiation losses at the tip. After the flow impinges the tip surface, it continues down the inside of the pyramid surface as it heats, where it eventually exits the pyramid at its “valley”. The hottest region should therefore be in the “valley” of the pyramid, where the view factor is the smallest, which hopefully limits the re-radiation. The results will therefore focus on the temperature on the surface, since this will directly affect the radiation losses.



(a)

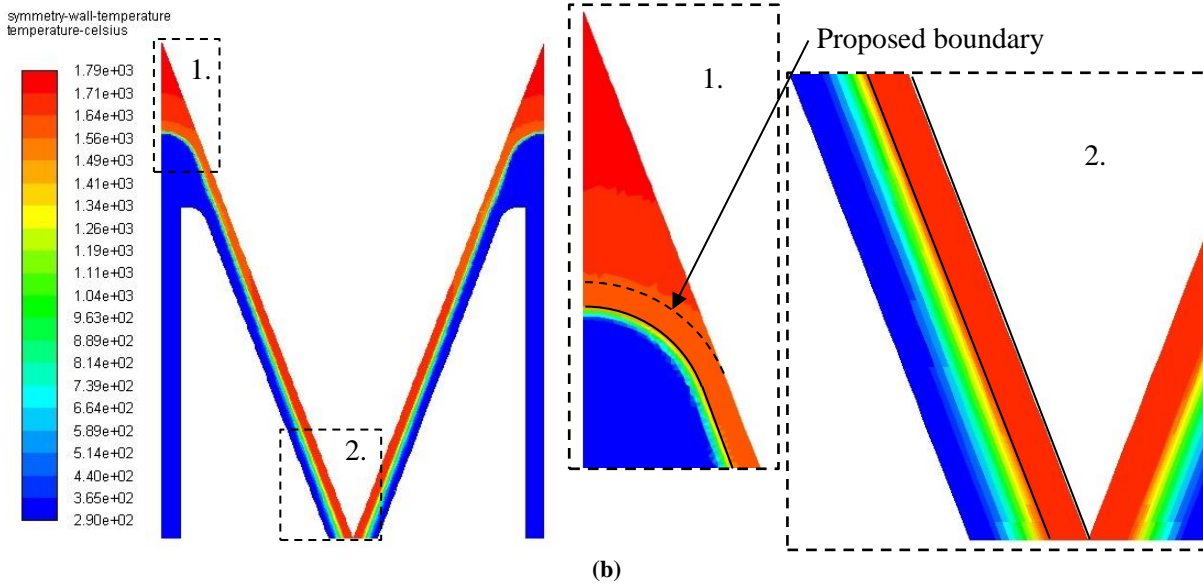


**Figure 6.6: The temperature distribution: (a): in °C, on the surface of the representative hexagonal pyramid; and (b): the symmetry wall of the computational model.**

The temperature distribution on the surface of the representative hexagonal pyramid absorber is displayed in Figure 6.6a. The results show that the maximum temperatures are much higher than the melting point of carbon steel (1 425 °C to 1 540 °C), let alone the temperature limit for structural stability. This is due to the low thermal conductivity of the HTF, solar salt ( $k = 0.045 \text{ W/m}\cdot\text{K}$ ), which hinders heat transfer on the surface that quickly propagates through the steel shell to penetrate the fluid (refer to Figure 6.6b). This is emphasised by the large thermal gradient that is visible in Zoom Area 2 of Figure 6.6b. The image shows a relatively equal temperature distribution in the steel, followed by a sharp decline in temperature as the heat fails to penetrate the HTF. This is even more evident when one notices that the inner region of the fluid shows the same inlet temperature. This problem can easily be solved by adding internal heat transfer fins that will enhance the heat transfer capabilities between the surface of the steel shell and the HTF. It will also allow the inlet velocity to increase, which will further enhance the heat transfer through convective heat transfer.

Another point of discussion is the high temperatures at the tip of the pyramid, which are visible in Figure 6.6). The idea of the design, as mentioned earlier, is for the cool impinging fluid to cool down the tip of the pyramid to limit re-radiation at the tip. This holds true for the steel shell close to the impinging wall, which can be seen in Figure 6.6a, with the cooled regions clearly visible. Unfortunately, the tip heats significantly further from the impinging surface, making the tip redundant, as it may contribute to thermal losses. A proposal for the future design of the pyramid is to curve the tip of the pyramid with the inner concave surface, as can be seen in the proposed design in Figure 6.6b. By doing so, the heat on the pyramid's surface can be removed much more effectively, which will cool the surface to much lower temperatures, which will, in turn, reduce the re-radiation thermal losses.

Figure 6.7 displays the efficiency at which the thermal flux's heat incident is extracted on the surface. This is calculated using the following equation:

$$\eta_{thermal} = \left( 1 - \frac{\dot{Q}_{cond} + \dot{Q}_{rad}}{\dot{Q}_{tot}} \right) \times 100 \quad (6-1)$$

The net thermal conduction and radiation that leaves the surface of the absorber is defined as  $\dot{Q}_{cond}$  and  $\dot{Q}_{rad}$  respectively (although the conduction term has shown to be negligible). The  $\dot{Q}_{tot}$  defines the total flux absorbed on the absorber surface.

From the figure, it is confirmed that almost all the heat incident on the tip of the pyramid is lost due to re-radiation, with the tip of the pyramid eventually accounting for less than 2%. The figure also shows that the decreased view factor seen in the trenches of the absorber has a significant effect on the receiver's thermal performance, with the thermal performance being much higher and reaching low values of almost 80%. It is important to note, however, that the overall thermal performance is low, with the average thermal efficiency being 48.3%. As discussed earlier, this is due to the low thermal heat transfer between the steel shell and the HTF, which causes the surface temperatures to increase to unproportioned levels, with the outer surface averaged temperature computed to be 1 780 °C.

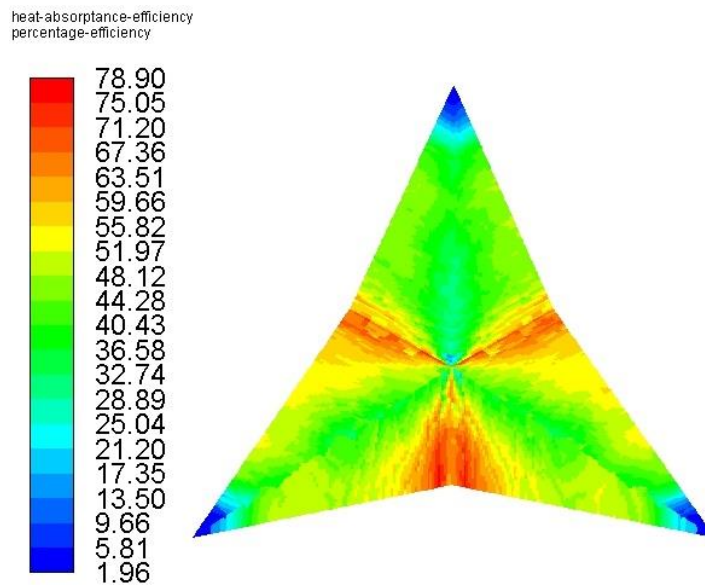


Figure 6.7: The contour plot of the efficiency at which the flux incident on the surface of the hexagonal pyramid absorber is extracted or utilised.

### 6.3.3 Sensitivity study

#### 6.3.3.1 Inlet flow velocity

From the results obtained with the current absorber design, it can be concluded that the absorber's performance is not practical. The analysis, however, has shown promising prospects of the design. There are ways to improve the design's performance without changing the geometry. By increasing the mass flow rate of the inlet, one will increase the convective heat transfer rate, which also reduces the shell temperature and therefore also the re-radiation losses. This comes at the price of lowering the outlet temperature. The flow rate will be increased to study the absorber's performance in practical temperature ranges, and therefore to obtain more information about the losses present at those temperatures.

The results obtained in Figure 6.8 are as a result of rerunning the CFD model, but with varying the inlet velocity. From the graph depicted in Figure 6.8, the outlet temperature and the average surface temperature are depicted as a function of the fluid inlet velocity. The outlet temperature shows a rapid reduction in temperature as the flow is increased, only illustrating again how poorly the design can effectively transfer the heat to the fluid. As the flow velocity magnitude increases, the temperature flattens to a temperature that is close to the inlet temperature of 290 °C. The increase of the fluid flow

does, however, increase the convective heat transfer rate, which is evident with the lowering of the average surface temperature that is seen.

This temperature, in slight contrast to the outlet temperature, reduces less dramatically. The reduction nonetheless shows that the increased flow increases the heat transfer rate from the surface to the HTF, causing the average surface temperature to be lower. This graph therefore shows that the surface temperature could be lowered by adjusting the fluid flow, but this comes at the expense of a lowered outlet temperature.

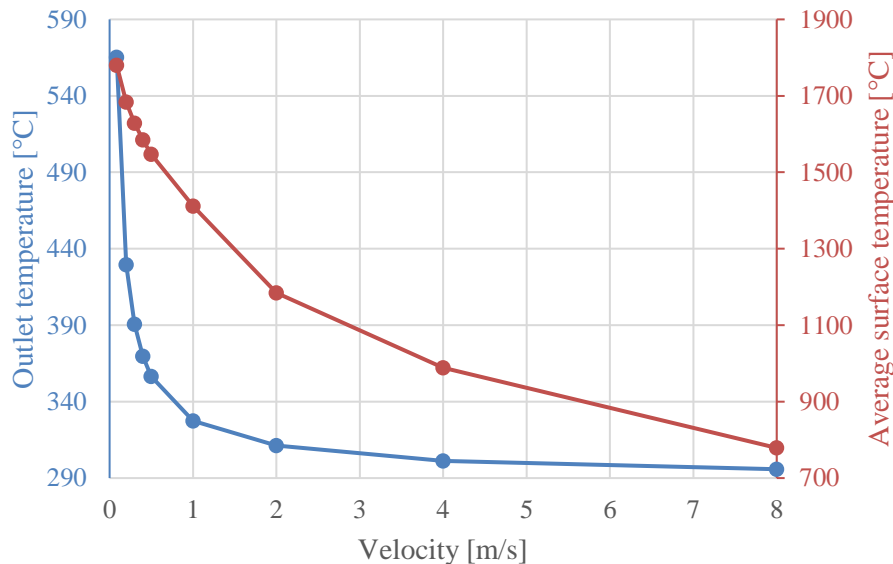


**Figure 6.8: A graphic representation of the effect of the inlet velocity on the outlet temperature and average surface temperature.**

Figure 6.9 illustrates the percentage thermal loss the absorber experiences at different inlet fluid flow velocities, as well as the increased pressure loss experienced with the increased flow. There is a clear correlation with the average surface temperature and the radiation losses, with the radiation losses being a function of the average surface temperature to the power of four (refer to Equation (2-4)). As the fluid velocity increases, the temperature decreases (as seen in Figure 6.8), causing the percentage thermal losses to reduce. The increased flow comes at the cost of increased pressure drop, which requires increased pumping power. As typical in heat exchangers, there is a trade-off between the thermal efficiency and the pressure drop. The grey line graph is the result of creating non-dimensional variables by dividing the pressure drop and the percentage thermal losses by their respective maximum values, followed by adding these two variables. It should be noted that the generation of the grey line curvature is merely to display a method of optimising the trade-off. No consideration was made to determine the weight that each variable should contribute and was therefore assumed to be equal (although this may be a poor assumption). A curve results that shows the optimal point at the lowest point of the curve, which in this case is at about 2 m/s. This optimal point refers to the trade-off that is present between the pressure drop and the thermal efficiency, and not the thermal performance of the absorber. This point in inlet flow velocity also causes the surface temperature to drop within practical temperatures. A summary of varying the inlet velocity as a sensitivity study is tabulated in Table 6.3.

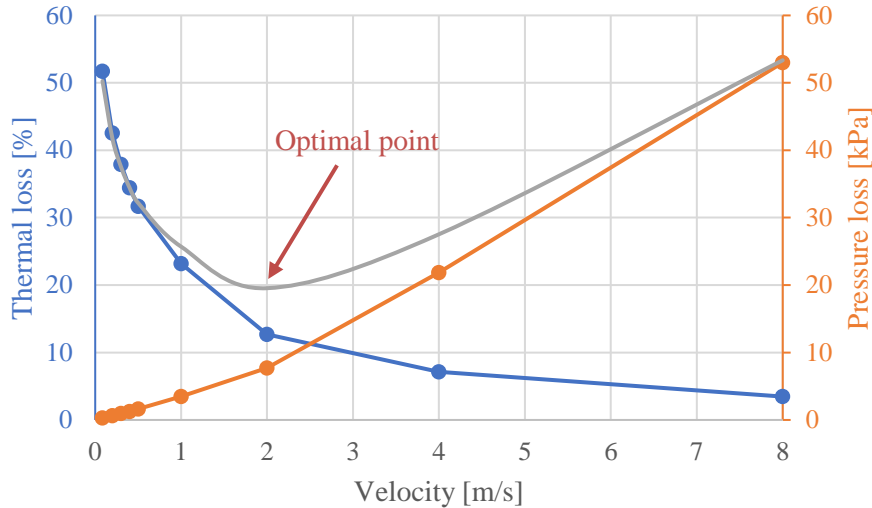


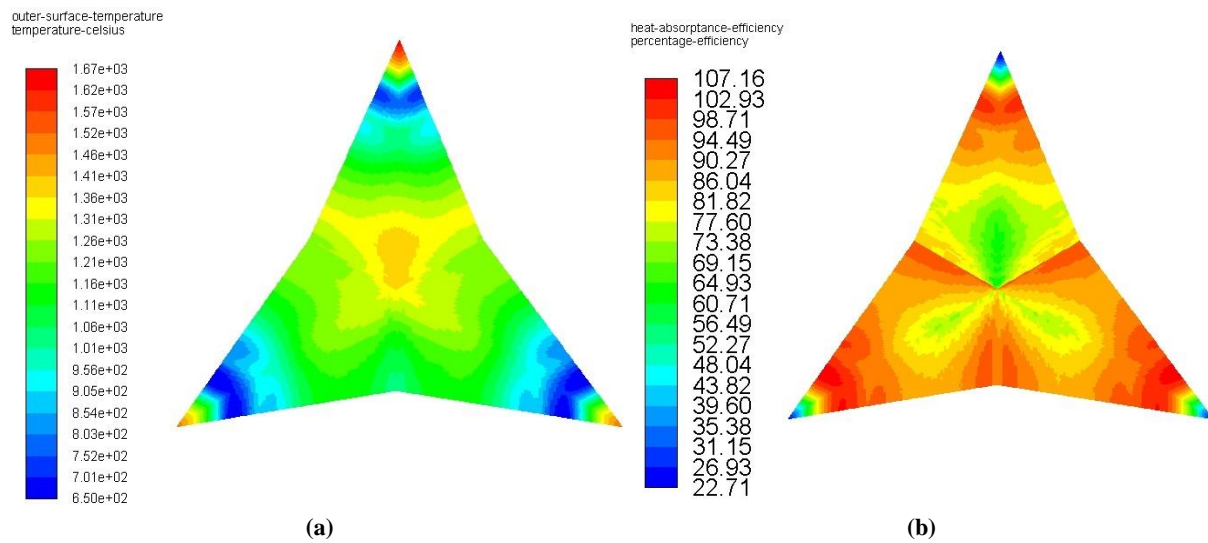
Figure 6.9: A graphic representation of the thermal loss percentage and pressure loss as a function of the fluid inlet velocity. Displayed with the grey line is the optimisation curve illustrating the non-dimensional adding of the two variables.

Table 6.3: Summary of the results obtained from the inlet flow sensitivity study conducted

Inlet velocity (m/s)	Outlet temperature (°C)	Outer surface temperature average (°C)	Heat extracted (W)	Radiation heat loss (W)	Pressure loss (kPa)	Thermal efficiency (%) (total heat = 7 778 W)
0.085	565.4	1 780	3 754	4 024	0.28	48.26
0.2	429.6	1 684	4 466	3 312	0.63	57.42
0.3	390.7	1 629	4 829	2 950	0.95	62.08
0.4	369.7	1 585	5 099	2 679	1.23	65.56
0.5	356.5	1 547	5 312	2 466	1.64	68.29
1	327.4	1 412	5 976	1 803	3.50	76.82
2	311.2	1 185	6 792	986.8	7.72	87.31
4	301.2	988.9	7 222	556.1	21.9	92.85
8	295.8	778.9	7 509	269.5	53.0	96.54

When conducting a similar analysis on the design, but this time at the optimal flow velocity, one can see how the performance changes with a change in flow. Figure 6.10 shows the contour plots of the temperature distribution on the surface and the efficiency at which the flux incident on the surface of the hexagonal pyramid absorber is extracted or utilised. The temperature distribution that is shown in Figure 6.10a does not change significantly from the first analysis, except for the much lower temperatures. It is pleasing to see that the bulk of the expected heat that is incident on the upper region of the pyramid is effectively removed, except for the tips of the pyramid. The tips of the absorber heat up more significantly compared to the other temperatures, again emphasising the tip’s reluctance to successfully transfer heat. This is once again reflected in the efficiency at which the heat is extracted at the surface, shown in Figure 6.10b, where the tips give the lowest performance with values as low as 22.7%. Generally, the efficiency at which the heat is extracted is higher than the first analysis. This is mainly due to the low surface temperatures that do not permit such a high radiation loss.

When comparing the two efficiency plots with one another, it is interesting to note that the efficiency at the regions close to the impinging zone now provide the highest values with the optimal flow analysis, which was not evident in the first analysis. What is even more surprising is that the efficiency exceeds 100%. This may be explained by the fact that the enhanced heat transfer caused by the impinging flow causes heat from the surrounding regions to redirect and cross this boundary, resulting in heat fluxes higher than the local heat flux generated in that region. As predicted, the higher fluid flow enhances the impingement heat transfer, which now dominates the efficient heat transfer in the “valleys” of the absorber caused by a low view factor. The contour plot shown in Figure 6.10b re-establishes the necessity to find techniques to enhance the heat transfer in the valley regions of the pyramid absorber by adding, for example, thermal fins that would enable the heat to penetrate the HTF more effectively. The unrealistic temperatures at the pyramid tips remain. This can be alleviated by removing tip material, as mentioned previously.



**Figure 6.10:** The contour plots of: (a): the temperature distribution; and (b): the efficiency at which the flux incident on the surface of the hexagonal pyramid absorber is extracted or utilised.

### 6.3.3.2 Channel thickness ( $P_1$ )

A limited study was also conducted on the channel thickness parameter  $P_1$ , as displayed in Figure 6.2. With the HTF having showed poor heat transfer capabilities, the problem could be mitigated by narrowing the channel through which the fluid flows, therefore getting more fluid exposed to the heated surface. The study built a similar model, but narrowed the channel to a quarter of the original design. By employing the same boundary conditions and requirements, the inlet flow velocity increased by a factor of 1.82 to 0.155 m/s to maintain the required outlet temperature. This result already indicates that the heat is transferred more effectively to the fluid. A summary of these results is displayed in Table 6.4.

**Table 6.4:** A summary of the results of the original test case compared to the current case where the  $P_1$  channel thickness parameter was reduced

Case	Inlet velocity (m/s)	Outlet temperature (°C)	Outer surface temperature average (°C)	Heat extracted (W)	Radiation heat loss (W)	Pressure loss (kPa)	Thermal efficiency, $\eta_{thermal}$ (%)
Original	0.085	565.4	1 780	3 754	4 024	0.28	48.26
New ( $\frac{1}{4} P_1$ )	0.155	563.9	1 107	6 881	890.7	13.0	88.54

The results displayed in Table 6.4 generally show an immense improvement in results, with the most noticeable results being the thermal efficiency that almost doubles to 88.5%.

This is due to more fluid flowing close to the heated surface, which causes the fluid to heat up much quicker, as well as decreasing the surface temperature, which reduces the re-radiation losses as a knock-on effect. The increased flow also adds to the additional enhanced heat transfer. This, however, comes at the price of a corresponding large increase in immense pressure drop over the design to push the flow through the thin channel. In the previous parameter sensitivity study, the 2 m/s fluid flow case showed a similar thermal efficiency of 87%, but had a pressure drop of less than 40%. The reduction in channel thickness therefore has the great disadvantage of causing a large pressure drop, but with the advantage of creating a thermally efficient absorber with a temperature outlet that meets the requirements. This study is merely preliminary, but only emphasises the small adjustments that can be made to improve the current absorber design and the inevitable compromises that must be found when designing these types of absorbers. More in-depth parameter analysis on this and other parameters should be considered to make the conclusions more concrete.

## 6.4 Summary and Conclusion

This chapter focuses on the receiver's thermal performance by analysing a representative section of the absorber surface area. The following can be summarised and concluded from the analyses in this chapter:

- The design of the absorber that was analysed was inspired by work done by Garbrecht et al. (2012). From the design presented by these authors, although the performance presented was superb, the tip of the pyramid showed questionable results. This provided a reason to improve on the proposed model by applying the concave impingement zone that would allow for improved heat transfer at the tip, although the model neglected the heat transfer fins of the design of Garbrecht et al. (2012). Results showed the expected improvement in heat transfer at the impingement region. General cooling in the upper region of the pyramid was also found, with the cool impinging fluid extracting the bulk of the heat at the top, although the excessive material at the tip allowed for most of the heat to be lost through re-radiation at the tip. The study concluded that the absorber design that was tested must be improved to overcome the heat transfer challenges.
- The application of a realistic heat flux over the absorber surface area was proven to be necessary in the analysis of the design and showed that the design could extract the heat that is mainly situated at the upper region of the pyramid. The design proved the theory that the cool HTF could effectively extract heat at the upper regions, leaving the hottest regions in the trenches of the absorber design.
- The thermal efficiency of the test case design performed poorly, with the thermal efficiency percentage not exceeding the 50% mark, which is much lower than the reported efficiencies that were presented earlier in the chapter by other receivers. The preliminary sensitivity studies did, however, show significant improvements in efficiency values by adjusting flow velocities and outlet channel thickness dimensions, which, for instance, improved the efficiency to over 88%, coming at the cost of an increased pressure drop. This indicates that the design has much potential, especially when implementing heat transfer enhancement techniques that were neglected in this study, such as heat transfer fins.
- The study neglected the effects of natural convection around the absorber area, although this was justified with the current design being a closed-cavity receiver design, therefore hindering the flow of air over the absorber area. The re-radiation heat that was reported could also be seen as conservative results, since it is assumed that all the radiation that exists past the computational

domain that was created is lost, although the secondary reflector design of the receiver would, in reality, reflect a fraction of the heat back to the absorber area.

- It can be concluded from the analysis conducted on the given design that the design could have benefitted from better scoping with much cruder, simpler first-order analyses. This would have provided a design that gave much more promising results from the first analysis and making the process of optimising the design much more refined with a smaller parameter range, would additional optimisation be conducted.
- This chapter also concludes that the current HTF is not ideal for heat transfer purposes, and other fluids should be considered to improve on the design from the fluid's perspective.

## Chapter 7 Technical evaluation, conclusion and recommendations

### 7.1 Technical evaluation

The previous chapters described analyses that were conducted on the different aspects of the receiver design. These analyses focus on the optical and thermal performance of the receiver. Receiver designs, however, are typically assessed on their overall performance. This subsection therefore summarises and analyses the receiver design by taking the results obtained in the previous chapters and putting them into perspective through a technical evaluation of the receiver's performance.

The performances of the different stages of the receiver and the entire simulated system is summarised in Table 7.1. This table is a summary of the original design, which shows the results of the benchmark test cases, the improved design, which showcases the best results after sensitivity studies, as well as the performance results of the new proposed design introduced in Chapter 5.5. It should be noted that the results displayed in the improved design section of the table only consider the results that were obtained for the cases that met the minimum requirements. For example, the thermal efficiency given in Table 7.1 shows a value of 88.5%. The study, however, had better performance results, but did not meet the outlet temperature requirement. The new proposed design assumes that the optical and thermal performance results are independent, and that the thermal performance conducted applies to the new design. The receiver efficiency was calculated by only considering the aperture-to-absorber efficiency (which is the effect the secondary collector has on the receiver) and the thermal efficiency.

**Table 7.1: Summary of the performance values (in percentages) for the different stages of the central receiver system**

	<b>Field-to-aperture efficiency (1)</b>	<b>Aperture capture efficiency (2)</b>	<b>Aperture -to- absorber efficiency (3)</b>	<b>Thermal efficiency (4)</b>	<b>System efficiency (before power cycle) ((1) × (2) × (3) × (4))</b>	<b>Receiver efficiency ((3) × (4))</b>
<b>Original design (a)</b>	85.2*	90**	68	48.3	25.19	32.84
<b>Improved design (b)</b>	86	90	79	88.5***	54.11	69.92
<b>New proposed design (c)</b>	86	79.2	93.1	88.5****	56.12	82.39

\* Value deducted from optimal performance obtained and change in performance from original aperture angle

\*\* Assume efficiency of inflated receiver design, since small design could be part of a fly eye or similar design

\*\*\* Only considered performance values of cases that fulfilled all the requirements

\*\*\*\* Assumed the thermal efficiency obtained in (b)

Table 7.1 portrays a strong image of the low efficiencies (32.8% receiver efficiency) at which the original design would function. It also shows that the few sensitivity studies that were conducted already showed significant improvement, more than doubling the original receiver's efficiency. From the analysis, it is clear that limited improvements can still be made on the field-to-aperture efficiencies when one looks at the receiver, with the majority of the improvements to be made by improving the field efficiency. The aperture capture efficiency relies predominantly on the aperture area. This is also mostly limited for design purposes. It can easily be increased by inflating the dimensions of the design. This would, however, put a strain on the structural design.

The efficiencies therefore mostly rely on the design of the secondary reflector or cavity, as well as the absorber's performance, especially with the proposed design. The author's proposed receiver design, which mainly changes the design of the secondary reflector, greatly improves the receiver design's overall performance, with an estimation of over 12% improvement to over 82% receiver efficiency. The sensitivity analysis for the absorber thermal analysis has shown that much improvement can still be made for the thermal performance of the current absorber design, which would also greatly improve the design's efficiency, which results in a competitive prospect as a receiver. As mentioned in earlier chapters, values obtained for receivers at plants such as Solar Two (85.6% to 88%) (Pacheco et al., 2002) and the MSEE (cavity measurements ranging from 86% to 88%) (Bergan, 1986) are greater than the receiver efficiencies calculated for all designs tested in this study. Preliminary sensitivity studies on selected parameters have shown that great improvements can still be made to the receiver design to make it a competitive prospective receiver design.

## 7.2 Summary and conclusion

The approach of using numerical models to help evaluate a design's performance is a powerful means of analysing and improving engineering work. For this study, a proposed receiver design was analysed optically by using the MCRT approach within the SolTrace environment. The results obtained in this analysis followed a thermal analysis by making use of CFD. This was done with the final goal to analyse the receiver design's performance, and to conclude whether the design is or could be feasible. Sensitivity studies were conducted on various parameters to analyse the prospects of improvement.

The following can be concluded on the work that was done in this study:

- The literature study on the different fields of CSP technologies reiterated the great need to develop CSP technology to make these technologies more efficient and cost effective. Literature also indicated that the greatest margins for improvement lie in central receiver systems, with the receiver technologies showing the greatest room for efficiency improvements. With this knowledge, an in-depth study was conducted on the history and development of central receiver technology, with the focus on existing, proposed and potential future receiver designs, and potential areas for improvement. One of the biggest challenges currently faced in receiver design is the handling of high-temperature HTFs and the losses associated with them, as well as making these technologies more cost-effective to be more competitive to other existing base-load utility systems
- The proposed receiver design that was evaluated and tested numerically required different models. Literature studies and validation helped with choosing and understanding the limitations of using different models. These models included the MCRT approach for optical analyses, the transitional SST RANS turbulence model for jet impingement CFD simulations and the models proposed by Iqbal (1983) to simulate the sun's position and its DNI. The DNI modelling was made more realistic by applying approximation models of temperature and humidity by using weather data. This also makes it possible to synthesise DNI data from weather data, which has not yet been witnessed by the author, and may even have applications outside the scope of CSP development and modelling. The solar tracking model was deemed accurate enough (errors predominantly being less than 2°) and the DNI approximations were deemed realistic enough to analyse the receiver. The PS-10 heliostat field was chosen as a benchmark for the receiver design to provide a realistic flux for the design. It has been noticed that the DNI predominantly plays a weighting factor for an annual analysis, although the contribution has not been quantified.
- A new modelling approach was developed for the SolTrace MCRT environment that discretises a complex geometry into irregular triangles by making use of the meshing platform within ANSYS. This not only provides the great benefit of analysing a wider range of geometries using the MCRT

approach, but also allows for evaluating previous analyses in more detail, without certain geometry simplification assumptions. Validation studies conducted by applying this new modelling approach to curved surfaces provided an understanding of the limitations of applying this approach to curved complex surfaces for MCRT analyses. This new modelling approach also has the extra benefit of converting surface fluxes simulated within the SolTrace environment to heat sources for CFD simulations within ANSYS Fluent, which was also used in the study and will be discussed later. It is noted that the validation did include a case where the factors of slope errors and incident ray direction were considered. Therefore, it cannot yet be concluded with full certainty that the model provides the broad-based application, although the current results look promising.

- The optical analysis conducted on the aperture and its angle sensitivity showed that the angle plays a minimal role in the performance of the receiver from an optical perspective (studies were not conducted to determine the effect of the aperture angle on the thermal losses), although the results are questionable when considering the assumptions that were made, such as fixed focal lengths of heliostats, eliminating atmospheric attenuation, and only considering solar noon for the annual aperture analysis. Analyses confirmed that the year-averaged aperture flux profile is similar to the equinox noon profile, which helps to simplify year-round performance analyses by reducing the analysis to one time and date. For the receiver tested, the results showed that the secondary reflector cavity design hinders rather than assists performance. Sensitivity studies point to many improvements that can be made with small alterations. In the process of optical testing, a new secondary reflector cavity concept was conceived that showed immense optical performance improvements with initial optical testing, with both efficiency and absorber flux distribution profile proving to be much better. In general, the author noted that the optical analysis is a study with a much broader scope of content to consider than initially anticipated.
- The absorber design was introduced for the thermal analysis. The setup used a heat flux profile generated using the MCRT approach within SolTrace with the new modelling approach that was developed (as discussed earlier). This heat flux proved to be very important, since most of the heat flux was incident on a region (the tip of the pyramid absorber) where the highest temperatures were generated and showed the poorest performance in terms of extracting heat. The initial thermal analysis of the absorber surface of the receiver showed poor results, with the design being unable to effectively remove the heat generated on the surface of the absorber. This causes significant re-radiation losses to the extent that more heat is lost than is gained. Sensitivity studies, however, showed that the results could be greatly improved (up to almost double the thermal performance of the case study) by applying changes to the design or requirements. By improving the thermal heat transfer of the design, the temperatures on the surface of the absorber decrease, which results in lower re-radiation losses.
- An initial technical evaluation of the receiver's performance provided some perspective on the predominant issues with the current receiver design, and what margins of improvement the sensitivity studies have shown for the few parameters that were tested. The breakdown of the performance of every single aspect of the central receiver design (excluding the power block performance) also provided some perspective on the bottlenecks in the system performance. The results amplify the results of other literature that indicates that receiver design improvements are essential for overall central receiver system performance improvements.
- The design has shown considerable complexities that may influence the techno-economic feasibility of the design. Simplification of the design is therefore paramount for the design to have a future value

### 7.3 Recommendations and future work

The receiver design is still in its early phases of testing and development. Therefore, many aspects can still be considered for future work. These include the following:

- A techno-economic feasibility study should be conducted for the current as well as the new proposed design, since developing highly efficient CSP technologies could lead to the undermining of the overall LEC, which could compromise the future value of this development.
- For more accurate numerical modelling, it is best to apply models that are as accurate as possible. This especially applies to DNI modelling, where the best model would be one based on the region's actual weather data. Future studies should maybe consider using data obtained for a typical meteorological year of a specific location, which is based on actual weather data. Future studies should also include a more accurate sun shape, rather than assuming a pillbox-shaped sun.
- This study is mostly based on the development of an interface that integrates the optical and thermal side of the central receiver system using SolTrace (MCRT approach), ANSYS DX and Fluent (CFD) software. This work has provided the groundwork to eventually develop a program or interface that assists the user to simulate not only central receiver systems, but also parabolic dishes with any form of receiver design. This is only realisable if this interface is further developed.
- For the optical side of the receiver, many improvements should be made to effectively lead the incident rays towards the absorber area. This can be done by improving the secondary reflector cavity design. The author proposes a new design that could be used as a test case design to optimise the receiver's optical performance. In general, the optics of this type of receiver is much more complex than the author has anticipated. A more in-depth study with the correct assumptions is therefore recommended.
- The thermal analysis has shown that the current absorber design is not good enough for application. However, the study has shown that an improvement in heat transfer would dramatically improve the design's performance. Enhanced heat transfer techniques, such as improving the impingement heat transfer, applying heat transfer fins in the flow region, removing the excess material at the tip of the design and optimising the design by adjusting the parameters shown in Figure 6.2 are just some of the ways to improve the design's thermal performance. An initial first order analysis of the current design will help to obtain the ballpark design parameters needed to initiate a study of optimising the design.
- Studying the effects of impingement heat transfer on concave surfaces and/or other surfaces would provide a better understanding of how to improve heat transfer on applicable designs, such as this absorber design.
- The current receiver design does not provide options for fluid distribution for both the incoming cold HTF and the returning hot HTF. Future studies should investigate this problem.
- The receiver's design should be developed in such a way as to be scalable for different heliostat field designs and sizes.
- This study omitted natural convection for the thermal analysis, with the assumption that the current design would limit convection to the extent of preventing it from taking place. Further work should consider natural and forced convection for different cavity designs, secondary reflectors and receivers with no covers. The effect of re-radiation should also be studied in more detail.

## References

- Abengoa Solar. (2018). *South Africa*. Retrieved March 14, 2018, from [http://www.abengoasolar.com/web/en/plantas\\_solares/plantas\\_propias/sudafrica/](http://www.abengoasolar.com/web/en/plantas_solares/plantas_propias/sudafrica/).
- Alanne, K., & Saari, A. (2006). Distributed energy generation and sustainable development. *Renewable and Sustainable Energy Reviews*, 10(6), 539–558.
- Alley, R., Hewitson, B., Hoskins, B., Joos, F., Jouzel, J., Kattsov, V., . . . Matsuno, T. (2014). *Summary for Policymakers* (2nd ed.). Cambridge: Cambridge University Press.
- Amsbeck, L., Buck, R., Heller, P., Jedamski, J., & Uhlig, R. (2008). Development of a tube receiver for a solar-hybrid microturbine system. *Proceedings of the 14th SolarPACES Conference*. Las Vegas, USA, 4–7 March 2008.
- ANSYS. (2018). Academic Research Fluent, Release 19.1.
- ANSYS Fluent. (2006). *Determining turbulence parameters*. Retrieved August 15, 2018, from <https://www.sharcnet.ca/Software/Fluent6/html/ug/node217.htm>.
- Arasu, A. V., & Sornakumar, T. (2007). Design, manufacture and testing of fiberglass reinforced parabola trough for parabolic trough solar collectors. *Solar Energy*, 81(10), 1273–1279.
- AT Kearney. (2010). *Solar thermal electricity 2025: clean electricity on demand: attractive STE cost stabilize energy production*. Retrieved March 2, 2018, from [https://www.atkearney.de/documents/856314/1214532/BIP\\_Solar\\_Thermal\\_Electricity\\_2025.pdf](https://www.atkearney.de/documents/856314/1214532/BIP_Solar_Thermal_Electricity_2025.pdf).
- Avila-Marin, A. L. (2011). Volumetric receivers in solar thermal power plants with central receiver system technology: a review. *Solar Energy*, 85(5), 891–910.
- Balzar, A., Stumpf, P., Eckhoff, S., Ackermann, H., & Grupp, M. (1996). A solar cooker using vacuum-tube collectors with integrated heat pipes. *Solar Energy*, 58(1-3), 63–68.
- Battleson, K. (1981). *Solar power tower design guide: Solar thermal central receiver power systems. A source of electricity and/or process heat*. Livermore, CA: Sandia National Labs Report.
- Baughn, J., Hechanova, A., & Yan, X. (1991). An experimental study of entrainment effects on the heat transfer from a flat surface to a heated circular impinging jet. *Journal of Heat Transfer (Transactions of the American Society of Mechanical Engineers)*, 113(4), 1023–1025.
- Baughn, J., Yan, X., & Masbah, M. (1992). The effect of Reynolds number on the heat transfer distribution from a flat plate to an impinging jet. *ASME Winter annual meeting*.
- Baum, V., Aparasi, R., & Garf, B. (1956). High-power solar installations. *Teploenergetika*, 3(6), 31–39.
- Becker, M., Bohmer, M., Meinecke, W., & Unger, E. (1989). Volumetric receiver evaluation. Cologne: DLR.
- Behar, O., Khellaf, A., & Mohammedi, K. (2013). A review of studies on central receiver solar thermal power plants. *Renewable and Sustainable Energy Reviews*, 23(1), 12–39.

- Behnia, M., Parneix, S., & Durbin, P. (1998). Prediction of heat transfer in an axisymmetric turbulent jet impinging on a flat plate. *International Journal of Heat and Mass Transfer*, 41(12), 1845–1855.
- Belhomme, B., Pitz-Paal, R., Schwarzbozl, P., & Ulmer, S. (2009). A new fast ray-tracing tool for high-precision simulation of heliostat fields. *Journal of Solar Energy Engineering*, 131(3), 031002.
- Bennett, S. (2007). *The encyclopedia of energy*. Delhi: Global Media.
- Bergan, N. (1986). *Testing of the molten salt electric experiment solar central receiver in an external configuration*. Livermore, CA: Sandia National Labs.
- Bienert, W., Rind, H., & Wolf, A. (1979). Conceptual design of an open cycle air Brayton solar receiver: Phase 1 final report, DTM-79-1 prepared under contract no. 955135 for California Institute of Technology Jet Propulsion Laboratory.
- Binotti, M., De Giorgi, P., Sanchez, D., & Manzolini, G. (2016). Comparison of different strategies for heliostats' aiming point in cavity and external tower receivers. *Journal of Solar Energy Engineering*, 138(2), 021008.
- Bird, R., & Hulstrom, R. (1981). Review, evaluation and improvement of direct irradiance models. *Journal of Solar Energy Engineering*, 103(3), 182–192.
- Björkman, N. (2014). *Master's thesis - Heliostat design*. Stockholm: KTH Institutionen för Energiteknik.
- Blanco, M. J., Amieva, J. M., & Mancillas, A. (2005). The Tonatiuh Software Development Project: an open source approach to the simulation of solar concentrating systems. *ASME 2005 International Mechanical Engineering Congress and Exposition – January 2005.*, 157–164.
- Blanco-Muriel, M., Alarcon-Padilla, D. C., Lopez-Moratalla, T., & Lara-Coira, M. (2001). Computing the solar vector. *Solar Energy*, 70(5), 431–441.
- Boerema, N., Morrison, G., Taylor, R., & Rosengarten, G. (2012). Liquid sodium versus Hitec as a heat transfer fluid in solar thermal central receiver systems. *Solar Energy*, 86(9), 2293–2305.
- Bohn, M. S., & Green, H. J. (1989). Heat transfer in molten salt direct absorption receivers. *Solar Energy*, 42(1), 57–66.
- BrightSource. (2014). *Ivanpah project facts*. Retrieved March 14, 2018, from [http://www.brightsourceenergy.com/stuff/contentmgr/files/0/8a69e55a233e0b7edfe14b9f77f5eb8d/folder/ivanpah\\_fact\\_sheet\\_3\\_26\\_14.pdf](http://www.brightsourceenergy.com/stuff/contentmgr/files/0/8a69e55a233e0b7edfe14b9f77f5eb8d/folder/ivanpah_fact_sheet_3_26_14.pdf).
- BrightSource. (2018). *Coalinga*. Retrieved March 14, 2018, from <http://www.brightsourceenergy.com/coalinga#.WqlahehuaUl>.
- Buck, R., Barth, C., Eck, M., & Steinmann, W. (2006). Dual-receiver concept for solar towers. *Solar Energy*, 80(10), 1249–1254.
- Buck, R., Brauning, T., Denk, T., Pfander, M., Schwarzbozl, P., & Tellez, F. (2002). Solar-hybrid gas turbine-based power tower systems (REFOS). *ASME Journal of Solar Energy Engineering*, 124(1), 2–9.
- Burden, R., & Faires, J. (2011). *Numerical analysis* (9th ed.). Boston, MA: Brooks/Cole.

- Butel, G., Coughenour, B., Macleod, H., Kennedy, C., Olbert, B., & Angel, J. (2011). second-surface silvered glass solar mirrors of very high reflectance. *In High and Low Concentrator Systems for Solar Electric Applications VI. 8108*, p. 81080L. International Society for Optics and Photonics.
- Calvert, J. (1982). Polar ice melting. *Earth and Space Science News*, 63(8), 170–172.
- Cengel, Y., & Ghajar, A. (2015). *Heat and mass transfer: fundamentals and applications* (5th ed.). New York, NY: McGraw-Hill.
- Chanaoui, M., Vaudreuil, S., & Bounahmidi, T. (2016). The 6th International Conference on Sustainable Energy Information Technology (SEIT 2016): Benchmark of concentrating solar power plants: historical, current and future technical and economic development. *Procedia Computer Science*, 83(1), 782–789.
- Chang, Z., Li, X., Xu, C., Chang, C., & Wang, Z. (2014). Numerical simulation on the thermal performance of a solar molten salt cavity receiver. *Renewable Energy*, 69, 324–335.
- Chen, H., Chen, Y., Hsieh, H., & Siegel, N. (2007). Computational fluid dynamics modeling of gas-particle flow within a solid-particle solar receiver. *Journal for Solar Energy Engineering*, 129(2), 160–170.
- Choudhury, C., & Sehgal, H. (1986). A Fresnel strip reflector-concentrator for tubular solar-energy collectors. *Applied Energy*, 23(2), 143–154.
- Clausing, A. (1981). An analysis of convective losses from cavity solar central receivers. *Solar Energy*, 27(4), 295–300.
- Cooper, D., Jackson, D., Launder, B., & Liao, G. (1993). Impinging jet studies for turbulence model assessment. Part I: Flow-field experiments. *International Journal of Heat and Mass Transfer*, 36(10), 2675–2684.
- Cooper, P. (1969). The absorption of radiation in solar stills. *Solar Energy*, 12(3), 333–346.
- Coussirat, M., Van Beeck, J., Mestres, M., Egusguiza, E., Buchlin, M., & Escaler, X. (2005). Computational fluid dynamics, modeling of impinging gas-jet systems: I. Assessment of eddy viscosity models. *Journal of Fluids Engineering*, 127(4), 691–703.
- Coventry, J., & Pye, J. (2014). Heliostat cost reduction – where to now? *Proceedings of 20th SolarPACES Conference*. Beijing, China, 16–19 September 2014, 60–70.
- Craig, K. J., Marsberg, J., & Meyer, J. P. (2016). Combining ray tracing and CFD in the thermal analysis of a parabolic dish tubular cavity receiver. *Proceedings of the 21st SolarPACES Conference*. Cape Town, South Africa, 13–16 October 2015.
- Craig, K., Harkness, A., Kritzing, H., & Hoffmann, J. (2010). Analysis of AP1000 reactor vessel cavity and support cooling. *European Nuclear Conference, Barcelona, Spain*.
- Craig, K., Moghimi, M., Rungasamy, A., Marsberg, J., & Meyer, J. (2016). Finite-volume ray tracing using computational fluid dynamics in linear focus CSP applications. *Applied Energy*, 183, 241–256.

- Craig, K., Slootweg, M., & Meyer, J. (2018). Heat transfer enhancement in molten salt central receiver using jet impingement. *Southern African Solar Energy Conference (SASEC 2018), 25–27 June 2018*.
- Craig, K., Slootweg, M., Meyer, J., Robbins, S., Kotzé, J., Honiball, R., . . . Moll, W. (2018). CFD simulation of solar receiver jet impingement heat transfer: RANS vs LES. *Proceedings of the 16th International Heat Transfer Conference (IHTC-16), 10–15 August 2018*.
- Craig, O., Brent, A. C., & Dinter, F. (2017). The current and future economics of concentrated solar power (CSP) in South Africa. *South African Journal of Industrial Engineering*, 28(3), 1-14.
- CSP World. (2015a). *CESA 1 (PSA)*. Retrieved March 13, 2018, from <http://cspworld.org/cspworldmap/cesa-1-psa>.
- CSP World. (2015b). *SSPS-CRS (PSA)*. Retrieved March 13, 2018, from <http://cspworld.org/cspworldmap/ssps-crs-psa>.
- CSP World. (2015c). *Themis solar tower*. Retrieved March 13, 2018, from <http://cspworld.org/cspworldmap/themis-solar-tower>.
- CSP World. (2018). *Acme solar thermal tower*. Retrieved March 14, 2018, from <http://cspworld.org/cspworldmap/acme-solar-thermal-tower>.
- De Wit, C., Goudriaan, J., & Van Laar, H. (1978). *Simulation of simulation, respiration and transpiration of crops*. Wageningen, The Netherlands.
- Duffie, A., & Beckman, A. (1991). *A solar engineering of thermal processes* (2nd ed.). New York, NY: Wiley.
- Dunn, R. I., Hearps, P. J., & Wright, M. N. (2012). Molten-salt power towers: newly commercial concentrating solar storage. *Proceedings of the IEEE*, 100(2), 504–515.
- Eco-friendly-world. (2018). *Solar power plant in Sevilla*. Retrieved March 14, 2018, from [https://www.eco-friendly-world.com/Page/Solar\\_power\\_plant\\_\\_\\_Sevilla](https://www.eco-friendly-world.com/Page/Solar_power_plant___Sevilla).
- Eddhibi, F., Ben Amara, M., Balghouthi, M., & Guizani, A. (2015). Optical study of solar power plants. *Journal of Physics: Conference Series*, 012018, 1–7.
- Ernst & Young and Fraunhofer Institute for Solar Energy Systems (Fraunhofer). (2011). *Middle East and North Africa (MENA) region assessment of the local manufacturing potential for concentrated solar power (CSP) projects, The World Bank, final report*. Retrieved February 26, 2018, from <http://siteresources.worldbank.org/INTMENA/Resources/CSP-Job-Study-Eng-Sum.pdf>.
- European Academies' Science Advisory Council (EASAC). (2011). *Concentrating solar power: its potential contribution to a sustainable energy future*. Germany: German Academy of Sciences Leopoldina.
- European Research Community on Flow, T. a. (1992). *Case 25: Normally-impinging jet from a circular nozzle*. Retrieved July 25, 2018, from <http://cfm.mace.manchester.ac.uk/ercoftac/>.

- European Solar Thermal Electricity Association (ESTELA). (2010). *Solar Thermal Electricity Europe and Industria Initiative (STE-EII): Implementing Plan 2010–2012*. Retrieved February 26, 2018, from <https://setis.ec.europa.eu/system/files/Solar%20CSP%20EII%202010-2012%20IP.pdf>.
- European Union. (2007). *Concentrating solar power – from research to implementation*. Retrieved March 14, 2018, from [http://www.solarpaces.org/wp-content/uploads/2007\\_concertrating\\_solar\\_power\\_en.pdf](http://www.solarpaces.org/wp-content/uploads/2007_concertrating_solar_power_en.pdf).
- Evans, G., Houf, W., Grief, R., & Growe, C. (1985). *Gas particle flow within a high temperature cavity including the effects of thermal radiation*. Denver, CO: ASME.
- Falcone, P., Noring, J., & Hruby, J. (1985). *Assessment of a solid particle receiver for a high temperature solar central receiver system*. Livermore, CA: Sandia National Labs.
- Fang, J., Wei, J., Dong, X., & Wang, Y. (2011). Thermal performance simulation of a solar cavity receiver under windy conditions. *Solar Energy*, 85(1), 126–138.
- Forsberg, C. W., Peterson, P. F., & Zhao, H. (2007). High-temperature liquid-fluoride-salt closed-Brayton-cycle solar power towers. *Journal of Solar Energy Engineering*, 129(2), 141–146.
- Francia, G. (1968). Pilot plants of solar steam-generating stations. *Solar Energy*, 12(1), 51–64.
- Frank, K. (2003). *The power of light* (1st ed.). New York, NY: McGraw-Hill.
- Frohlich, C., & Brusa, R. (1981). Solar radiation and its variation in time. *Solar Physics*, 74(1), 209–215.
- Frohlich, C., & Wehrli, C. (1981). Spectral distribution of solar irradiance from 25000 nm to 250 nm. Davos: Private Communication.
- Garbrecht, O., Al-Sibai, F., Kneer, R., & Wiegardt, K. (2012). Numerical investigation of a new molten salt central receiver design. *Proceedings of 18th SolarPACES Conference*. Marrakech, Morocco, 11–14 September 2012.
- Garbrecht, O., Al-Sibai, F., Kneer, R., & Wiegardt, K. (2013). CFD-simulation of a new receiver design for a molten salt solar power tower. *Solar Energy*, 90, 94–106.
- Gardon, R., & Akfirat, J. (1965). The role of turbulence in determining the heat transfer characteristics of impinging jet. *International Journal of Heat and Mass Transfer*, 8(10), 1261–1272.
- General Electric Renewable Energy. (2016). *Ashalim Power Station, Israel*. Retrieved March 14, 2018, from [https://www.gerenewableenergy.com/content/dam/gepower-renewables/global/en\\_US/downloads/brochures/solar-csp-ashalim-gea32278.pdf](https://www.gerenewableenergy.com/content/dam/gepower-renewables/global/en_US/downloads/brochures/solar-csp-ashalim-gea32278.pdf).
- German Aerospace Centre (DLR). (2007). *WP 1: Review of CSP and desalination technology*, DLR. Retrieved March 5, 2018, from [http://www.dlr.de/tt/Portaldata/41/Resources/dokumente/institut/system/projects/aqua-csp/WP01\\_AQUA-CSP-Technologies-Final.pdf](http://www.dlr.de/tt/Portaldata/41/Resources/dokumente/institut/system/projects/aqua-csp/WP01_AQUA-CSP-Technologies-Final.pdf).
- Geyer, M., Lüpfer, E., Osuna, R., Esteban, A., Schiel, W., Schweitzer, A., . . . Mandelberg, E. (2002). EURO TROUGH: parabolic trough collector developed for cost-efficient solar power

- generation. *Proceedings of the 11th SolarPACES Conference*. Zurich, Switzerland, 2–3 September 2002.
- Giostri, A., & Macchi, E. (2016). An advanced solution to boost sun-to-electricity efficiency of parabolic dish. *Solar Energy*, *139*, 337–354.
- Gonzalez, M. M., Palafox, J. H., & Estrada, C. A. (2012). Numerical study of heat transfer by natural convection and surface thermal radiation in an open cavity receiver. *Solar Energy*, *86*(4), 1118–1128.
- Google.org. (2011). *RE<C: heliostat frame design*. Retrieved March 19, 2018, from [https://www.google.org/pdfs/google\\_heliostat\\_frame\\_design.pdf](https://www.google.org/pdfs/google_heliostat_frame_design.pdf).
- Goswami, R., Negi, B., Sehgal, H., & Sootha, G. (1990). Optical designs and concentration characteristics of a linear Fresnel reflector solar concentrator with a triangular absorber. *Solar Energy Materials*, *21*(2–3), 237–251.
- Hafez, A., Soliman, A., El-Metwally, K., & Ismail, I. (2016). Solar parabolic dish Stirling engine system design, simulation and thermal analysis. *Energy Conversion and Management*, *126*, 60–75.
- Heller, P., Pfänder, M., Denk, T., Tellez, F., Valverde, A., Fernandez, J., & Ring, A. (2006). Test and evaluation of a solar powered gas turbine system. *Solar Energy*, *80*(10), 1225–1230.
- Herzog, A., Lipman, T., Edwards, J., & Kammen, D. (2001). Renewable energy: a viable choice. *Environment*, *43*(10), 2–18.
- Hildebrandt, A. F., & Rose, K. A. (1985). Receiver design considerations for solar central receiver hydrogen productions. *Solar Energy*, *35*(2), 199–206.
- Hildebrandt, A., Haas, G., Jenkins, W., & Colaco, J. (1972). Large-scale concentration and conversion of solar energy. *EOS*, *53*, 684–692.
- Hischier, I., Hess, D., Lipinski, W., Modest, M., & Steinfeld, A. (2009). Heat transfer analysis of a novel pressurised air receiver for concentrated solar power via combined cycles. *Journal of Thermal Science and Engineering Applications*, *1*(4), 041002.
- Ho, C. K. (2018). Particle Technology Working Group (PTWG) for Global Collaboration on High-Temperature Solar-Thermal Particle Research. *Proceedings of the 22nd SolarPACES Conference*. Casablanca, Morocco, 2–5 March 2018.
- Ho, C., & Iverson, B. (2014). Review of high-temperature central receiver designs for concentrating solar power. *Renewable and Sustainable Energy Reviews*, *29*, 835–846.
- Hock, R. (2005). Glacier melt: a review of processes and their modelling. *Progress in Physical Geography*, *29*(3), 362–391.
- Hoegh-Guldberg, O. (1999). Climate change, coral bleaching and the future of the world's coral reefs. *Marine and Freshwater Research*, *50*(1), 839–866.
- Hoffschmidt, B. (2014). Receiver for Solar Tower Systems. Cologne: DLR.

- Hoffschmidt, B., Téllez, F. M., Valverde, A., Fernandez, J., & Fernandez, V. (2003). Performance evaluation of the 200-kWth HiTRec-II open volumetric air receiver. *Journal of Solar Energy Engineering*, 125(1), 87–94.
- Hofmann, J., & Gretz, J. (1980). The 1 MW (el) Experimental solar power plant of the European Community. *Electric Power Systems Research*, 3(1–2), 13–24.
- Hoogendoorn, C. (1977). The effect of turbulence on heat transfer at a stagnation point. *International Journal of Heat and Mass Transfer*, 20(12), 1333–1338.
- Höök, M., & Xu, T. (2013). Depletion of fossil fuels and anthropogenic climate change – a review. *Energy Policy*, 52, 797–809.
- Howell, J. R., Siegel, R., & Mengüç, M. P. (2010). *Thermal radiation heat transfer* (5th ed.). Boca Raton, FL: CRC Press – Taylor & Francis Group.
- Hruby, J., & Burolla, V. (1984). *Solid particle receiver experiments: velocity measurements*. Sandiego, CA: Sandia.
- Infaimon. (2016). *Plantas solares que recurren a sistemas de visión artificial para el alineamiento de espejos*. Retrieved March 14, 2018, from <https://blog.infaimon.com/plantas-solares-recurren-sistemas-vision-artificial-alineamiento-espejos/>.
- International Energy Agency (IEA). (2010). *Technology roadmap: concentrating solar power*. Retrieved March 3, 2018, from [https://www.iea.org/publications/freepublications/publication/csp\\_roadmap.pdf](https://www.iea.org/publications/freepublications/publication/csp_roadmap.pdf).
- International Renewable Energy Agency (IRENA). (2012). Concentrating solar power. *Renewable energy technologies: cost analysis series*, 1(2/5). Retrieved February 26, 2018, from [https://www.irena.org/documentdownloads/publications/re\\_technologies\\_cost\\_analysis-csp.pdf](https://www.irena.org/documentdownloads/publications/re_technologies_cost_analysis-csp.pdf).
- Iqbal, M. (1983). *An introduction to solar radiation*. Ontario: Academic Press, Inc.
- IRENA. (2018). *Global Energy Transformation: A roadmap to 2050*. Abu Dhabi: International Renewable Energy Agency.
- James, R., Washington, R., Schleussner, C., Rogelj, J., & Conway, D. (2017). Characterizing half-a-degree difference: a review of methods for identifying regional climate responses to global warming targets. *Wiley Interdisciplinary Reviews: Climate Change*, 8(2), e457.
- Jebasingh, V., & Herbert, G. (2016). A review of solar parabolic trough collector. *Renewable and Sustainable Energy Reviews*, 54(1), 1085–1091.
- Joly, M., Antonetti, Y., Python, M., Gonzalez, M., Gascou, T., Scartezzini, J. L., & Schuler, A. (2013). Novel black selective coating for tubular solar absorbers based on a sol-gel method. *Solar Energy*, 94, 233–239.
- Jun, W., Yaoming, Z., Deyou, L., & Su, G. (2008). Introduction of the first solar power tower system in China. *Proceedings of ISES World Congress 2007*, 1738–1742.

- Kannan, N., & Vakeesan, D. (2016). Solar energy for future world: a review. *Renewable and Sustainable Energy Reviews*, 62, 1092–1105.
- Kasten, F. (1965). A new table and approximation formula for the relative optical air mass. *Archiv für Meteorologie, Geophysik und Bioklimatologie, Serie B*, 14(2), 206–223.
- Kesselring, P., & Selva, C. S. (1986). *The IEA/SSPS solar thermal power plants – facts and figures – final report*. Berlin: Springer.
- Kim, K., Moujaes, S. F., & Kolb, G. J. (2010). Experimental and simulation study on wind affecting particle flow in a solar receiver. *Solar Energy*, 84(2), 263–270.
- Kleih, J. (1991). Dish-Stirling test facility. *Solar Energy Materials*, 24(1), 231–237.
- Kodama, T., Gokon, N., Matsubara, K., Yoshida, K., Koikari, S., Nagase, Y., & Nakamura, K. (2014). Flux measurement of new beam-down solar concentrating system in Miyazaki for demonstration of thermochemical water splitting reactors. *Energy Procedia*, 49, 1990-1998.
- Kolb, G. (2007). *Heliostat cost reduction study*. Albuquerque, NM: Sandia National Labs.
- Korzynietz, R., Quero, M., & Uhlig, R. (2012). SOLUGAS – future solar hybrid technology. *Proceedings of the 18th SolarPACES Conference*. Marrakech, Morocco, 11–14 September 2012.
- Kretzschmar, H., & Gauché, P. (2012). Hybrid pressurized air receiver for the sunspot cycle. *Proceedings of the 1st South African Solar Energy Conference (SASEC)*. Stellenbosch, South Africa, 21–23 May.
- Kribus, A., Ries, H., & Spirkl, W. (1995). Inherent limitations of volumetric solar receivers. *Solar Engineering: Proceedings of the ASME Solar Energy Conference, 19–24 March 1995, Maui, Hawaii*.
- Kribus, A., Zaibel, R., Carey, D., Segal, A., & Karni, J. (1998). A solar-driven combined cycle power plant. *Solar Energy*, 62(2), 121–129.
- Lal, M. K. (2017). *Master's thesis – Solar tower heliostat field layout optimization: a black-box optimizer*. Aachen: RWTH.
- Lata, J., Rodriguez, M., & De Lara, M. (2008). High flux central receivers of molten salts for the new generation of commercial stand-alone solar power plants. *Journal of Solar Energy Engineering*, 130(2), 021002.
- Le Houérou, H. (1996). Climate change, drought and desertification. *Journal of Arid Environments*, 34(1), 133–185.
- Leary, P., & Hankins, J. (1979). User's guide for MIRVAL: a computer code for comparing designs of heliostat-receiver optics for central receiver solar power plants.
- Leckner, B. (1978). The spectral distribution of solar radiation at the earth's surface – elements of a model. *Solar Energy*, 20(2), 143–150.

- Lee, D., Chung, Y., & Won, S. (1999). The effect of concave surface curvature on heat transfer from a fully developed round impinging jet. *International Journal of Heat and Mass Transfer*, 13(42), 2489–2497.
- Lee, J., & Lee, S. (1999). Stagnation region heat transfer of a turbulent axisymmetric jet impingement. *Experimental Heat Transfer*, 12(2), 137–156.
- Leonardi, E. (2012). Detailed analysis of the solar power collected in a beam-down central receiver system. *Solar Energy*, 86(2), 734–745.
- Lewis, N. (2007). Toward cost-effective solar energy use. *Science*, 315(5813), 798–801.
- Li, L., Ceventry, J., Bader, R., Pye, J., & Lipiński, W. (2016). Optics of solar central receiver systems: a review. *Optics Express*, 24(14), A985–A1007.
- Li, X., Kong, W., Wang, Z., Chang, C., & Bai, F. (2010). Thermal model and thermodynamic performance of molten salt cavity receiver. *Renewable Energy*, 35(5), 981–988.
- Liao, Z., & Faghri, A. (2016). Thermal analysis of a heat pipe solar central receiver for concentrated solar power tower. *Applied Thermal Engineering*, 102, 952–960.
- Lilliestam, J., & Pitz-Paal, R. (2018). Concentrating solar power for less than USD 0.07 per kWh: finally the breakthrough? *Renewable Energy Focus*, 26, 17-21.
- Louche, A., Maurel, M., Simonnot, G., Peri, G., & Iqbal, M. (1987). Determination of Ångström's turbidity coefficient from direct total solar irradiance measurements. *Solar Energy*, 38(2), 89–96.
- Lovegrove, K., & Stein, W. (2012). *Concentrator solar power technology: principle development and applications* (1st ed.). Cambridge: Woodhead Publishing.
- Lovegrove, K., Taumofolau, T., Paitoonsurikarn, S., Siangsukone, P., Burgess, G., Luzzi, A., . . . Major, G. (2007). *Paraboloidal dish solar concentrators for multi-megawatt power generation*. Beijing: Solar World Congress.
- Lubkoll, M., Von Backström, T. W., Harms, T., & Kröger, D. G. (2015). Initial analysis on the novel spiky central receiver air pre-heater (SCRAP) pressurized air receiver. *Energy Procedia*, 69, 461–470.
- Lytle, D., & Webb, B. (1994). Air jet impingement heat transfer at low nozzle-plate spacing. *International Journal of Heat and Mass Transfer*, 37(12), 1687–1697.
- Mächler, M. (1983). *Master's thesis – Parameterization of solar irradiation under clear skies*. Vancouver: University of British Columbia.
- Martin, H. (1977). Heat and mass transfer between impinging gas jets and solid surfaces. *Advances in Heat Transfer*, 13, 1–60.
- Martinek, J., & Weimer, A. W. (2013). Evaluation of finite volume solutions for radiative heat transfer in a closed cavity solar receiver for high temperature solar thermal processes. *International Journal of Heat and Mass Transfer*, 58(1–2), 585–596.

- Mathur, S., Kandpal, T., & Negi, B. (1991). Optical design and concentration characteristics of linear Fresnel reflector solar concentrators – I. Mirror elements of varying width. *Energy Conversion and Management*, 31(3), 205–219.
- Mathur, S., Kandpal, T., & Negi, B. (1991). Optical design and concentration characteristics of linear Fresnel reflector solar concentrators - II. Mirror elements of equal width. *Energy Conversion and Management*, 31(3), 221–232.
- Mazumder, R., Kandpal, T., & Mullick, S. (1987). Design and optical performance analysis of seasonally adjusted discrete mirror solar concentrators. *Energy Conversion and Management*, 27(2), 237–246.
- McClatchey, R., & Selby, J. (1972). Atmospheric transmittance from 0.25 to 38.5  $\mu\text{m}$ : computer code LOWTRAN-2.
- Meehl, G., Zwiers, F., Evans, J., Knutson, T., Mearns, L., & Whetton, P. (2000). Trends in extreme weather and climate events: issues related to modelling extremes in projections of future climate change. *Bulletin of the American Meteorological Society*, 81(3), 427–436.
- Meier, A. (1999). A predictive CFD model for a falling particle receiver/reactor exposed to concentrated sunlight. *Chemical Engineering Science*, 54(13–14), 2899–2905.
- Merz, B. (2015). *Controlling climate change: The Paris Agreement - an analysis*. Retrieved November 25, 2006, from <http://controllingclimatechange.net/news/>.
- Miller, R., Amatya, R., Brushett, F., Campanella, A., Goksin, K., Macko, J., . . . Tuller, H. (2015). *The future of solar energy*. Massachusetts, MA: Massachusetts Institute of Technology.
- Mills, D. (2004). Advances in solar thermal electricity technology. *Solar Energy*, 76(1–3), 19–31.
- Moghimi, M. (2017). *Dissertation – Optical, thermal and economic optimisation of a linear fresnel collector*. Pretoria: University of Pretoria.
- Mohammad, I. (2012). Design and development of a parabolic dish solar water heater. *International Journal of Applied Engineering Research*, 2(1), 822–830.
- Mokhtar, M. (2011). *The beam-down solar thermal concentrator: experimental characterization and modelling*. Masdar: Masdar Institute of Science and Technology.
- Montes, M., Rovira, A., Martínez-Val, J., & Ramos, A. (2012). Proposal of a fluid flow layout to improve the heat transfer in the active absorber surface of solar central cavity receivers. *Applied Thermal Engineering*, 35, 220–232.
- Morin, G., Dersch, J., Platzer, W., Eck, M., & Häberle, A. (2012). Comparison of linear Fresnel and parabolic trough collector power plants. *Solar Energy*, 86(1), 1–12.
- Morrell, R. (2017). *National Physical Laboratory: Kaye & Laby*. Retrieved October 15, 2018, from [http://www.kayelaby.npl.co.uk/general\\_physics/2\\_3/2\\_3\\_7.html](http://www.kayelaby.npl.co.uk/general_physics/2_3/2_3_7.html).
- Mukai, T., Horigome, T., Ikeda, N., & Sakamoto, T. (1985). A 1MWe solar thermal electric power pilot plant (Sunshine Project). *Thermo-Mechanical Solar Power Plants. Solar Energy R&D in the European Community*, 2, 52–61.

- Munoz, J., Martinez-Val, J., & Ramos, A. (2011). Thermal regimes in solar-thermal linear collectors. *Solar Energy*, 85(5), 857–870.
- Mustafa, M., Abdelhady, S., & Elweteedy, A. (2012). Analytical study of an innovated solar power tower (PS10) in Aswan. *International Journal of Energy Engineering*, 2(6), 273–278.
- Mutuberria, A., Pascual, J., Guisado, M., & Mallor, F. (2015). Comparison of heliostat field layout design methodologies and impact on power plant efficiency. *Proceedings of the 20th SolarPACES Conference*. Beijing, China, 16–19 September 2014, 1360–1370.
- Negi, B., Mathur, S., & Kandpal, T. (1989). Optical and thermal performance evaluation of a linear Fresnel reflector solar concentrator. *Solar and Wind Technology*, 6(5), 589–593.
- New Energy Update: CSP. (2013). *Baring the secrets of Khi Solar One*. Retrieved March 14, 2018, from <http://analysis.newenergyupdate.com/csp-today/markets/baring-secrets-khi-solar-one?sthash.x5xJEr1y.mjjo>.
- Nicholls, R., & Cazenave, A. (2010). Sea-level rise and its impact on coastal zones. *Science*, 328(5985), 1517–1520.
- Noone, C. J., Torrilhon, M., & Mitsos, A. (2012). Heliostat field optimization: a new computationally efficient model and biomimetic layout. *Solar Energy*, 86(1), 792–803.
- Nozik, A. (1978). Photoelectrochemistry: applications to solar energy conversion. *Annual Review of Physical Chemistry*, 29(1), 189–222.
- NREL. (2013). *Concentrating solar power projects – Julich Solar Tower*. Retrieved March 13, 2018, from [https://www.nrel.gov/csp/solarpaces/project\\_detail.cfm/projectID=246](https://www.nrel.gov/csp/solarpaces/project_detail.cfm/projectID=246).
- NREL. (2014a). *ACME Solar Tower*. Retrieved March 14, 2018, from [https://www.nrel.gov/csp/solarpaces/project\\_detail.cfm/projectID=262](https://www.nrel.gov/csp/solarpaces/project_detail.cfm/projectID=262).
- NREL. (2014b). *Ivanpah solar electric-generating system*. Retrieved March 14, 2018, from [https://www.nrel.gov/csp/solarpaces/project\\_detail.cfm/projectID=62](https://www.nrel.gov/csp/solarpaces/project_detail.cfm/projectID=62).
- NREL. (2014c). *Sierra Sun Tower*. Retrieved March 14, 2018, from [https://www.nrel.gov/csp/solarpaces/project\\_detail.cfm/projectID=63](https://www.nrel.gov/csp/solarpaces/project_detail.cfm/projectID=63).
- NREL. (2015). *Atacama-1*. Retrieved March 14, 2018, from [https://www.nrel.gov/csp/solarpaces/project\\_detail.cfm/projectID=3275](https://www.nrel.gov/csp/solarpaces/project_detail.cfm/projectID=3275).
- NREL. (2016a). *Ashalim Plot B*. Retrieved March 14, 2018, from [https://www.nrel.gov/csp/solarpaces/project\\_detail.cfm/projectID=277](https://www.nrel.gov/csp/solarpaces/project_detail.cfm/projectID=277).
- NREL. (2016b). *Crescent Dunes Solar Energy Project*. Retrieved March 14, 2018, from [https://www.nrel.gov/csp/solarpaces/project\\_detail.cfm/projectID=60](https://www.nrel.gov/csp/solarpaces/project_detail.cfm/projectID=60).
- NREL. (2016c). *Khi Solar One*. Retrieved March 14, 2018, from [https://www.nrel.gov/csp/solarpaces/project\\_detail.cfm/projectID=244](https://www.nrel.gov/csp/solarpaces/project_detail.cfm/projectID=244).
- NREL. (2017a). *Gemasolar thermosolar plant*. Retrieved March 14, 2018, from [https://www.nrel.gov/csp/solarpaces/project\\_detail.cfm/projectID=40](https://www.nrel.gov/csp/solarpaces/project_detail.cfm/projectID=40).

- NREL. (2017b). *NOOR III*. Retrieved March 14, 2018, from [https://www.nrel.gov/csp/solarpaces/project\\_detail.cfm/projectID=4293](https://www.nrel.gov/csp/solarpaces/project_detail.cfm/projectID=4293).
- NREL. (2017c). *Planta Solar 10*. Retrieved March 14, 2018, from [https://www.nrel.gov/csp/solarpaces/project\\_detail.cfm/projectID=38](https://www.nrel.gov/csp/solarpaces/project_detail.cfm/projectID=38).
- NREL. (2017d). *Planta Solar 20*. Retrieved March 14, 2018, from [https://www.nrel.gov/csp/solarpaces/project\\_detail.cfm/projectID=39](https://www.nrel.gov/csp/solarpaces/project_detail.cfm/projectID=39).
- NREL. (2018). *MIDC SPA Calculator*. Retrieved 04 20, 2018, from <https://midcdmz.nrel.gov/solpos/spa.html>.
- Olesen, G., Kvetny, M., & la Rovere, E. (2015). *Sustainable Energy Vision 2050*. Retrieved February 20, 2018, from <http://www.inforse.org/europe/VisionWorld.htm>.
- Orshan, M. (2010). *YouTube – Universal solar tracker*. Retrieved March 19, 2018, from [https://www.youtube.com/watch?v=\\_\\_RmvTdQFJ4](https://www.youtube.com/watch?v=__RmvTdQFJ4).
- Ortega, J. I., Burgaleta, J. I., & Téllez, F. M. (2008). Central receiver system solar power plant using molten salt as heat transfer fluid. *Journal of Solar Energy Engineering*, 130(2), 024501.
- Osuna, R., Olavarria, R., Morillo, R., Sanchez, M., Cantero, F., Fernandez-Quero, V., . . . Talegon, J. (2006). PS10, construction of a 11MW solar thermal tower plant in Seville, Spain. *Proceedings of 13th SolarPACES Conference*. Seville, Spain, 20–23 June.
- Pacheco, J., Bradshaw, R., Dawson, D., De La Rosa, W., Gilbert, R., Goods, S., . . . Prairie, M. (2002). *Final test and evaluation results from the Solar Two Project*. Albuquerque, NM: Sandia National Labs.
- Pacio, J., & Wetzel, T. (2013). Assessment of liquid metal technology status and research paths for their use as efficient heat transfer fluids in solar central receiver systems. *Solar Energy*, 93, 11–22.
- Panwar, N., Kaushik, S., & Kothari, S. (2011). Role of renewable energy sources in environmental protection: a review. *Renewable and Sustainable Energy Reviews*, 15(3), 1513–1524.
- Pifre, A. (1882). A solar printing press. *Nature*, 21(1), 503–504.
- Pitz-Paal, R., Dersch, J., Milow, B., Téllez, F., Ferriere, A., Langnickel, U., . . . Popel, O. (2005). Development steps for concentrating solar power technologies with maximum impact on cost reduction: results of the European ECOSTAR study. *ASME 2005 International Solar Energy Conference*, 773–779.
- Polat, S., Huang, B., Mujumdar, A., & Douglas, W. (1989). Numerical flow and heat transfer under impinging jets, a review. *Annual Review of Numerical Fluid Mechanics and Heat Transfer*, 2, 157–197.
- Price, H., Lupfert, E., Kearney, D., Zarza, E., Cohen, G., Gee, G., & Mahoney, R. (2002, May 1). Advances in parabolic trough solar power technology. *Journal of Solar Energy Engineering*, 124(2), 109–125.

- Proud Green Building. (2017). *Mirage to reality: Energy Department investment brings Crescent Dunes to life*. Retrieved March 19, 2018, from <https://www.proudgreenbuilding.com/news/mirage-to-reality-energy-department-investment-brings-crescent-dunes-to-life/>.
- Pye, J., Zheng, M., Asselineau, C., & Coventry, J. (2014). An exergy analysis of tubular solar-thermal receivers with different working fluids. *Proceedings of 20th SolarPACES Conference*. Beijing, China, 16–19 September 2014.
- Rabl, A. (1976). Comparison of solar concentrators. *Solar Energy*, 18(2), 93–111.
- Ramos, A., & Ramos, F. (2012). Strategies in tower solar power plant optimization. *Solar Energy*, 86(9), 2536–2548.
- Reda, I., & Andreas, A. (2004). Solar position algorithm for solar radiation applications. *Solar Energy*, 76, 577–589.
- Reicosky, D., Winkelman, L., Baker, J., & Baker, D. (1989). Accuracy of hourly air temperatures calculated from daily minima and maxima. *Agricultural and Forest Meteorology*, 46(3), 193–209.
- Rightley, M., Matthews, L., & Mulholland, G. (1992). Experimental characterization of the heat transfer in a free-falling-particle receiver. *Solar Energy*, 48(6), 363–374.
- Rodríguez-Sánchez, M., Marugan-Cruz, C., Acosta-Iborra, A., & Santana, D. (2014). Comparison of simplified heat transfer models and CFD simulations for molten salt external receiver. *Applied Thermal Engineering*, 73(1), 993–1005.
- Rodríguez-Sánchez, M., Sánchez-González, A., Acosta-Iborra, A., & Santana, D. (2017). Variable velocity in solar external receivers. *AIP Conference Proceedings*, 1850, p. 030043.
- Rodríguez-Sánchez, M., Sánchez-González, A., Marugán-Cruz, C., & Santana, D. (2014). New designs of molten-salt tubular-receiver for solar power tower. *Proceedings of the 19th SolarPACES Conference*. Las Vegas, USA, 17–20 September 2013.
- Rodríguez-Sánchez, M., Soria-Verdugo, A., Almendros-Ibáñez, J. A., Acosta-Iborra, A., & Santana, D. (2014). Thermal design guidelines of solar power towers. *Applied Thermal Engineering*, 63(1), 428–438.
- Röger, M., Amsbeck, L., Gobereit, B., & Buck, R. (2011). Face-down solid particle receiver using recirculation. *Journal of Solar Energy Engineering*, 133(3), 031009.
- Romero, M., & Steinfeld, A. (2012). Concentrating solar thermal power and thermochemical fuels. *Energy and Environmental Science*, 5(11), 9137–9674.
- Romero, M., Buck, R., & Pacheco, J. E. (2002). An update on solar central receiver systems, projects and technologies. *Journal of Solar Energy Engineering*, 124(2), 98–108.
- Romero, M., Marcos, M. J., Osuna, R., & Fernandez, V. (2000). Design and implementation plan of a 10 MW solar tower power plant based on volumetric-air technology in Seville (Spain). *Proceedings of the Solar 2000 Solar Power Life – Share the Energy*.

- Ross, M. (2013). *How the 1973 oil embargo saved the planet*. Retrieved March 1, 2018, from <https://www.foreignaffairs.com/articles/north-america/2013-10-15/how-1973-oil-embargo-saved-planet>.
- Roth, G. (1975). *Astronomy: a handbook*. Cambridge, MA: Sky Publishing Corporation.
- Sakakibara, J., & Hishida, K. (1997). Vortex structure and heat transfer in the stagnation region of an impinging plane jet (simultaneous measurements of velocity and temperature field by digital particle image velocimetry and laser induced fluorescence). *International Journal of Heat and Mass Transfer*, 40(13), 3163–3176.
- Sanchez-Gonzalez, A., & Santana, D. (2015). Solar flux distribution on central receivers: a projection method from analytical function. *Renewable Energy*, 74, 576–587.
- Schmitz, M., Schwarzbözl, P., Buck, R., & Pitz-Paal, R. (2006). Assessment of the potential improvement due to multiple apertures in central receiver systems with secondary concentrators. *Solar Energy*, 80(1), 111–120.
- Segal, A., & Epstein, M. (1997). Modelling of solar receiver for cracking of liquid petroleum gas. *Journal of Solar Energy Engineering*, 119(1), 48–51.
- Serrano-López, R., Fradera, J., & Cuesta-López, S. (2013). Molten salts database for energy applications. *Chemical Engineering and Processing: Process Intensification*, 73, 87–102.
- Shpilrain, E. (1991). Solar energy utilization in the USSR. *USSR Energy Conference*, 59–64.
- Singer, C., Buck, R., Pitz-Paal, R., & Müller-Steinhagen, H. (2010). Assessment of solar power tower driven ultrasupercritical steam cycles applying tubular central receivers with varied heat transfer media. *Journal of Solar Energy Engineering*, 132(2), 041010.
- Solaflect Energy. (2018). *Solaflect Energy – Gallery*. Retrieved March 19, 2018, from <http://www.solaflect.com/photos-of-solaflects-tracker-mounted-solar-panels-in-action/>.
- Solargis. (2016). *Solargis*. Retrieved November 23, 2016, from <http://solargis.com/assets/graphic/free-map/DNI/Solargis-World-DNI-solar-resource-map-en.png>.
- SolarPACES. (2018). *Morocco's Noor III solar tower CSP to deliver power by October*. Retrieved March 14, 2018, from <http://www.solarpaces.org/moroccos-noor-iii-solar-tower-csp-deliver-power-october/>.
- Solúcar. (2006). *Final technical progress report: 10 MW solar thermal power plant for Southern Spain*. Retrieved March 14, 2018, from [https://web.archive.org/web/20110811230017/http://ec.europa.eu/energy/res/sectors/doc/csp/ps10\\_final\\_report.pdf](https://web.archive.org/web/20110811230017/http://ec.europa.eu/energy/res/sectors/doc/csp/ps10_final_report.pdf).
- Sørensen, B., & Meibom, P. (2000). A global renewable energy scenario. *International Journal of Global Energy Issues*, 13(1).
- Spellning, J. (2012). *Concentrated solar power. Renewable energy technology*. Stockholm: KTH Institutionen för Energiteknik.
- Spencer, J. (1971). Fourier series representation of the position of the Sun. *Search*, 2(5), 172.

- SQM. (2018). *Concentrated solar power (CSP) systems*. Retrieved February 26, 2018, from [http://www.sqm.com/mv/en-us/products/industrialchemicals/thermo-solarsalts/concentratedsolarpower\(csp\)systems.aspx](http://www.sqm.com/mv/en-us/products/industrialchemicals/thermo-solarsalts/concentratedsolarpower(csp)systems.aspx).
- Stahl, K., Griffin, J., Matson, B., & Pettit, R. (1986). *Optical characterization of solid-particle solar central receiver materials*. Sandiego, CA: Sandia National Labs.
- Starks, P. J., Norman, J. M., Blad, B. L., Walter-Shea, E. A., & Walthall, C. (1991). Estimation of shortwave hemispherical reflectance (Albedo) from bidirectionally reflected radiance data. *Remote Sensing of Environment*, 38(2), 123–134.
- StateImpact. (2012). *Solar power tower to produce enough energy for 180 000 homes*. Retrieved March 26, 2018, from <https://stateimpact.npr.org/pennsylvania/2012/12/17/energy-department-to-fund-projects-integrating-solar-with-fossil-fuel-plants/solar-power-tower-to-produce-enough-energy-for-180000-homes/>.
- Stine, W., & Geyer, M. (2014). *Power from the sun*. Retrieved November 23, 2016, from <http://www.powerfromthesun.net/Book/chapter09/chapter09.html>.
- Swift, L. (1976). Algorithm for solar radiation on mountain slopes. *Water Resources Research*, 12(1), 108–112.
- Tan, T., & Chen, Y. (2010). Review of study on solid particle solar receivers. *Renewable and Sustainable Energy Reviews*, 14(1), 265–276.
- Tan, T., Chen, Y., Chen, Z., Siegel, N., & Kolb, G. J. (2009). Wind effect on the performance of solid particle solar receivers with and without the protection of an aerowindow. *Solar Energy*, 83(10), 1815–1827.
- Tian, Y., & Zhao, C. (2013). A review of solar collectors and thermal energy storage in solar thermal applications. *Applied Energy*, 104, 538–553.
- Timinger, A., Spirkl, W., Kribus, A., & Ries, H. (2000). Optimized secondary concentrators for a partitioned central receiver system. *Solar Energy*, 69(2), 153–162.
- Trieb, F., Schillings, C., O'Sullivan, M., Pregger, T., & Hoyer-Klick, C. (2009). Global potential of concentrating solar power. *Proceedings of the 15th SolarPACES Conference*. Berlin, Germany, 15–18 September 2009.
- Trombe, F. (1957). Solar furnaces and their applications. *Solar Energy*, 1(2–3), 9–15.
- Turchi, C., Mehos, M., Ho, C. K., & Kolb, G. J. (2010). Current and future costs for parabolic trough and power tower systems in the US market. *Proceedings of the 16th SolarPACES Conference*. Perpigan, France, 21–24 September 2010.
- Tyner, C., Kolb, G., Prairie, M., Weinrebe, G., Valverde, A., & Sanchez, M. (1996, 10 16). *Solar power tower development: recent experiences*. Albuquerque, NM: Sandia National Labs. Retrieved March 14, 2018, from <https://www.osti.gov/servlets/purl/505159>.
- Uddin, N. (2008). *Dissertation – Turbulence modelling of complex flows in CFD*. University of Stuttgart: Faculty of Aerospace Engineering and Geodesy.

- United Nations. (2015). Paris Agreement. Paris: United Nations.
- US Atmosphere. (1976). *US standard atmosphere*. Washington, DC: Government Printing Office.
- Vant-Hull, L. (2013). Issues with beam-down concepts. *Energy Procedia, Proceedings of the SolarPACES 2013 International Conference*, 49, 257-264.
- Vant-Hull, L. L., & Hildebrandt, A. F. (1976). Solar thermal power system based on optical transmission. *Solar Energy*, 18(1), 31–39.
- Vast Solar. (2019, February 12). *Vast Solar Projects*. Retrieved from Vast Solar: <https://vastolar.com/projects/>
- Viskanta, R. (1993). Heat transfer to impinging isothermal gas and flame jets. *Experimental Thermal and Fluid Sciences*, 6(2), 111–134.
- Vittitoe, C. N., & Biggs, F. (1977). *HELIOS: a computer program for modeling the solar thermal test facility: a users guide*. Albuquerque, NM: Sandia National Labs.
- Walzel, M. D., Lipps, F. W., & Vant-Hull, L. L. (1977). A solar flux density calculation for a solar tower concentrator using a two-dimensional hermite function expansion. *Solar Energy*, 19(3), 239–253.
- Wang, W. (2015). *Development of an impinging receiver for solar dish-Brayton systems*. KTH Royal Institute of Technology.
- Wei, X., Lu, Z., Wang, Z., Yu, W., Zhang, H., & Yao, Z. (2010). A new method for the design of the heliostat field for solar tower power plant. *Renewable Energy*, 35(9), 1970–1975.
- Wendelin, T., Dobos, A., & Lewandowski, A. (2013). SolTrace: a ray-tracing code for complex solar optical system. *NREL – Technical Report*, 303, 275–300.
- White, F. (2011). *Fluid mechanics* (7th ed.). New York, NY: McGraw-Hill.
- Wikipedia. (2018). *Heliostat*. Retrieved March 15, 2018, from <https://en.wikipedia.org/wiki/Heliostat>.
- Wikipedia. (2018). *Stewart platform*. Retrieved March 19, 2018, from [https://en.wikipedia.org/wiki/Stewart\\_platform#/media/File:Hexapod\\_general\\_Anim.gif](https://en.wikipedia.org/wiki/Stewart_platform#/media/File:Hexapod_general_Anim.gif).
- Winston, R., & Hiterberger, H. (1975). Principles of cylindrical concentrators for solar energy. *Solar Energy*, 17(4), 255–258.
- Wordpress.com. (2013). *The solar power towers of Seville, Spain*. Retrieved March 19, 2018, from <https://kitskinny.wordpress.com/2013/09/06/the-solar-power-towers-of-seville-spain/>.
- WorldWeatherOnline.com. (2018). *Historical average weather*. Retrieved January 9, 2018, from <https://www.worldweatheronline.com/seville-weather-averages/andalucia/es.aspx>.
- Wu, S., Xiao, L., Cao, Y., & Li, Y. (2010). A parabolic dish/AMTEC solar thermal power system and its performance evaluation. *Applied Energy*, 87(2), 452–462.

- Wu, W., Gobereit, B., Singer, C., Amsbeck, L., & Pitz-Paal, R. (2011). Direct absorption receivers for high temperatures. *Proceedings of the 17th SolarPACES Conference*. Granada, Spain, 20–23 September 2011.
- Yan, X., & Saniei, N. (1998). Heat transfer measurements from a flat plate to a swirling impinging jets. *Heat Transfer*, 5, 497–502.
- Yang, K., Huang, G., & Tamai, N. (2001). A hybrid model for estimating global solar. *Solar Energy*, 70(1), 13–22.
- Yu, Q., Wang, Z., & Xu, E. (2012). Simulation and analysis of the central cavity receiver's performance of solar thermal power tower plant. *Solar Energy*, 86(1), 164–174.
- Zhang, H., Baeyens, J., Degrève, J., & Gacères, G. (2013). Concentrated solar power plants: review and design methodology. *Renewable and Sustainable Energy Reviews*, 22, 466–481.
- Zhu, G., Wendelin, T., Wagner, M., & Kutscher, C. (2014). History, current state, and future of linear Fresnel concentrating solar collectors. *Solar Energy*, 103(1), 639–652.
- Zuckerman, N., & Lior, N. (2006). Jet impingement heat transfer: physics, correlations and numerical modelling. *Advances in Heat Transfer*, 39, 565–631.

## Appendix A Solar Tracking and DNI Iqbal model

### A.1 Solar tracking numerical model

The Iqbal model is defined with the assumption that the earth rotates around the sun in an elliptical orbit and that this orbit remains constant over a long period. In reality, the earth's orbit is influenced by other celestial bodies, but these factors are approximated as negligible. The leap year cycle is also omitted in this model. By using the technique of a Fourier series type of expansion, Spencer (1971) developed an expression for the reciprocal of the square of the earth's radius vector, more commonly known as the eccentricity correction factor of the earth's orbit,  $E_0$ :

$$E_0 = \left(\frac{r_0}{r}\right)^2 = 1.000110 + 0.034221 \cos \Gamma + 0.001280 \sin \Gamma + 0.000719 \cos 2\Gamma + 0.000077 \sin 2\Gamma \quad (\text{A-1})$$

The eccentricity correction factor is defined in terms of the day angle,  $\Gamma$ . The day angle, in radians, is expressed by the following:

$$\Gamma = 2\pi \frac{d_n - 1}{365}, \quad (\text{A-2})$$

where  $d_n$  refers to a Julian Day, ranging from 1 on 1 January to 365 on 31 December.

Accurately modelling the sun requires defining time equally accurately. A solar day is the interval of time as the sun appears to complete one cycle around a stationary observer on earth, and although it is commonly thought to be 24 hours, this is not necessarily the case. The days vary throughout the year, with the following two being the principle factors:

- The earth sweeps unequal areas on the ecliptic plane as it revolves around the sun.
- The earth's axis is tilted with respect to the ecliptic plane.

These factors could cause discrepancies of up to 16 minutes. Discrepancies are accounted for using the equation of time,  $E_t$  (in minutes), and is measured relative to a perfect uniform terrestrial motion. As formulated by Spencer (1971) (rectified in 1998 by M. Oglesby):

$$E_t = 229.18[0.0000075 + 0.001868 \cos \Gamma - 0.032077 \sin \Gamma - 0.014615 \cos 2\Gamma - 0.04089 \sin 2\Gamma] \quad (\text{A-3})$$

According to literature, the formulated equation is accurate to an error of 0.0025 rad, which is equivalent to approximately 35 seconds. The eccentricity of time, the Iqbal model compared to the NREL's SPA model, is displayed graphically in Figure A.1. From the figure, it is clear that the Iqbal model compares well with NREL's model.

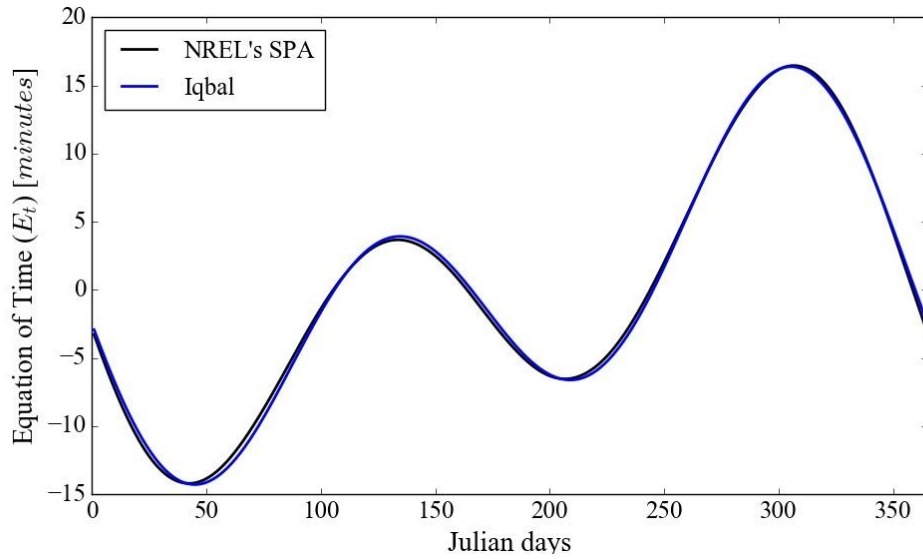


**Figure A.1: A graphic representation of the eccentricity of time ( $E_t$ ) as a function of Julian days.**

Time, as we know it on earth, can also be divided into two entities: local apparent time (LAT) (also called true solar time (TST) in some literature) and local standard time (LST). These two methods of keeping track of time came about by simplifying time on a global scale. The earth is divided into standardised time zones, which correlate with the international standard meridians. These meridian lines are multiples of  $15^\circ$  east or west of Greenwich, England. This conveniently divides the globe into 24 sections, hence 24 one-hour sections. Countries are assigned a time zone depending on their location. This could also change if the country applies daylight savings time. This is called LST. The LST method could cause challenges, since the time zones are not continuous. Therefore, discrepancies follow whenever the location of interest is not on the meridian. Unfortunately, much weather-related data (such as temperature and wind velocities) is recorded using this time-logging method. LAT uses the sun's location to keep track of time, which is a more convenient method, especially for solar tracking. The following equation is therefore used to convert LST to LAT:

$$LAT = LST + \frac{4(L_e - L_s) + E_t}{60}, \quad (\text{A-4})$$

where  $L_e$  is the local longitude and  $L_s$  is the standard longitude.

If one could imagine the sun revolving around the earth, the plane along which it revolves would be called the ecliptic plane. The earth's polar axis is inclined at an angle of approximately  $23.5^\circ$  from the normal to the ecliptic plane and stays constant throughout the year. If one were to draw a line between the centres of the sun and the earth, the angle that is formed between this line and the equatorial plane (the plane that cuts through the equator) is an ever-changing variable. This angle is of great importance for solar tracking and is called the solar declination,  $\delta$ . The solar declination angle is illustrated in Figure A.2.

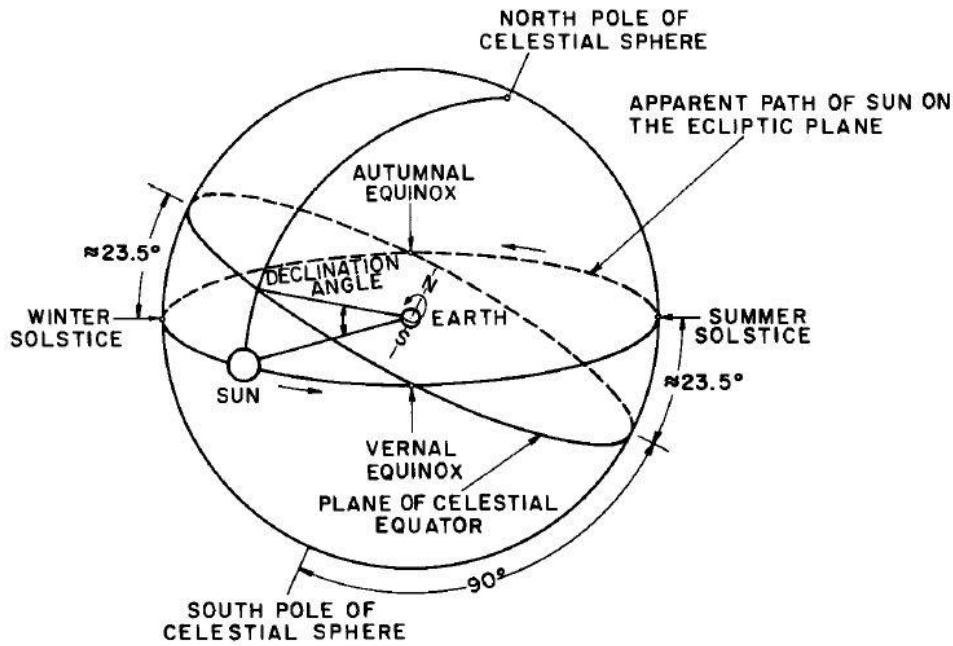


Figure A.2: A schematic illustration of a celestial sphere showing the sun's apparent path around the earth (Iqbal, 1983).

The angle varies between  $+23.5^\circ$  at the summer solstice and  $-23.5^\circ$  at the winter solstice, reaching zero at the vernal and autumnal equinoxes. Take note that the seasonal terms refer to the northern hemisphere for the sake of consistency in literature. Many authors have developed expressions for this declination (Roth, 1975). The following is the expression of Spencer (1971) in degrees:

$$\delta = \frac{180}{\pi} [0.006918 - 0.399912 \cos \Gamma + 0.070257 \sin \Gamma - 0.006758 \cos 2\Gamma + 0.000907 \sin 2\Gamma - 0.002697 \cos 3\Gamma + 0.00148 \sin 3\Gamma] \quad (\text{A-5})$$

This equation is also constructed using the Fourier series expansion technique, with a maximum error of 0.0006 rad. In reality, the solar declination changes slightly over a four-year period due to the leap year cycle. This is neglected in the formulation of the expression. For the expressions that follow, it is also assumed that the solar declination stays constant throughout the day. The maximum error value that can be obtained is less than  $0.5^\circ$  (which occurs at the equinoxes).

With the solar declination expressed, one can calculate the trigonometric relationships between the solar position in the sky and the surface coordinates on earth. For this to be done, one should first define the variables to be considered. This could be done as illustrated by Iqbal (1983) and depicted in Figure A.3.

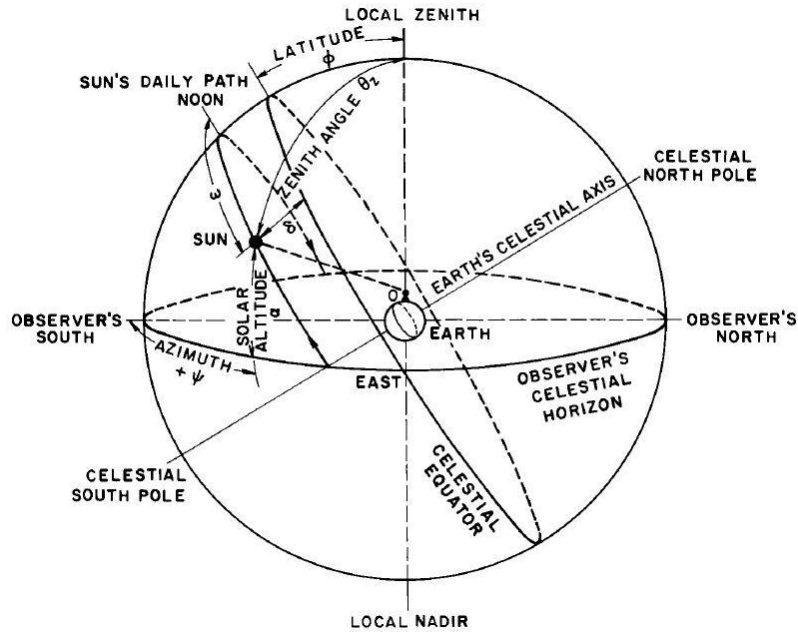


**Figure A.3:** A schematic illustration of the celestial sphere and sun's coordinates relative to a fixed point on earth at point O (Iqbal, 1983).

As shown in Figure A.3, the earth is positioned at the centre of a celestial sphere. The observer positioned on the earth's surface at point O has a corresponding position in the celestial sphere called the observer's or local zenith. The opposite point is called the nadir. The observer's celestial horizon is the circle on the plane that forms normal to the axis between the zenith and the centre of the earth. The zenith angle,  $\theta$ , is the angle between the local zenith and the line joining the observer's point and the sun, an angle that can vary between  $0^\circ$  and  $90^\circ$ . The solar altitude (also called the solar elevation),  $\alpha$ , is the complement of the zenith angle. The solar azimuth,  $\psi$ , is the angle measured at the local zenith between the plane formed by the line between the observer and the sun, the line between the observer and the local zenith, and the plane formed by the circle passing through the observer's poles and the zenith (observer's meridian). The solar azimuth values vary in the range of  $\pm 180^\circ$ , with east being positive, west being negative and south being zero. The hour angle,  $\omega$ , is the angle measured at the celestial pole between the observer's meridian and the solar meridian. The hour angle is zero at solar noon and changes  $15^\circ$  every hour, with morning being negative and afternoon being positive. The geographical latitude is represented by the symbol  $\phi$  (north being positive).

With these variables defined, trigonometric relations between the centre of the solar disk of the sun and the horizontal surface of the observer can be made. These relations are well known, and are summarised as follows:

$$\omega = 15(12 - LAT) \tag{A-6}$$

as well as,

$$\theta = \cos^{-1}(\sin \delta \sin \phi + \cos \delta \cos \phi \cos \omega) \tag{A-7}$$

and,

$$\psi = \cos^{-1}\left(\frac{\sin \alpha \sin \phi - \sin \delta}{\cos \alpha \cos \phi}\right). \tag{A-8}$$

The earth's refractive atmosphere is assumed to have a negligible influence on the apparent solar altitude, and according to the errors given by Iqbal, this assumption is valid, with the error ranging from 0' at noon to 34' at the horizon. The apparent solar altitude is, however, slightly dependent on the atmospheric temperature and pressure. This dependence is only noticeable at degrees of 80° to 90°, where the effect is at its maximum.

The day length ( $N_d$ ) can also be calculated for a specific day, and is calculated in hours as follows:

$$N_d = \frac{2}{15} \cos^{-1}(-\tan \phi \tan \delta) \quad (\text{A-9})$$

The time of sunrise and sunset (LAT) is then easily calculated using the following expression:

$$t_{\text{sunrise,sunset}} = 12 \mp \frac{N_d}{2} \quad (\text{A-10})$$

## A.2 Direct normal irradiance model

As explained in Chapter 3.3 the Iqbal Parameterisation C cloudless sky DNI model consists of the following parameters:

- Transmittance to direct irradiance due to Rayleigh scattering effects of air molecules,  $\tau_r$
- Transmittance to direct irradiance due to absorption by ozone,  $\tau_o$
- Transmittance to direct irradiance due to absorption by uniformly mixed gases,  $\tau_g$
- Transmittance to direct irradiance due to absorption by water vapour,  $\tau_w$
- Transmittance to direct irradiance due to attenuation by aerosols,  $\tau_a$

This will be discussed in the following subsections.

### Rayleigh scattering effect of air molecules

The transmittance to direct irradiance due to the Rayleigh scattering effects of air molecules ( $\tau_r$ ) is a function of the relative optical air mass ( $m_a$ ). When radiation travels through a medium, in our case the atmosphere, the molecules attenuate energy. The larger the number of molecules, which is also a function of the distance through the medium, the greater the attenuation for a single solar ray. The optical mass is simply stated as the density ( $\rho$ ) of the medium integrated over its path length ( $s$ ), and can be expressed as follows:

$$m_{act} = \int_0^{\infty} \rho ds \quad (\text{A-11})$$

where the integration is simply from the upper limits of the atmosphere to the earth's surface. Since the slant path of the solar ray depends on the wavelength, the equation only applies to monochromatic light. The relative optical mass ( $m_r$ ) is defined as the ratio of the optical path along the oblique trajectory to the vertical path in the zenith direction, or analytically expressed as follows:

$$m_r = \int_0^{\infty} \rho ds / \int_0^{\infty} \rho dz \quad (\text{A-12})$$

where  $dz$  would represent the zenith direction. To further solve this equation, the density variation of an actual atmosphere is required. This information is generally available, although only for a standard atmosphere. Kasten (1965) solved this equation by using the air density profile of the Air Research and

Development Command (ARDC) atmosphere model (1959), as well as the refractive index at wavelength  $0.7 \mu\text{m}$ . From tables, the following formula was approximated:

$$m_r = (\cos \theta + 0.15(93.885 - \theta)^{-1.253})^{-1} \quad (\text{A-13})$$

The accuracy of this formula is better than 0.1% for zenith angles up to  $86^\circ$ . These values are, however, only applicable for standard sea level air pressure ( $P_0 = 101.325 \text{ kPa}$ ). This should hence be modified using the following expression to obtain the relative optical air mass:

$$m_a = m_r \left( \frac{P}{P_0} \right) \quad (\text{A-14})$$

The local pressure at certain altitudes can be read from tables. White (2011), however, gives an accurate relation, which is a function of the altitude above sea level:

$$P = P_0 \left( 1 - \frac{BZ_{alt}}{T_0} \right)^{\frac{g}{RB}} \quad (\text{A-15})$$

where the following standard values are assumed, as given by the international agreement (US Atmosphere, 1976):

$$T_0 = 288.16 \text{ K}$$

$$B = 0.00650 \text{ K/m}$$

$$R = 287 \text{ m}^2/(\text{s}^2 \cdot \text{K})$$

The expression is only valid for the lower portion of the atmosphere, called the troposphere, up to an altitude of 11 km. This is obviously more than acceptable for the analyses, since the locations of solar farms rarely exceed altitudes of 3 000 m.

The transmittance to direct irradiance due to Rayleigh scattering effects of air molecules ( $\tau_r$ ) for parameterisation model C is then expressed as a function of the relative optical air mass ( $m_a$ ) as follows:

$$\tau_r = e^{-0.0903m_a^{0.84}(1+m_a-m_a^{1.01})} \quad (\text{A-16})$$

### Absorption by uniformly mixed gases

The transmittance to direct irradiance due to the absorption by uniformly mixed gases ( $\tau_g$ ) is also a function of the relative optical air mass. Iqbal's parameterisation model C proposed the following formula to define this transmittance:

$$\tau_g = e^{-0.0127 \cdot m_a^{0.26}} \quad (\text{A-17})$$

### Absorption by ozone

The transmittance to direct irradiance due to absorption by ozone ( $\tau_o$ ) is, like the transmittance due to the absorption by mixed gases, a function of the relative optical mass, but more specifically for ozone. The reason the relative optical ozone mass is treated separately to that of the clean, dry air is because of the distinct different concentration profile that ozone has compared to the rest of the air molecules. Ozone can also be handled separately, since the distribution is conveniently well specified.

The transmittance due to absorption by ozone can be written as follows:

$$\tau_o = 1 - \alpha_o \quad (\text{A-18})$$

where  $\alpha_o$  is the absorptance of the direct irradiance by ozone. The reason for formulating  $\tau_o$  in terms of  $\alpha_o$  has to do with the fact that several researchers have studied the absorptance of the direct irradiance of ozone. For Iqbal's parameterisation model C, the following expression for absorptance by ozone was proposed:

$$\alpha_o = 0.1611 \cdot U_3(1 + 139.48U_3)^{-0.3035} - 0.002715 \cdot U_3(1 + 0.044U_3 + 0.0003U_3^2)^{-1} \quad (\text{A-19})$$

where  $U_3$  is the relative optical path length of ozone, which is given by:

$$U_3 = l \cdot m_r \quad (\text{A-20})$$

with  $l$  representing the thickness of the vertical ozone layer in centimetres if all the ozone in a vertical column of unit area was brought to normal temperature and surface pressure (NTP). For the Iqbal model, there is no proposed expression to estimate the ozone thickness. In a model proposed by Yang, Huang and Tamai (2001), an expression was given to estimate the thickness of the ozone layer. This expression would simplify analyses, hence it was decided to use this expression, which is:

$$l = 0.44 - 0.16 \sqrt{\left(\frac{\phi - 80}{60}\right)^2 + \left(\frac{y - 120}{263 - \phi}\right)^2} \quad (\text{A-21})$$

with

$$y = d_n \quad \text{for} \quad d < 300$$

$$y = d_n - 366 \quad \text{for} \quad d \geq 300$$

This expression is hence a function of the latitude ( $\phi$ ) as well as the day of the year.

### Absorption by water vapour

The transmittance to direct irradiance due to absorption by water vapour ( $\tau_w$ ) is also defined in terms of its absorptance ( $\alpha_w$ ), for the same reason as with the transmittance due to the absorption by ozone, which is that much research has already been done to determine correlations for the absorptance of these media. For the sake of completeness, transmittance in terms of absorptance for water vapour is given:

$$\tau_w = 1 - \alpha_w \quad (\text{A-22})$$

The expression for  $\alpha_w$  proposed by Iqbal is given as follows:

$$\alpha_w = 2.4959 \cdot U_1[(1 + 79.034U_1)^{0.6828} + 6.385U_1]^{-1} \quad (\text{A-23})$$

with  $U_1$  being the pressure-corrected relative optical path length of precipitable water, defined similarly as  $U_3$ , which is given by:

$$U_1 = w \cdot m_r \quad (\text{A-24})$$

where  $w$  is the reduced precipitable water in centimetres. Leckner (1978) presented the following formula, which expresses precipitable water in terms of relative humidity ( $\phi_r$ ):

$$w = 0.493 \left( \frac{\phi_r p_s}{T} \right) \quad (\text{A-25})$$

with  $T$  representing the ambient temperature in Kelvin, and  $p_s$  representing the partial pressure of water vapour in saturated air. The following semi-empirical equation expresses this:

$$p_s = e^{26.23 - \frac{5416}{T}} \quad (\text{A-26})$$

### Attenuation by aerosols

This model's transmittance to direct irradiance due to attenuation by aerosols ( $\tau_a$ ) is based on spectral attenuation at the two wavelengths commonly used by meteorological networks, 0.38 and 0.5  $\mu\text{m}$ . These are the wavelengths at which there is minimal molecular (ozone specifically) absorption. There are, however, equations available that express the aerosol transmittance in terms of the Ångström's turbidity ( $\beta$ ), which is a function of the visibility, and  $\alpha$ , which represents the average particle size in the atmosphere. Mächler (1983) proposed the following expression:

$$\tau_a = (0.12445\alpha - 0.0162) + (1.003 - 0.125\alpha) \cdot e^{-\beta m_a (1.089\alpha + 0.5123)} \quad (\text{A-27})$$

$\alpha$  can be assumed to be the value of 1.3, while the Ångström's turbidity can be equated using the equation developed by McClatchey and Selby (1972) and others. The equation, however, when compared to actual data from that approximate region, was not adequate. The value was therefore assumed to be constant with a value of  $\beta = 0.07$ , according to values obtained by Louche, Maurel, Simonnot, Peri and Iqbal (1987).

## Appendix B Transformation from mesh element to SolTrace primitive geometry

Due to a lack of proper documentation on the transformation of primitive geometries in SolTrace, the following description is provided, with an irregular triangle being used as an example.

The information needed to define a typical flat irregular triangle in SolTrace is the coordinates, aim points, the rotation around the z-axis, as well as the coordinates of each corner of the triangle on an x-y plane. The problem with this way of defining the element aperture is that one is unable to clarify how the transformation occurs without documentation. If one assumes that the translation occurs after the rotation around the origin, there are still at least 12 different ways of rotating the element. This is if one assumes that the rotation occurs using either one of the two conventions: the Euler angle or the Tait-Bryan angle rotations (both providing six possible sequences of rotation axes).

This documentation provides the reader with the procedure of transforming the element where it lies in its position that one would analyse to the position where one could obtain the information needed as input for SolTrace.

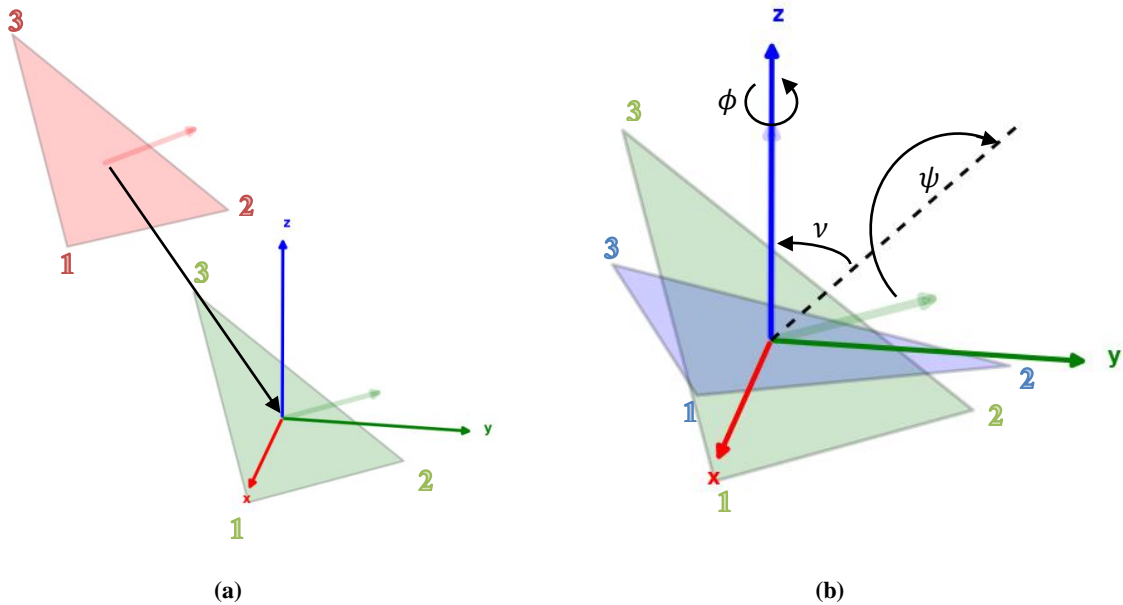


Figure B.1: The transformation of a mesh element to a SolTrace primitive irregular triangle illustrated with the image on the left: (a): displaying the translation to the origin and the picture on the right; and (b): displaying the rotation around the origin.

One needs to define a reference point for the object to start. This reference point around which the object will rotate is needed. For simplicity, the author decided to use the centroid of the triangle as reference point by taking the average of the coordinates of the three corners of the triangle. The defined reference point will be used as input values for the x-, y- and z-coordinates in the SolTrace System Stage section. The element is then translated to the origin point by subtracting the reference point's coordinates from each corner's coordinates. This is formulated in Equation (B-1) and illustrated in Figure B.1a.

$$\begin{bmatrix} x \\ y \\ z \end{bmatrix}_{\text{translate}} = \begin{bmatrix} x \\ y \\ z \end{bmatrix}_{\text{corner}} - \begin{bmatrix} x \\ y \\ z \end{bmatrix}_{\text{ref}} \quad (\text{B-1})$$

The normal vector of the triangle plane can now be calculated by having the cross product of the two vectors that move from one corner to the other two corners. For simplicity, it is assumed that the corner one is using as the point of origin is labelled 1, and the other two corners are labelled 2 and 3. The cross product, which also represents the normal vector of the plane, is then calculated as follows:

$$\vec{v}_{normal} = \langle x_1 - x_2, y_1 - y_2, z_1 - z_2 \rangle \times \langle x_2 - x_3, y_2 - y_3, z_2 - z_3 \rangle \quad (\text{B-2})$$

The aim points that will be used in SolTrace are then calculated as follows:

$$\begin{bmatrix} x \\ y \\ z \end{bmatrix}_{aim} = \begin{bmatrix} x \\ y \\ z \end{bmatrix}_{ref} + \begin{bmatrix} v_x \\ v_y \\ v_z \end{bmatrix}_{normal} \quad (\text{B-3})$$

With the coordinates and aim points calculated, the next step is to rotate the geometry. In this instance, rotation is defined by three variables,  $\phi$ ,  $\nu$  and  $\psi$ . Consider the illustration given in Figure B.1b.

- $\phi$  represents the angle of rotation about the z-axis, also known as roll
- $\nu$  represents the angle of rotation about the y-axis, also known as pitch
- $\psi$  represents the angle of rotation about the x-axis, also known as yaw

Firstly, it is assumed that there is no rotation about the z-axis. One can therefore assume that the value corresponding to the rotation around the z-axis ( $\phi$ ) is zero. The other two variables are calculated as follows:

The normal vector's ( $v_{normal}$ ) x and z components are used to form a new vector that represents the vector that would form after the pitch rotation takes place. The new vector, represented as  $v_\nu$ , is constructed as a unit vector as follows:

$$v_\nu = \frac{\langle v_{normal,x}, 0, v_{normal,z} \rangle}{\sqrt{v_{normal,x}^2 + v_{normal,z}^2}} \quad (\text{B-4})$$

The angle  $\nu$  is then calculated as follows:

$$\nu = \sin^{-1} \left( \frac{v_{\nu,x}}{\sqrt{v_{\nu,x}^2 + v_{\nu,z}^2}} \right) \quad (\text{B-5})$$

One could use the following equation to calculate the yaw angle ( $\psi$ ):

$$\psi = -\cos^{-1}(v_\nu \cdot v_{normal}) \quad (\text{B-6})$$

With the angles of rotations calculated, one can calculate the rotation matrices for each axis. These are represented with the following three forms of rotation matrices:

$$\begin{aligned}
 R_z(\phi) &= \begin{bmatrix} \cos \phi & -\sin \phi & 0 \\ \sin \phi & \cos \phi & 0 \\ 0 & 0 & 1 \end{bmatrix} \\
 R_y(\nu) &= \begin{bmatrix} \cos \nu & 0 & \sin \nu \\ 0 & 1 & 0 \\ -\sin \nu & 0 & \cos \nu \end{bmatrix} \\
 R_x(\psi) &= \begin{bmatrix} 1 & 0 & 0 \\ 0 & \cos \psi & -\sin \psi \\ 0 & \sin \psi & \cos \psi \end{bmatrix}
 \end{aligned} \tag{B-7}$$

With the separate rotation matrices calculated, one can calculate one overall rotation matrix as follows:

$$R(\phi, \nu, \psi) = R_z(\phi)R_y(\nu)R_x(\psi) \tag{B-8}$$

The transformed coordinates on the x-y plane can now be calculated using the rotation matrix and the coordinates of the transformed triangle. This is done using the following equation:

$$\begin{bmatrix} x \\ y \\ z \end{bmatrix}_{transform} = \begin{bmatrix} R(\phi, \nu, \psi) \end{bmatrix} \begin{bmatrix} x \\ y \\ z \end{bmatrix}_{translate} \tag{B-9}$$

This equation is used for each corner of the triangle. The transformed coordinates are then used as the x- and y-coordinates in the aperture editor. One will note that the z-coordinate will be zero or close to zero. This is to be expected, since the triangle aperture is meant to be rotated onto the x-y plane.

## Appendix C Model integration

As mentioned in Chapter 2.4, the SolTrace MCRT software enables the user to simulate and analyse the performance of solar systems using primitive geometries to construct the model. It also allows the user to simplify certain tasks by having a built-in scripting platform, which allows the user to define which tasks have to be performed and automated. This is of utmost importance for the user, since the processes to be implemented in this study requires a vast number of variables that would need to be adjusted and changed. The challenge of applying the automation of processes between different platforms, such as linking SolTrace with a general-purpose high-level programming language such as Python, can also be overcome through this scripting platform. These interconnectable tools provide the user with the ease of constructing and integrating the different models, with the focus especially being on integrating the solar tracking, DNI model, solar field layout and receiver design, and performing data analysis and post-processing activities.

This subsection will give a brief explanation of how these processes are interlinked to perform the tasks required to set up the SolTrace simulations, as well as the process of coupling SolTrace to the thermal analysis, which occurs in the ANSYS Fluent environment. Refer to the flow chart depicted in Figure C.1 for a visual description of how the different processes are linked.

The author developed a graphical user interface (GUI) that would be used as a platform through which some variables that are typical for central receiver system analysis could be easily changed. This would also simplify the process of analysis and optimisation, since the GUI centralises everything, giving the user a good overview of what would be analysed. The GUI is divided into four sections: location, plant setup, analysis and post-processing. These sections provide the user with a great variety of options and open-input textboxes, with the location section providing options such as latitude, longitude and time zone. The plant setup allows the user to select a coordinate file for the heliostat field and to define the dimensions of elements such as the tower, the analysis giving solar tracking, DNI and SolTrace setup options, and post-processing, allowing the user to select which files are to be exported. A snapshot of the GUI setup is displayed in Figure C.2.

Once the setup has been defined in the GUI simulation setup, the Solve button is selected. This will generate a summary of the information in a text file. This simulation instruction file is central to deliver commands to all other scripts and programs. Together with the simulation instruction file being generated, the script processing the mesh file of the receiver is activated, depending on whether the user selected the receiver to be simulated or not. If this process takes place, the user is asked which parts of the named selections of the design should be simulated. The user will also attribute certain optical properties to the different named selections by selecting the properties from a predefined optical property library listed in a separate Microsoft Excel spreadsheet. The converted information is condensed into a text file that will be fed into SolTrace later.

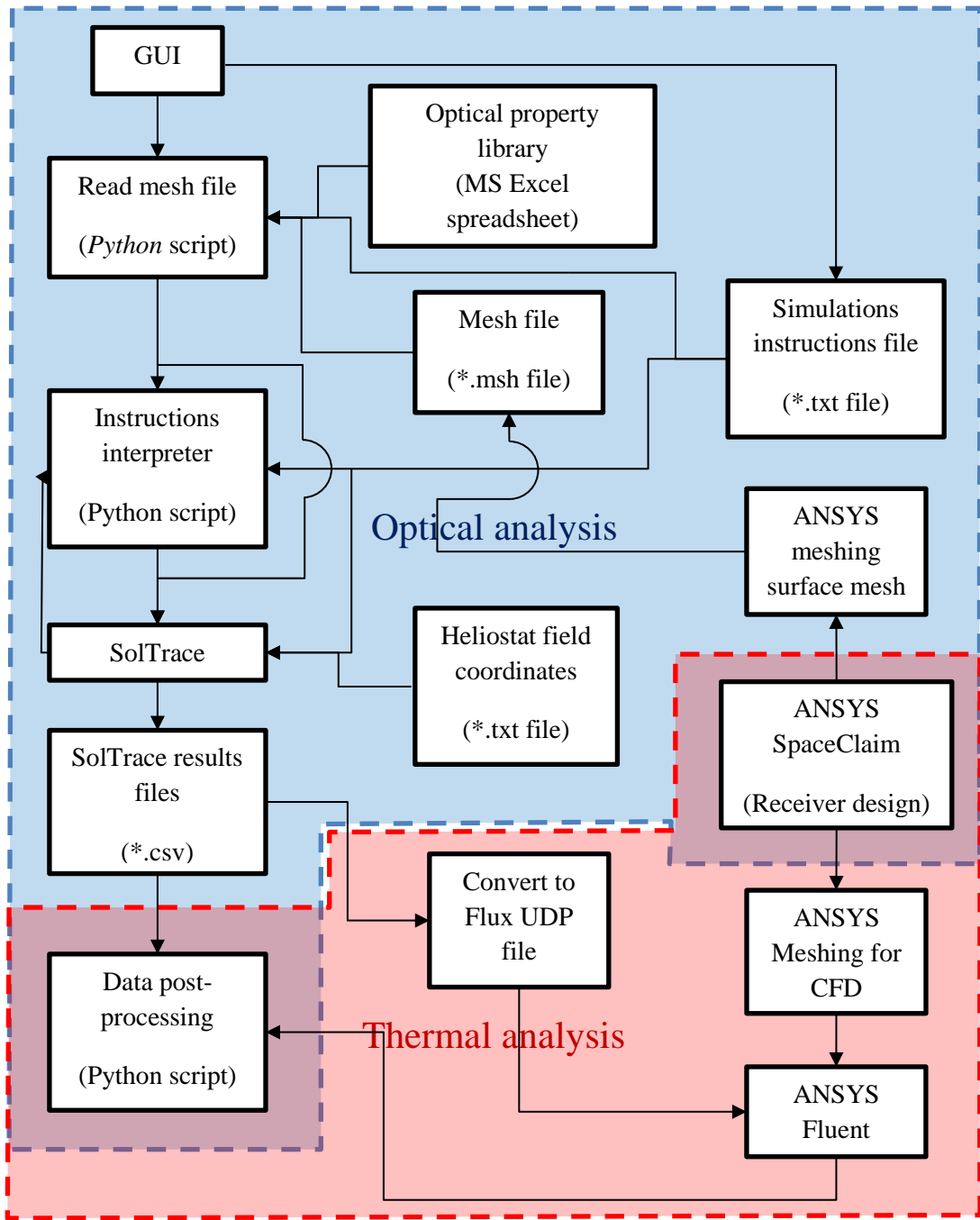
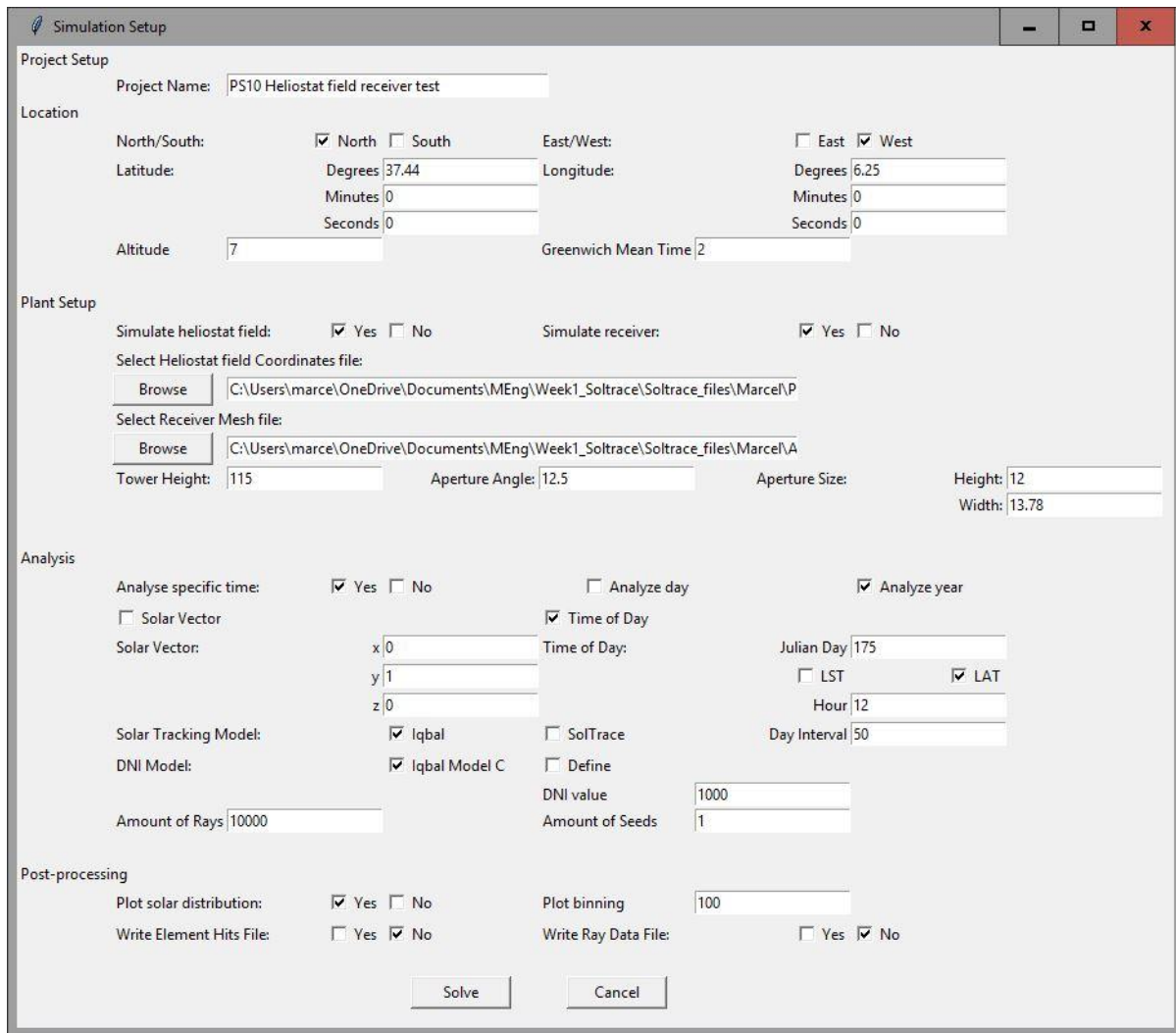


Figure C.1: A flow chart description of the processes followed during the optical and thermal analyses.



**Figure C.2: The GUI that was developed by the author allows the user to set up an analysis on a central platform.**

Once the meshed design conversion process has been completed, the process continues to a Python script that handles other instructions, typically those instructions that require several simulations to take place, such as simulating the heliostat field for an annual cycle. This script also activates the script developed for the SolTrace simulation to take place automatically (refer to Appendix H). Here, again, the simulation instruction file provides the necessary inputs for the correct simulation to take place. If it were selected that the heliostat field should be simulated, the script will prompt the selected heliostat coordinate file to provide the software with the location of every single heliostat. Once the simulation is completed, the SolTrace simulation provides the user with the data files the user selected in the GUI. These files could be used to be converted to an interpolation file that would then be used as a thermal heat source condition for the receiver in the ANSYS Fluent environment during the thermal analysis, or information could be extracted from the files to portray other optical results. Refer to Appendix G for more information regarding the implementation of the variable heat source within ANSYS Fluent.

## Appendix D Polynomial response surface analysis for aperture optimisation

Table D.1: A summary of the norm of the difference between the polynomial response surface approximation and the actual data for different orders

		Polynomial order for the Julian days' axis														
		0	1	2	3	4	5	6	7	8	9	10	11	12	13	14
Polynomial order for the aperture angle direction	0	1292.748	1185.635	902.653	901.930	515.657	429.805	59.010	45.305	37.023	36.282	34.599	29.681	25.541	22.684	20.789
	1	1292.747	1185.633	902.590	901.866	515.531	429.654	57.899	43.848	35.224	34.444	32.666	27.404	22.855	19.609	17.382
	2	1292.725	1185.609	902.558	901.834	515.476	429.588	57.405	43.193	34.405	33.607	31.782	26.343	21.571	18.096	15.655
	3	1292.725	1185.609	902.558	901.834	515.476	429.588	57.404	43.192	34.404	33.606	31.781	26.342	21.570	18.093	15.652
	4	1292.725	1185.609	902.558	901.834	515.476	429.588	57.404	43.192	34.404	33.606	31.781	26.342	21.570	18.092	15.651
	5	1292.725	1185.609	902.558	901.834	515.476	429.588	57.404	43.192	34.404	33.605	31.780	26.341	21.569	18.091	15.650
	6	1292.725	1185.609	902.558	901.834	515.476	429.588	57.404	43.192	34.404	33.605	31.780	26.341	21.569	18.091	15.649
	7	1292.725	1185.609	902.558	901.834	515.476	429.588	57.404	43.192	34.404	33.605	31.780	26.341	21.568	18.090	15.649
	8	1292.725	1185.609	902.558	901.834	515.476	429.588	57.404	43.192	34.404	33.605	31.780	26.341	21.568	18.090	15.648
	9	1292.725	1185.609	902.558	901.834	515.476	429.588	57.404	43.192	34.403	33.605	31.780	26.341	21.568	18.090	15.648
	10	1292.725	1185.609	902.558	901.834	515.476	429.588	57.404	43.192	34.403	33.605	31.780	26.340	21.568	18.090	15.648
	11	1292.725	1185.609	902.558	901.834	515.476	429.588	57.404	43.192	34.403	33.605	31.780	26.340	21.568	18.089	15.648
	12	1292.725	1185.609	902.558	901.834	515.476	429.587	57.404	43.192	34.403	33.605	31.780	26.340	21.568	18.089	15.647
	13	1292.725	1185.609	902.558	901.834	515.476	429.587	57.404	43.192	34.403	33.605	31.779	26.340	21.567	18.089	15.647
	14	1292.725	1185.609	902.558	901.834	515.476	429.587	57.404	43.192	34.403	33.605	31.779	26.340	21.567	18.089	15.647

If one considers the results displayed in Table D.1, it will be noted that an increase in the order for the polynomial shows a decrease in the norm, meaning that the response surface more accurately represents the data. It is, however, not necessary to take the highest order to construct the response surface, and in some cases, it might provide a misrepresented response surface if the order is too high. It was hence decided to choose an order two orders higher than the minimum. When considering the order in the direction of the aperture angle, there is a relatively major drop from the first to the second order. An order to the power of 4 was therefore selected. The polynomial order for the Julian days' axis sees a significant drop in the norm from the fifth to the sixth order, therefore choosing two orders above the sixth order to ensure accuracy (an order of 8 in the direction of the Julian days' axis).

## Appendix E Sensitivity studies on the impingement models

To ensure that the validation studies conducted in Chapter 4.3 were done without any unforeseen variable influencing the results, sensitivity studies were conducted on various parameters on the boundary conditions. Inlet boundary conditions would include the velocity profiles and turbulence intensity variations, while sensitivities on the outlet boundary conditions would mainly be influenced by the outlet position. The influence of constant properties is also compared to the piecewise-linear interpolation of air properties and its effect on the Nusselt number calculations.

### E.1 Outlet boundary

Since various researchers have tested the flat plate impingement model, there is a proposed minimum boundary distance for the computational domain. There is, however, no proposed boundary distance for the concave surface impingement model. A simple test, in which three distances were tested to evaluate the sensitivity of the outlet boundary, was conducted. The model displayed in Figure 4.15b indicates the outlet boundary that was tested. The user opted for three distances: no boundary ( $0 d$ ),  $1.54 d$  and  $3.08 d$ . With all other variables remaining constant, the following results were obtained (see Figure E.1):

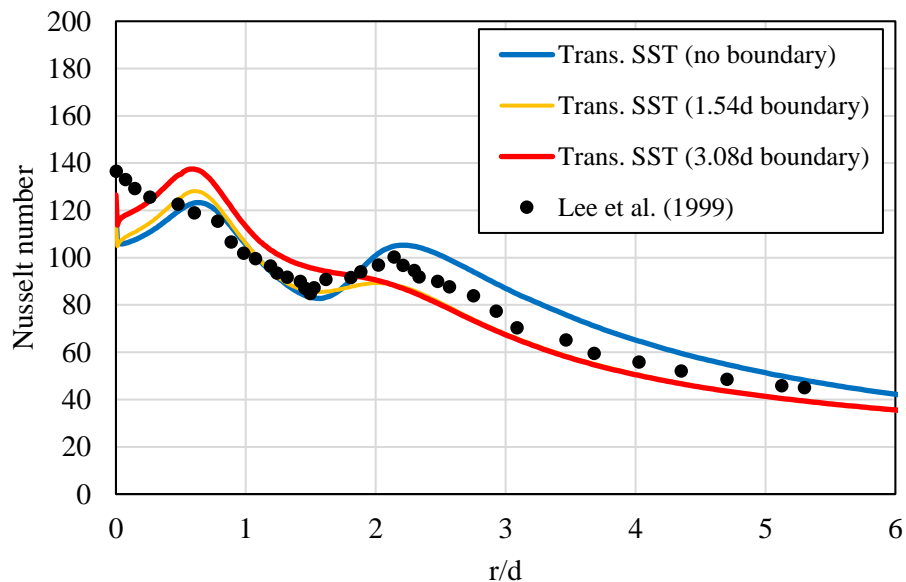


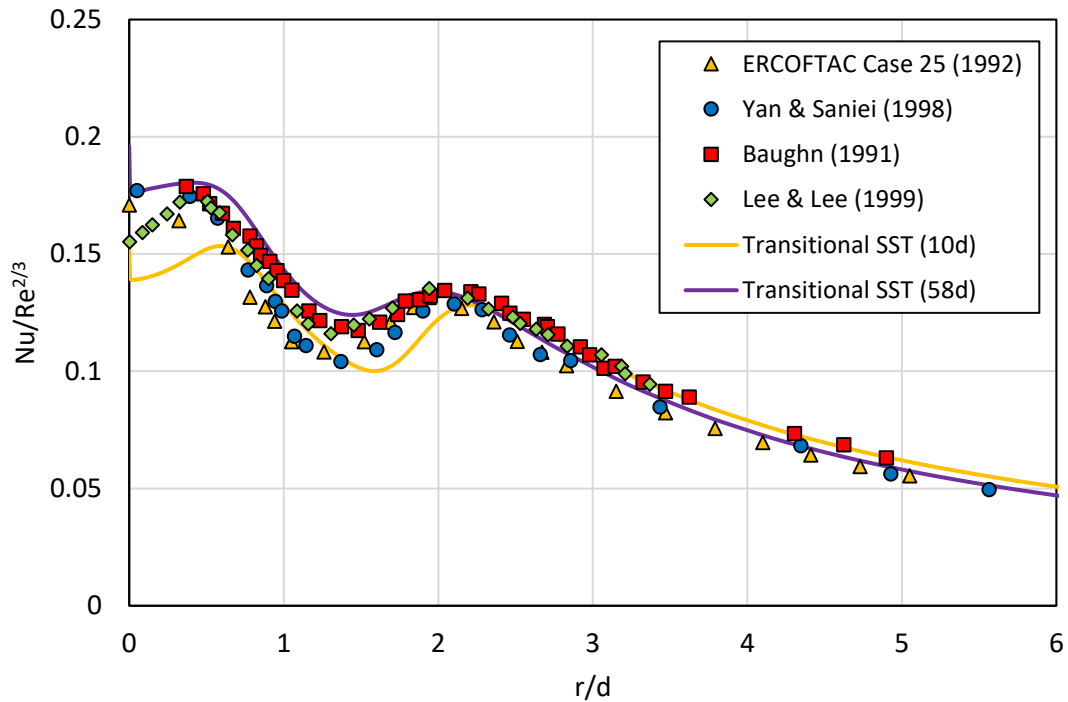
Figure E.1: The outlet boundary length sensitivity study, with the outlet boundary distance being  $0 d$ ,  $1.54 d$  and  $3.08 d$  from the concave surface end.

From the results obtained, it is clear that, scholarly having no simulated boundary, the results are very different to the results of a boundary. Comparing the two models with boundaries, there still seem to be discrepancies in the results, especially for the results between the point of impingement and the non-dimensional radius of 2, although any results further away seem to converge. It was assumed that the biggest boundary tested ( $3.08 d$ ) would not change dramatically for boundaries with larger distances, and therefore it was decided that this value would be sufficient for the validation analysis that followed.

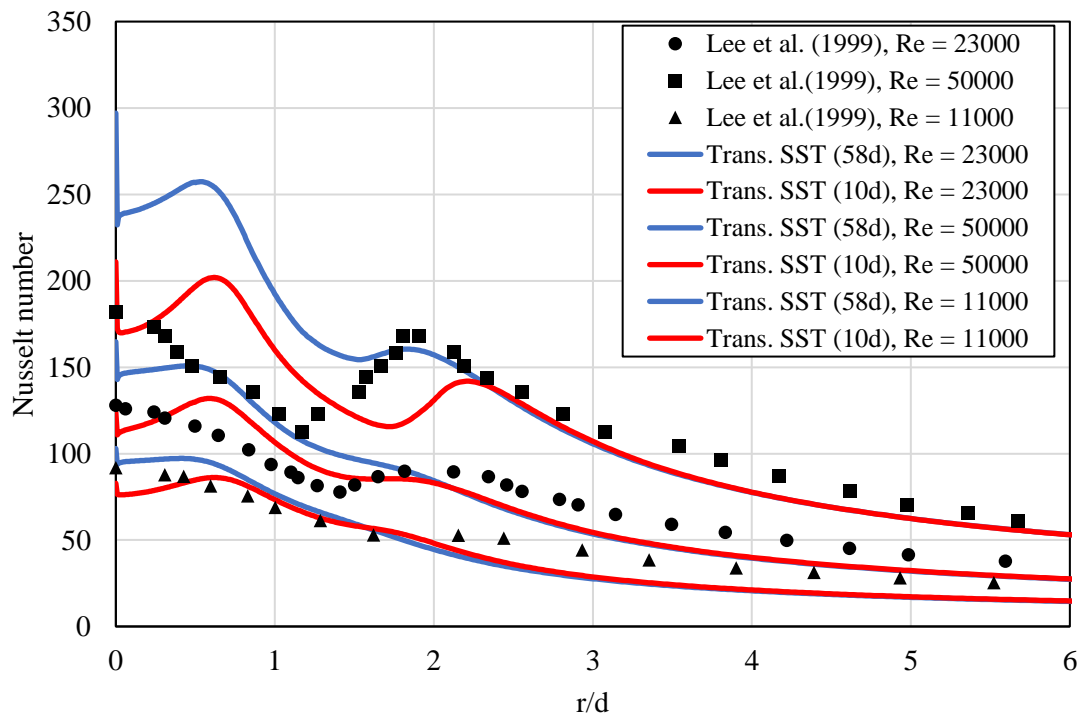
### E.2 Fully developed inlet profiles

According to Cengel and Ghajar (2015), for engineering applications, a tube length 10 times the diameter ( $d$ ) of the tube is sufficient for the turbulent flow of the pipe to fully develop. This is much shorter than the experimental setup of Lee and Lee (1999) for the flat plate impingement setup, and Lee et al. (1999) for the concave surface setup, which used a length of  $58 d$ . To ensure that the inlet flow

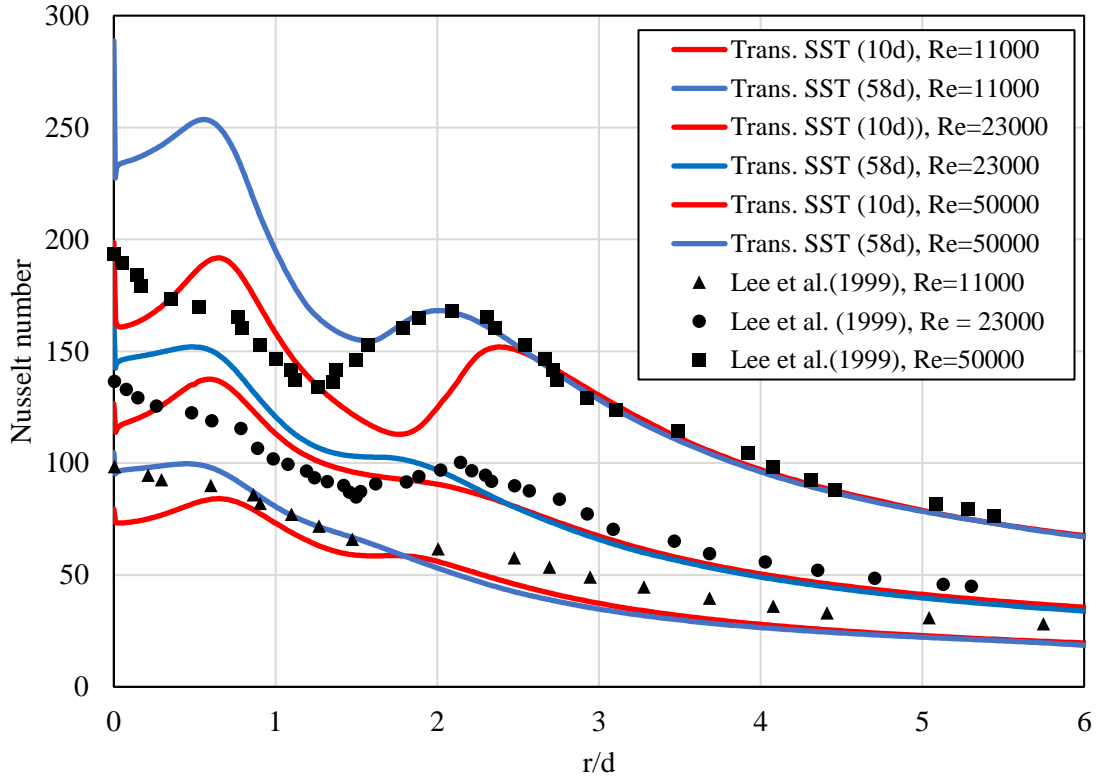
profile is developed fully enough for the study, the heat transfer results were compared with one another. Both pipe length setups were given the same inlet conditions, with a constant velocity equivalent to  $Re = 23\ 000$  (for the flat plate test). The turbulence intensity of the ANSYS Fluent standard built-in constant value of 5% was given. The results for the flat surface and the  $d/D = 0.056$  and  $0.089$  concave wall surface are displayed in Figure E.2.



(a)



(b)



(c)

**Figure E.2:** The inlet profiles of a 10 *d* vs 58 *d* tube length compared for: (a): the flat plate; (b):  $d/D = 0.056$ ; and (c):  $d/D = 0.089$  concave wall surface impingement models.

The results clearly show that, with both the flat plate and the concave surface, a significant difference in Nusselt number profiles is created with different lengths of tubes, especially in the double-peak ranging from the stagnation point up to dimensionless radii of 2.5.

The assumption therefore that a tube of length 10 *d* would be sufficient for a fully developed flow is wrong for impingement flow, since impingement heat transfer is clearly sensitive to the velocity profile at the tube outlet. For the validation study in Chapter 4.3.1 and Chapter 4.3.2, a velocity profile of 58 *d* was used.

### E.3 Inlet turbulence kinetic energy

During the initial analysis, it was noted that the inlet conditions other than the velocity had an influence on the results. To determine how much of an influence this has on the results, the test was conducted with the inlet turbulence kinetic energy (*k*) used as a variable. The turbulent kinetic energy correlates with the turbulence intensity, with the relationship defined as follows (ANSYS Fluent, 2006):

$$k = \frac{3}{2} (u_{avg} I)^2 \quad (E-1)$$

The average velocity of the fluid flow is represented by  $u_{avg}$  and the turbulence intensity by *I*. The test case of Lee et al. (1999) with diameter ratio  $d/D = 0.056$ , nozzle distance  $L/d = 2$  and Reynolds number  $Re = 50\,000$  was used to witness the influence that the turbulence at the inlet boundary has on the results, and can be seen in Figure E.3.

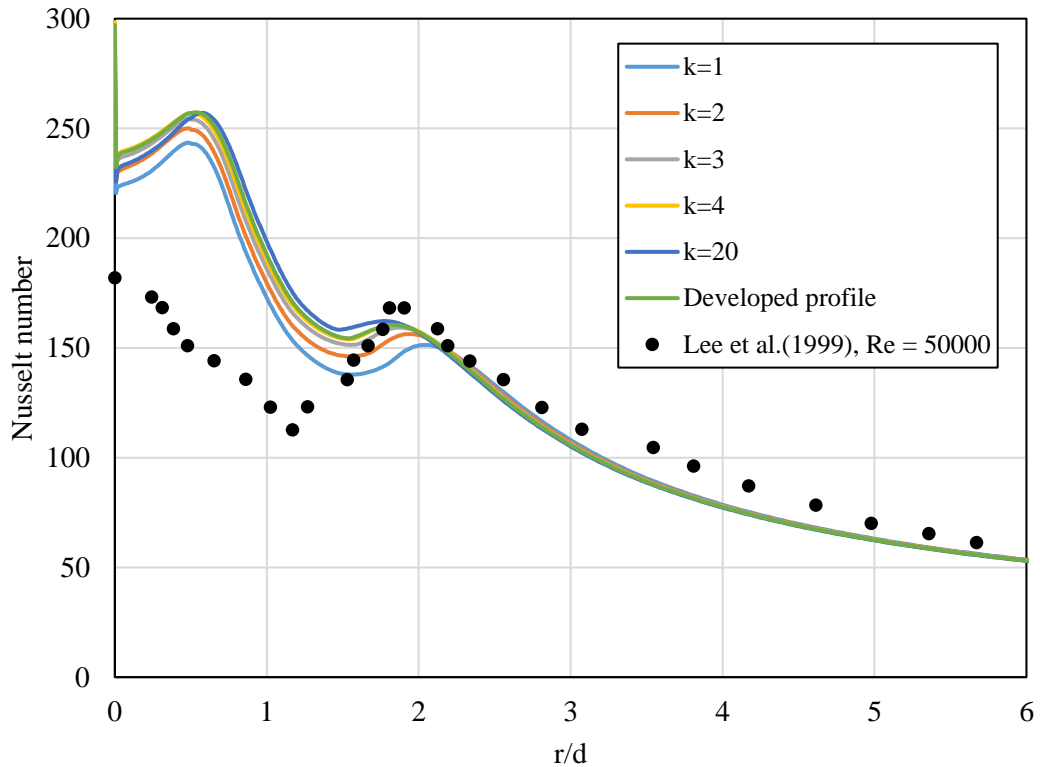


**Figure E.3: A comparison of the heat transfer effect of the different turbulence kinetic energy values ( $k$ ) on a concave surface, using the setup of Lee et al. (1999) as a test case for  $d/D = 0.056$ .**

Take note that the turbulence kinetic energy values were implemented at a distance of  $10d$  from the nozzle exit. From the results displayed in Figure E.3, it is interesting to see that the turbulence condition only has an effect on the region where the first and second Nusselt number peak is developed, after which these values converge to a similar profile further away from the impinging point.

The magnitudes of the two peaks increase with an increase in the  $k$ -values (and therefore an increase in the turbulence intensity). It is also interesting to note that the profile of the  $k$ -value at the inlet does not have a significant effect on the results. The average  $k$ -value for the implemented profile is approximately  $5.5 \text{ m}^2/\text{s}^2$ .

The test case of  $d/D = 0.089$  diameter ratio was also modelled for the same Reynolds number, also altering the  $k$ -values. The following results were obtained:

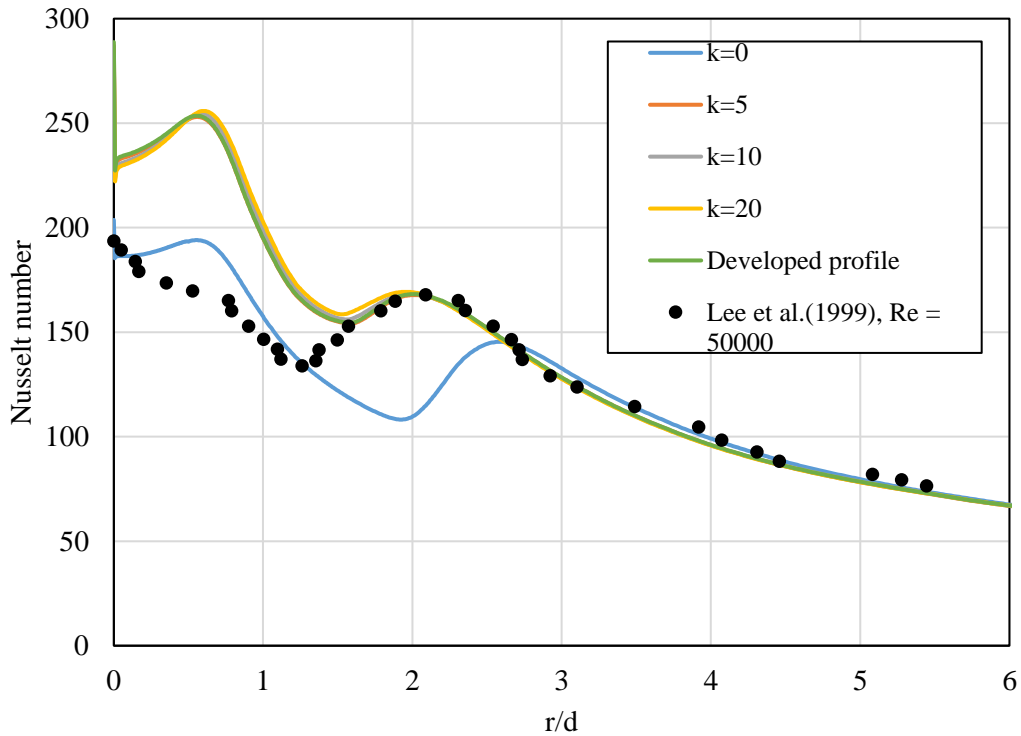


**Figure E.4:** A comparison of the heat transfer effect of the different turbulence kinetic energy values ( $k$ ) on a concave surface, using the setup of Lee et al. (1999) as a test case for  $d/D = 0.056$ .

With the  $k$ -values ranging from 0 to 20 in larger intervals, one can better observe how a great change in the turbulence kinetic energy at the inlet has a great effect on the heat transfer at the impingement region. There does not seem to be a major difference in the heat transfer for  $k$ -values larger than 5, as no turbulence intensity significantly reduces the peak heat transfers and shifts the second peak much further from the impinging zone compared to the other results. In this case, it is reconfirmed that the turbulence kinetic energy profile does not play a major role.

One could therefore conclude that the turbulence conditions defined at the model's inlet do not have a significant effect on the peak predictions of the heat transfer coefficient, except if one would like to apply small turbulence kinetic energy values. It also has an insignificant effect on the heat transfer further from the impingement zone.

#### E.4 Constant vs piecewise linear fluid properties

Lastly, a sensitivity study was conducted to define the fluid properties as constant versus fluid properties as a function of temperature. The author assumed that a piecewise linear approximation of the air properties using the tabled values from Cengel and Ghajar (2015) would be a more accurate way of modelling the setup. However, to see how much of an effect it has on the results, the test case for the diameter ratio  $d/D = 0.089$  and Reynolds number of 50 000 was used for comparison. The results obtained are shown in Figure E.5.

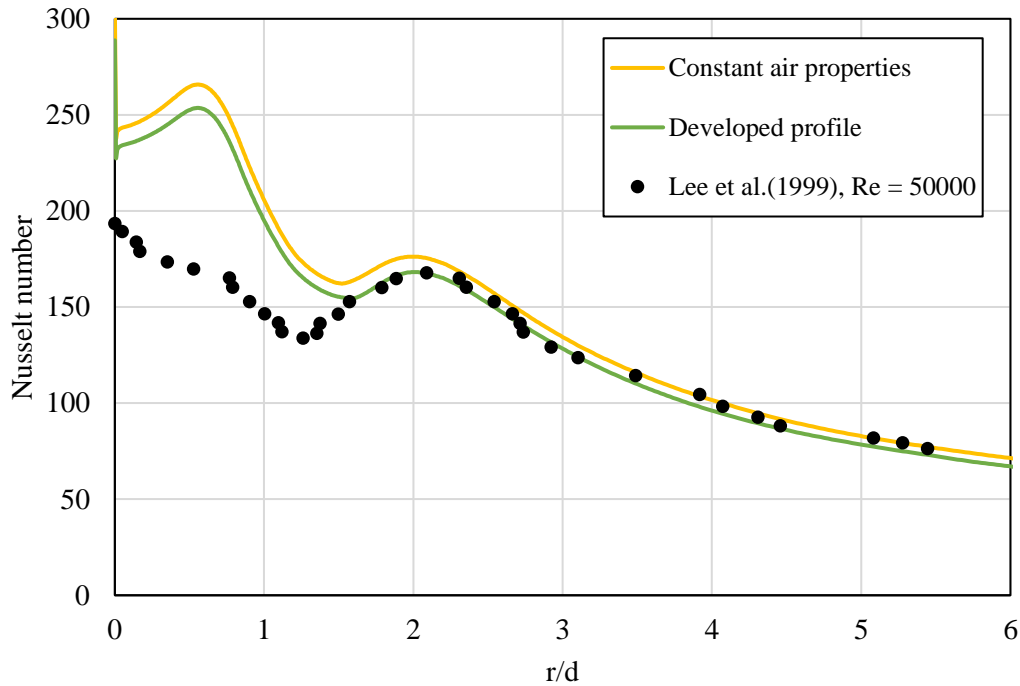
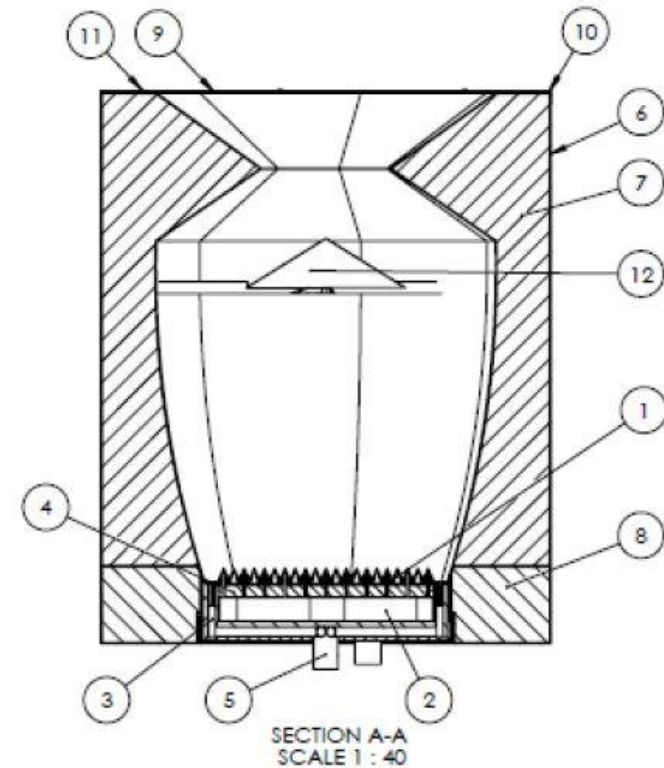
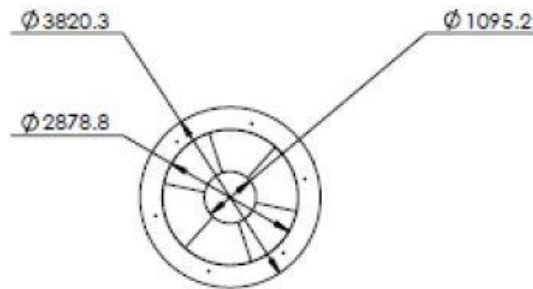
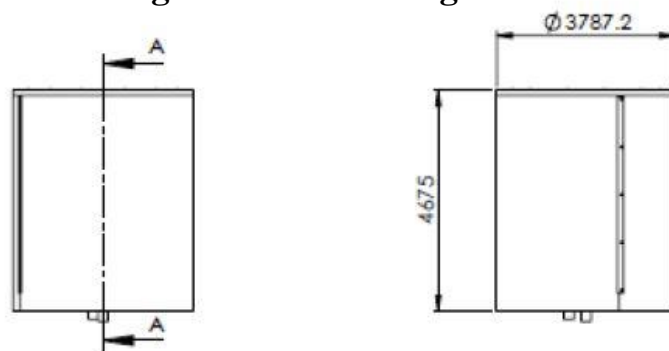


Figure E.5: A comparison between constant fluid properties and temperature-dependent fluid properties for the test case of Lee et al. (1999) with a diameter ratio of  $d/D = 0.089$  and  $Re = 50\ 000$ .

It is clear from the results displayed that there is a difference in the results, especially in the impingement region that forms the two peaks for the heat transfer coefficient. The more accurate temperature-dependent air properties are therefore implemented, especially for the modelling of these test cases.



### Appendix F Original receiver design

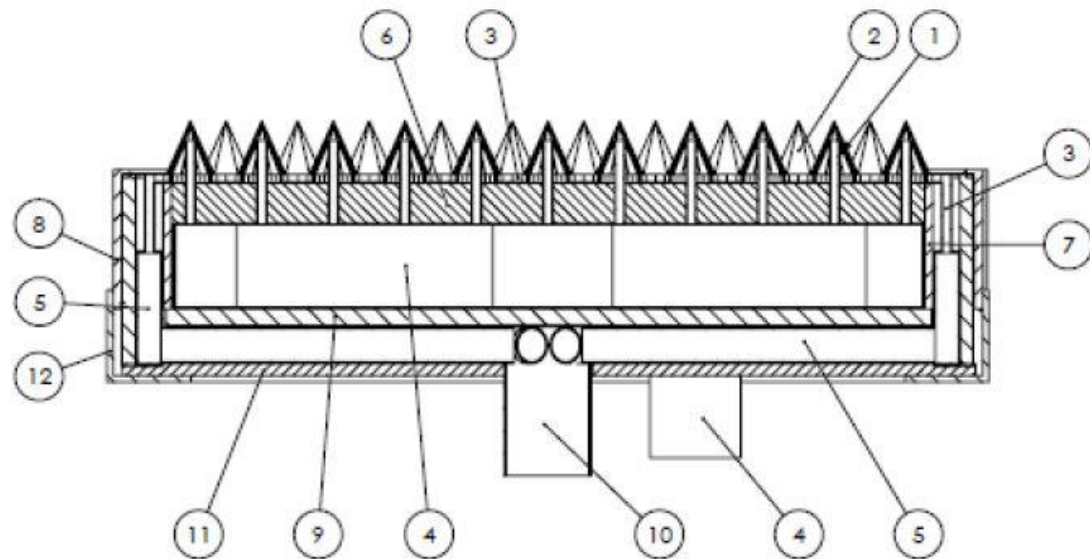
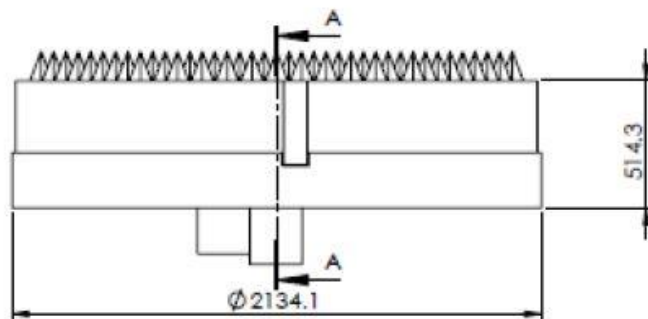


ITEM NO.	QTY.	DESCRIPTION	PART NUMBER	MATERIAL
1	1	Cold fluid piping sub assembly	MOX-SB01	310S STAINLESS STEEL
2	1	Cold fluid reservoir large	MOX-P04	310S STAINLESS STEEL
3	6	Hot fluid piping sub assembly	MOX-SB02	310S STAINLESS STEEL
4	1	Insulation interior	MOX-P06	MOLDIT D CASTABLE REFRACTORY
5	1	Hot fluid outlet	MOX-P10	310S STAINLESS STEEL
6	2	Outer cover	MOX-P15	316L STAINLESS STEEL
7	6	Insulation for outer cover	MOX-P16	MOLDIT D CASTABLE REFRACTORY
8	1	Insulation bottom	MOX-P17	MOLDIT D CASTABLE REFRACTORY
9	1	Glass cover	MOX-P18	SOLAR GLASS
10	1	Glass cover retaining ring	MOX-P19	316L STAINLESS STEEL
11	16	Hex bolt M20 x 2.5 x 80	B18.2.3.6M	STEEL
12	1	Cavity centre mirror	MOX-P20	316L STAINLESS STEEL

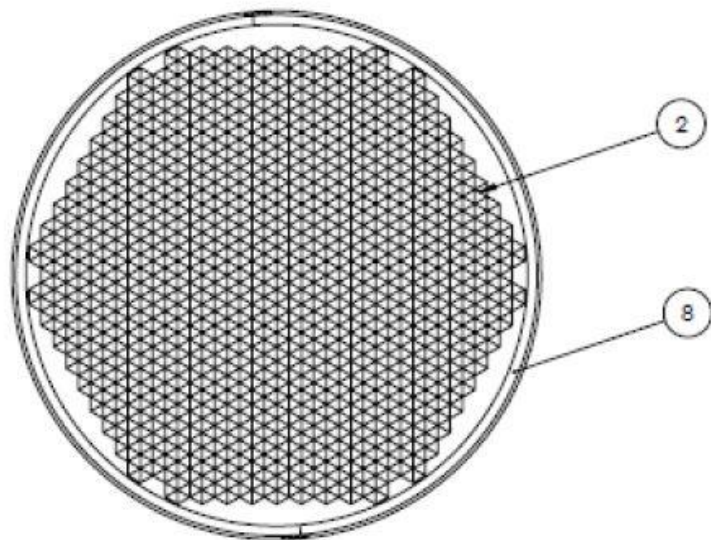
1. I declare that this assignment is my own work and I have read and understand the University's policy in this regard.  
 2. I declare that this drawing is my own original work.  
 3. I have not used any other student's work to hand in as my own.  
 4. I do not intend to allow anyone to copy my work with the intention of passing it off as his or her own work.

**SolidWorks Student Edition**  
**For Academic Use Only**

TOLERANCES	ITEM NR	QTY	DESCRIPTION	MATERIAL	ONDERDEEL NR
FROM - TO	ITEM NO	QUANTITY	BESKRYWING	MATERIAL	PART NR
0 - 6	VAN				
6 - 30	SURNAME	DA SILVA		M.C.	TITEL
30 - 100	STUDENTE NO	12020924		M	ASSEMBLY 1 OF 2
100 - 300	PROJEKSE				DRAWING NR
300 - 1000	PROJECTIE				DASILVA-005
1000 - 3000	ANGLES	1°			DATE
3000 - PLUS					2015/05/24



SECTION A-A  
SCALE 1 : 12



ITEM NO.	QTY.	DESCRIPTION	PART NUMBER	MATERIAL
1	325	Inner pyramid shell and pipe	MOX-P01	310S STAINLESS STEEL
2	325	Outer pyramid shell	MOX-P02	310S STAINLESS STEEL
3	30	Hot pipe down pipe	MOX-P03	310S STAINLESS STEEL
4	1	Cold fluid reservoir large	MOX-P05	310S STAINLESS STEEL
5	6	Hot fluid reservoir large	MOX-P07	310S STAINLESS STEEL
6	1	Insulation interior	MOX-P08	MOLDIT D CASTABLE REFRACTORY
7	1	Insulation in between	MOX-P09	MOLDIT D CASTABLE REFRACTORY
8	2	Retaining ring for piping system	MOX-P11	316L STAINLESS STEEL
9	1	Insulation back	MOX-P12	MOLDIT D CASTABLE REFRACTORY
10	1	Hot fluid outlet	MOX-P10	310S STAINLESS STEEL
11	1	Insulation back top	MOX-P13	MOLDIT D CASTABLE REFRACTORY
12	1	Retaining cover ring	MOX-P14	316L STAINLESS STEEL

1. I declare that this assignment is my own work and I have not copied or plagiarized any part of the University's policy in this regard.
2. I have not used any software to create this drawing or any other work.
3. I have not used any other student's work to hand in as my own.
4. I have not allowed, and will not allow, anyone to copy my work with the intention of passing it off as his or her own work.

TOLERANCES	ITEM NR	QUANTITY	BESKRYWING	MATERIAAL	ONDERDEEL NR
FROM-TO	ITEM NO	QUANTITY	DESCRIPTION	MATERIAL	PART NR
0-6	VAN		DA SILVA	M.C.	TITEL
6-30	SURNAME		DA SILVA	M	ASSEMBLY 2 OF 2
30-100	STUDENTE NO		12020924		TEKENING NR
100-300	STUDENTE NR				DASILVA-005
300-1000	PROJEKSE		UNIVERSITEIT VAN PRETORIA	A3	SKAAL
1000-3000	PROJECTIE		UNIVERSITY OF PRETORIA		SCALE
3000-PLUS					DATUM
ANGLES					DATE

## Appendix G Volumetric heat source implementation in ANSYS Fluent

Modelling thermal characteristics within the ANSYS Fluent CFD environment is an established and well-known method of computational modelling and prediction. In some cases, as was done during this study, the optical modelling of the solar receiver model was done on another platform, which in this study's case was the MCRT software SolTrace. In this section, the author introduces an approach that uses ANSYS Fluent features for the integration of the optical and thermal modelling by mapping the optical flux as a volumetric heat source within ANSYS Fluent.

The process to implement a source variation-based profile as source term within ANSYS Fluent is as follows:

1. When the Fluent case is set up, activate one user-defined scalar (UDS-0) for all cell zones (fluent and solid), and one user-defined memory (UDM-0) location under the user-defined section.
2. Under the heading initialisation, patch the value zero to UDS-0 and UDM-0 after selecting all the available zones.
3. In file/interpolate, select the cell zones that represent the heat source zones. Read the \*.ip file that provides the data of the flux that needs to be interpolated. If there are numerous interpolation files for different cell zones, select the cell zone with the intended interpolation file separately. This will interpolate the file to the UDS.
4. Interpret the user-defined function (UDF) by selecting the file under user-defined/functions/interpreted. When the UDF is selected, click Interpret. Following the explanation of the execution of the volumetric heat source implementation is the script of the UDF.
5. To copy the data from the UDS to the UDM, execute the command `uds_to_udm` in user-defined/execute on demand.
6. The UDS can now be switched off since the data is copied into the memory. This also saves computational memory during simulations.
7. The heat source can now be assigned to the corresponding cell zones by selecting the `udf solar_heat` as energy source term within the cell zone conditions of interest.

### G.1 UDF script

```
#include "udf.h"
#include "sg.h"
/*=====*/
DEFINE_ON_DEMAND(copy_uds_to_udm)
{
Domain* d=Get_Domain(1);
Thread *t;
cell_t c;
thread_loop_c(t,d)
{
begin_c_loop(c,t)
{
C_UDMI(c,t,0)=C_UDSI(c,t,0);
}
end_c_loop(c,t)
}
return;
```



```
}  
/*=====*/  
DEFINE_SOURCE(solar_heat,c,t,dS,eqn)  
{  
  real source;  
  dS[eqn]=0.0;  
  source=C_UDMI(c,t,0);  
  return source;  
}  
/*=====*/
```

## Appendix H Script for SolTrace simulation

The MCRT software SolTrace has a scripting environment that provides the user with the ability to automate otherwise difficult or time-consuming processes or setups. The following script is the general script that was used during optical analyses, although a few alterations were made in the process of simulation for the user's convenience. Some sections of the script were excluded, either since the mathematics had already been included in the study, or since the scripting becomes repetitive or redundant.

The script, which is in the format \*.lk, includes the following steps of the setup of the model, as well as the solving and post-processing actions:

- Import commands generated within the general-purpose, high-level programming language Python
- Import the central receiver heliostat field coordinates
- Sun unit vector calculations
- DNI calculations
- Configuration of sun shape
- Configuration of optical property data set
- Addition and configuration of the heliostat field and aperture
- Import and configure the receiver
- Tracing configuration
- Calculate and generate the required files

### H.1 SolTrace script

```

/* *****
   Python Commands
   ***** */
// Import commands from spreadsheet or text file

cwd("C:/Soltrace_files/Soltrace_Data");
py_file = open('simulation_list.txt', 'r');

xrow = [];
j = 0;
simulation_list = [];
line="";

while ( read_line( py_file, line ) )
{
    xrow = split(line, ',');
    simulation_list[j] = xrow[0];
    j = j + 1;
}
outln(simulation_list);
north_south = to_real(simulation_list[0]);
latitude_degrees = to_real(simulation_list[1]);
latitude_minutes = to_real(simulation_list[2]);
latitude_seconds = to_real(simulation_list[3]);

```



```
east_west = to_real(simulation_list[4]);
longitude_degrees = to_real(simulation_list[5]);
longitude_minutes = to_real(simulation_list[6]);
longitude_seconds = to_real(simulation_list[7]);
altitude = to_real(simulation_list[8]);
gmt = to_real(simulation_list[9]);
lst_or_lat = to_real(simulation_list[10]);
analyse_specific_time = to_real(simulation_list[11]);
solar_vector = to_real(simulation_list[12]);
track_model = to_real(simulation_list[13]);
dni_model = to_real(simulation_list[14]);
x = to_real(simulation_list[15]);
y = to_real(simulation_list[16]);
z = to_real(simulation_list[17]);
days = to_real(simulation_list[18]);
hour = to_real(simulation_list[19]);
amount_of_rays = to_real(simulation_list[20]);
dni_value = to_real(simulation_list[21]);
simulate_aperture = to_real(simulation_list[22]);
heliofield_file = simulation_list[27];
simulate_heliofield = to_real(simulation_list[29]);
simulate_receiver = to_real(simulation_list[30]);
project_name = simulation_list[31];
tower_height = to_real(simulation_list[32]);
aperture_angle = to_real(simulation_list[33]);
aperture_height = to_real(simulation_list[34]);
aperture_width = to_real(simulation_list[35]);
element_hit_file = to_real(simulation_list[36]);
ray_data_file = to_real(simulation_list[37]);
amount_of_seeds = to_real(simulation_list[38]);

/* *****
   SOLTRACE SCRIPT OF PS10 HELIOSTAT FIELD
   ***** */

cwd("C:/Users/marce/OneDrive/Documents/MEng/Week1_Soltrace/Soltrace_
files/Marcel");
ProjectName = project_name;

/* *****
   Coordinates of Elements
   ***** */
// Positive x = West
// Positive y = Zenith
// Positive z = North

// Coordinates of receiver
P2 = [0,tower_height,0];
```



```
// Import coordinates from spreadsheet or text file

file = open(heliofield_file, 'r');

element_coordinates = [[]];
xrow = [];
j = 0;
line="";

while ( read_line( file, line ) )
{
    xrow = split(line, ',');
    element_coordinates[j][0] = to_real(xrow[0]);
    element_coordinates[j][1] = to_real(xrow[1]);
    element_coordinates[j][2] = to_real(xrow[2]);
    j = j + 1;
}
no_heliostats = j;

/* *****
    Calculate Sun Unit Vector
    ***** */
//Calculations already included in the study

/* *****
    configure Direct Normal Irradiance
    ***** */
//Calculations already included in the study

/* *****
    configure Sun Shape
    ***** */
if (define_solar_vector == 1 || use_Muhammad_Iqbal == 1)
{
    Sun.useldh = false;
}
else
{
    Sun.useldh = true;
}
Sun.x = s[0];
Sun.y = s[1];
Sun.z = s[2];
Sun.lat = Phi;
Sun.day = dn;
Sun.hour = LAT;
Sun.shape = 'p';
```



```
Sun.halfwidth = 4.65;
sunopt(Sun);

/* *****
   configure an optical property data set
   ***** */

py_file = open('Soltrace_Data\\boundary_optics.txt', 'r');

xrow = [];
j = 0;
optical_properties = [];
line="";

while ( read_line( py_file, line ) )
{
    xrow = split(line, ',');
    optical_properties[j][0] = to_real(xrow[0]);
    optical_properties[j][1] = xrow[1];
    optical_properties[j][2] = xrow[2];
    optical_properties[j][3] = to_real(xrow[3]);
    optical_properties[j][4] = to_real(xrow[4]);
    optical_properties[j][5] = to_real(xrow[5]);
    optical_properties[j][6] = to_real(xrow[6]);
    optical_properties[j][7] = to_real(xrow[7]);
    optical_properties[j][8] = to_real(xrow[8]);
    optical_properties[j][9] = to_real(xrow[9]);
    optical_properties[j][10] = to_real(xrow[10]);
    j = j + 1;
}
no_optics = j;

clearoptics(); // remove any optical properties currently defined

for (j=0; j<(no_optics); j++)
{
    k = 1;
    i = 0;
    while (j > i)
    {
        if (optical_properties[j][2] == optical_properties[i][2])
            k = 0;
        i++;
    }
    if (k == 1)
    {
        addoptic(optical_properties[j][2]); // adds element to
current stage
    }
}
```

```

general_optics_front.refl = optical_properties[j][3];
general_optics_front.trans = optical_properties[j][4];
general_optics_front.errslope = optical_properties[j][5];
general_optics_front.errspec = optical_properties[j][6];
general_optics_back.refl = optical_properties[j][7];
general_optics_back.trans = optical_properties[j][8];
general_optics_back.errslope = optical_properties[j][9];
general_optics_back.errspec = optical_properties[j][10];

        opticopt( optical_properties[j][2], 1,
general_optics_front);
        opticopt( optical_properties[j][2], 2,
general_optics_back);
    }
}

/* *****
    add heliostat field
***** */

y_aper_aim = tand(aperture_angle)*(-1);
aperture_aim = [0,y_aper_aim,1];
outln("aperture_aim = "+aperture_aim);

clearstages(); // clear the system

if (simulate_heliofield == 1)
{
    addstage( 'heliostat_field' );

    // we need to set the current stage to be active so we can add
elements to it
    activestage( 'heliostat_field' );

    for (j=0; j<(no_heliostats); j++)
    {
        addelement(); // adds element to current stage

        heliostat_width = 12.84;
        heliostat_height = 9.45;
        k = 115; // constant
        f = 359.83; // focal length
        c = 1/(2*f);

        Heliostat_details.en = true;
        Heliostat_details.x = element_coordinates[j][0];
        Heliostat_details.y = element_coordinates[j][1];
        Heliostat_details.z = element_coordinates[j][2];
    }
}

```



```
//calculate normal vector
t = [];
n = [];
t_mag = sqrt(pow((P2[0] - Heliostat_details.x),2) +
pow((P2[1] - Heliostat_details.y),2) + pow((P2[2] -
Heliostat_details.z),2));
t[0] = (P2[0] - Heliostat_details.x)/t_mag;
t[1] = (P2[1] - Heliostat_details.y)/t_mag;
t[2] = (P2[2] - Heliostat_details.z)/t_mag;

n[0] = (t[0]+
s[0])/(sqrt(2*(1+(s[0]*t[0]+s[1]*t[1]+s[2]*t[2]))));
n[1] = (t[1] +
s[1])/(sqrt(2*(1+(s[0]*t[0]+s[1]*t[1]+s[2]*t[2]))));
n[2] = (t[2] +
s[2])/(sqrt(2*(1+(s[0]*t[0]+s[1]*t[1]+s[2]*t[2]))));

Heliostat_details.ax = Heliostat_details.x + k*n[0];
Heliostat_details.ay = Heliostat_details.y + k*n[1];
Heliostat_details.az = Heliostat_details.z + k*n[2];
Heliostat_details.zrot = 0;
Heliostat_details.aper =
['r',heliostat_width,heliostat_height,0,0,0,0,0,0];
Heliostat_details.surf = ['p',c,c,0,0,0,0,0,0];
Heliostat_details.optic = optical_properties[0][2];

elementopt( j, Heliostat_details );
}
/* *****
add a single flat surface as flat receiver
***** */

addstage( 'flat_aperture_stage' );

activestage( 'flat_aperture_stage' );

Flat_aperture_details.virtual = true;
Flat_aperture_details.multihit = false;
Flat_aperture_details.tracethrough = false;
Flat_aperture_details.x = P2[0];
Flat_aperture_details.y = P2[1];
Flat_aperture_details.z = P2[2];
Flat_aperture_details.ax = P2[0] + aperture_aim[0];
Flat_aperture_details.ay = P2[1] + aperture_aim[1];
Flat_aperture_details.az = P2[2] + aperture_aim[2];
Flat_aperture_details.zrot = 0;
```

```

stageopt('flat_aperture_stage',Flat_aperture_details);

addelement(); // adds element to current stage

Receiver_details.en = true;
Receiver_details.x = 0;
Receiver_details.y = 0;
Receiver_details.z = 0;
Receiver_details.ax = 0;
Receiver_details.ay = 0;
Receiver_details.az = 1;
Receiver_details.zrot = 0;
Receiver_details.aper =
['c',1.0952,0,0,0,0,0,0,0];//[ 'r',aperture_width,aperture_height,0,0
,0,0,0,0];
Receiver_details.surf = ['f',0,0,0,0,0,0,0,0];
Receiver_details.optic = optical_properties[1][2];
elementopt( 0, Receiver_details );
}
/* *****
Import receiver elements
***** */

if (simulate_receiver == 1)
{
py_file = open('Soltrace_Data\\receiver_coordinates.txt', 'r');
xrow = [];
j = 0;
receiver_coordinates = [];
line="";

while ( read_line( py_file, line ) )
{
xrow = split(line, ',');
receiver_coordinates[j][0] = to_real(xrow[0]);
receiver_coordinates[j][1] = to_real(xrow[1]);
receiver_coordinates[j][2] = to_real(xrow[2]);
receiver_coordinates[j][3] = to_real(xrow[3]);
receiver_coordinates[j][4] = to_real(xrow[4]);
receiver_coordinates[j][5] = to_real(xrow[5]);
receiver_coordinates[j][6] = to_real(xrow[6]);
receiver_coordinates[j][7] = to_real(xrow[7]);
receiver_coordinates[j][8] = to_real(xrow[8]);
receiver_coordinates[j][9] = to_real(xrow[9]);
receiver_coordinates[j][10] = to_real(xrow[10]);
receiver_coordinates[j][11] = to_real(xrow[11]);
receiver_coordinates[j][12] = to_real(xrow[12]);
receiver_coordinates[j][13] = to_real(xrow[13]);
}
}

```



```
        receiver_coordinates[j][14] = to_real(xrow[14]);
        j = j + 1;
    }
    no_receiver_elements = j;

    addstage( 'receiver_stage' );

    activestage( 'receiver_stage' );

    Receiver_details.virtual = false;
    Receiver_details.multihit = true;
    Receiver_details.tracethrough = false;
    if (simulate_heliofield == 1)
    {
        Receiver_details.x = P2[0];
        Receiver_details.y = P2[1];
        Receiver_details.z = P2[2];
        Receiver_details.ax = P2[0] + aperture_aim[0];
        Receiver_details.ay = P2[1] + aperture_aim[1];
        Receiver_details.az = P2[2] + aperture_aim[2];
        Receiver_details.zrot = 0;
    }
    else
    {
        Receiver_details.x = 0;
        Receiver_details.y = 0;
        Receiver_details.z = 0;
        Receiver_details.ax = 0;
        Receiver_details.ay = 0;
        Receiver_details.az = 1;
        Receiver_details.zrot = 0;
    }
    stageopt('receiver_stage',Receiver_details);

    for (j=0; j<(no_receiver_elements); j++)
    {
        addelement(); // adds element to current stage
        receiver_details.en = true;
        receiver_details.x = receiver_coordinates[j][0];
        receiver_details.y = receiver_coordinates[j][1];
        receiver_details.z = receiver_coordinates[j][2];
        receiver_details.ax = receiver_coordinates[j][3];
        receiver_details.ay = receiver_coordinates[j][4];
        receiver_details.az = receiver_coordinates[j][5];
        receiver_details.zrot = receiver_coordinates[j][6];
        receiver_details.aper =
['i',receiver_coordinates[j][7],receiver_coordinates[j][8],receiver_
```



```
coordinates[j][9],receiver_coordinates[j][10],receiver_coordinates[j]
][11],receiver_coordinates[j][12],0,0];
    receiver_details.surf = ['f',0,0,0,0,0,0,0,0];
    for (k=0; k<(no_optics); k++)
    {
        if (receiver_coordinates[j][14] ==
optical_properties[k][0])
        {
            receiver_details.optic =
optical_properties[k][2];
        }
    }
    receiver_details.comment = receiver_coordinates[j][13];

    elementopt( j, receiver_details );
}
/* *****
start the trace
***** */

for (seed=1; seed<(amount_of_seeds+1); seed++)
{
    traceopt({ 'rays'= amount_of_rays , 'maxrays' =
10*amount_of_rays , 'seed'=seed , 'cpus'=5 , 'include_sunshape'=true
, 'optical_errors'=true} );
    trace();

/* *****
Write all Ray Data to File
***** */

    Inters=nintersect();

    if (ray_data_file == 1)
    {
        j=0;
        k=0;
        TEMP = "PosX,PosY,PosZ,Element,Stage,RayNumber";
        fileID=cwd() + '\\Soltrace_Data\\' + ProjectName +
'\\trace_results_day_'+dn+'_hour_'+LAT+'_seed_'+seed+'_angle_'+apert
ure_angle+'_rays_'+amount_of_rays;

        if (file_exists(fileID))
            {remove_file(fileID);}
        file = open(fileID,'w');
        write_line(file,TEMP);
        while (j < Inters)
        {
```



```
temp=raydata(j);
if (temp[6]!=0)
{
    TEMP =
temp[0]+", "+temp[1]+", "+temp[2]+", "+temp[6]+", "+temp[7];
    write_line(file,TEMP);
    k = k+1;
}
j=j+1;
}
close(fileID);
}
```